NOTICE

The quality of this microform is heavily dependent upon the quality of the original thesis submitted for microfilming. Every effort has been made to ensure the highest quality of reproduction possible.

If pages are missing, contact the university which granted the degree.

Some pages may have indistinct print especially if the original pages were typed with a poor typewriter ribbon or if the university sent us an inferior photocopy.

Reproduction in full or in part of this microform is governed by the Canadian Copyright Act, R.S.C. 1970, c. C-30, and subsequent amendments.

AVIS

La qualité de cette microforme dépend grandement de la qualité de la thèse soumise au microfilmage. Nous avons tout fait pour assurer une qualité supérieure de reproduction.

S'il manque des pages, veuillez communiquer avec l'université qui a conféré le grade.

La qualité d'impression de certaines pages peut laisser à désirer, surtout si les pages originales ont été dactylographiées à l'aide d'un ruban usé ou si l'université nous a fait parvenir une photocopie de qualité inférieure.

La reproduction, même partielle, de cette microforme est soumise à la Loi canadienne sur le droit d'auteur, SRC 1970, c. C-30, et ses amendements subséquents.

A Three Dimensional Model for Vertical Piles in Sand

Tuong Quy Nguyen

A Thesis

in

The Department

of

Civil Engineering

Presented in Partial Fulfillment of the Requirements

for the Degree of Doctor of Philosophy at

Concordia University

March 1991

ISBN 0-315-64756-6

ABSTRACT

A Three Dimensional Model for Vertical Piles in Sand

Tuong Quy Nguyen, Ph.D.

Concordia University, 1991

Theoretical and experimental investigations on the bearing capacity of vertical single piles in sand were conducted. A three dimensional model was developed utilizing the method of slices to incorporate salient features previously neglected in conventional bearing capacity theories. These features include adopting punching shear as the principal mode of failure and taking into account the interdependence between point resistance and skin friction. In this investigation, the punching shear failure was formulated by assuming a variable failure mechanism associated with a variable shearing resistance mobilized along critical surfaces. The theoretical model suggests that the relatively constant point resistance below the critical depth may be explained by a variable failure mechanism becoming more restricted with the increase of depth. The model, however, appears to concur with recent findings which indicate that the average unit skin friction continues to increase with depth. It is also clearly demonstrated that the model can realistically predict the existing skin friction once the point resistance is known.

Laboratory tests were conducted on large model piles instrumented with pressure transducers and load cells. A sand placing technique was developed and calibrated to ensure the reproducibility of the desired sand density. A design procedure is proposed and examined against the present experimental data as well as available laboratory and field test results. Recommendations are given for future research work in this field.

ACKNOWLEDGEMENTS

The research program was conducted at Concordia under the supervision of Dr. A.M. Hanna. Foremost, I am indebted to Dr. Hanna for his constant interest in this investigation. His assistance, patience and valuable encouragement throughout the research is greatly appreciated. I wish to express my deep and sincere gratitude to him for his insightful wisdom of a Zen master who knows "the best way to tame a wild horse is to let it roam in a well-fenced green meadow to its heart content".

I would like to thank Dr. H.B. Poorooshasb for his consistent support of quality laboratory teaching throughout the years. His kind advices at critical times will always be treasured.

I want to especially thank Dr. M.R. Madhav (a visiting professor from the Institute of Technology, Kanpur, India) for many stimulating and fruitful discussions during his stay at Concordia University in 1986-1987. Helpful comments received from Dr. Gopal Ranjan (Roorkee University, Roorkee, India) are acknowledged.

I am thankful to many individuals whom I have contacted at various stages of this research, either directly or by correspondence, for their comments:

- Dr. G.G. Meyerhof (Nova Scotia Technical College)
- Dr. J.M. Duncan (Virginia Polytechnic Institute and State University)
- Professor J.C. Osler (McGill University).

Thanks also go to Mr. T. Heasman and his staff in the Machine Shop, Mr. L. Stanké and Mr. J. Elliot, Technical Officers, for many hours of consultation.

Mr. R. Lombardo and Mr. D. Roy deserve special mentions for their highly professional assistance during the experimental program. Thanks are also due Mr. D. Juras, who provided superb technical support for all electronic equipments; and my brother, Mr. Trong Tuan Nguyen, Architect, for help with the technical drawings. I am thankful to the National Research Council of Canada for the financial assistance during the first three years of this research program.

Ms. Jane Venettacci kindly and patiently helped in typing this thesis. Arrangement in the final format is due Dr. Ashraf Ghaly's wizardry with the Macintosh.

I could not have returned to school without the encouragement of my parents. Neither could I have managed my prolonged sojourn at Concordia University without my wife, Kim Thoa, whom I am deeply indebted for her support, patience and understanding.

TO

MY WIFE

AND

MY PARENTS

TABLE OF CONTENTS

LIST OF SYMBOLS

A_p	=	Cross section area of pile tip
A_s	=	Surface area of pile shaft
a_i	=	Generating area of slice i
B	=	Diameter of pile
b	=	A coefficient associated with a log-spiral
C	=	Perimeter of pile
D	=	Pile embedment length
D_R	=	Relative density of sand
e	=	Void ratio
e_{max}	=	Maximum void ratio
e_{min}	=	Minimum void ratio
f_s	=	average unit skin friction
f_z	=	Local unit skin friction
F_i	=	External force on slice i
F_N	=	Normal force acting on side of central wedge
F_T	=	Shear force acting side of central wedge
FH_i	=	Horizontal component of F_i
FV_i	=	Vertical component of F_i
K_o	=	Coefficient of earth pressure at-rest
K_z	=	Coefficient of earth pressure on pile shaft
K_s^*	=	Equivalent coefficient of earth pressure on pile shaft
K_T	=	Coefficient of earth pressure on tangential plane
K_s	=	Local coefficient of earth pressure on pile shaft
L_1	=	Length of vertical boundary of zone of influence
N_c, N_q, N_γ	=	Bearing capacity factors
N_q^*	=	Equivalent bearing capacity factor
$N_{\gamma q}$	=	Resultant bearing capacity of N_q and N_γ
N_1	=	Normal force acting on terminal radial surface
N_i, N_{i+1}	=	Normal components of side forces of slice i

N_i' = Normal component of basal force of slice i

Q_p = Point resistance of pile

Q_s = Skin friction of pile

Q_u = Ultimate bearing capacity of pile

q_p = Unit point resistance of pile

r = Radius of a log-spiral

r_o = Reference radius of a log-spiral

R = Radius of influence

T_1 = Shear force acting on terminal radial surface

T_i' = Tangential component of basal force of slice i

T_i, T_{i+1} = Tangential components of side forces of slice i

v_i = Volume of slice i

W_c = Weight of central cone of soil beneath pile tip

W_1, W_2, W_3 = Weights of soil

w_i = Weight of slice i

x_i = Basal slope of slice i

β = Inclination of terminal radial surface

γ = Bulk unit weight of soil

γ' = Effective unit weight of soil

δ = Angle of friction between pile shaft and sand

δ_z = Local angle of friction between pile shaft and sand

ΔQ_p = Point resistance corresponding to central angle of rotation $\Delta\zeta$

ΔQ_s = Skin friction corresponding to central angle of rotation $\Delta\zeta$

$\Delta\zeta$ = Central angle of rotation

$\Delta\theta_i$ = Apex angle of slice i

θ = Apex angle of radial shear zone

θ_i = Polar angle of a point on a log-spiral

ρ_i = Distance from pile axis to centroid of generating area a_i of slice i

ρ_G = Distance from pile axis to centroid of a plane area

σ_m = Mean normal ground stress

σ_o' = Effective vertical stress at pile tip level

σ_r' = Effective normal stress on pile shaft

σ_z' = Effective vertical stress at depth z

τ_f = Shear stress on pile shaft

$\underline{\phi}$	=	Angle of shearing resistance of sand
$\bar{\phi}$	=	Average angle of shearing resistance of two-layered soil
ϕ_B	=	Locally mobilized angle of shearing resistance on log spiral
ϕ_β	=	Locally mobilized angle of shearing resistance on terminal radial surface
ϕ_{Bi}	=	Mobilized angle of shearing resistance at mid-point of base of slice i
ϕ_{Si}, ϕ_{Si+1}	=	Average angles of shearing resistance along sides of slice i
ψ	=	Basal angle of central wedge
ω_i, ω_{i+1}	=	Inclinations of sides of slice i

LIST OF FIGURES

LIST OF TABLES

CHAPTER 1

INTRODUCTION

1.1 GENERAL

Piles have become increasingly preferred over shallow foundations in carrying heavy loads, especially if the soil strength at shallow depth is inadequate to support the foundation loads. In effect, piles are relatively long and slender structural members used to transmit loads through weak soil strata to a deeper and more competent soil or rock formation. In evaluating the adequate safety against failure of a single pile driven in sand, it is customary to separate the pile bearing capacity into two independent components: the point resistance and the skin friction. While there is some theoretical basis for computing the former, the estimation of the latter depends virtually on empirical rules. Fortunately, since separating pile bearing capacity into independent components is entirely artificial, a distinct possibility emerges for a more rational approach which may account for the interdependence between point resistance and skin friction within the same failure mechanism. In addition, most assumptions on failure mechanisms in conventional bearing capacity theories for deep foundations appear simplistic in the face of much more complex failure modes of piles in sand. Postulates such as "invariable shear patterns, associated with a general shear failure under plane strain conditions" abound in literature. The unsatisfactory outcomes, however, clearly demonstrate that conventional bearing capacity theories are hardly adequate in explaining several important experimental results, even with further speculative postulates.The critical depth concept for piles in sand is an outstanding example in question. In view of these serious limitations, rational approaches are clearly needed to provide a firm theoretical basis for estimating the ultimate bearing capacity of an axially loaded single pile in sand.

1.2 PURPOSE AND SCOPE OF THESIS

The main objectives of the present investigation are:

a. To review and discuss the limitations of basic assumptions of important bearing capacity theories for piles in sand.

b. To develop a theoretical model which is capable of incorporating three salient features usually neglected in previous pile bearing capacity theories. Firstly, the bearing capacity problem is treated as an axisymmetric case. Secondly, punching shear failure is adopted as the principal failure mode for piles in sand. And finally, the interdependence between point resistance and skin friction is taken into account in the same failure mechanism.

1.3 ORGANIZATION OF THESIS

A brief literature review of the subject of this thesis is presented in chapter 2. The present investigation is theoretical, supplemented by an experimental program involving load tests on model piles. In chapter 3, a description of types of equipment, materials, test set-up and procedure is presented, followed by results of load tests on two instrumented model piles. The development of a three dimensional model for pile bearing capacity, which adopts the punching shear failure mode and takes into account the interdependence between point resistance and skin friction of a single pile in sand, appears in chapter 4. Following a parametric study which identifies important variables affecting pile bearing capacity, the validity of the proposed model is confirmed by analysis of laboratory and field load tests. Chapter 4 concludes with a practical design procedure for estimating bearing capacity of single piles driven in sand. Conclusions drawn from the present study and recommendations for future study are given in chapter 5.

CHAPTER 2

LITERATURE REVIEW

2.1 GENERAL

Although numerous studies have been reported in the literature over the years, most present-day foundation engineers still have to rely heavily on a few semi-empirical design charts (i.e. Meyerhof, 1976; Coyle and Castello, 1981) in their preliminary designs of pile foundations in cohesionless soils. Before any attempt to develop more rational solutions, it is prudent to be well acquainted with basic assumptions employed in previous investigations. In this chapter, important bearing capacity theories for deep foundations are briefly reviewed, with an emphasis on the limitations of failure mechanisms assumed therein.

2.2 ULTIMATE BEARING CAPACITY

There are two conventional approaches in calculating the ultimate bearing capacity of a single pile in cohesionless soils: the static approach, which relates the measured soil properties to the pile load capacity; and the dynamic approach, which estimates the load capacity of a driven pile from analysing pile driving data. Only the static approach is reviewed here because of its direct relevance to the present study.

The ultimate bearing capacity of a single pile driven in a homogeneous sand deposit consists of two components: the load transmitted along the pile shaft and the load at the pile tip. These two components are usually referred to as the skin friction and point resistance, respectively (Fig. 2.1).

Hence,

$$Q_u = Q_s + Q_p \qquad \text{... (2.1)}$$

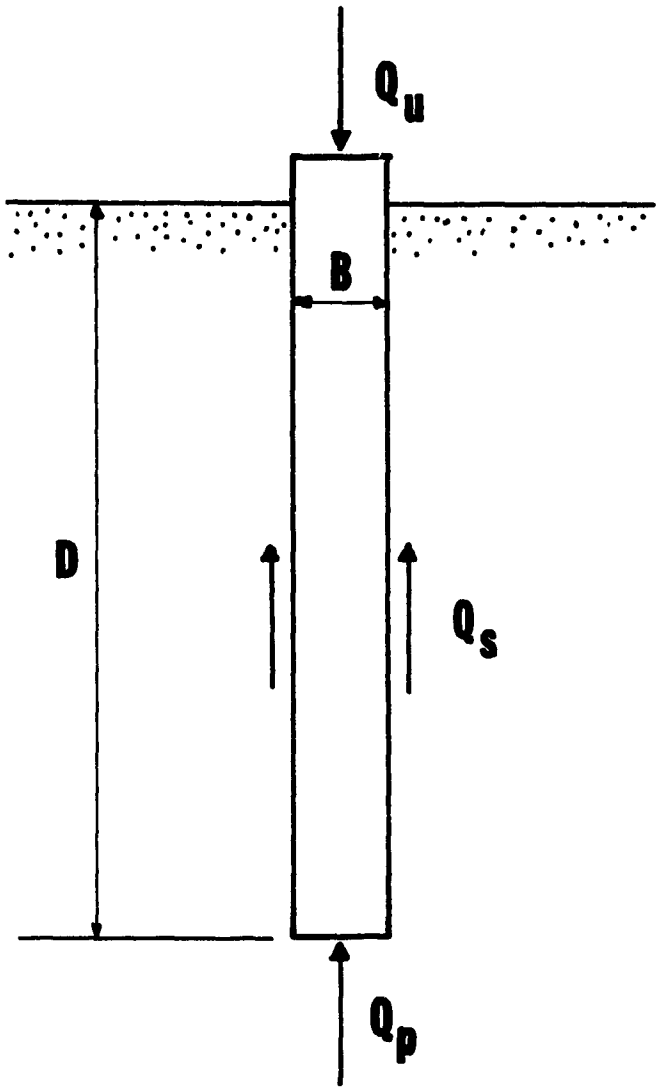

Fig. 2.1 Basic Pile Foundation Problem

where

Q_u = ultimate bearing capacity of pile

Q_s = skin friction

Q_p = point resistance.

2.2.1 Skin Friction

The skin friction has been usually evaluated by integrating the pile-sand shear stress τ_f at depth z over the surface area of the shaft. The shear stress τ_f is normally assumed to be proportional to the effective normal stress σ'_n exerted on the pile by the surrounding sand at the same depth.

Thus,

$$\tau_f = \sigma'_n \tan \delta_z \qquad \text{...(2.2)}$$

Where:

δ_z = angle of friction between pile and sand at depth z.

The effective normal stress σ'_n can be expected in terms of the effective vertical stress σ'_z as:

$$\sigma'_n = K_z \sigma'_z \qquad \text{... (2.3)}$$

Where

K_z = coefficient of lateral earth pressure on pile shaft at depth z.

By combining Eq. (2.2) and (2.3),

$$\tau_f = \sigma'_z K_z \tan \delta_z$$

Then,

$$Q_s = \int_0^D C \tau_f \, dz$$

$$Q_S = C \int_0^D \sigma_z' K_z \tan \delta_z \, dz \qquad \text{... (2.4)}$$

Where

C = pile perimeter

D = pile embedment length.

The effective vertical stress σ_n' is conventionally assumed to be equal to the effective overburden pressure at the same depth $\gamma' z$, while K_z and δ_z take on average values K_s and δ, respectively, over the entire pile length.

$$Q_s = C (K_s \tan \delta) \int_0^D \gamma' z \, dz = \frac{1}{2} C (K_s \tan \delta) \gamma' D^2$$

$$Q_s = \left(\frac{1}{2} K_s \gamma' D \tan \delta\right) A_s = f_s A_s \qquad \text{... (2.5)}$$

Where

A_s = surface area of pile shaft of length D

γ' = effective unit weight of sand

$f_s = \frac{1}{2} K_s \gamma' D \tan \delta$ = average unit skin friction over pile embedment length D.

Eq. (2.5) appears simple but entails difficulties in application, especially in estimating the average coefficient of earth pressure K_s. The magnitude of K_s has been found to depend on many factors, such as angle of shearing resistance, deformation characteristics and the initial state of stress of the sand deposit, pile shape (straight-sided or tapered), pile installation method, and loading direction (McClelland et al., 1967). Figure 2.2 shows some typical

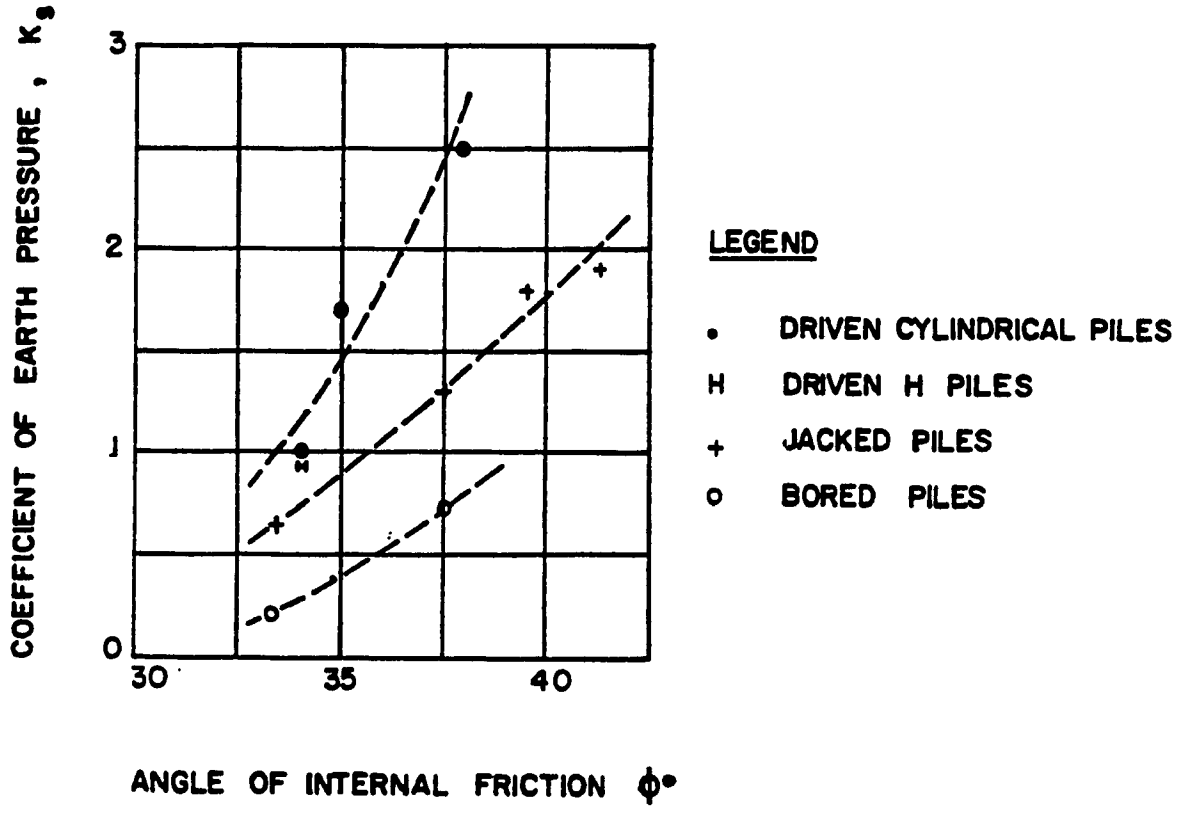

Fig. 2.2 Coefficient of Earth Pressure on Pile Shaft of Piles in Sand (Meyerhof, 1976)

values of K_s. The average angles of friction between sand and different pile materials were determined by Potyondy (1961) and Broms & Silberman (1964), using direct shear machines. Table 2.1 provides representative values of δ.

Measurements of skin friction on instrumented piles driven in relatively homogeneous sand deposits (D'Appolonia & Romualdi, 1963; Mohan et al., 1963; Vesic, 1967; Coyle & Sulaiman, 1967) generally suggested that the local unit skin friction f_z distribution along pile shafts is parabolic, similar to that in Fig. 2.3. The reduction of the local unit skin friction in the lower region of pile shafts driven in sand was attributed to the associated decrease in the lateral earth pressure caused by the radial movement of sand within the shear zone developed in the pile tip vicinity (Mohan et al., 1963).

Extensive experimental work using full-scale piles in laboratory conditions (Kerisel, 1961; Vesic, 1967) and pile load tests in the field (Vesic, 1967; Tavenas, 1971; Hanna & Tan, 1973) showed that the average unit skin friction f_s increases linearly with depth, as indicated by Eq. (2.5), only to a critical depth varying from approximately 10 pile diameters in loose sand to about 20 pile diameters in dense sand. Beyond this critical depth, f_s reaches asymptotically a constant value which depends only on the sand density and not on the effective overburden pressure (Fig. 2.4). Recently, further accumulation of field evidences tends to challenge this conclusion. Coyle and Castello (1981) analyzed a large number of pile load tests and proposed design charts which clearly showed the unit skin friction f_s continue to increase with depth. Concurring with this view, Kulhawy (1984) argued that the apparent limiting value of f_s was purely coincidental, and even the whole critical depth concept was a fallacy.

2.2.2 Point Resistance

The ultimate point resistance of an axially loaded vertical pile in sand is conventionally

Table 2.1: Angle of Friction Between Sand and Pile Material.

PILE MATERIAL	POTYONDY (1961)		BROMS & SILBERMAN (1964)
	SURFACE CONDITION	δ/ϕ	δ
STEEL	SMOOTH	0.54	20°
	ROUGH	0.76	
WOOD	PARALLEL TO GRAIN	0.76	0.75 ϕ
	AT RIGHT ANGLE TO GRAIN	0.88	
CONCRETE	SMOOTH	0.76	0.66 ϕ
	GRAINED	0.88	
	ROUGH	0.98	

REMARK:

ϕ = angle of shearing resistance of sand (degrees).

δ = angle of friction between sand and pile material (degrees).

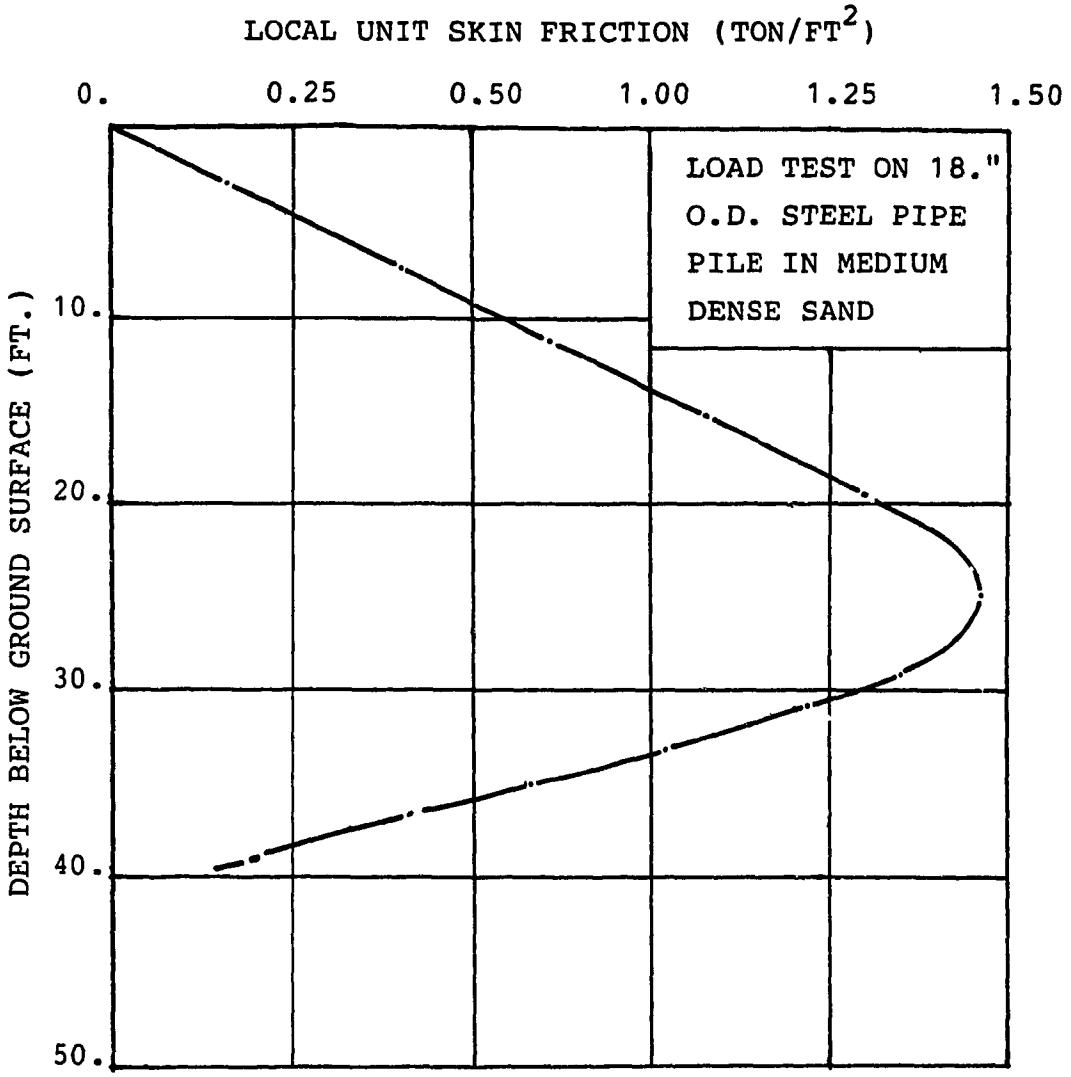

Fig. 2.3 Distribution of Local Unit Skin Friction Along Pile Shaft (Vesic,1967)

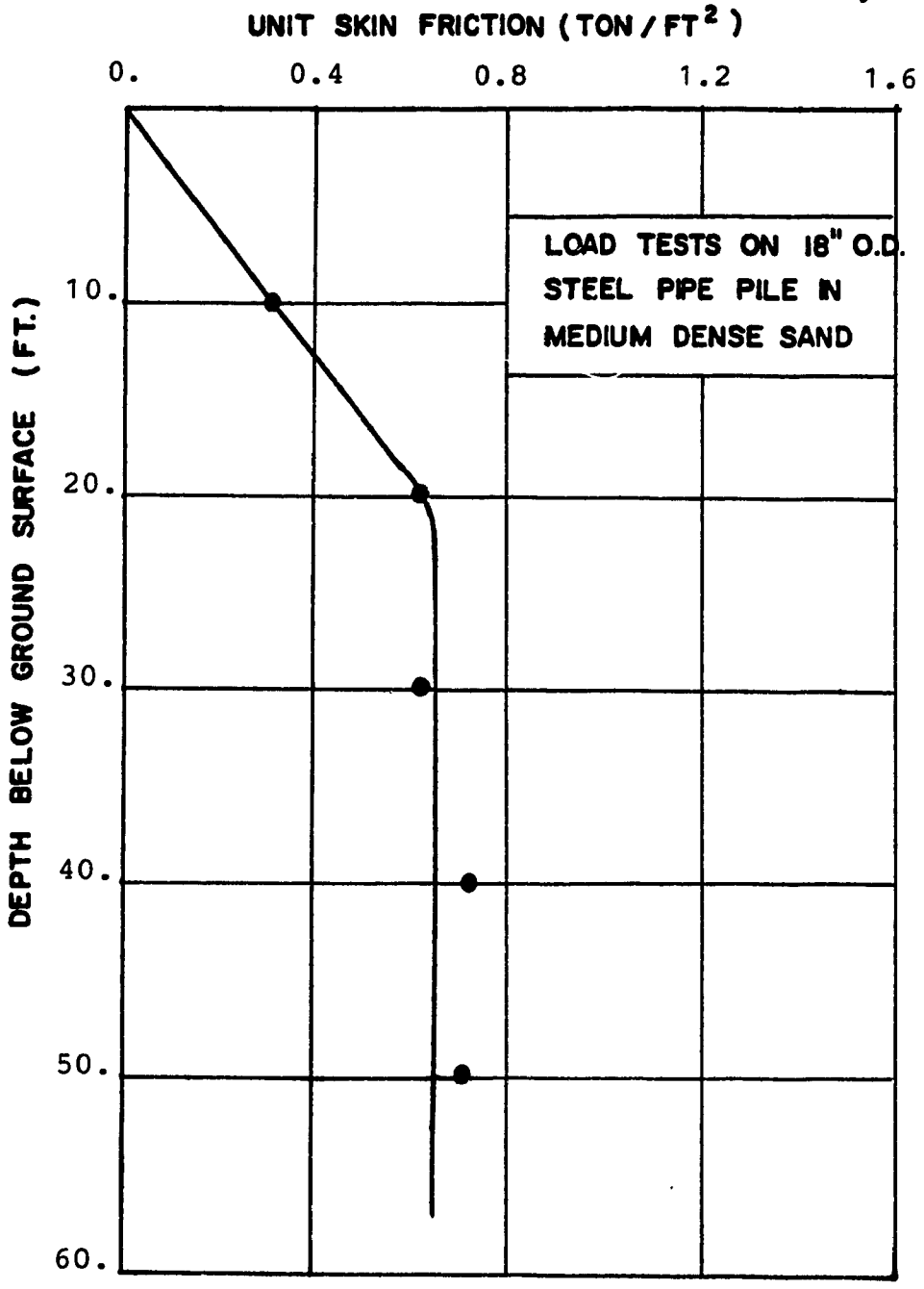

Fig. 2.4 Variation of Unit Skin Friction with Depth (Vesic,1967)

evaluated by:

$$Q_p = (\sigma'_o N_q) A_p \quad \text{... (2.6)}$$

Where

σ'_o = effective vertical stress at the pile tip level

N_q = a bearing capacity factor

A_p = cross section area of pile tip.

Historically, the evaluation of N_q for piles evolved from an early solution for the problem of a rigid stamp penetrating into an incompressible rigid solid (Prandtl, 1921; Reissner, 1924). Later, approximate theoretical methods following the same general approach were used to solve bearing capacity problems in soils. Many failure mechanisms were proposed to estimate the ultimate point resistance of piles. Terzaghi (1943) extended his solution for the bearing capacity of a shallow foundation to the case of a single pile. The mechanism of pile failure involves the downward movement of the cone BCB', which in turn causes the soil to be displaced outward and upward with the failure surfaces ending at the pile tip level (Fig. 2.5). This soil movement is resisted by the weight of an annulus of soil depicted in cross section by D'B'BDEAA'E', the skin friction between the pile shaft and the soil and by the shear forces resisting upward movement of the annulus along its outer surface area. As the degree of shear mobilization of soil on this surface is unknown, Terzaghi suggested the point resistance of a single pile may be estimated by:

$$q_p = 1.3c N_c + \gamma_1 D N_q + 0.6 \gamma B N_\gamma \quad \text{... (2.7)}$$

where

N_c, N_q, N_γ = bearing capacity factors

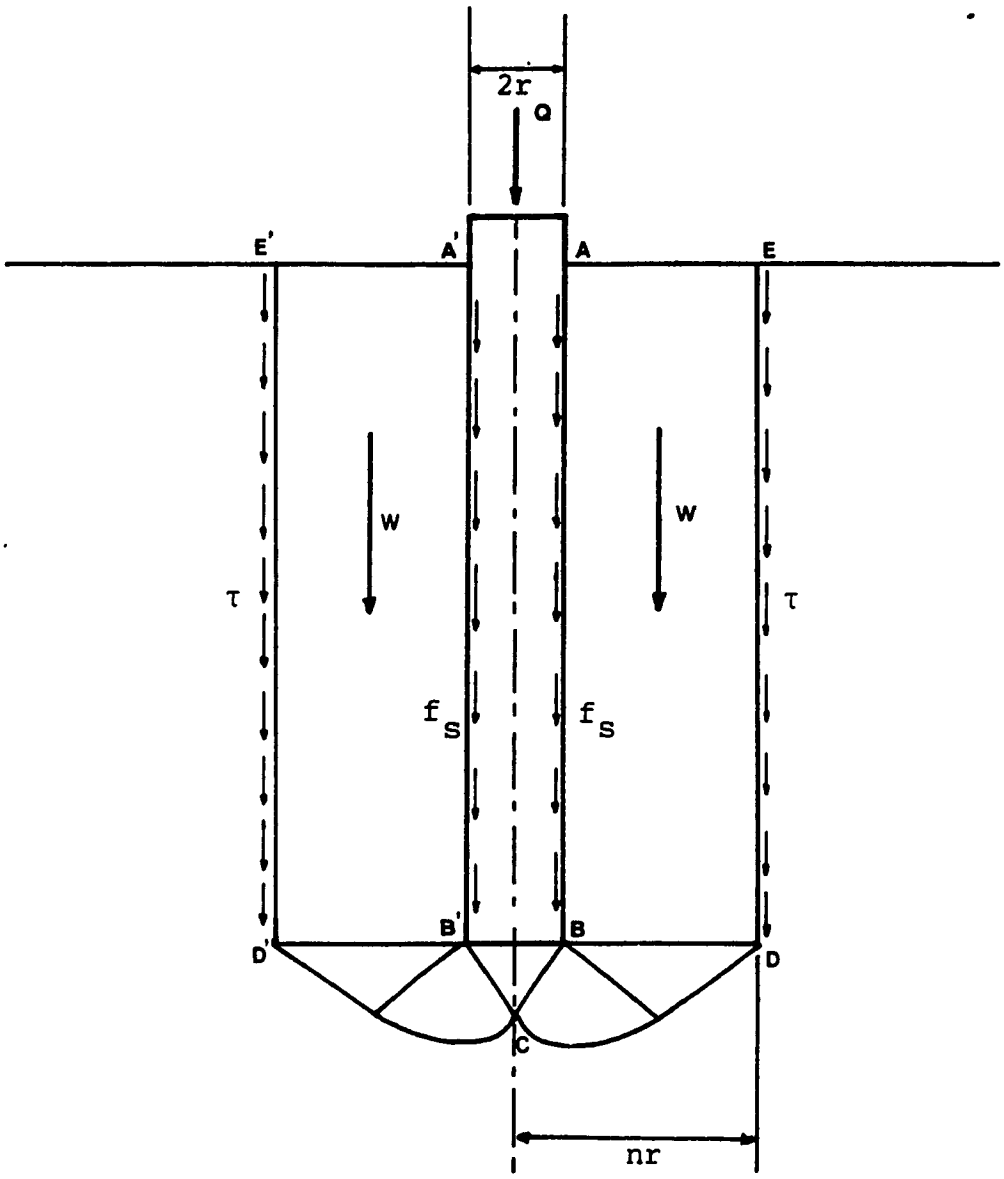

Fig. 2.5 Terzaghi's Assumed Failure Mechanism (Terzaghi, 1943)

c = soil cohesion

D = pile embedment length

γ = soil unit weight.

Eq. (2.7) is almost identical to the expression for the ultimate bearing capacity of a shallow circular foundation except for the term ($\gamma_1 D$) which now represents the pressure at the pile tip level exerted by the resultant effects of the weight of the soil annulus, the pile shaft skin friction, and the shear forces on the outer surface of the soil annulus. The value of γ_1 is given as:

$$\gamma_1 = \gamma + 2\frac{f_s + n\tau}{(n^2 - 1)r} \qquad \text{... (2.8)}$$

where

f_s = average skin friction along pile shaft

τ = average shear stress on outer surface of the soil annulus

n = a factor indicating the magnitude of the outer radius of the soil annulus

r = pile radius

γ = soil unit weight.

The value of n should be selected to minimize q_p in Eq. (2.7) for given values of f_s, τ, γ and ϕ. According to Terzaghi, the unit skin friction f_s can be computed by assuming full shear mobilization along the pile shaft, but estimating τ presents a difficult problem to solve due to the incomplete shear mobilization in the soil on the outer surface of the soil annulus. Terzaghi identified the volume compressibility of the sand as the primary factor influencing this shear mobilization process. As Terzaghi did not propose a specific procedure to estimate the shear stress τ and the unit skin friction f_s (Eq. 2.8), his theory suffers serious limitations in practical applications. Despite this drawback, Terzaghi's model apparently stands out as the first original three dimensional analysis of pile bearing capacity which takes into account the

combined effect of shaft friction and base resistance in the same failure mechanism.

To account for the depth effect on the ultimate bearing capacity of strip foundation, Meyerhof (1951) developed a general bearing capacity theory based on an assumed failure mechanism as shown in Fig. 2.6. Three failure zones are identified: ABC is an elastic wedge, BCD is a radial shear zone bounded by a section of the log spiral CD and BDEF is a mixed shear zone. The plane BE is denoted as an equivalent free surface with normal and shear stresses, p_o and s_o, acting on it. The position of BE is specified once its slope β is determined. The correct β is the one resulting in p_o and q_o values that simultaneously satisfy the equilibrium of the wedge BEF and the state of stress on BE established from Mohr's circle on the basis of failure conditions on the plane BD and DE. Once the equivalent free surface is known, the analysis follows the classical superposition method (Terzaghi, 1943) which takes into account the contribution of c, p_o, γ and ϕ to the bearing capacity of a strip foundation, and gives the expression:

$$q_u = cN_c + p_o N_q + \frac{1}{2}\gamma B N_\gamma \qquad \text{... (2.9)}$$

For strip foundation at great depth, the failure surface does not reach the ground surface but reverts back onto the foundation shaft. Eq. (2.9) is further simplified in case of strip foundation in sand:

$$q_u = \frac{1}{2}\gamma B N_{\gamma q} \qquad \text{... (2.10)}$$

where $N_{\gamma q}$ is a resultant bearing capacity factor combining N_γ and N_q.

Meyerhof's theory is among the earliest attempts to incorporate the effect of foundation shaft friction on the ultimate bearing capacity of a strip footing at any depth. Although this

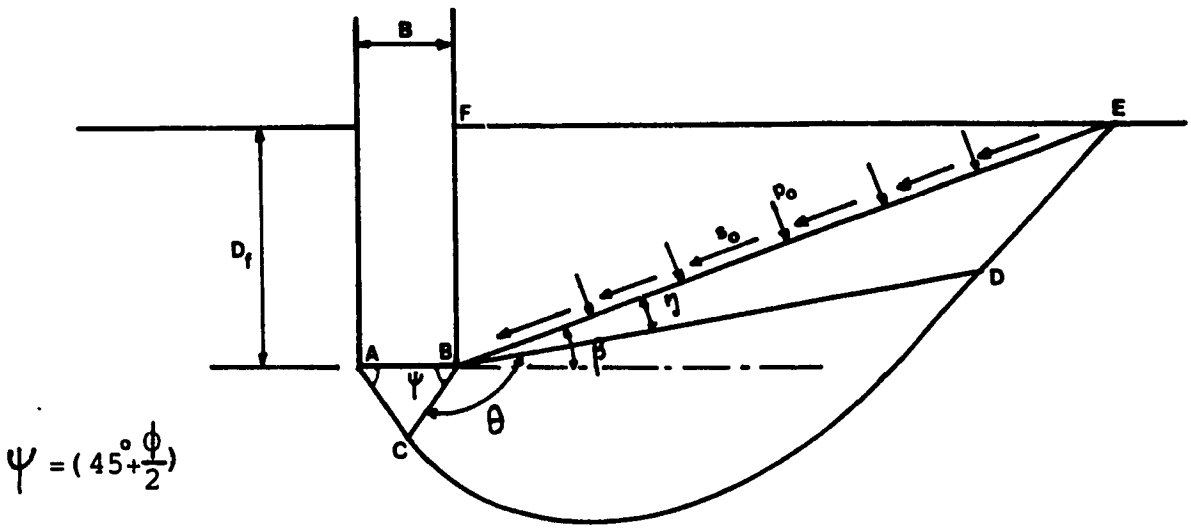

(a) Shallow Foundation

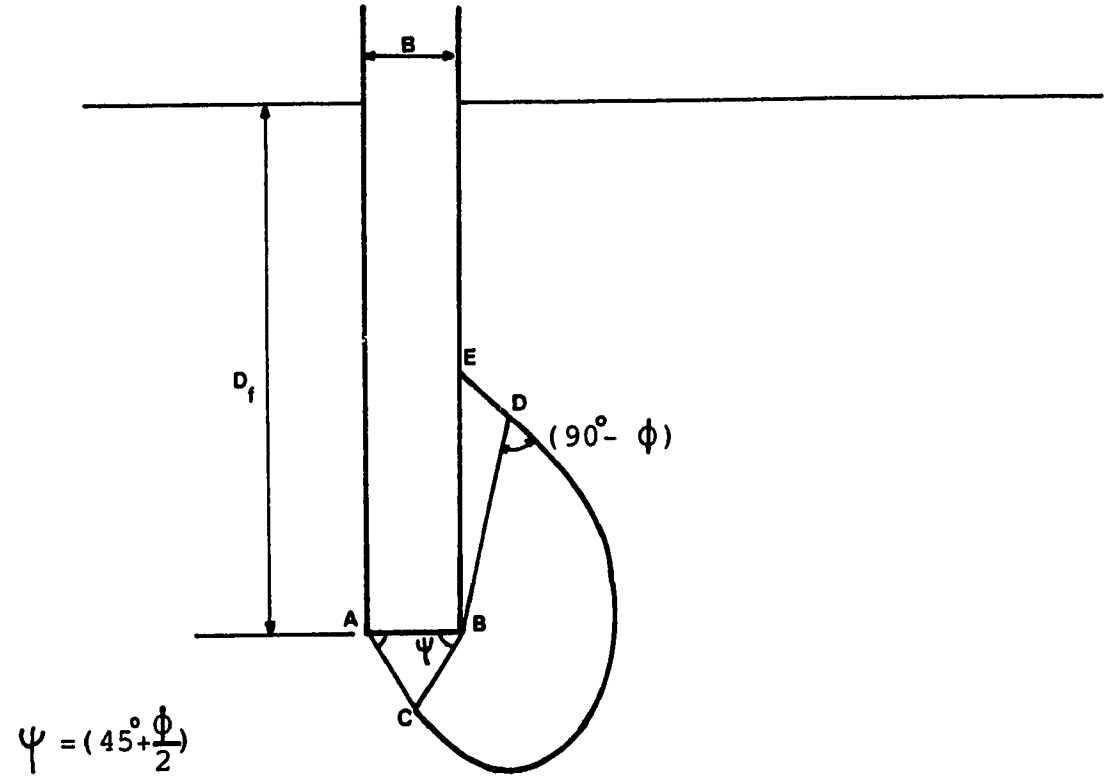

(b) Deep Foundation

Fig. 2.6 Failure Surfaces Assumed by Meyerhof (1951)

theory can account for the influence of the shaft roughness, δ/ϕ, it is yet adequate to incorporate the effect of initial stress, implicitly indicated by the lateral earth coefficient K_o at-rest, on the shaft friction. In Meyerhof's approach, the earth coefficient at the shaft, K_s, must be assumed in advance (i.e., K_s = 0.5 for loose sand and 1.0 for dense sand). In addition, the failure mechanism postulated in Meyerhof's theory, which assumes that the general shear failure surface reverts back on to the shaft at great depth, has not yet been observed experimentally (Vesic, 1967; Durgunoglu and Mitchell, 1973).

Skempton et al. (1953) presented a three dimensional analytical model to estimate the bearing capacity of a single pile in sand. In the analysis, the assumed failure mechanism includes curved surfaces having circles as their vertical cross sections. These circles start at the apex of the cone and become tangent to vertical lines at the level of the pile tip. Fig. 2.7 shows one such circle with center at O and radius r. It passes through point C and becomes tangent to the vertical line at point E. The center O, thus, always lies at the pile tip level (i.e., line AE). The forces acting on a trial failure surface containing the central angle $\delta\theta$ include: the skin friction δs, the soil weight δP, the shear force $\delta\tau$ on the cylindrical surface EF, the soil reaction δR, and the resultant force δQ_P on the central wedge ACA'. The force δQ_p is assumed to act at one third the distance CE from the cone apex. Equilibrium conditions of zone ACE and the wedge ACA' enable δQ_p to be calculated for a central angle $\delta\theta$ and subsequently the bearing capacity factor N_q. Many trial calculations are performed with the circle center assuming different positions along the pile tip level until a minimum value of N_q is obtained.

If the influence of shear forces mobilized in the sand mass above the pile level is neglected (ie., $\delta s = \delta\tau = 0$), then N_q is found to be a unique function of ϕ. In this case, the radius b of the disturbed zone increases from 2B to 4.5B as ϕ increases from 30° to 45°.

To account for the effects of shear forces on the cylindrical surface EF, it was suggested

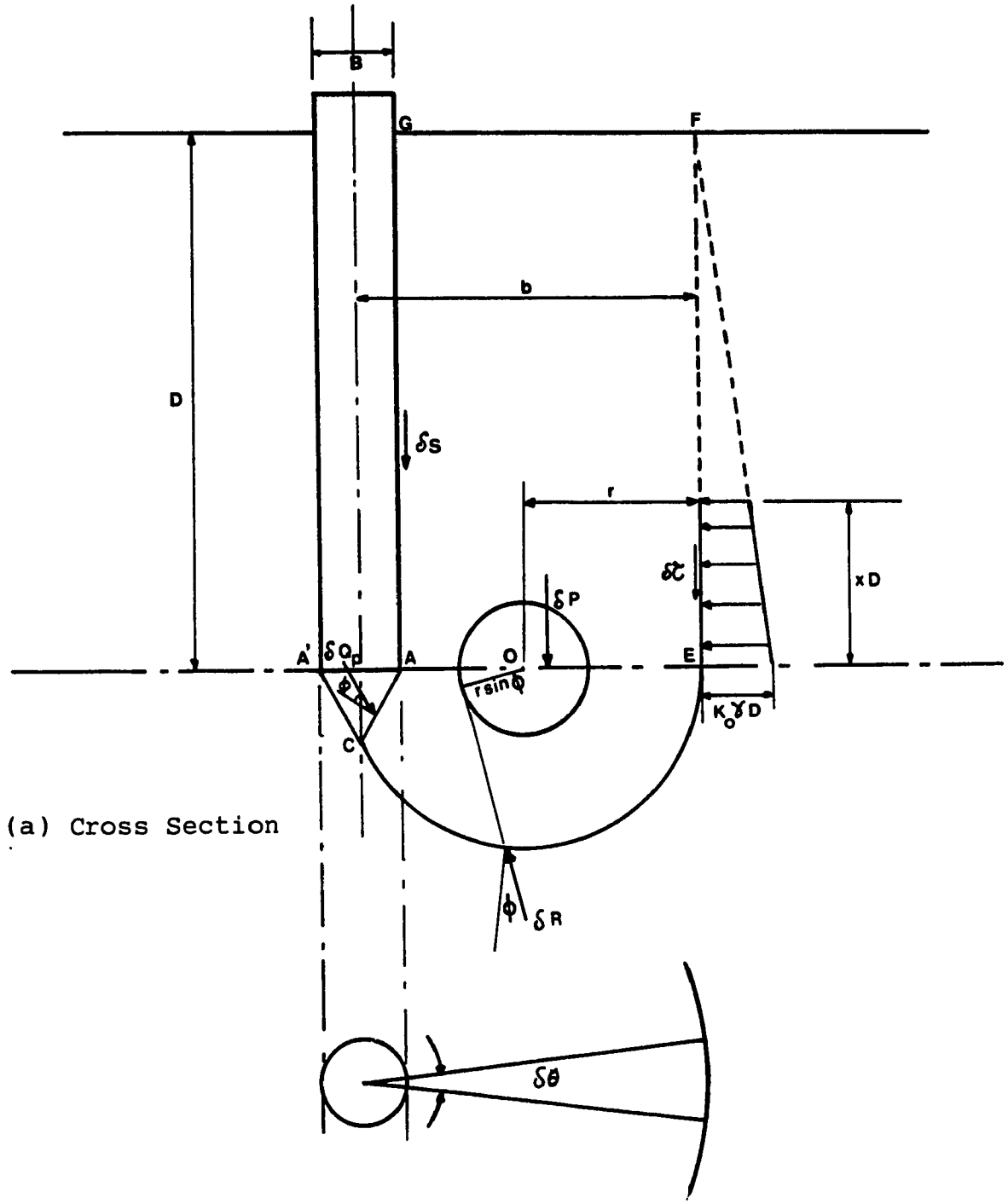

Fig. 2.7 Forces Acting on Slip Surfaces Containing Central Angle $\delta\psi$ in Skempton's Model (After Skempton et al., 1953)

that the shear stress τ at depth z may be estimated by:

$$\tau = K_o \gamma z (\tan \phi) \quad \text{... (2.11)}$$

where

K_o = coefficient of earth pressure at-rest

γ = unit weight of sand.

This shear stress is applied over a length equal to xD where the factor x varies with the sand relative density D_R. The relationship between x and D_R is shown in Fig. 2.8. Under these assumptions, N_q becomes a function of both ϕ and the relative depth D/B.

Berezantzev et al. (1961) introduced a failure mechanism quite similar to Terzaghi's for single piles in sand (Fig. 2.9). According to this scheme, sand compaction under the pile tip causes the soil annulus to move downwards with respect to the remaining sand mass, resulting in the direction of the shear force T being opposite to its counterparts in Terzaghi's and Skempton et al.'s failure mechanisms. The surcharge q_T at the pile tip level, calculated as the difference between the weight W of the annulus of soil and the shear force T on the outer surface of this volume, is also expressed as:

$$q_T = \alpha_T \gamma D \quad \text{... (2.12)}$$

where

α_T = a coefficient, dependent on D/B and ϕ

γ = unit weight of sand

D = pile embedment length

B = pile diameter

ϕ = angle of shearing resistance of sand.

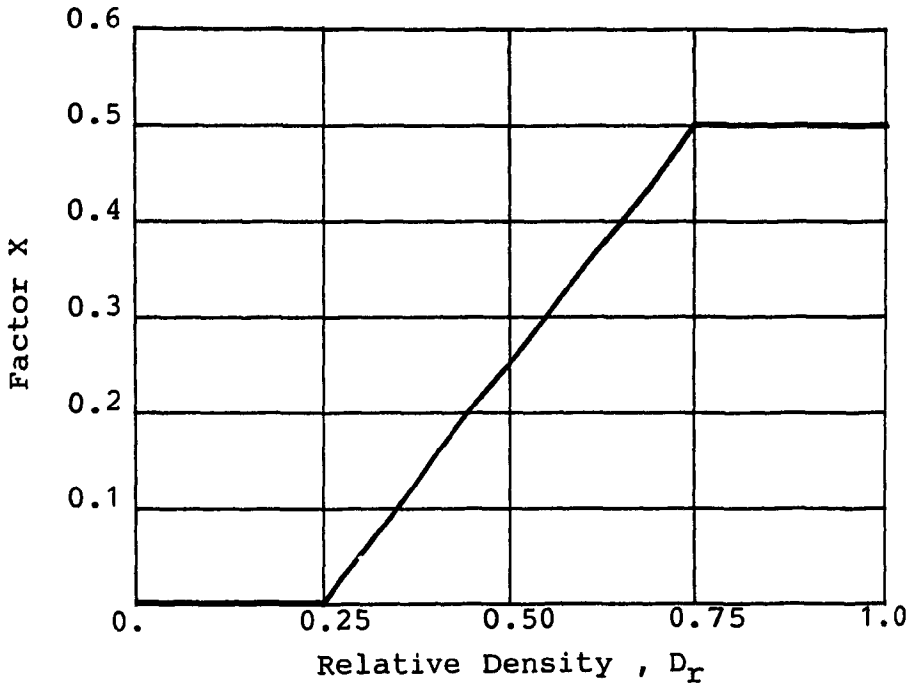

Fig. 2.8 Assumed Variation of Factor x with Relative Density (After Skempton et al., 1953)

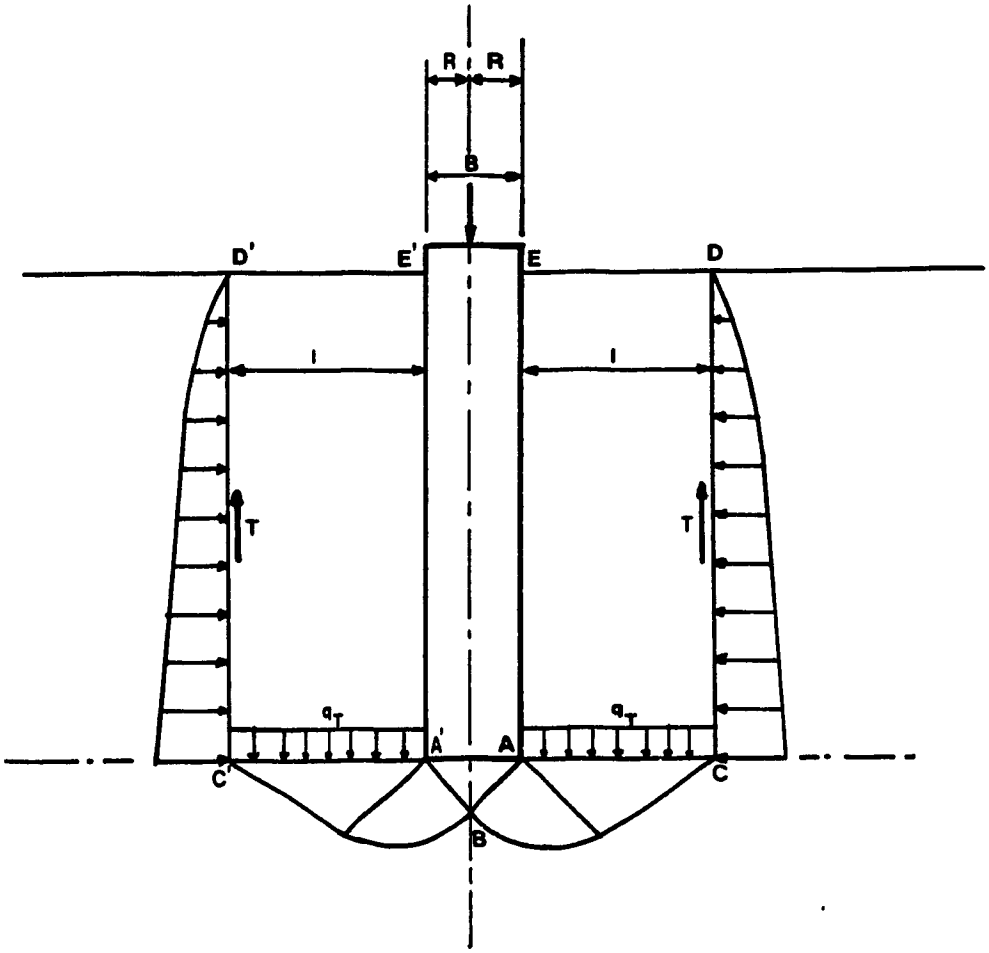

Fig. 2.9 Failure Mechanism Assumed by Berezantzev et al. (After Berezantzev et al., 1961)

The unit point resistance of a single pile is given by:

$$q_u = A_k \gamma B + B_k q_T \qquad \ldots (2.13)$$

where A_k and B_k are bearing capacity factors.

The radius of the annulus of soil, the lateral soil pressure on its outer surface, and the coefficients in Eq. (2.13) are calculated from the theory of limit equilibrium as applied in axisymmetric problems in a granular medium. It is interesting to note that Berezantzev's approach precludes the coupled effect of skin friction and point resistance in the same failure mechanism, in contrast to Terzaghi's assumption Eq. (2.8). After reviewing different bearing capacity theories for piles, Norlund (1963) and Vesic (1967) concluded that Berezantzev's theory provided the best agreement with their experimental data.

Hu (1965) suggested a new failure mechanism for computing the ultimate bearing capacity of a strip foundation at any depth. The failure surface is shown in cross section in Fig. 2.10. It includes a triangular wedge OCO', a radial shear zone OCE bounded by a section of a log spiral having its pole at O and becoming tangent to a vertical plane at E, and an overburden OEFG. The stress at every point in the wedge OCO' and the zone OCE reaches the state of plastic equilibrium while in the zone OEFG, the stress is a state of mixed shear. The interface OE is considered as an internal surface along which full shear mobilization takes place. The overburden is assumed to comprise two weights, P_1 and P_2, acting through the centroids of the areas OEH and EFGH. It is further assumed that the shear resistance along the outer vertical failure surface EF and the skin friction along the foundation shaft OG, do not enter in the derivation of the ultimate bearing capacity q_u as given by:

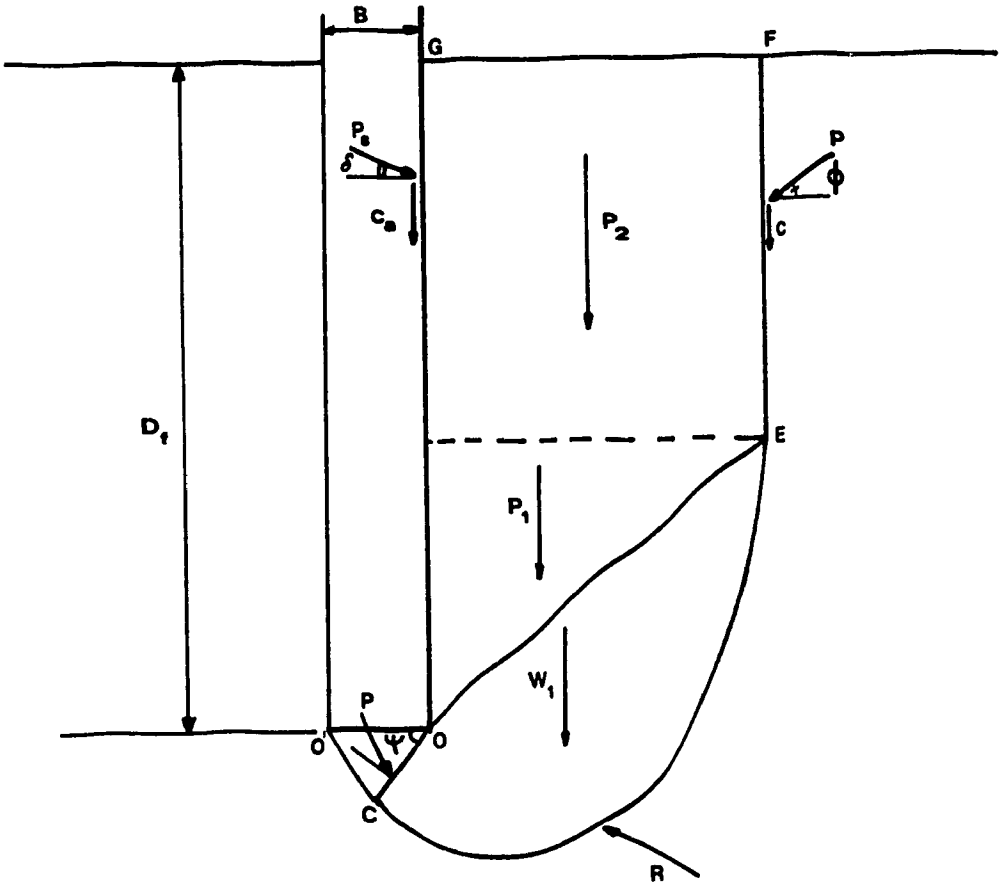

Fig. 2.10 Hu's Assumed Failure Mechanism (Hu, 1965)

$$q_u = cN_c + p_o N_q + \frac{1}{2}\gamma BN_\gamma \qquad \ldots (2.14)$$

where

p_o = overburden pressure at foundation level.

The shear resistance along EF and OG must be added to q_u to obtain the final base resistance. Eq. (2.15) is further combined to give:

$$q_u = cN_c + \gamma \overline{3}N_{\gamma q} \qquad \ldots (2.15)$$

where $N_{\gamma q}$ is a resultant bearing capacity factor.

The distinct feature of Hu's analysis lies in the assumption that a single failure surface is used to calculate N_c and $N_{\gamma q}$ and, as such, indicates a deviation from the conventional approach of using two different failure surfaces in deriving N_c, N_q and N_γ (Terzaghi, 1943; Meyerhof, 1951).

Durgunoglu and Mitchell (1973) adopted Hu's failure mechanism and developed a theoretical basis for evaluating the static cone resistance. They derived a resultant bearing capacity factor $N_{\gamma q}$ as a function of the apex angle of the cone, the angle of shearing resistance ϕ, the relative depth D/B, the base roughness δ/ϕ, the earth pressure coefficient on the shaft K_s, and the coefficient of earth pressure at-rest K_o. The analysis is an improvement on Hu's theory, taking into account important parameters, such as K_o, K_s, and δ/ϕ, normally neglected in previous theories. Like Hu's model, the failure mechanism in Durgunoglu and Mitchell's theory is not perceived as entirely congruent with experimental evidences, especially at lower depths (Al-Awkati, 1975). Developing a relationship between K_o and K_s, and including Q_s calculations in the same failure mechanism, are among desirable features still lacking in Durgunoglu and Mitchell's analysis, which requires an empirical estimate of K_s in advance.

Vesic (1967) introduced a two dimensional failure mechanism to account for the local or punching shear failure of a long rectangular foundation in sand at shallow depth (D/B < 4). As presented in Fig. 2.11 the shear pattern consists of an elastic wedge ABC sandwiched between two plastic zones ACE and BCD bounded by sections of log spirals CE and CD having their poles located at point A and B, respectively. The failure surface develops only to a limited extent well below the pile tip level. By assuming the weight of the soil in the failure zones to be negligible compared to the overburden pressure, and adopting appropriate stresses along the limiting surface BD and AE, Vesic's analysis gives the following expression for N_q:

$$N_q = e^{3.8\phi \tan \phi} \tan^2\left(45° + \frac{\phi}{2}\right) \qquad \text{... (2.16)}$$

Janbu and Senneset (1974) proposed a two dimensional variable failure mechanism which allows the critical shear zones beneath the pile tip to adjust themselves to failure conditions. The derived bearing capacity factor N_q is given by:

$$N_q = \tan^2\left(45° + \frac{\phi}{2}\right) e^{(\pi - 2\beta)\tan \phi} \qquad \text{... (2.17)}$$

in which the angle β is the inclination of the terminal radial planes AE and BD (Fig. 2.12). To account for the partially mobilized shear strength along the assumed failure surface, Janbu (1976) further developed Eq. (2.17) into a generalized form:

$$N_q = \tan^2\left(45° + \frac{\phi}{2}\right) e^{(\pi - 2\beta)(f \tan \phi)} \qquad \text{... (2.18)}$$

in which f = degree of shear mobilization. If β is selected within the range $-15° \le \beta \le +15°$, fairly good agreement with experimental data is obtained. With Eq. (2.18), Janbu apparently presented a refreshing outlook on the theory of bearing capacity of piles.

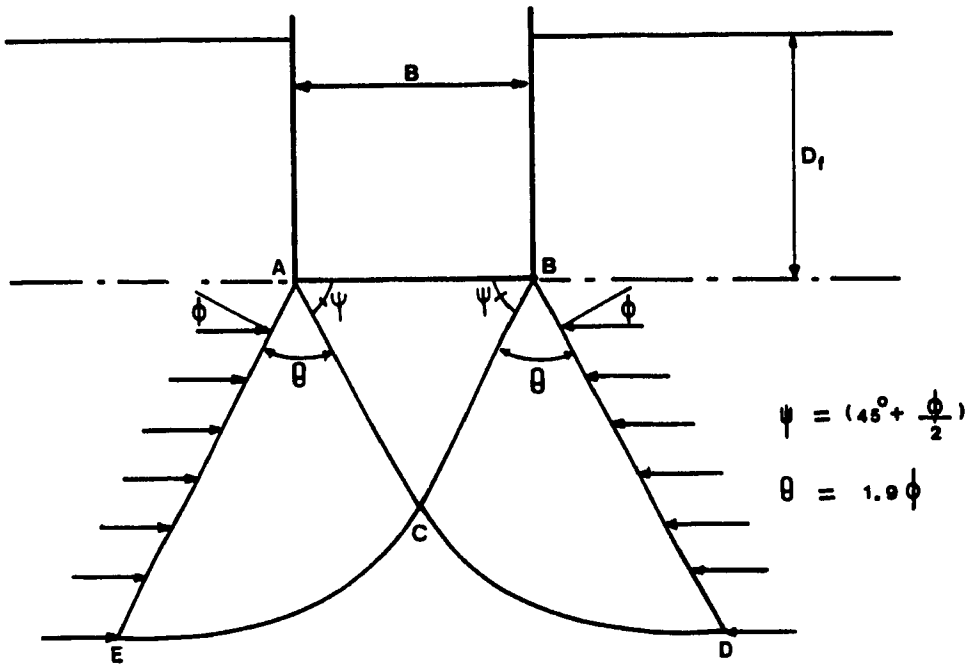

Fig. 2.11 Vesic's Assumed Failure Mechanism for Analysing Punching and Local Shear Failure (Vesic, 1967)

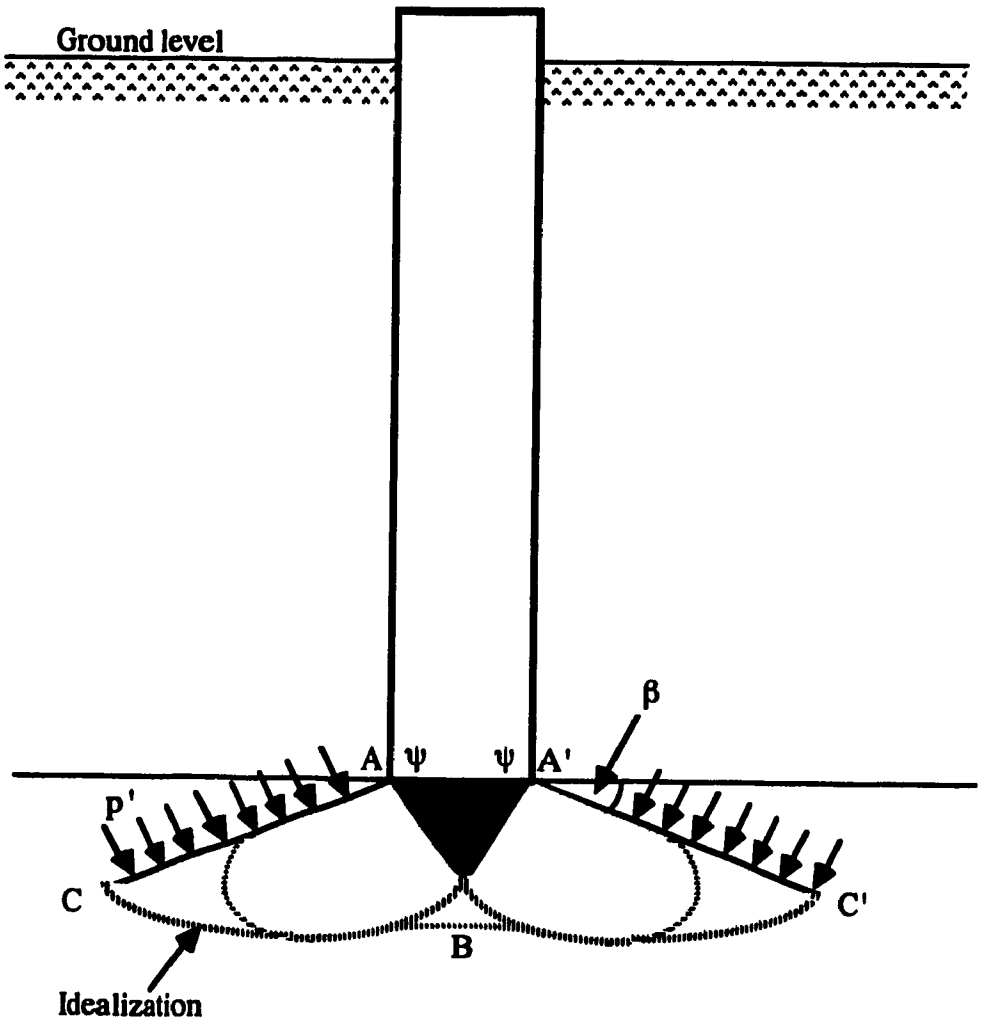

Fig. 2.12 Failure Mechanism Assumed by Janbu and Senneset (1974)

Accordingly, N_q no longer depends uniquely on ϕ but it is also a function of the extent of the "plasticized" zone under the pile tip, and the degree of shear mobilization along the log spiral boundary of this zone. In addition, Eq. (2.18) suggests that a variable failure mechanism may develop under the pile tip, although its mode of variation has not yet been adequately investigated. In this respect, how the angle β varies with ϕ, D/B or even K_o remains an interesting question for future research.

Vesic (1977) recommended another model capable of incorporating soil compressibility. The shear failure pattern was established from observations of model and full-size piles (Fig. 2.13). It consists of a highly compressed cone ABC (zone I), a radial shear zone BCD (zones II), and a plastic zone BC (zone III). The lateral expansion of the soil into zone III and the soil compression in zones I and II allow the pile to advance to lower depths. The average normal stress along BC is assume to be equal to the ultimate pressure needed to expand a spherical cavity in an infinite soil mass. The unit point resistance of a single pile is then given by:

$$q_p = cN_c + \sigma_m N_\sigma \qquad \text{... (2.19)}$$

where

N_c, N_σ = bearing capacity factors

σ_m = mean normal ground stress

$$\sigma_m = \left(\frac{1 + 2K_o}{3}\right)\sigma_o'$$

As the obtained values of N_q are a direct consequence of the assumed failure mechanism, it is not surprising to find serious discrepancies among published N_q values in the literature (Fig. 2.14). On the other hand, the notion that N_q is a unique function of ϕ gradually looses its appeal because it presents an overly simplistic view of a highly complicated phenomenon. For instance, Eq. (2.6) implies that the unit point resistance varies linearly with depth. However,

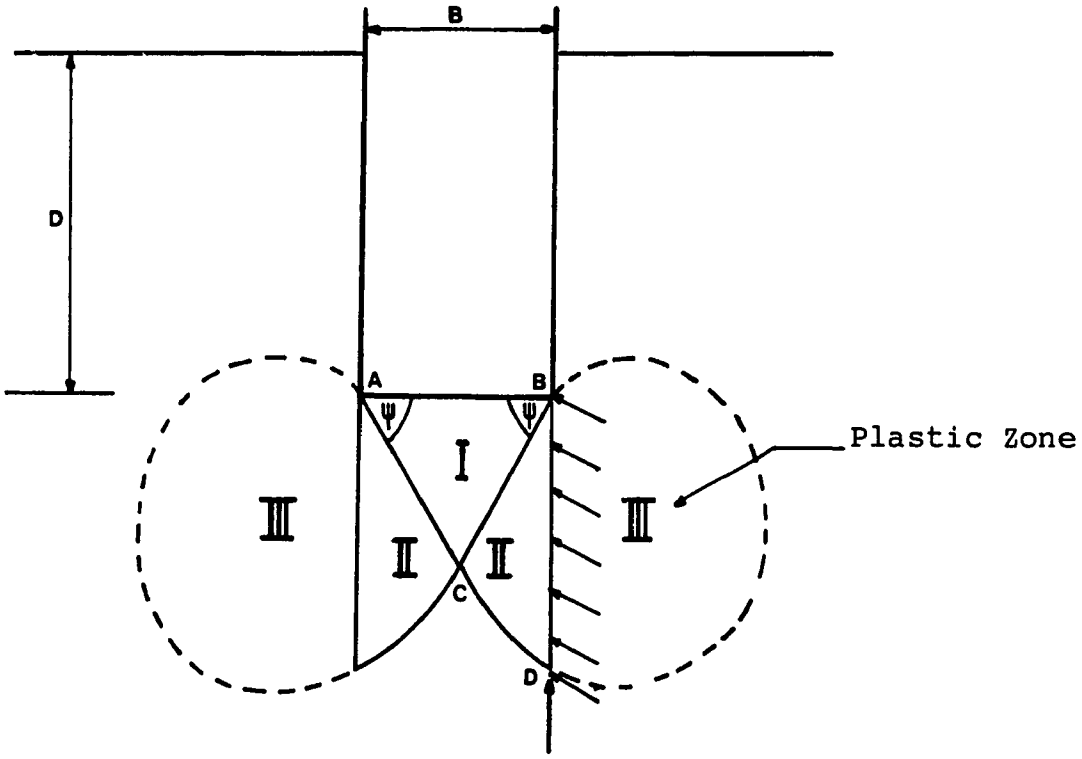

Fig. 2.13 Vesic's Assumed Failure Pattern Incorporating Soil Compressibility (After Vesic, 1977)

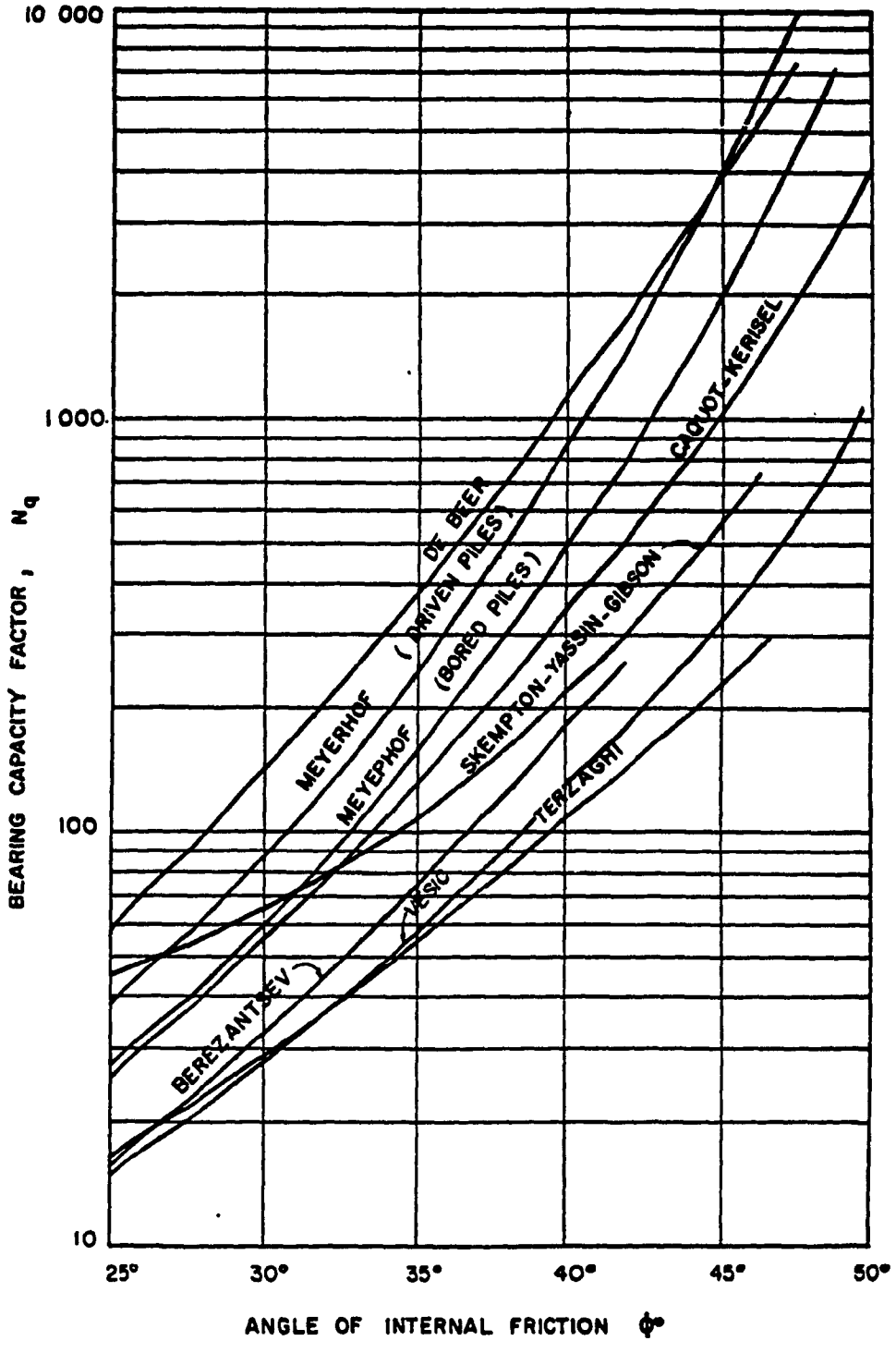

Fig. 2.14 Theoretical Bearing Capacity Factors for Deep Foundations (After Vesic, 1967)

important studies by Kérisel (1961, 1964), Kérisel et al. (1965), Vesic (1963, 1964, 1967) and Tavenas (1971) revealed that the unit point resistance increases only to a certain depth and then reaches a near constant value which depends only on the relative density of sand (Fig. 2.15). This phenomenon of critical depth was attributed to arching which resulted in a relative constant vertical stress along the lower portion of the pile shaft and in the pile tip immediate vicinity (Vesic, 1967). Experimental evidences of arching around the pile shaft were furnished by Robinsky et al. (1964) in their study of sand displacement around model piles using radiography techniques, and by Hanna and Tan (1973) who performed load tests on buried, instrumented model piles up to 1.5 in. in diameter. Meyerhof (1976) and Poulos and Davis (1980) subsequently incorporated Vesic's findings into practical design charts. While no additional experimental investigation was carried out on a scale comparable to those conducted by Kérisel (1961) and Vesic (1967), disagreements in the critical depth concept began to surface, especially after Vesic apparently abandoned further attempts advocating his initial working hypothesis (Vesic, 1977). Hanna and Tan (1973) also pointed out the important effect of "locked-in stresses" existing in their model piles after installation, and questioned the validity of analysing load distributions in piles without accounting for residual stresses. In 1981, Coyle and Castello proposed empirical design charts for piles in sand, which indicated that both the unit point resistance q_p and the average unit skin friction f_s continued to increase beyond the critical depth. In support of Coyle and Castello's charts, Zeitlen and Paikowsky (1982) suggested that the critical depth concept was not even necessary if proper allowances were made to account for the decrease of the angle of shearing resistance ϕ with increasing confining pressure. Accordingly, as ϕ decreased with depth, N_q and K_s also diminished with further pile penetration, resulting in relatively constant values of q_p and f_s. Kulhawy (1984) dismissed the critical depth concept altogether, and argued that both q_p and f_s continued to increase with depth. The rate of increase of q_p, however, decreased due to the reduction of rigidity of sand with depth. As for f_s, its rate of increase depended on the increasing overburden pressure and the decreasing K_o with depth.

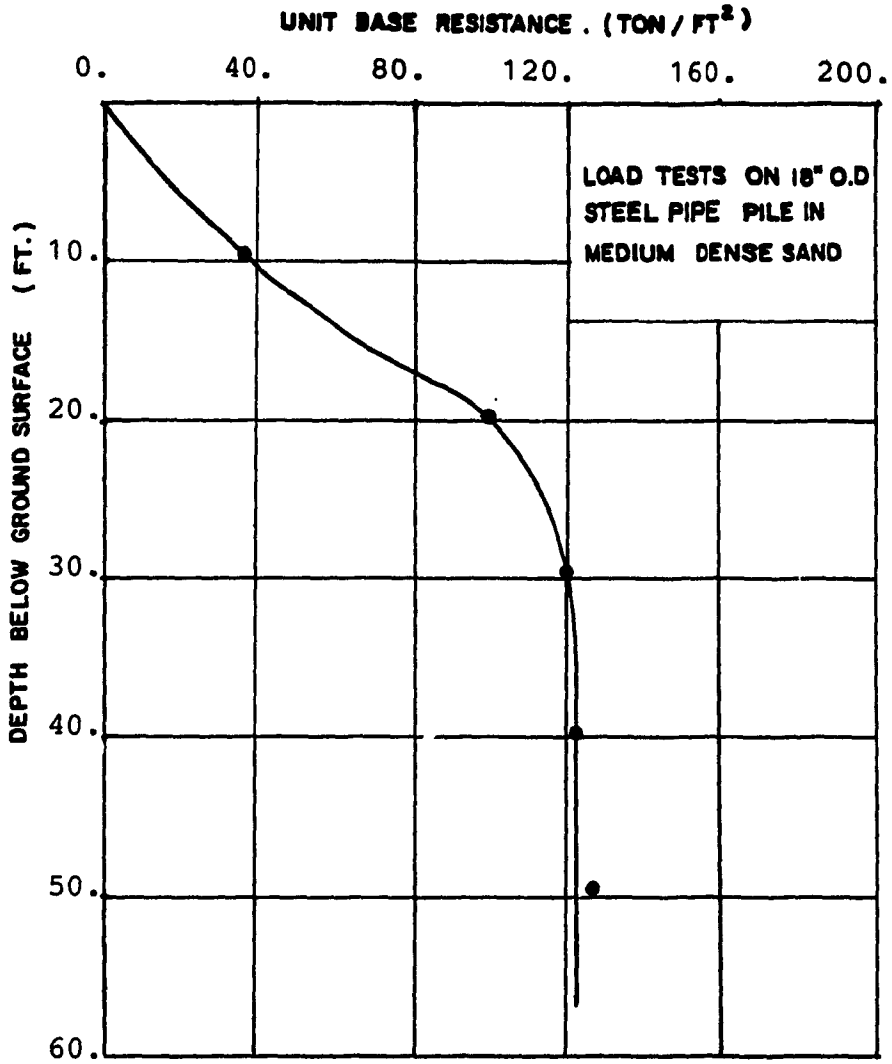

Fig. 2.15 Variation of Unit Point Resistance with Depth (After Vesic, 1967)

A different approach to the problem of point resistance originated from the work of Bishop et al (1945) in connection with metal indentation. They found that the point resistance of a deep circular indentor was bounded by the spherical and the infinitely long cylindrical cavity limit pressures. The solution of this kind was subsequently applied to the problem of bearing capacity of deep foundation in clays by Gibson (1950), Meyerhof (1951), and Ladanyi (1963, 1969). Skempton et al. (1953) and Ladanyi (1961) developed further analyses for the problem of deep point resistance in sands. A detailed survey of this approach was provided by Al-Awkati (1975).

2.3 DISCUSSION

Most failure mechanisms were established from observations of a limited number of load tests on model foundations. In many instances, an observed mode of failure at shallow depths was interpreted as the universal mode at greater depths (Durgonoglu & Mitchell, 1973). Sometimes, a failure mechanism was postulated with almost no solid supporting experimental evidence (i.e., Jaky, 1948; Meyerhof, 1951). On the other hand, even correctly observed failure mechanism of model foundations do not warrant similar behaviours under actual field conditions where scale effects may play an important role (Habib, 1974; Vesic, 1977). As a result, existing failure mechanisms discussed so far indicate wide variations in the assumed extent of the failure surface under the base of a deep foundation. For example, the failure surface may just barely develop in the immediate vicinity of the pile tip (i.e., Vesic, 1977), extend to some intermediate level below the foundation base (Vesic, 1967), end at the base level (i.e., Terzaghi, 1943; Skempton et al., 1953; Berezantzev et al., 1961), reach the ground level (i.e., Hu, 1965) or even revert back on to the shaft (i.e., Jaky, 1948; Meyerhof, 1951). Unfortunately, it is almost impossible to justify most of these failure mechanisms in the face of well supported experimental fact that, for piles in sands, the principal failure mode is by punching shear in which failure surfaces are almost invisible (Kerisel, 1961; Vesic, 1967; Robinsky and Morrison, 1964). Consequently, it is important for any rational theory on pile

bearing capacity in sand to incorporate the punching shear phenomenon in its analytical model.

Besides the assumed failure mechanism, some researchers tend to oversimplify the bearing capacity problem of pile by first analysing the case of a deep strip foundation and then applying certain experimental shape factors to the bearing capacity equation (i.e., Meyerhof, 1951; Durgunoglu & Mitchell, 1973). While this practice appears acceptable in foundation design due to its expediency in application, it contributes little to the understanding of actual pile behaviour in axisymmetric loading conditions. In this respect, Terzaghi (1943) also pointed out the invalidity of using the theory of earth pressure, which is valid only for plane state of deformation, in computing point resistance and skin friction on the pile shaft.

As for the interaction problem between pile tip and pile shaft, Terzaghi (1943) was apparently among the first ones to formulate a scheme introducing the effect of shaft friction into the pile bearing capacity equation (Eq. 2.8). Except for a few other theories (i.e., Meyerhof, 1951; Skempton et al., 1953; and Durgunoglu and Mitchell, 1973), the effect of skin friction along the pile shaft remains unaccounted for in most derivations of bearing capacity factors. This simplification implies the assumption that the foundation shaft and base interactions may be neglected so that at the ultimate load, both the foundation shaft and base move downward with respect to the surrounding soil sufficiently to mobilize simultaneously the skin friction and the point resistance. On this basis, the development of the ultimate bearing capacity of a single pile is usually treated as an uncoupled phenomena of point resistance and skin friction. This approach is yet successful in providing a solid theoretical foundation for estimating skin friction which, in its present state of development, continues to depend virtually on empirical methods. On the other hand, Vesic (1967) and Tavenas (1971) provided experimental evidences suggesting that there was a constant ratio between unit point resistance and unit skin friction for a given sand and pile installation method. As a result, investigations into a possible interdependence between skin friction and point resistance may open new

grounds for a more logical solution to the problem of bearing capacity of piles.

In summary, a rational bearing capacity theory for a single pile in sand should bring about improvements upon the shortcomings suffered by its predecessors. In this thesis, an attempt will be made to develop a theoretical model which incorporates some salient features commonly omitted in the existing pile bearing capacity theories. These features include:

1. Treating the pile bearing capacity as an axisymmetrical problem.
2. Adopting a failure mechanism consistent with the observed experimental fact that punching shear failure is the principal failure mode associated with piles.
3. Taking into account the interrelationships between skin friction and point resistance.

CHAPTER 3

EXPERIMENTAL STUDY AND TEST RESULTS

3.1 GENERAL DESCRIPTION OF EXPERIMENTAL SET-UP

The experimental set-up comprises a steel frame test tank 4 ft. x 7 ft. cross section and 7 ft. deep, designed for load tests on model test piles up to 5.5 ft. long. The placement of sand in the test tank is carried out by depositing sand through a distributing hopper installed on a carriage travelling back and forth over the test tank. Provisions are made to permit regulating the flow rate of sand, the speed of carriage travel and the height of fall of the sand.

Once the tank is filled, the model pile can be pushed vertically into the sand deposit by a strain-controlled screw jack attached to a loading column. The design will allow maximum combined test loads up to 10 ton vertical and 5 ton horizontal. After the completion of one test series in the tank, the sand will be transported to a storage tank by means of a vacuum suction system. This same system will be used to refill the test tank. A general view of the testing area is shown in Fig. 3.1.

3.2 TESTING FACILITIES

The main facility used in this experimental set-up consists of the sand distributing system, the sand conveying system and the loading equipment.

The sand distributing system has been developed to provide a reliable means for preparing uniform sand beds. The main features of this system include a carriage and a distributing hopper. The carriage is designed to run continuously on tracks over the 7 ft. long

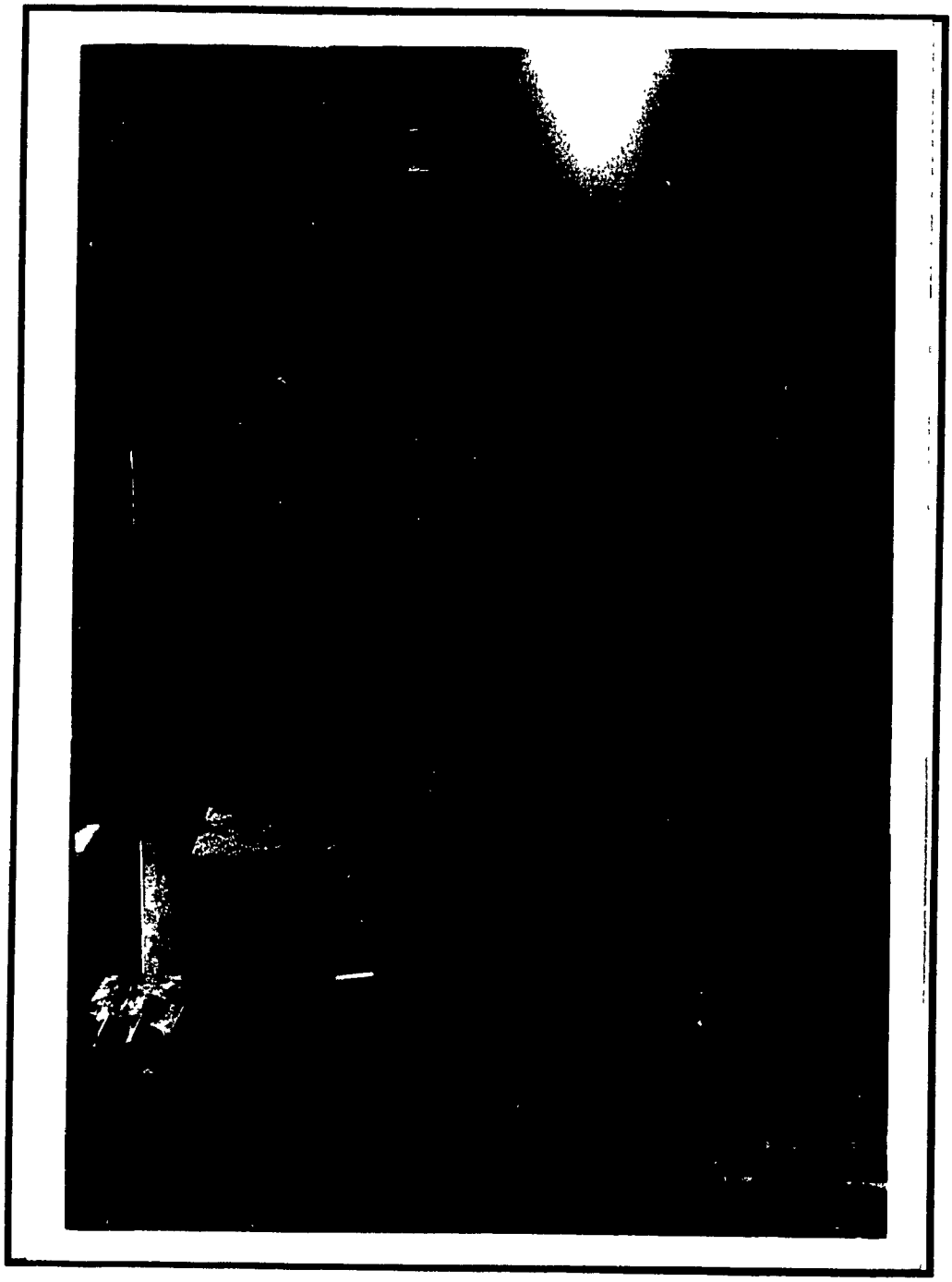

Fig. 3.1 General View of Testing Area

test tank and reverse its direction by automatic photo electric switches installed at each end of the test tank. The accelerating and decelerating to or from full travel speed is accomplished within 0.5 seconds. As a result of this short delay, a uniform sand deposit may be obtained within the central 6 ft. of the sand box.

The distributing hopper consists of a steel framed container (46.5 in. x 18 in. x 3.5 in.). The hopper bottom is provided with continuous double slots over its full length. The width of this slot can be adjusted by two bolts. A manual mechanism operated on springs and cables attached to an inverted steel angle is designed to provide a closing and opening gate for the double slots. The sand distributing hopper can be raised up or lowered down vertically into the test tank by a hand operated winch. The hopper may be secured at desired elevations by means of pins and holes drilled at 3 in. spacings on the guiding frame, which is bolted onto the chassis of the carriage. (Fig. 3.2 and 3.3).

The sand conveying system is designed to satisfy two basic requirements: to transport sand from the ground level to the storage bin located on top of the loading frame, and to empty the test tank after each test series. This system consists of a 10 H.P. vacuum pump connected to a storage bin and separator auxiliary tank (Fig. 3.4) by 2.5 in. diameter flexible hoses. The general arrangement of the system is shown in Fig. 3.5, with plastic enclosure in place during the testing program.

The loading equipment includes a motorized 15 ton capacity screw jack with 3 ft. maximum travel, mounted on a steel plate which is bolted onto a 4 in. x 6 in. x 5/16 in. loading column steel tubing. This set-up allows pushing of model piles vertically or at any angle up to 45° with the vertical by a system of a sleeve, a pin and supporting frames (Fig. 3.6). The combination of a gearshift, a gear reducer and an electronic speed-controlled device provide the screw jack with a loading and unloading speed varying from 0.01 to 1.0 in./minute (Fig. 3.7).

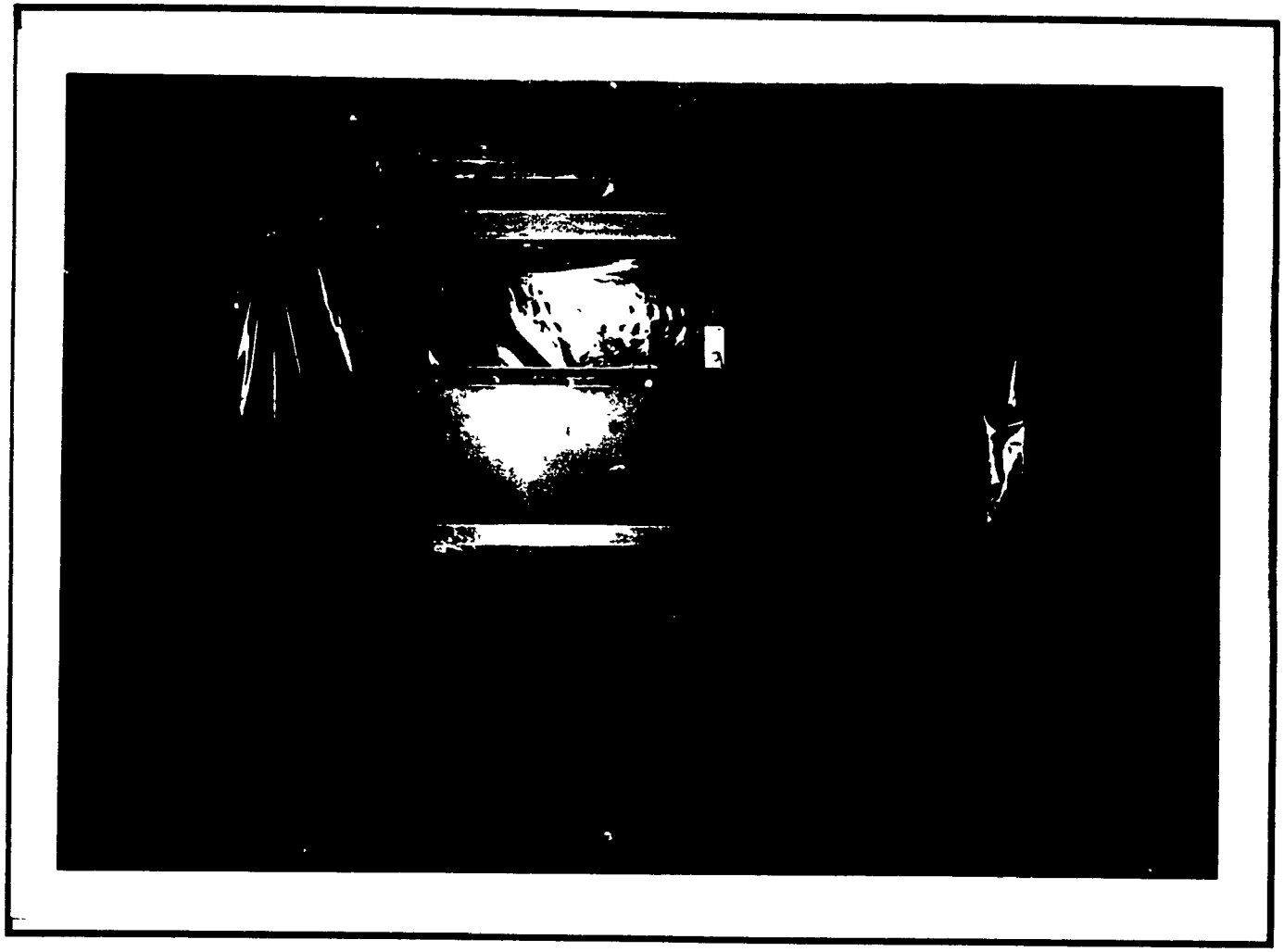

Fig. 3.2 Sand Spreading Hopper on Carriage (Front view)

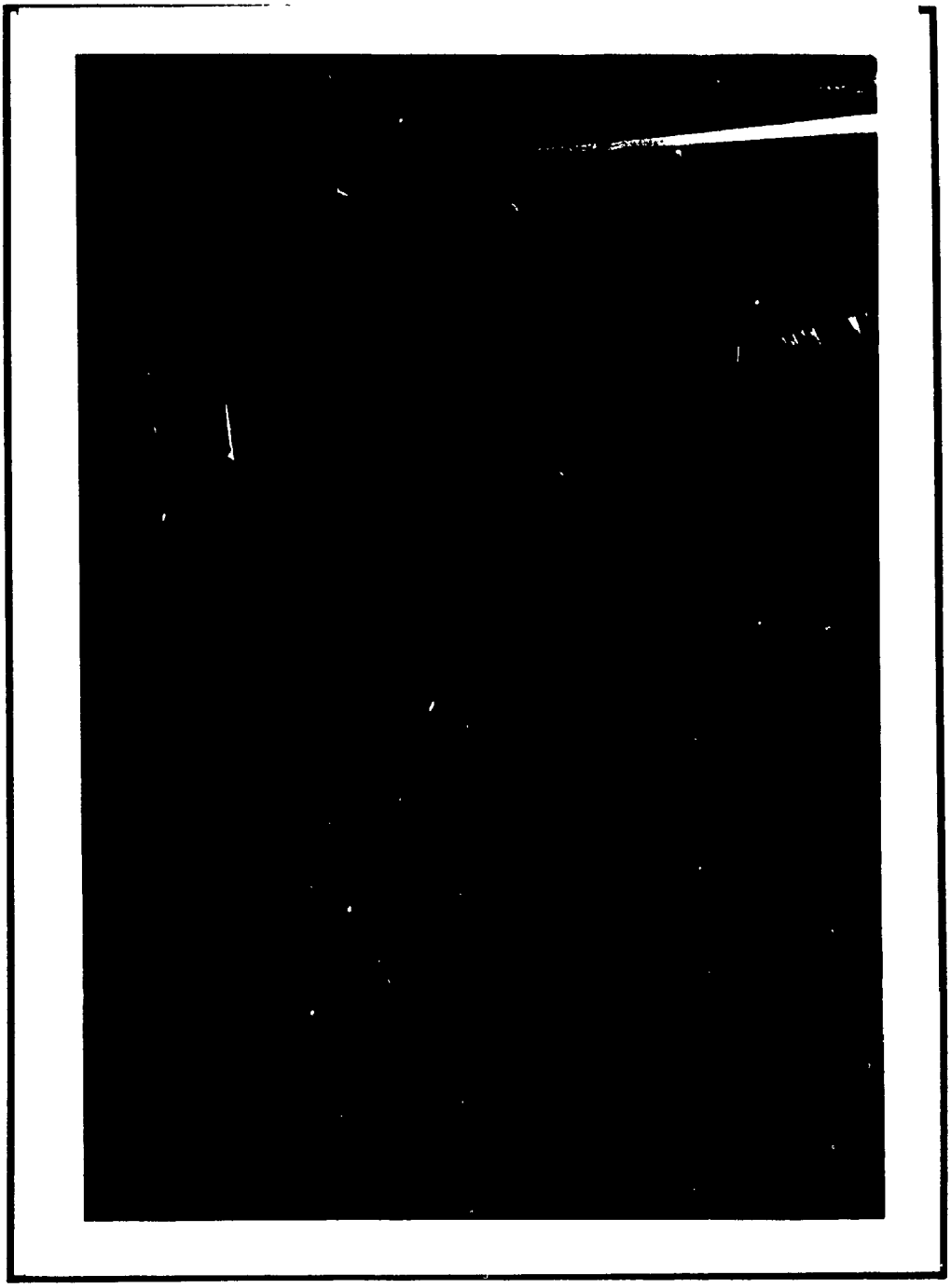

Fig. 3.3 Sand Spreading Hopper on Carriage (Rear View with Motor Drive Exposed)

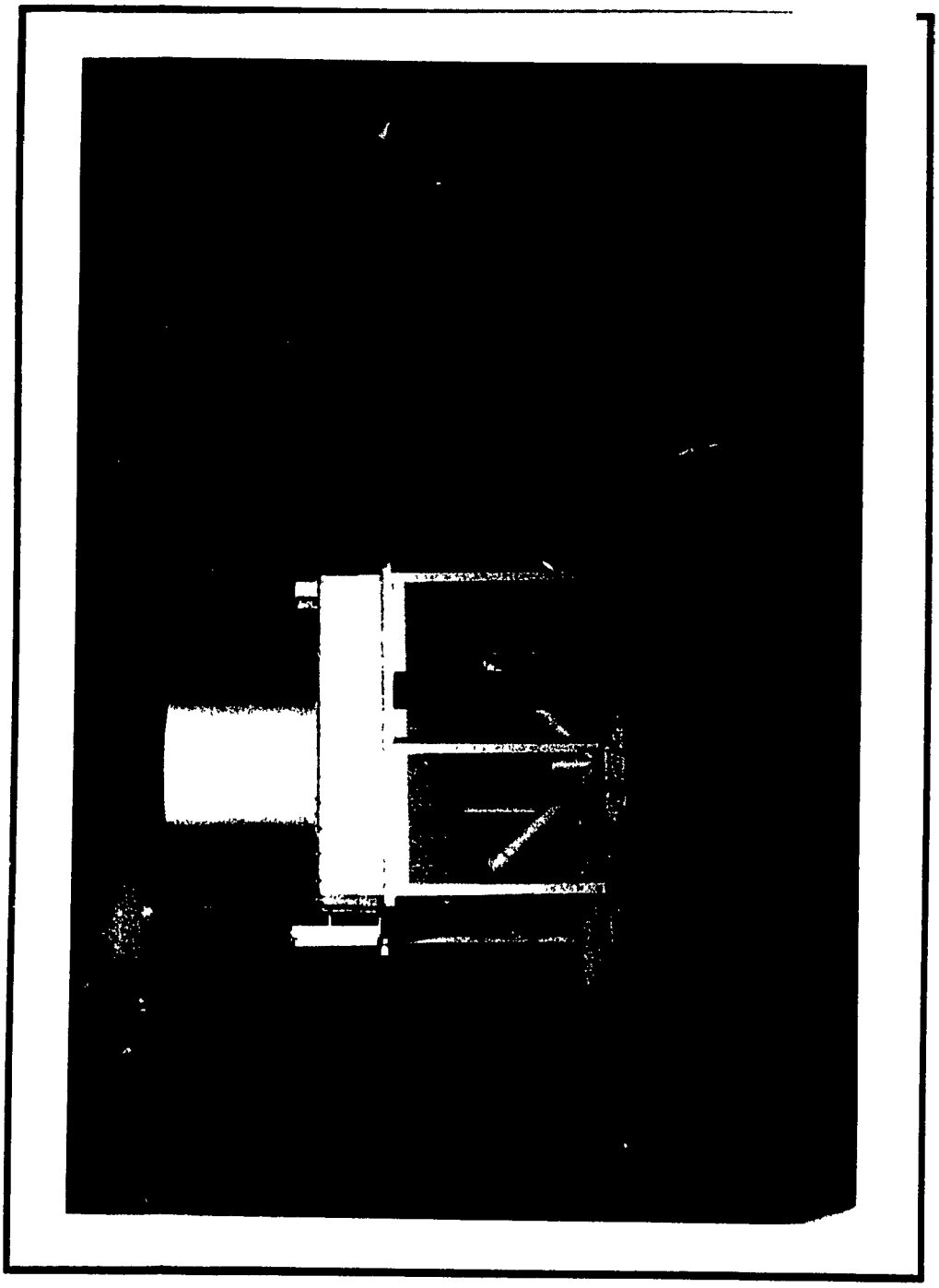

Fig. 3.4 Storage Bin and Separation Auxiliary Tank

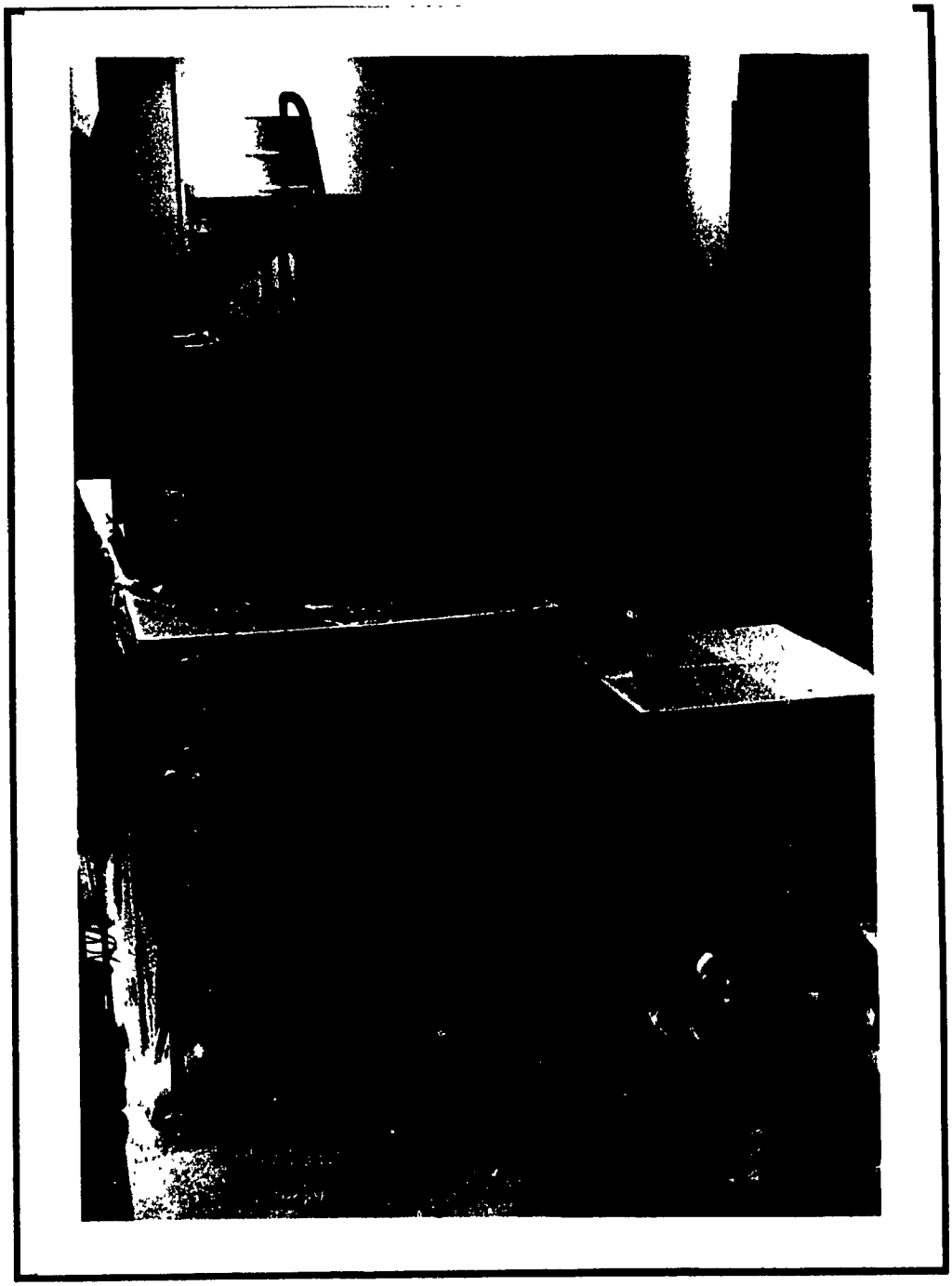

Fig. 3.5 General Arrangement of Sand Conveying System (With Plastic Enclosure)

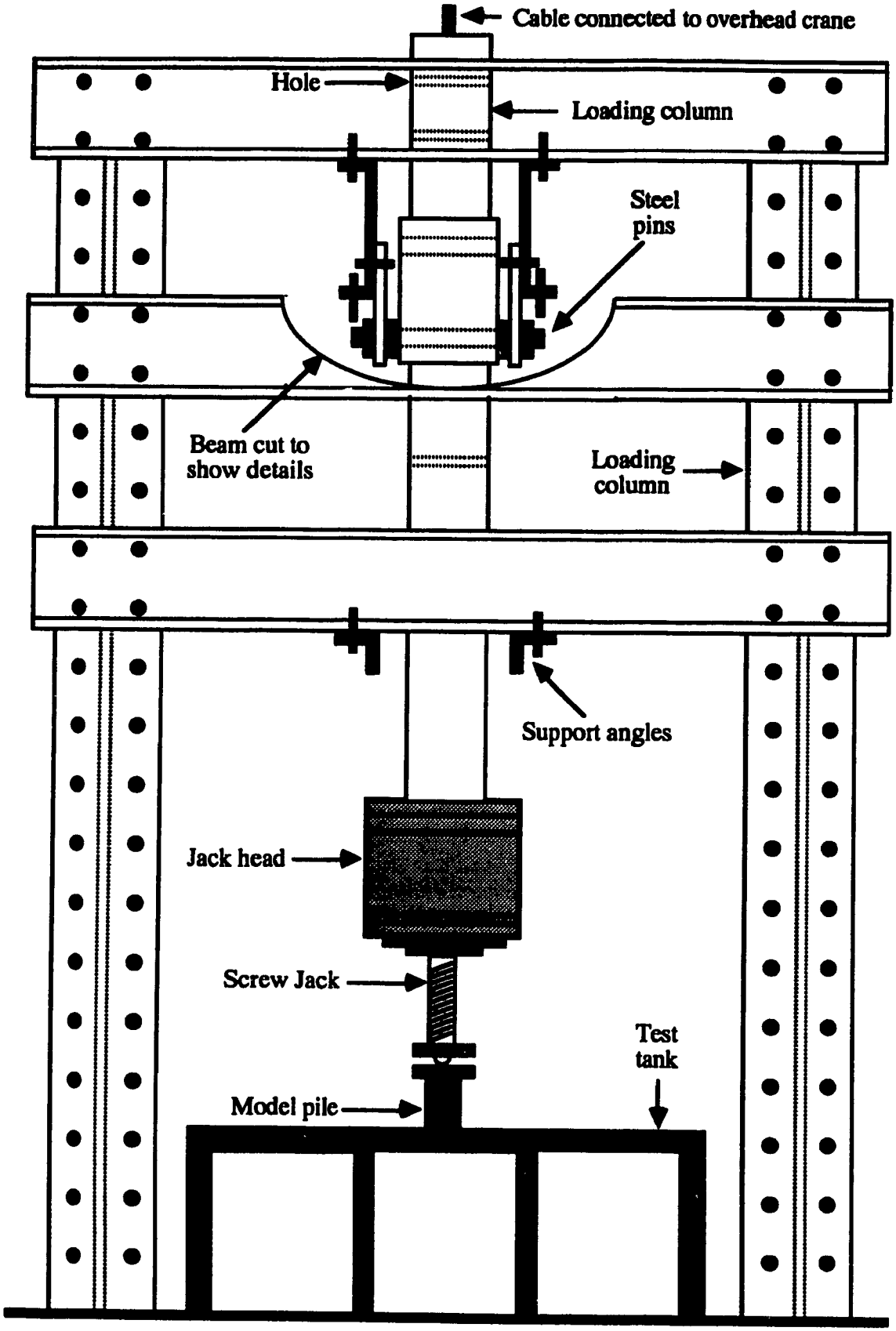

Fig. 3.6 Schematic Diagram of Loading System

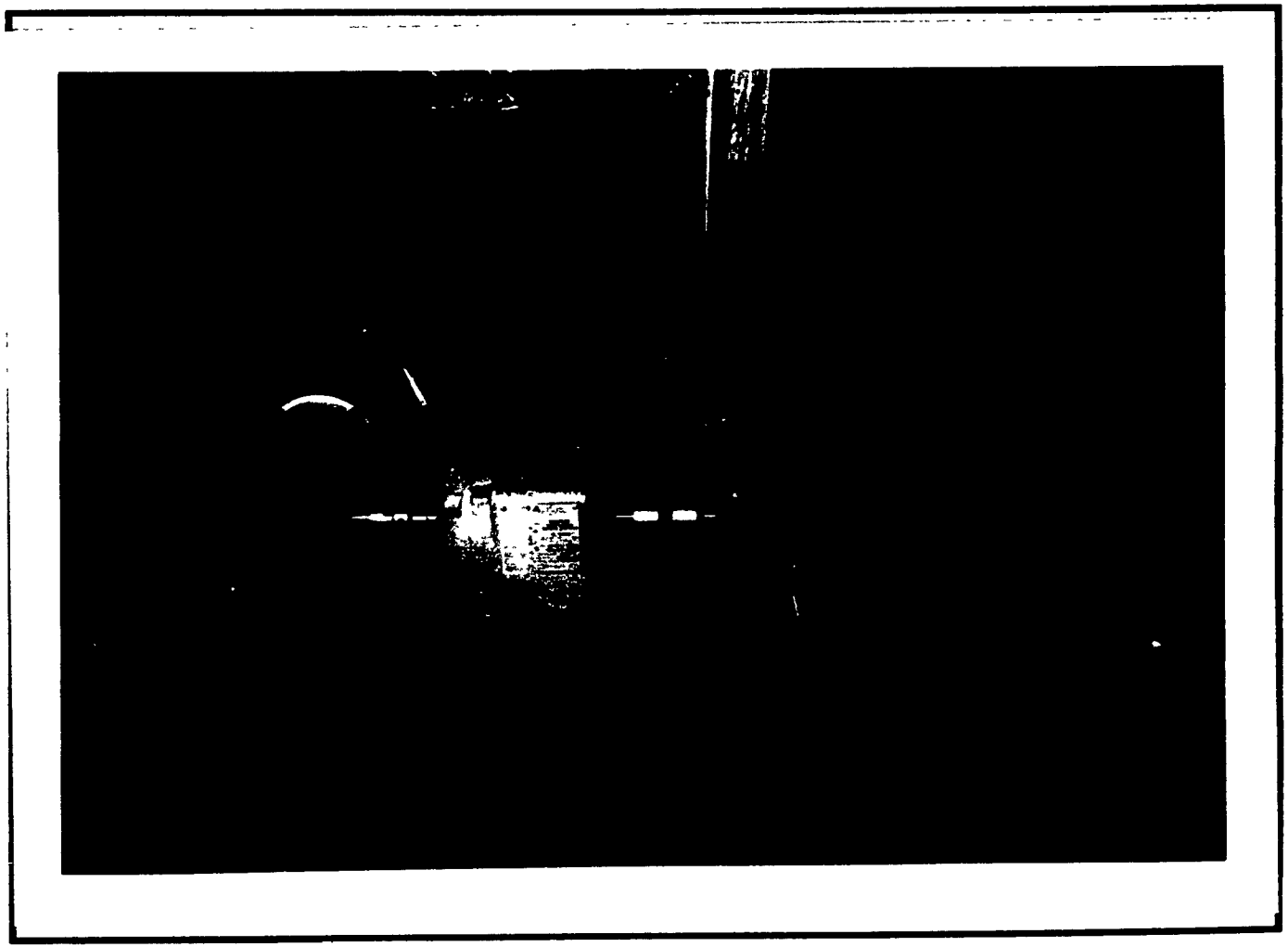

Fig. 3.7 A Close-up View of Loading Equipment

3.3 MODEL PILES

3.3.1 1.5 in. Diameter Model Pile

Two model piles were used in the investigation (Fig. 3.8). The first model pile is a steel pipe pile 67 in. long and 1.50 in. outside diameter (Fig. 3.9a). The load transmitted to the pile tip is measured by a load cell which has been designed to make use of available pressure transducers.

3.3.2 3 in. Diameter Model Pile

This model pile consists of steel and aluminium pipe sections (3 in. outside diameter) connected to a total length of 66 in. (Fig. 3.9b). Normal pressure acting along the pile shaft are measured by eight pressure transducers installed in the aluminium pipe sections which are split longitudinally into halves for easy access to instrumentations. The bottom of the pile is equipped with a stud load cell which measures the tip load. To ensure uniform surface conditions for both piles, sand paper was glued to the pile shafts and pile tips, and changed anew after each test. Detailed drawings of all components of the two model piles are provided in Appendix 4.

3.4 PROPERTIES OF SAND

All load tests in this investigation were performed in Morie sand (a clean, air-dried sand originating from Mauricetown, New Jersey, USA). The grain size distribution curve (Fig. 3.10) and detailed examination indicated a medium, uniform sand composed mostly of subangular quartz particles. Laboratory tests on this sand revealed a specific gravity equal to 2.66, maximum and minimum void ratios of 0.815 and 0.590 respectively, a uniformity coefficient of 1.45 and an effective grain size of 0.82 mm. The main physical characteristics of Morie sand are given in Table 3.1.

The angle of shearing resistance of Morie sand was determined from both triaxial tests

Fig. 3.8 1.5 in. and 3. in. Diameter Model Piles

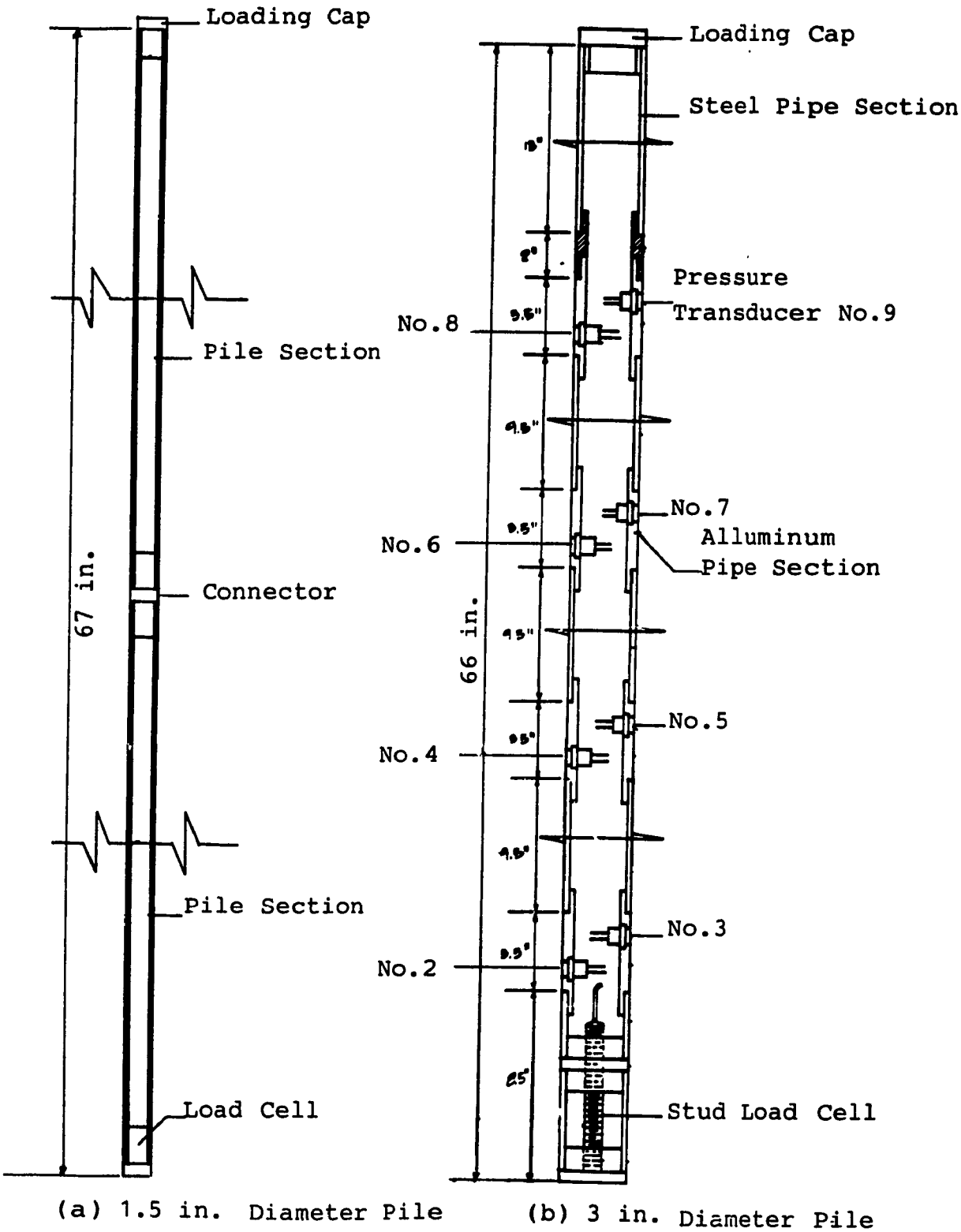

Fig. 3.9 Schematic Diagram of Model Piles

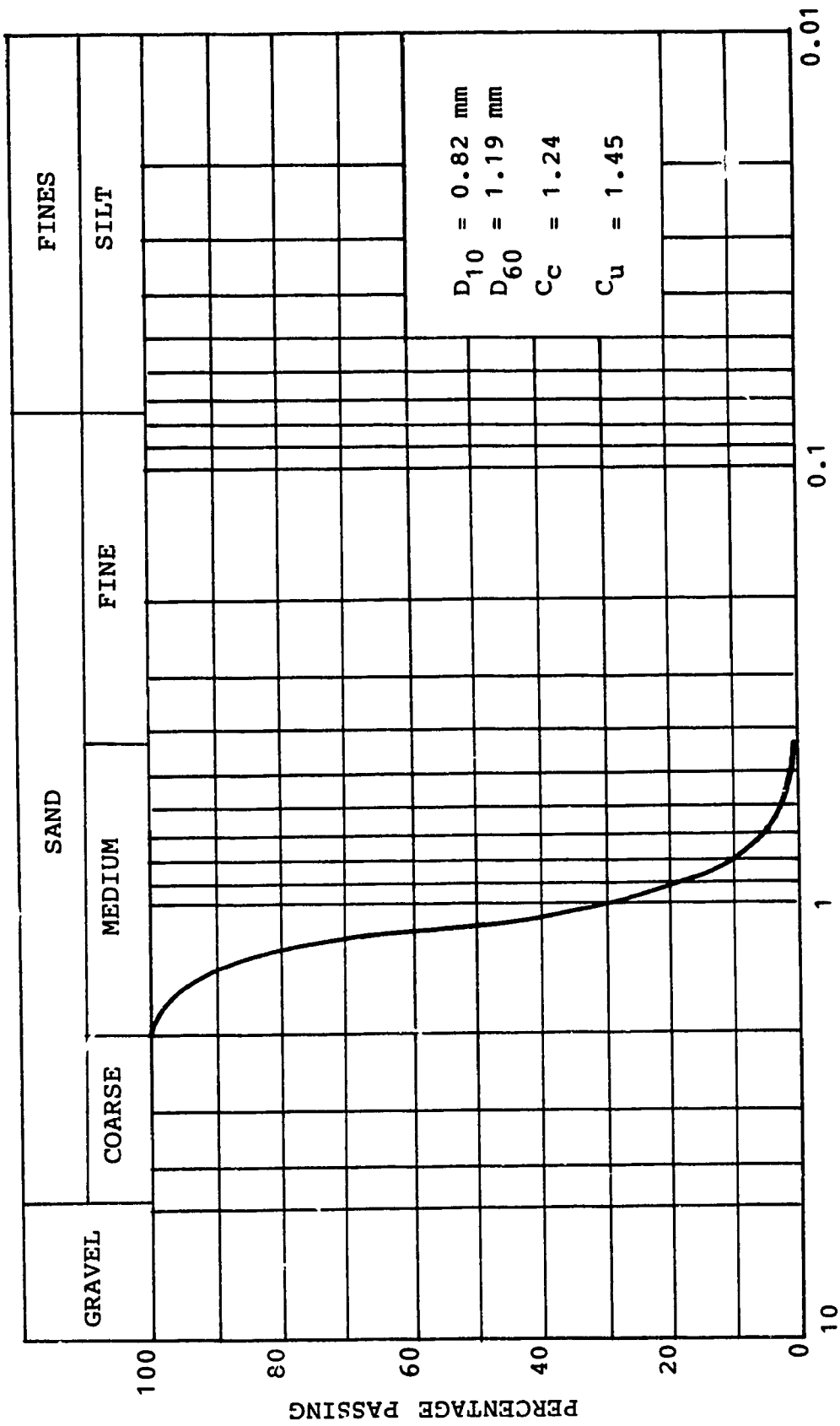

Fig. 3.10 Grain Size Distribution Curve of Morie Sand

Table 3.1: Physical Properties of Morie Sand.

Property	Value
Specific Gravity, G_s	2.66
Coefficient of Uniformity, C_u	1.45
Coefficient of Curvature, C_c	1.24
Grain Diameter at 10% passing, D_{10}	0.82 mm
Grain Diameter at 60% passing, D_{60}	1.19 mm
Grain Diameter at 30% passing, D_{30}	1.10 mm
Maximum Dry Density, γ_{max}	104.5 pcf
Minimum Dry Density, γ_{min}	91.5 pcf
Maximum Void Ratio, e_{max}	0.815
Minimum Void Ratio, e_{min}	0.590

and direct shear tests (Afram, 1984). The angle of friction between the sand paper and the sand were also measured by using direct shear tests (Afram, 1984). A summary of these results is included in Table 3.2. Further analysis of Afram's results shows that the relationship between the angle of shearing resistance ϕ and the void ratio e may be expressed in a simple form suggested by Kérisel (1961):

$$\tan \phi = \frac{0.547}{e} \text{ [Triaxial Test]} \quad \text{... (3.1)}$$

$$\tan \phi = \frac{0.588}{e} \text{ [Direct Shear Test]} \quad \text{... (3.2)}$$

$$\tan \phi = \frac{0.602}{e} \begin{bmatrix}\text{Direct Shear Test} \\ \text{Sand/Sand paper}\end{bmatrix} \quad \text{... (3.3)}$$

Eqs. (3.1), (3.2) and (3.3) are plotted in Fig. 3.11.

3.5 PLACING OF SAND AND CONTROL OF DENSITY

The sand deposit in the test tank was prepared by raining sand from the distributing hopper built on a carriage which travelled to and fro on elevated rails. Different unit weights of sand may be obtained, depending on the height of fall of the sand (i.e., the vertical distance from the bottom of the hopper to the sand surface), the width of slots at the hopper bottom, and the speed of the moving carriage. After a series of in-place calibration tests, a definite procedure was established for preparing a sand deposit at a specified density. The calibration work was performed by raining the sand over thin walled aluminium cans (3.4 in. dia. x 2.0 in.) strategically placed on the sand surface which had been initially levelled in the test tank. For each given height of fall of the sand, the raining process continued until it produced a layer about 3 in. thick on top of the density cans. Each density can was then carefully dug out by hand and by using a suction hose. During the excavation process, a cone of excess sand was

Table 3.2: A Summary of Shear Tests on Morie Sand (After Afram, 1984).

Type of Test	Void Ratio e	Relative Density D_R (%)	Angle of Shearing Resistance ϕ (deg.)
Triaxial	0.773	17.8	35.5
	0.724	40.4	37.0
	0.672	63.6	39.0
Direct shear	0.755	26.7	37.5
	0.705	48.9	39.5
	0.653	72.0	42.0
	0.613	89.8	44.3
Direct shear (sand/sand paper)	0.740	33.3	38.0
	0.700	51.1	40.3
	0.661	68.4	42.8
	0.606	92.9	45.5

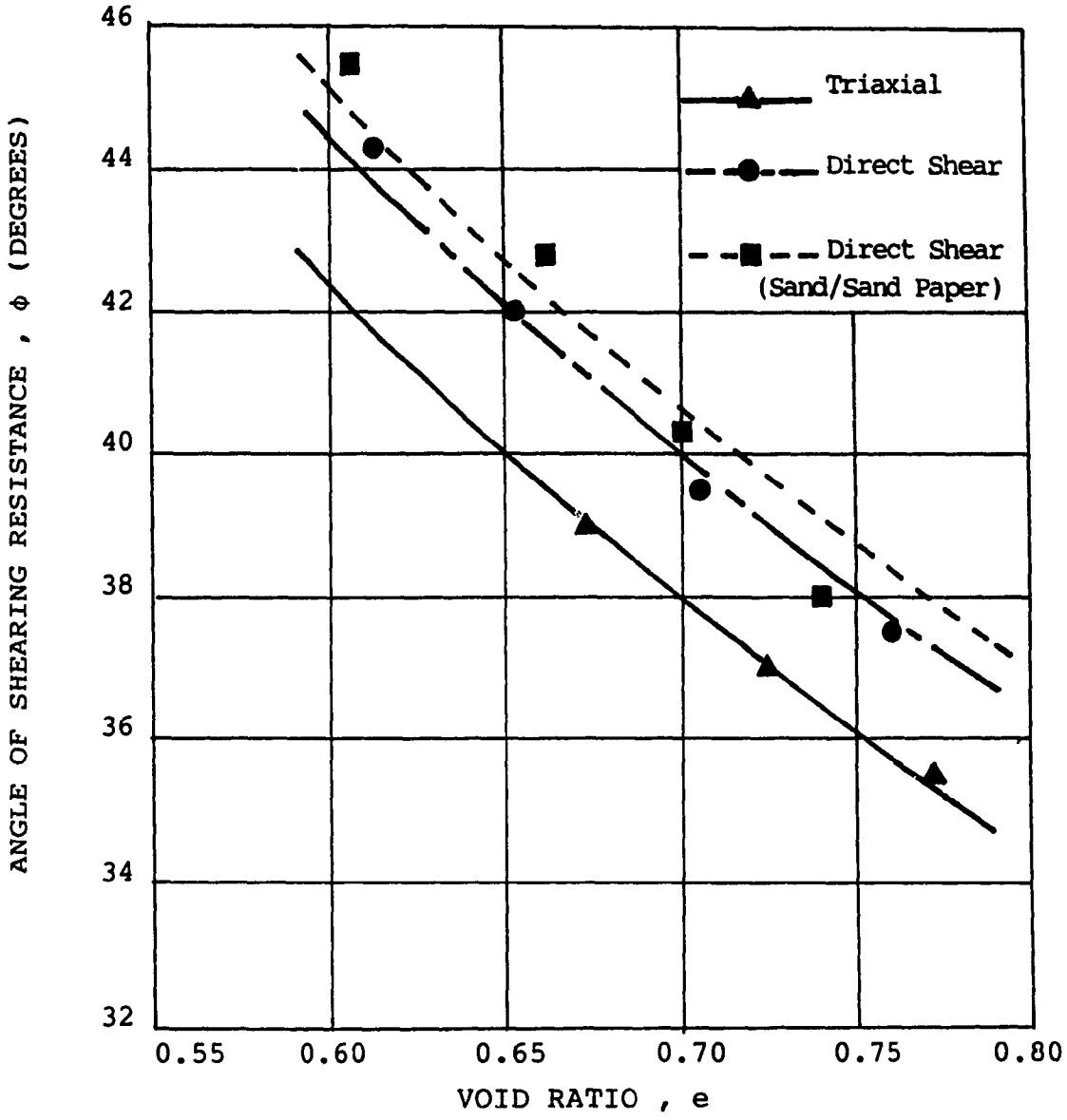

Fig. 3.11 Relationship Between Angle of Shearing Resistance ϕ and Void Ratio e for Morie Sand

kept on top of each can until it was gently scraped off, flushed at the rim with a thin straight edge. After weighing each can filled with sand, the density of the sand in the can could be calculated once the volume and the weight of the can were known. The slot at the bottom of the hopper was 1/8 in. wide and the carriage speed was maintained at 14 ft. per minute in all calibration tests. Figure 3.12 shows three patterns of density can arrangements used in the calibration program. Besides the 23 can arrangements, the 10 and 5 can arrangements offered additional data on the sand uniformity along the center line and the general area at the middle of the sand deposit where load tests on model piles would be subsequently performed. Table 3.3 summarizes the calibration results and Fig. 3.13 shows the variation of the sand density obtained as a function of the height of fall of sand. It can be seen that for Morie sand, the maximum density obtained by the present sand spreading procedure is about 99.6 pcf.

3.6 TESTING PROCEDURE

In each test series, a sand deposit was first prepared in the test tank by raining sand from a moving hopper (described in Section 3.4). The final sand level was kept at 2 in. below the top of the test tank. The loading column was then moved to the vertical position for the coupling of the screw jack and the model pile. The vertical pile was carefully checked by means of a level-protractor device and a plumb line. All necessary adjustments were made at this stage to secure an expected accuracy of ± 0.5 degree. After the model pile was pushed into the sand bed to the selected depth at a rate of 1.0 in. per minute, it was unloaded for mounting a load measuring device at the pile top. The load test was then started at a constant penetration rate of 0.01 in. per minute.

At an axial pile displacement equal to at least 30 percent of the pile diameter, the model pile was unloaded then pushed to the next depth level for another test. Figure 3.14 shows the 1.5 in. diameter pile being pushed into the sand deposit. The 6000 lb. capacity proving ring,

Table 3.3: Summary of Sand Density Calibration Test Results.

Test No.	Height of Fall (in.)	Number of Cans Used	Average Dry Unit Weight γ_d(pcf)
1	6	23	97.3
2	6	23	97.3
3	12	23	97.8
4	12	23	98.7
5	12	10	98.7
6	18	23	98.6
7	18	23	98.8
8	18	10	99.0
9	18	5	99.2
10	24	23	99.5
11	24	5	99.0
12	30	23	99.7
13	30	5	99.0
14	44	23	99.5
15	56	23	99.7

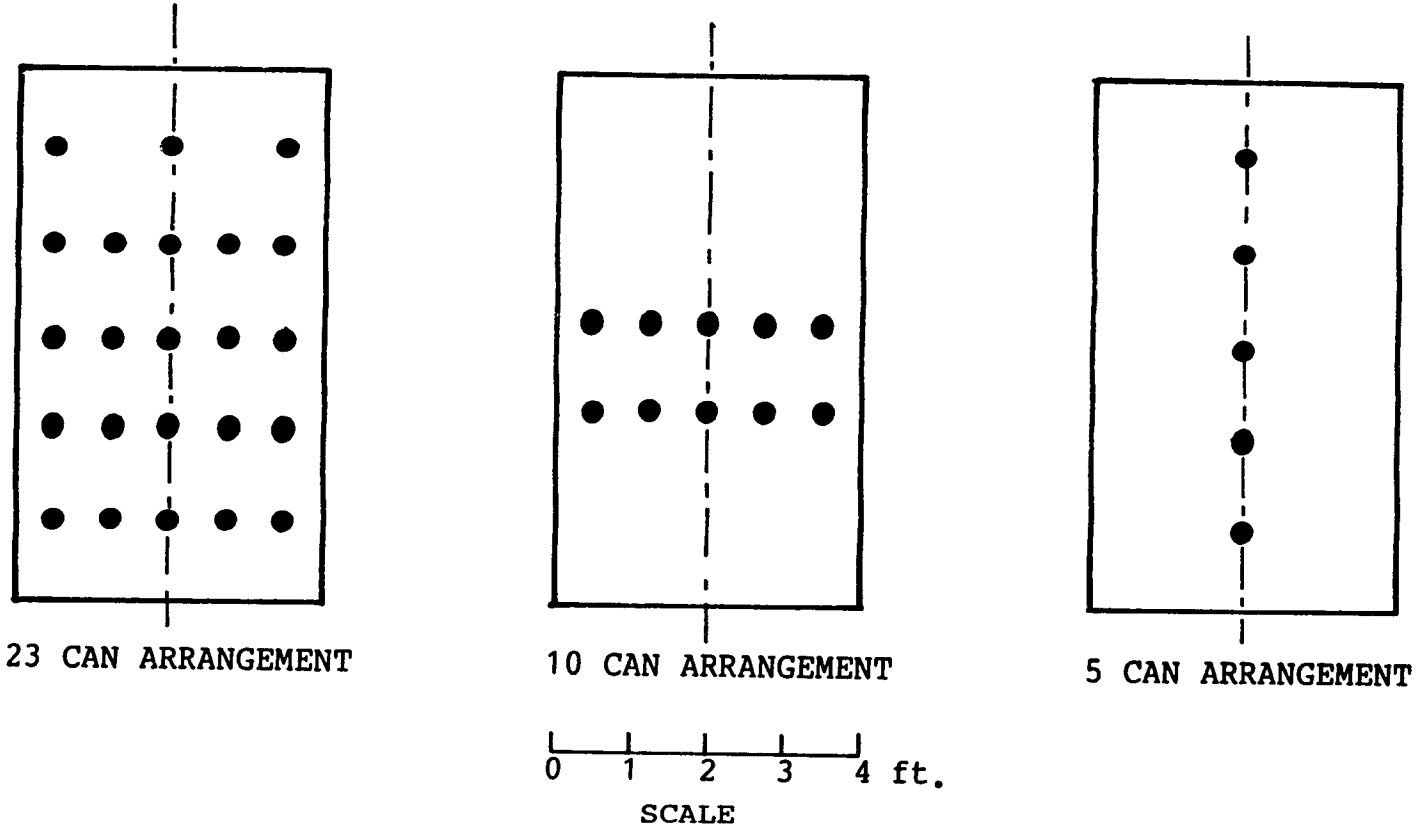

Fig. 3.12 Arrangement of Density Cans in Calibration Tests

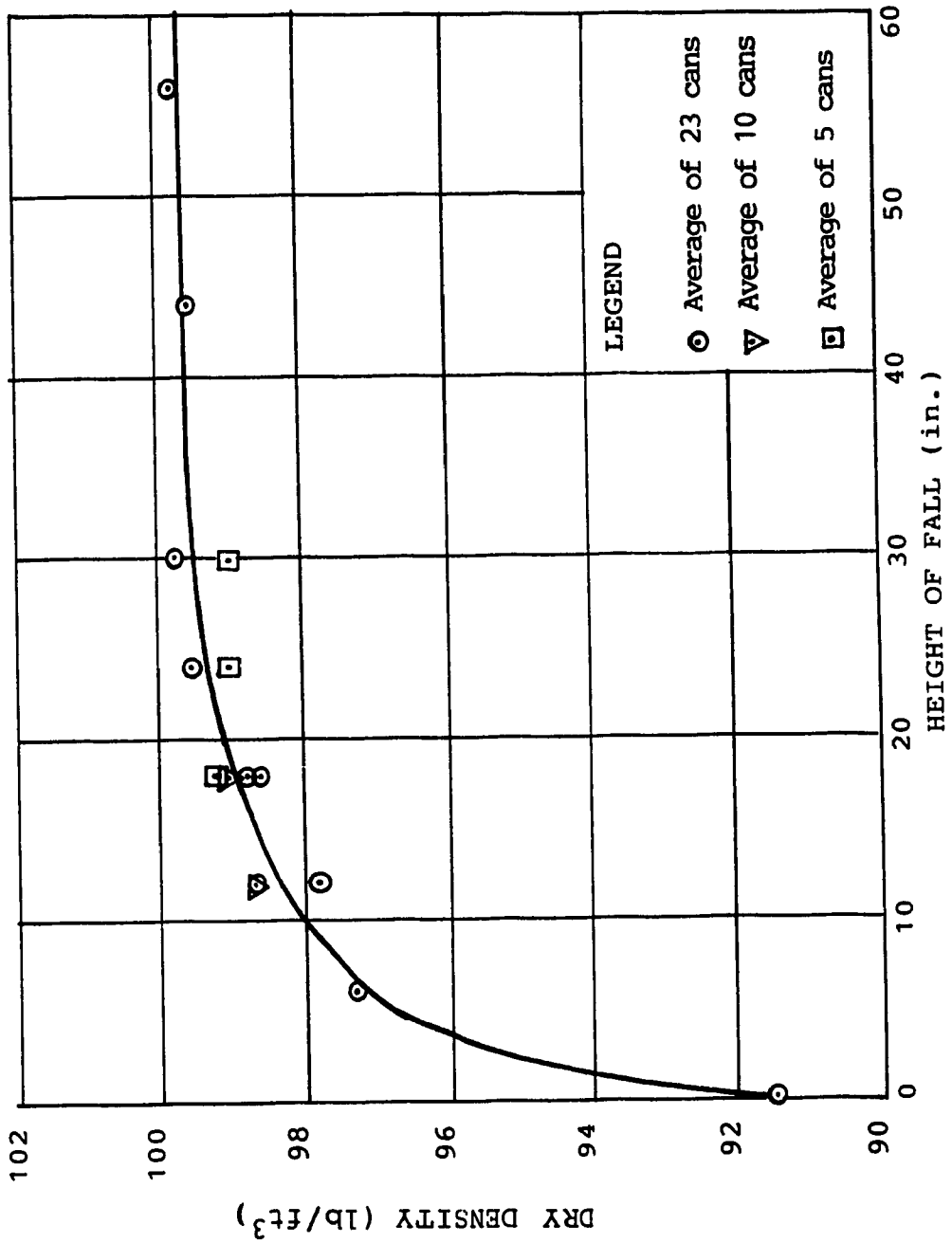

Fig. 3.13 Relationship Between Sand Density and Height of Fall

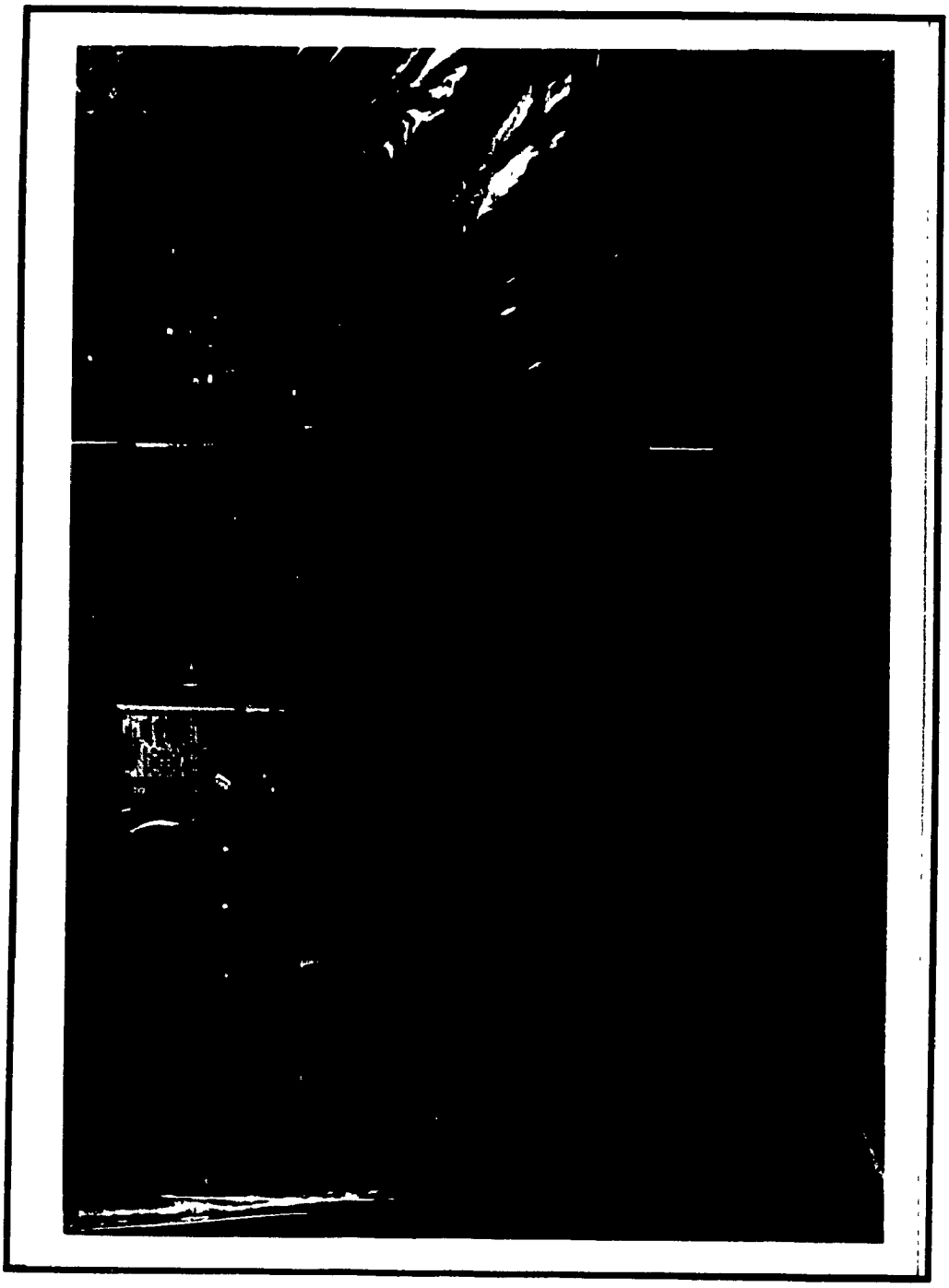

Fig. 3.14 Method of Pile Installation

installed between the pile loading cap and the screw jack, measured the applied axial load, and two dial gages provided axial pile displacement measurement at the pile top (Fig. 3.15). The proving ring readings, the load cell readings at the pile tip, and pile displacements were recorded manually at regular time interval.

The axial load applied on this pile was measured by a 20,000 lb. capacity flat load cell and the pile axial displacement was monitored by two dial gages. The stud load cell at the bottom of the pile provided measurements of tip loads. The over all view of the 3 in. diameter pile during a load test is shown in Fig. 3.16. Readings of the load cells at the top and bottom of the pile, and 4 pairs of pressure transducers along the pile shaft were recorded by a data acquisition system at selected time intervals. All detailed drawings of accessory parts for pile load test are given in Appendix 4.

3.7 TEST RESULTS

3.7.1 Experimental Program

A total of six tests, which included four tests on the 1.5 in. diameter pile and two tests on the 3 in. diameter pile, were performed in a medium sand deposit prepared to a relative density of 65.3%, (i.e. γ_d = 99.6 pcf) by raining sand from at least 44 in. above an existing sand level. In this investigation, the relative depth D/B of the 1.5 in. diameter pile was varied from 10 to 40, and from 10 to 20 for the 3 in. diameter pile.

3.7.2 Failure Loads

The ultimate axial loads Q_u, were determined by using Vesic's criteria (Vesic, 1967), which defines the ultimate load as the load at which the pile displacement rate first reaches its maximum. In practical terms, Q_u is taken to be that load at which the pile settlement passes into a steep and fairly straight tangent (Ranjan, 1970). The point resistance Q_p and the skin friction Q_s were determined from the value of the ultimate displacement of the pile in their

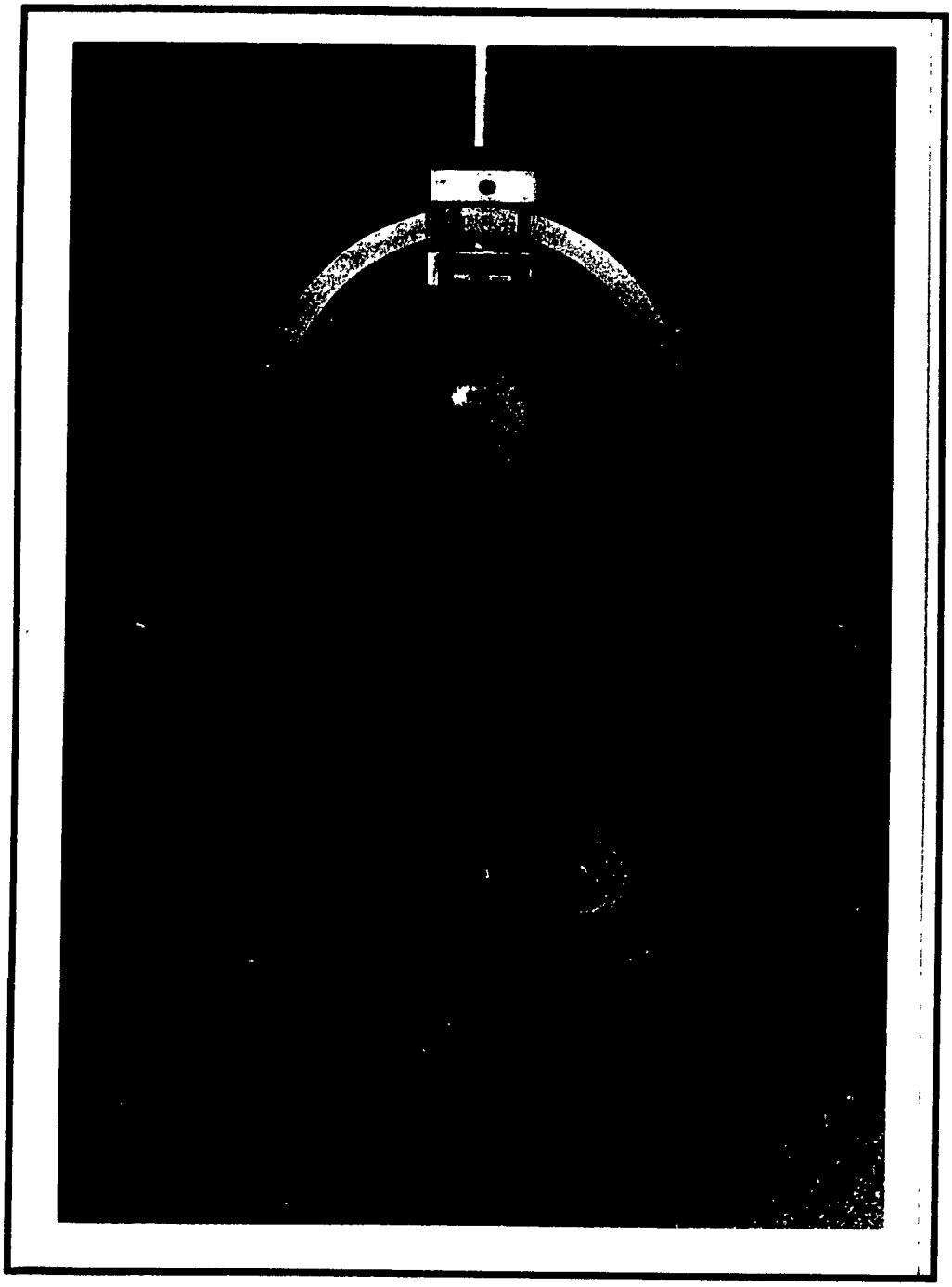

Fig. 3.15 A Load Test on 1.5 in. Diameter on Model Pile

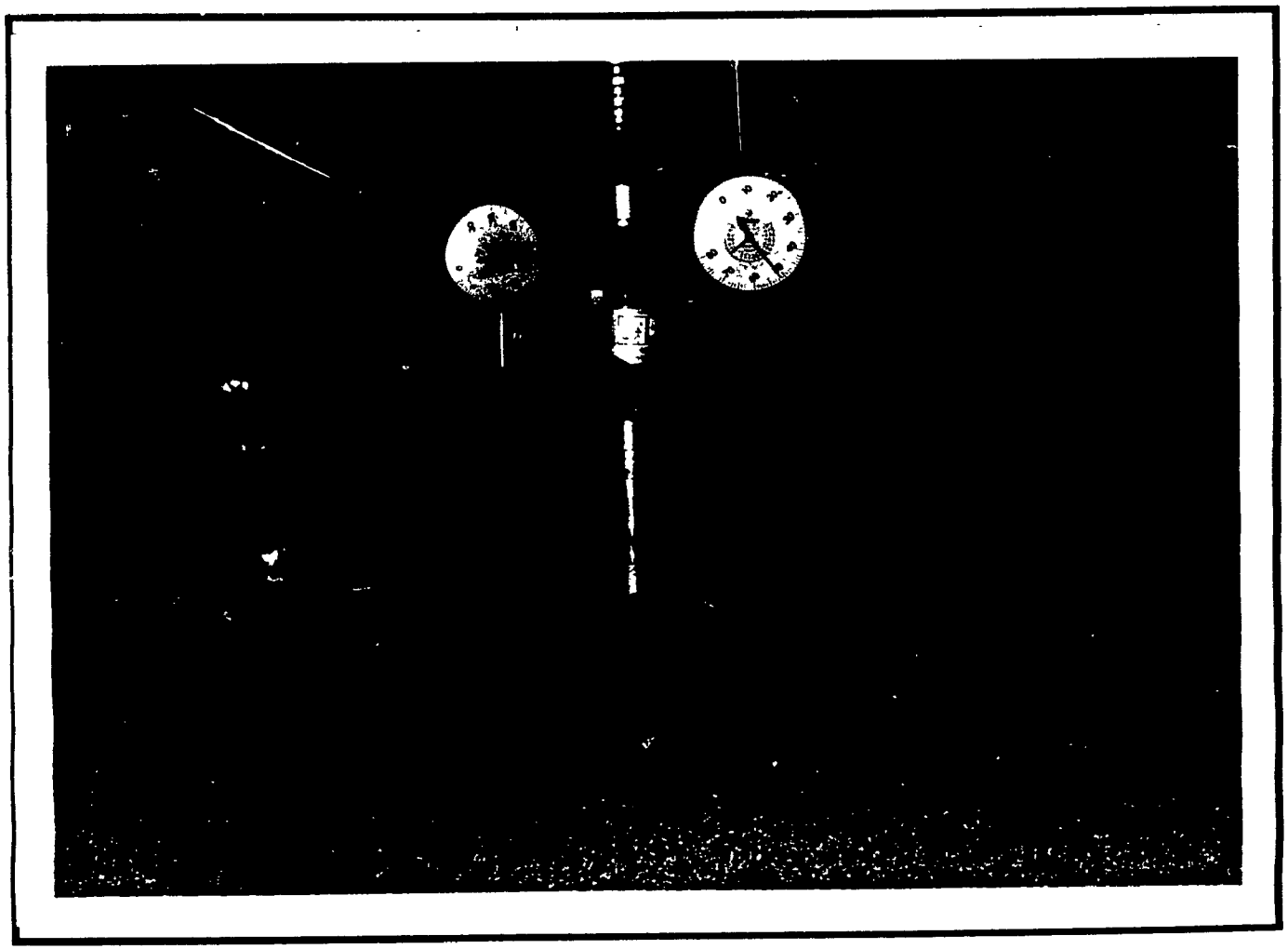

Fig. 3.16 A Load Test on 3 in. Diameter on Model Pile

corresponding load-settlement curves. The variations of the total load, tip load, and skin friction with axial pile displacement for each test are shown in Fig. 3.18 through Fig. 3.23. Significant results of the load tests are summarized in Table 3.4. The load test results for the 1.5 in. diameter pile were also plotted in Fig. 3.24.

3.7.3 Soil Pressure Along Pile Shaft

The variations of normal pressure, measured by pressure transducers at different levels on the pile shaft, with pile axial displacement are shown in Fig. 3.25 through Fig. 3.28. Table 3.5 summarizes the measured normal pressures corresponding to the ultimate displacement of the model pile.

Table 3.4: Results of Load Tests on Model Pile.

Type of Model Pile	Pile Test No.	Nominal Depth, D (in.)	Relative Depth D/B	Ultimate Bearing Capacity, Q_u (lbs.)	Point Resistance, Q_p (lbs.)	Skin Friction, Q_s (lbs.)
1.5 in. Diameter	A-1	15	10	483	348	135
	A-2	30	20	918	549	369
	A-3	45	30	1249	614	635
	A-4	60	40	2279	1344	935
3.0 in. Diameter	B-1	30	10	1980	1408	572
	B-2	60	20	4226	2681	1545

Table 3.5: Measured Normal Stress on Pile Shaft.

Pile Test No.	Pressure Transducer No.	Relative Depth of Transducer z/B	Ultimate Displacement of Pile (in.)	Measured Normal Stress on Pile Shaft (psi)
B-1	2	6.8	0.220	3.08
	3	6.3		3.80
	4	2.5		3.46
	5	2.0		3.75
B-2	2	16.8	0.250	5.82
	3	16.3		3.77
	4	12.5		6.03
	5	12.0		2.21
	6	8.2		4.89
	7	7.7		3.96
	8	3.8		1.53
	9	3.3		-----

Remark

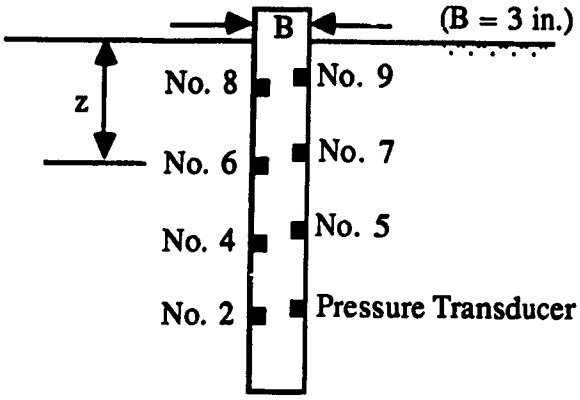

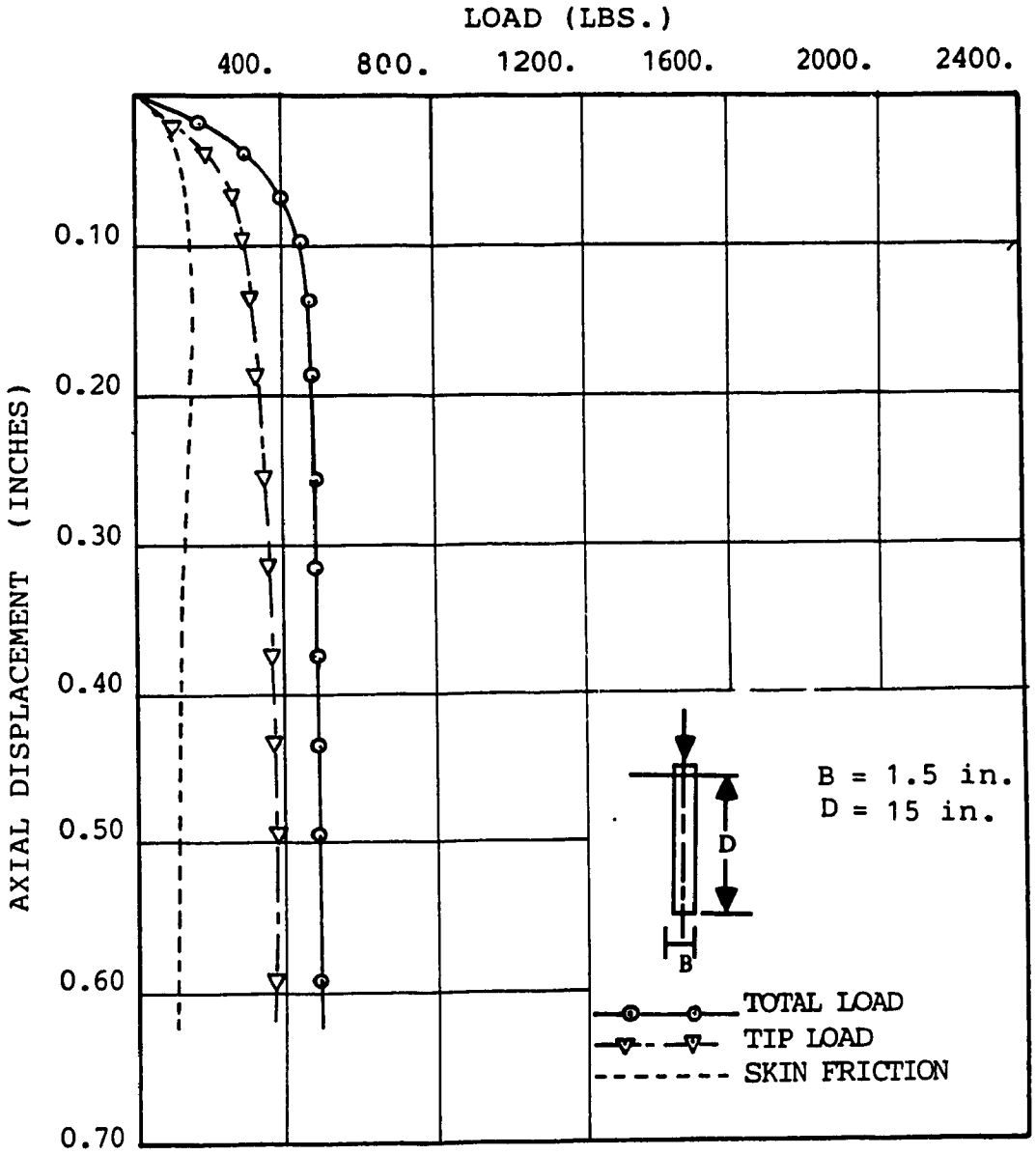

Fig. 3.17 Load-Displacement Curve for 1.5 in. Diameter Pile (D/B = 10)

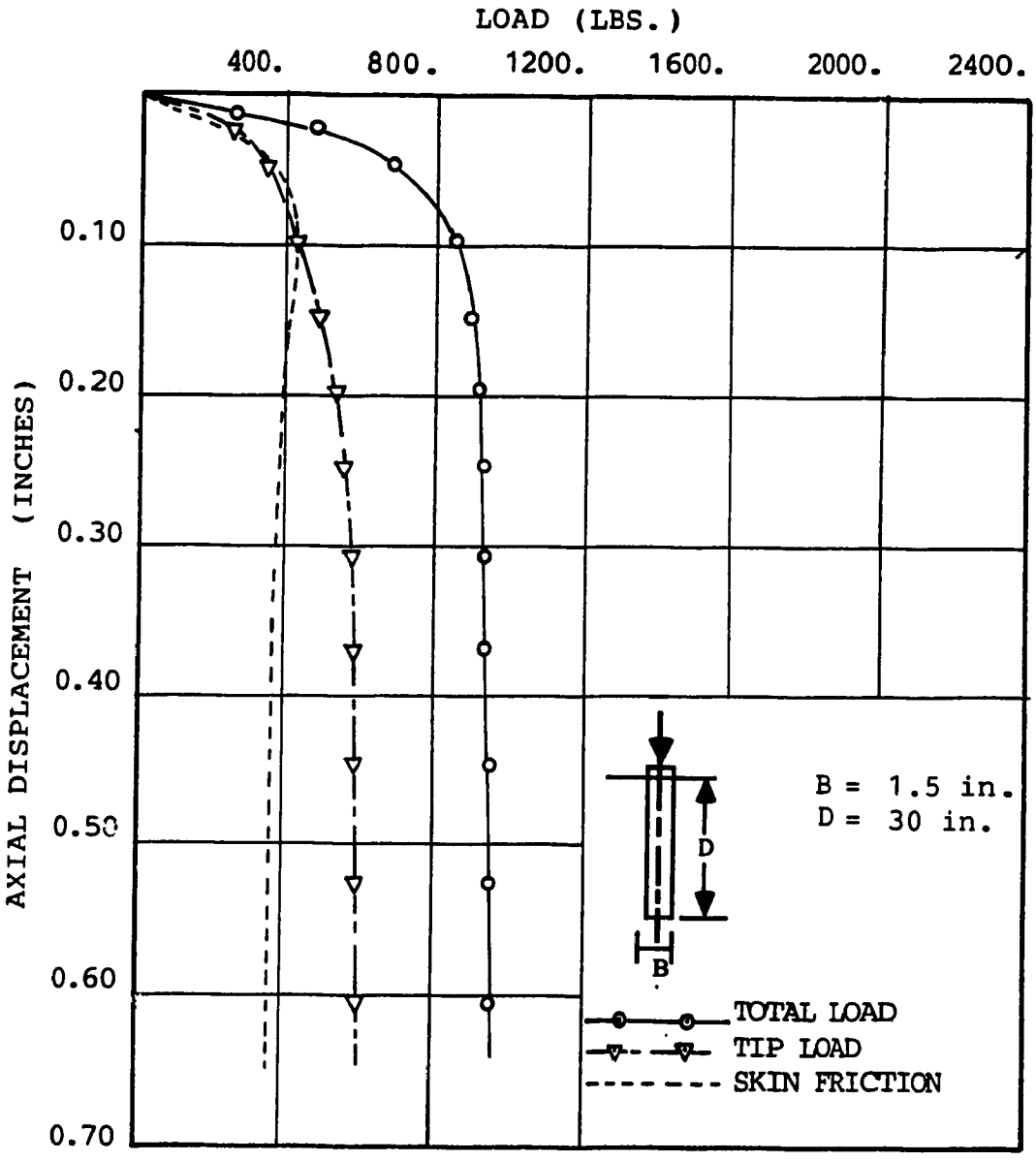

Fig. 3.18 Load-Displacement Curve for 1.5 in. Diameter Pile (D/B = 20)

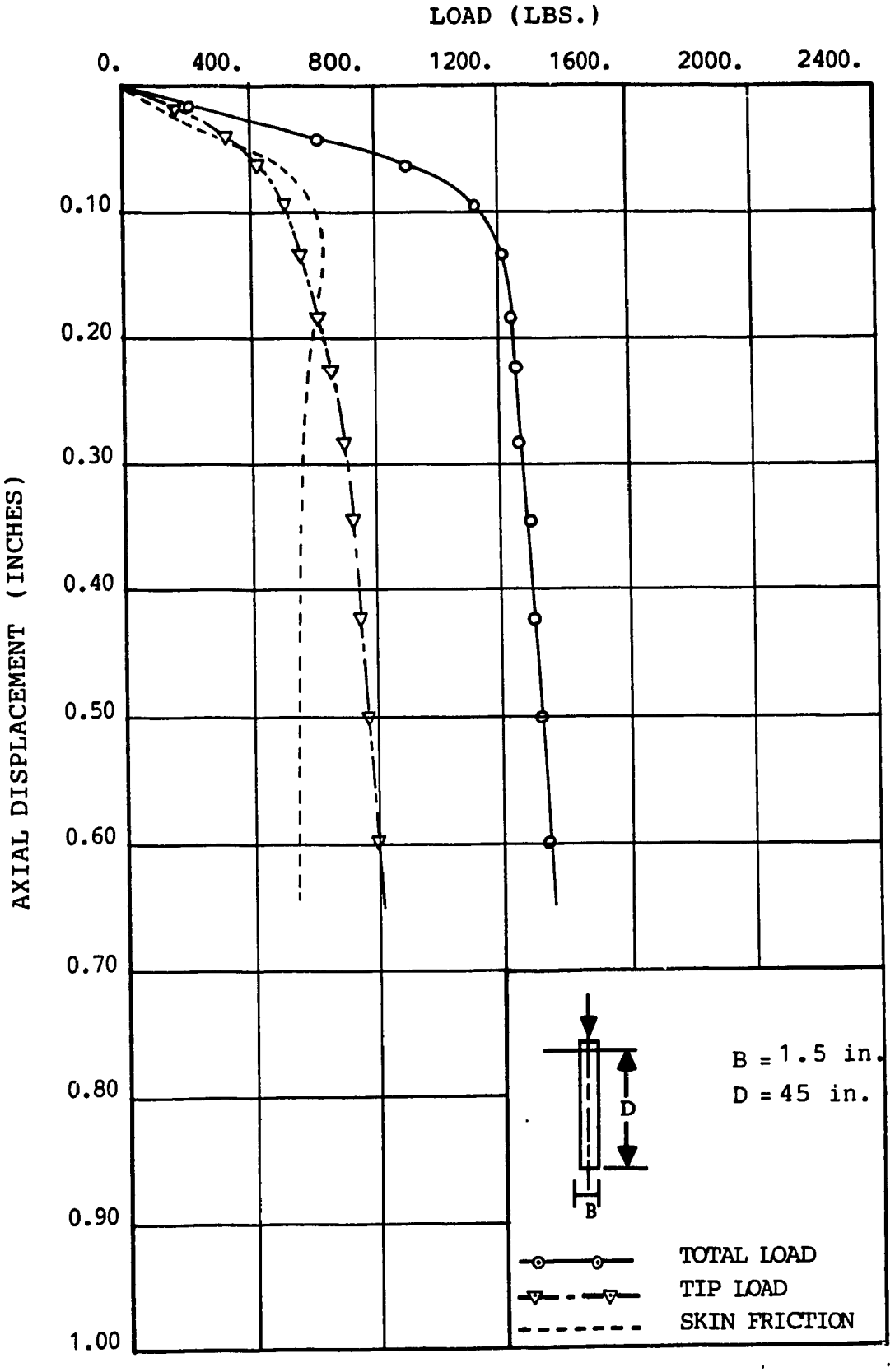

Fig. 3.19 Load-Displacement Curve for 1.5 in. Diameter Pile (D/B = 30)

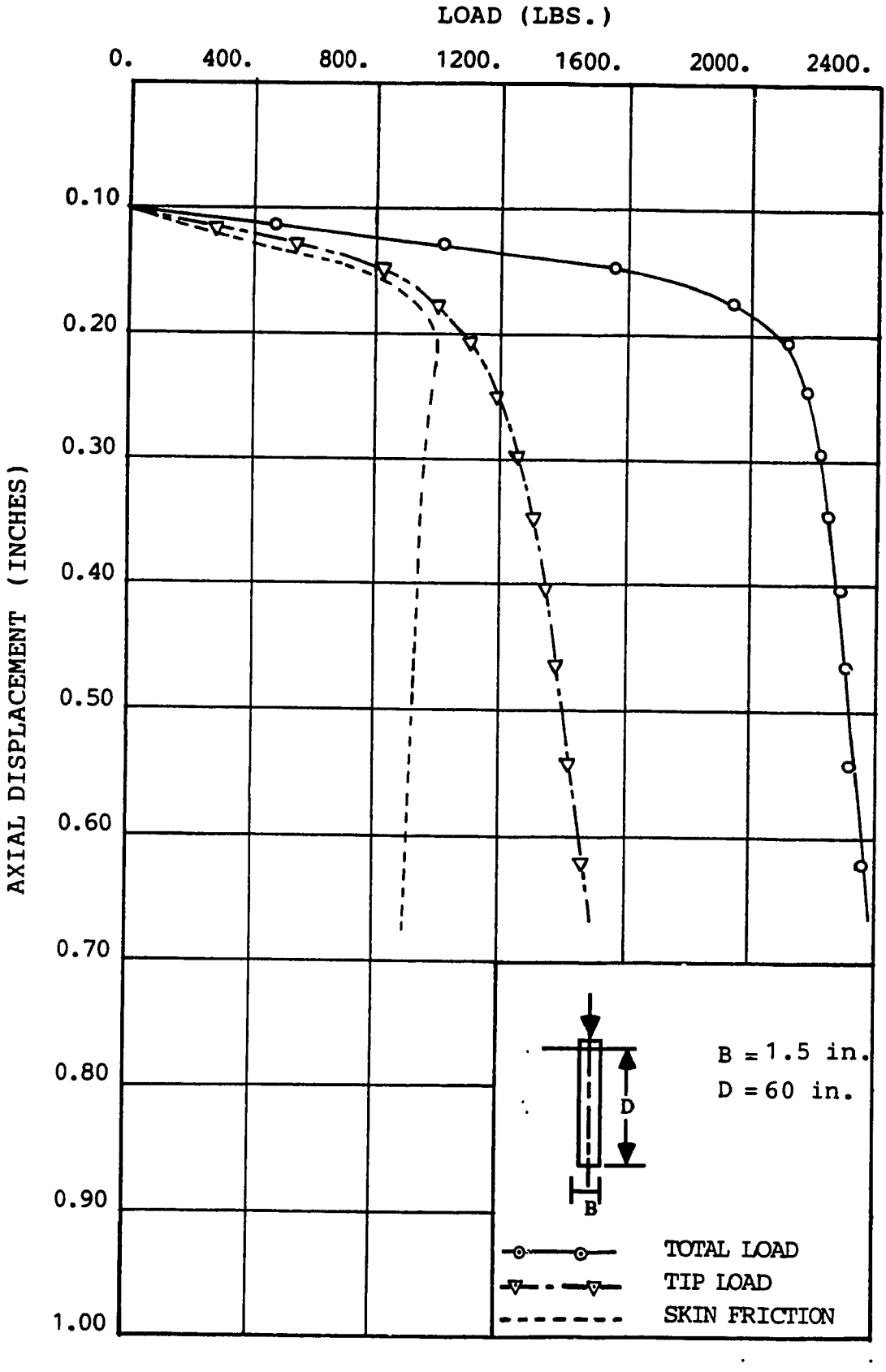

Fig. 3.20 Load-Displacement Curve for 1.5 in. Diameter Pile (D/B = 40)

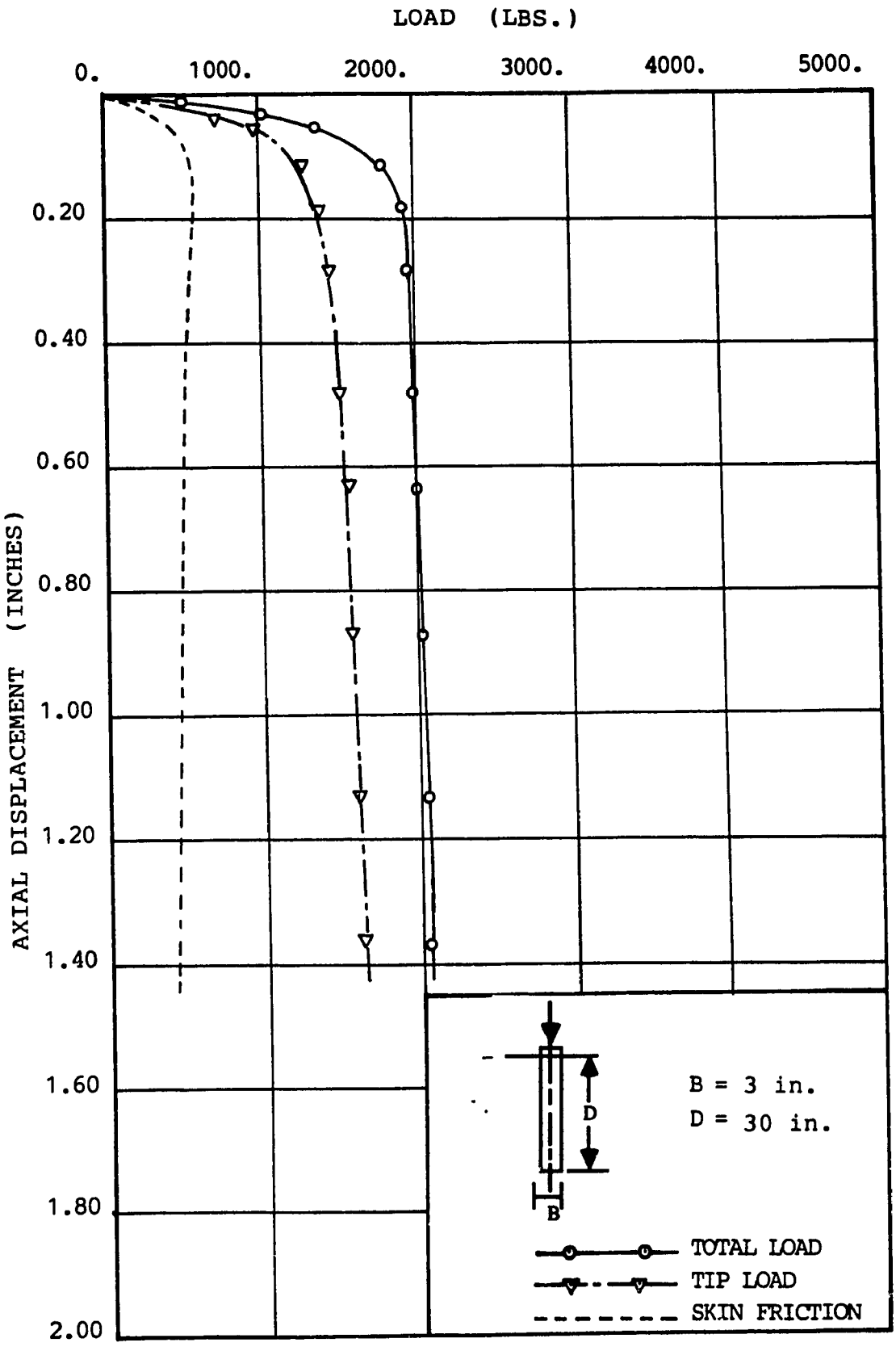

Fig. 3.21 Load-Displacement Curve for 3 in. Diameter Pile (D/B = 10)

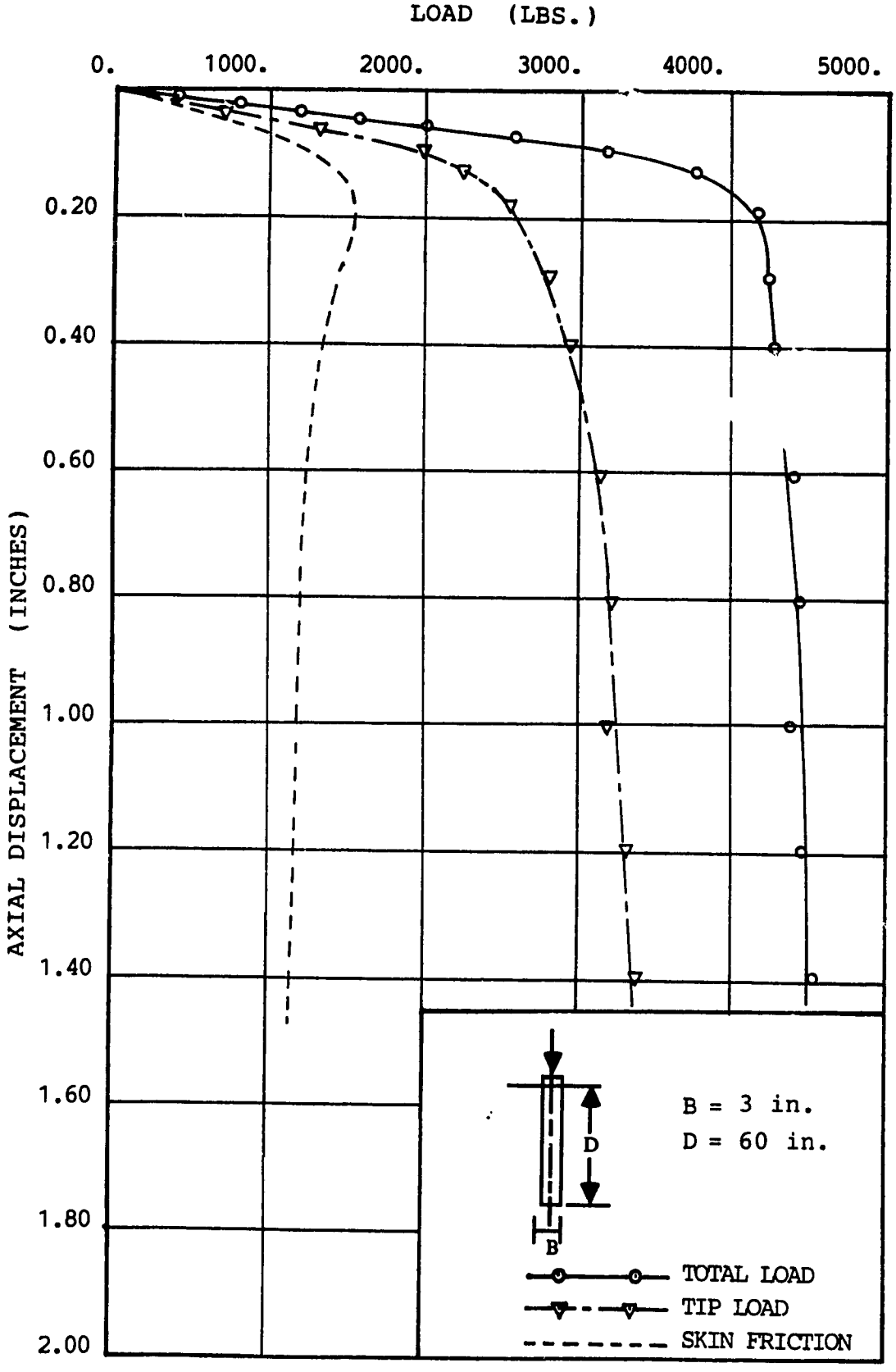

Fig. 3.22 Load-Displacement Curve for 3 in. Diameter Pile (D/B = 20)

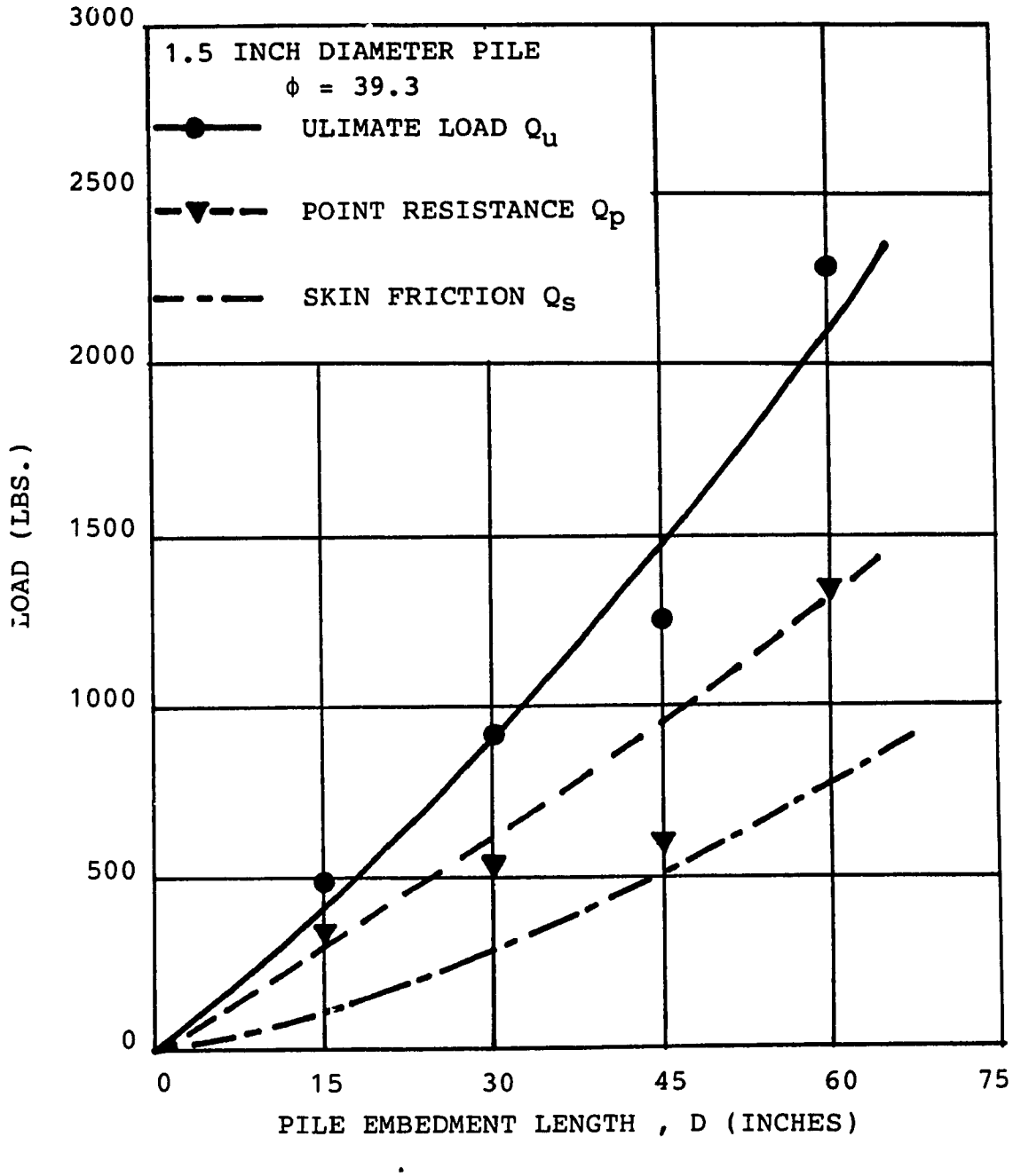

Fig. 3.23 Load Versus Depth for 1.5 in. Diameter Pile

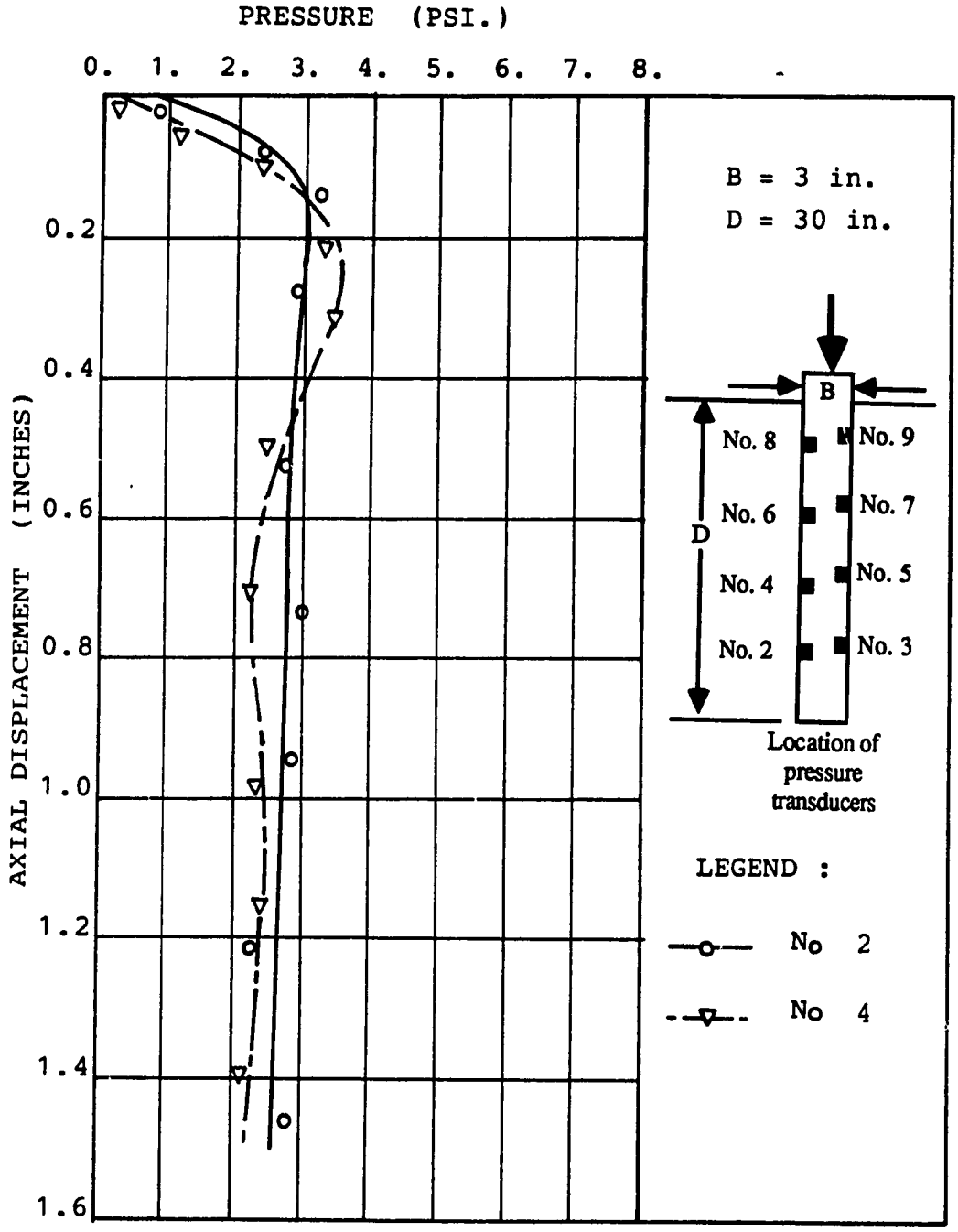

Fig. 3.24 Normal Pressure-Displacement Curve, D/B = 10

(Pressure Transducers Nos. 2, 4)

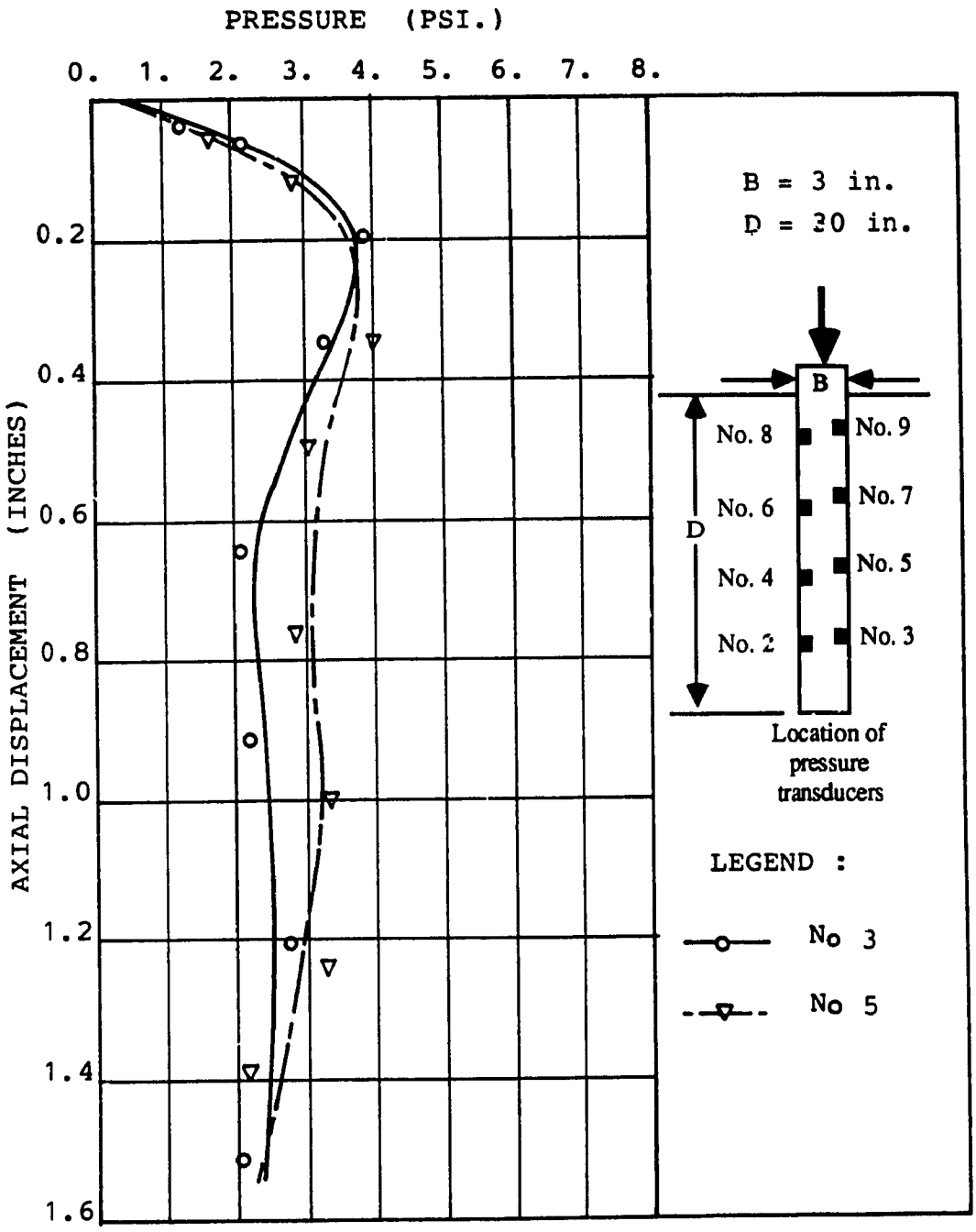

Fig. 3.25 Normal Pressure-Displacement Curve, D/B = 10

(Pressure Transducers Nos. 3, 5)

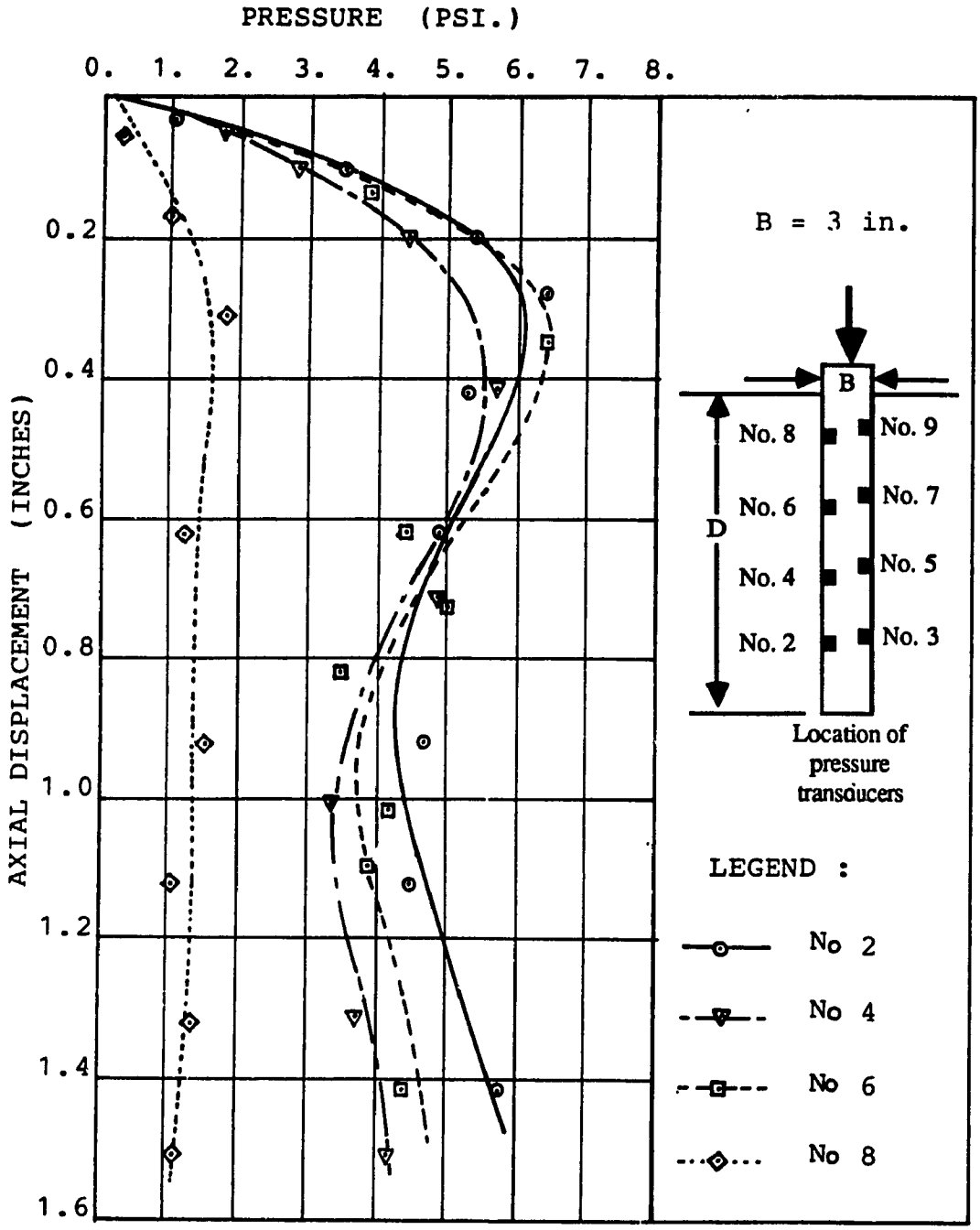

Fig. 3.26 Normal Pressure-Displacement Curve, D/B = 20

(Pressure Transducers Nos. 2, 4, 6, 8)

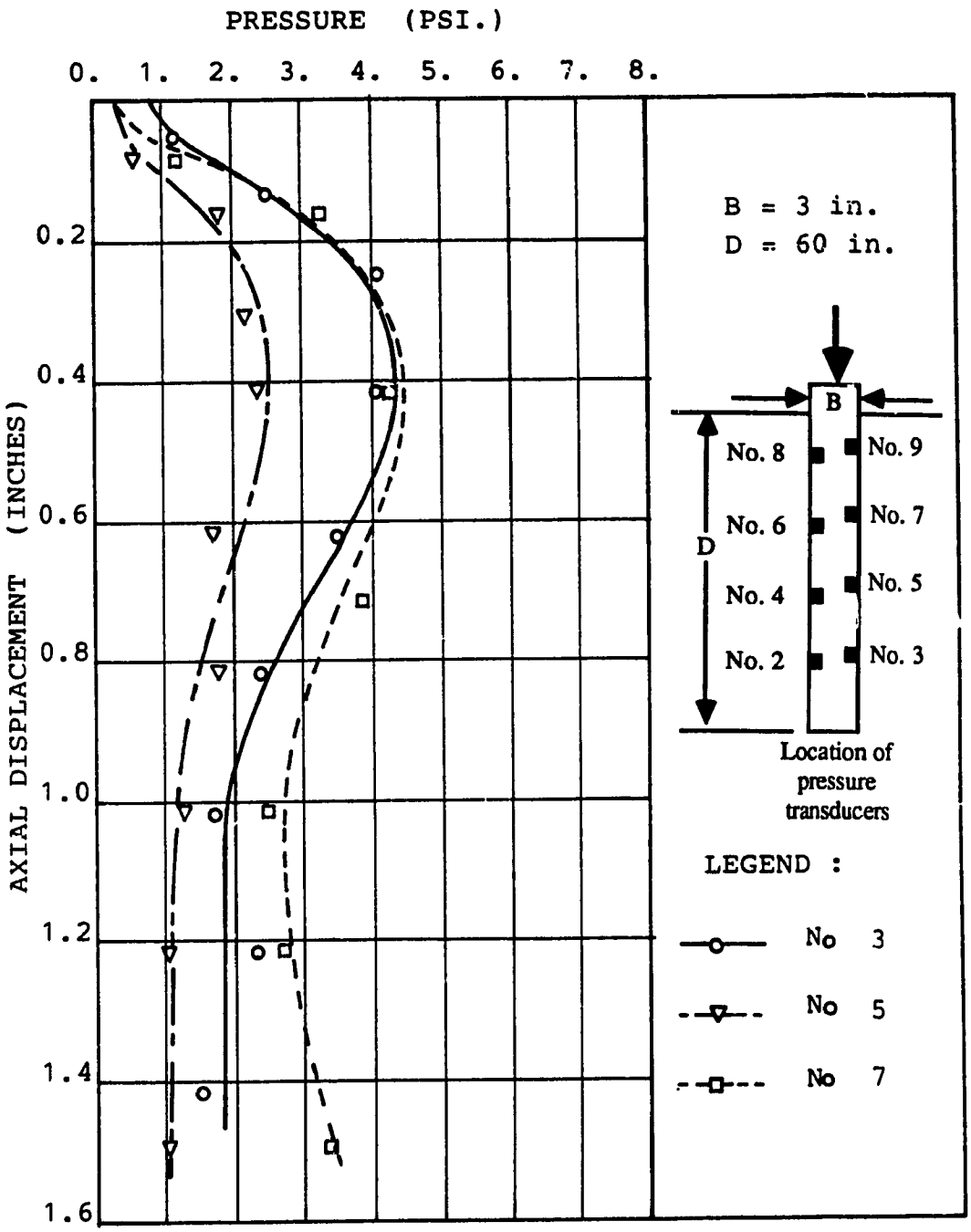

Fig. 3.27 Normal Pressure-Displacement Curve, D/B = 20

(Pressure Transducers Nos. 3, 5, 7)

CHAPTER 4

DEVELOPMENT AND VERIFICATION OF MODEL

4.1 GENERAL

When a circular pile is pushed into a sand mass to a given depth, a cone-shaped zone is formed below the pile tip (Robinsky and Morrison, 1964; Vesic, 1967). This zone moves together with the pile and behaves as if it is part of the pile itself (Fig. 4.1). During the penetration process, the sand around the pile tip is pushed downward and outward to provide space for the advancing pile. As a result, the sand mass in the vicinity of the pile undergoes varying degrees of displacement which becomes negligible beyond a certain distance from the pile axis. Outside this disturbed zone, the sand mass remains intact in its initial at-rest condition prior to the pile penetration. The lateral extent of this zone of influence, usually measured by the radius of influence (Széchy, 1960). As the shear failure patterns underneath the pile tip are not fully developed, this type of failure was referred to as punching shear failure (L'Herminier, 1953; Vesic, 1967) and experimentally demonstrated to be the exclusive failure mode of piles in sand (Vesic, 1967, 1977). The general shear failure modes assumed in almost all previous conventional bearing capacity theories of single piles in sand must be, therefore, considered as inconsistent with observed experimental evidences. In this chapter, a three dimensional model is developed in an attempt to account for the punching shear failure, and the interdependence between point resistance and skin friction of a vertical pile driven in sand.

4.2 FAILURE MECHANISM AND ASSUMPTIONS

For a given angle of shearing resistance ϕ of sand, pile relative depth D/B and coefficient of earth pressure at rest K_o before pile installation, the proposed critical shear surfaces in vertical section, as shown in Fig 4.2, consists of 3 zones:

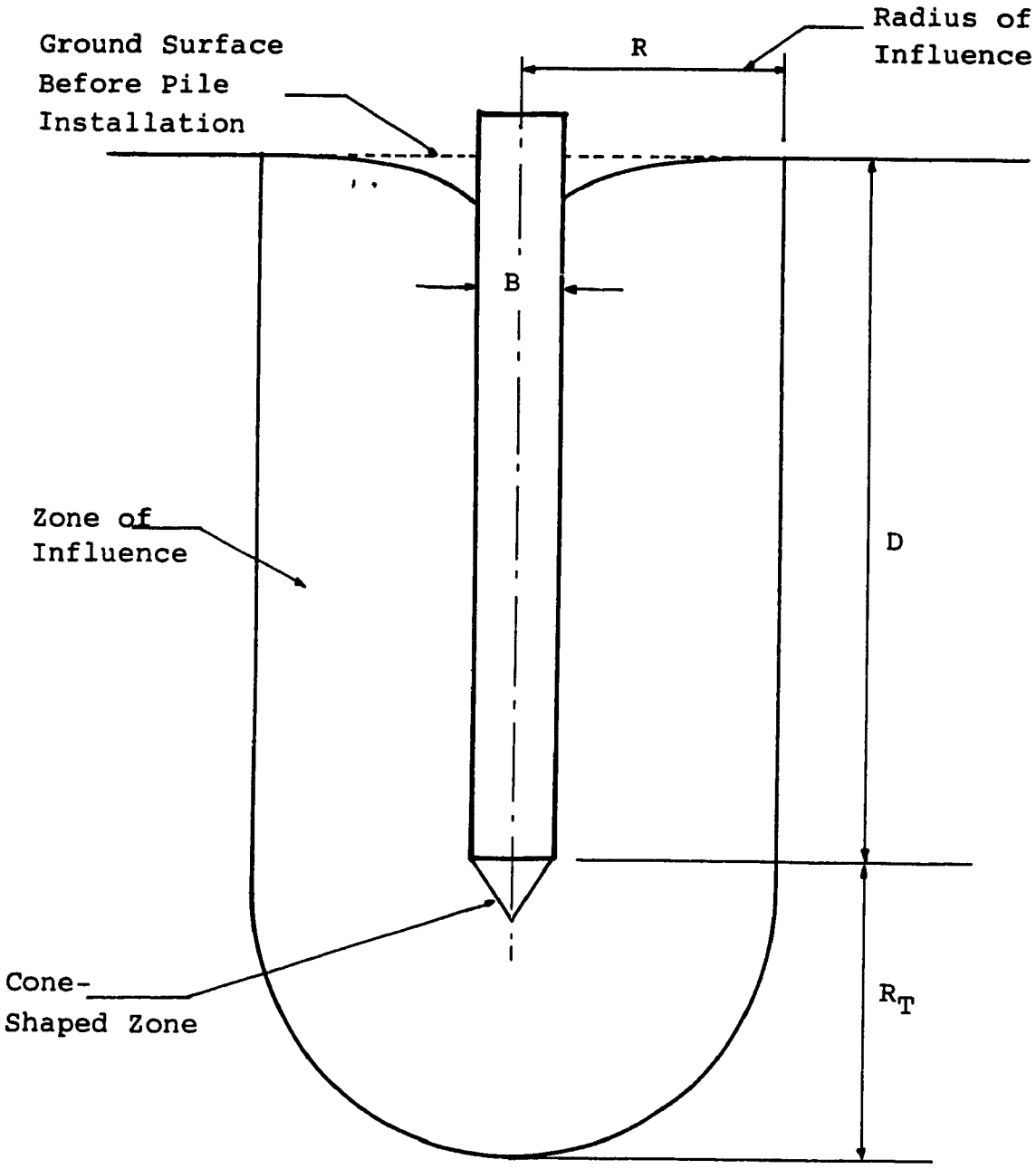

Fig. 4.1 Zone of Influence Around a Single Pile in Sand

1) Zone I is a wedge shaped zone aBa' located beneath the pile tip with its base angle ψ equal to $(\pi/4 + \phi/2)$.

2) Zone II consists of two radial shear zones Bac and Ba'c' bounded from below by the surfaces Bc and Bc', which are log spirals with their poles located at point a and a', respectively. These surfaces pass through the apex B of the wedge aBa' and terminate at points c and c' located at a horizontal distance from the pile axis equal to the radius of influence R (i.e., point c and c' lie on the cylindrical boundary surface of the zone of influence).

3) Zone III includes two trapezoid shaped zones of mixed shear, acde and a'c'd'e', bounded laterally by the pile shaft and the external boundaries de and d'e' of the zone of influence.

To be consistent with the fact that the assumed critical shear surfaces are not completely developed (i.e., punching shear failure), it is further assumed that:

i) The shearing resistance along Bc and Bc' is not fully mobilized. More specifically, the locally mobilized angle of shearing resistance ϕ_B varies along their lengths with its maximum value occurring at point B, equal to the angle of shearing resistance of sand and its minimum value equal to zero at point c and c'. At any arbitrary point j on the surfaces Bc and Bc', ϕ_B is assumed to be given by:

$$\phi_B = \left(1 - \frac{\theta_j}{\theta}\right)\phi \qquad \ldots (4.1)$$

in which θ_j and θ are shown in Fig. 4.2.

ii) The shearing resistance is fully mobilized along both sides aB and a'B of the central wedge aBa'.

iii) Along the terminal radial surfaces ac and a'c', the locally mobilized angle of shearing

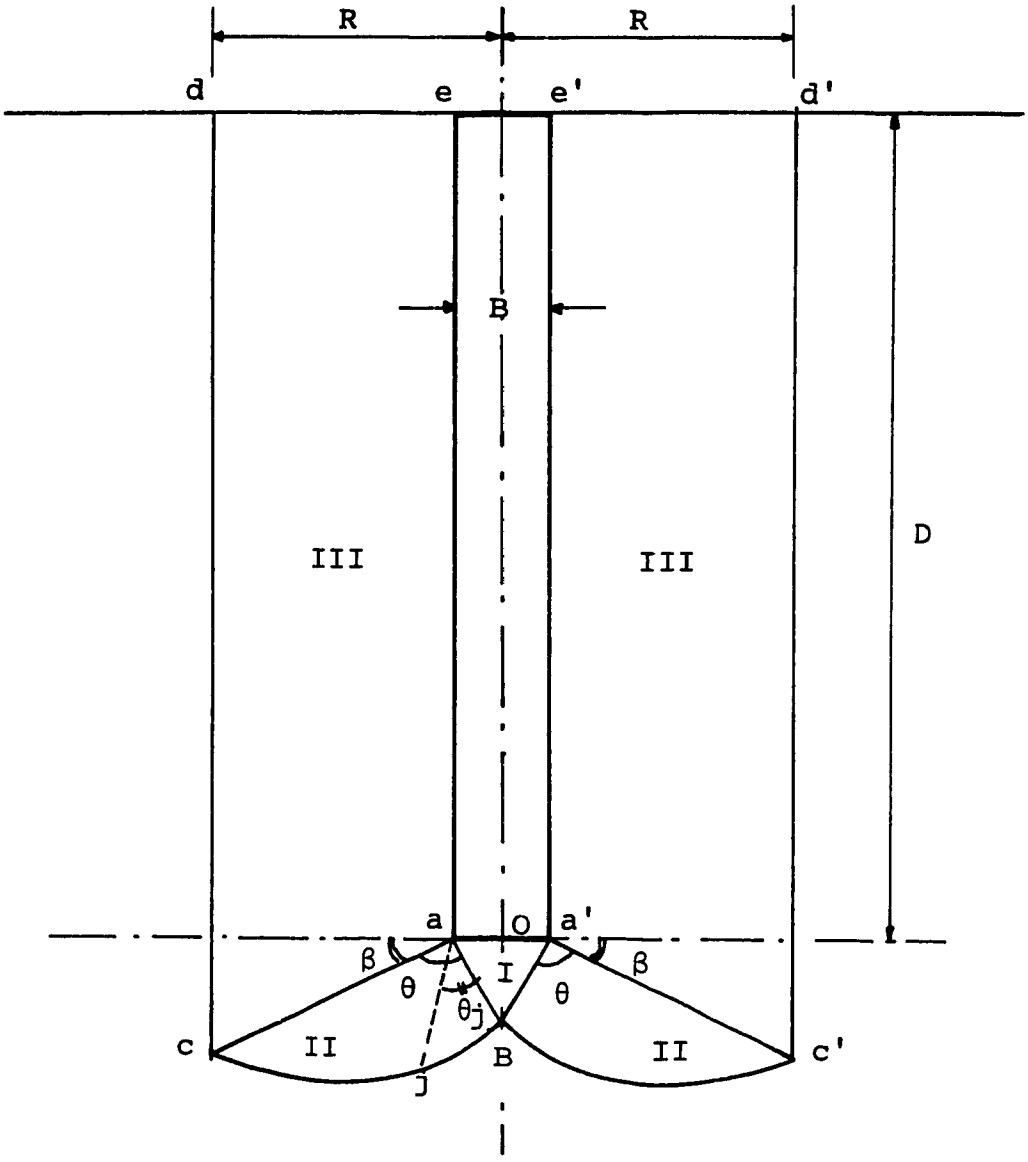

Fig. 4.2 Assumed Shear Failure Mechanism

resistance ϕ^*_β decreases linearly with the horizontal distance from the pile shaft, from a maximum value equal to ϕ at points a and a' to zero at point c and c'. In effect, the average mobilized angle of shearing resistance ϕ_β along ac and a'c' is equal to $\phi/2$.

iv) There is no shear on the boundary surfaces cd and c'd' of the zone of influence.

Once the failure mechanism is established, it is possible to proceed with a three dimensional analysis of the pile bearing capacity.

4.3 BASIC PRINCIPLES OF ANALYSIS

4.3.1 General

As the volume of sand involved in the failure mechanism of a single pile under axial load is axisymmetric, it suffices to consider only a sector of this volume generated by the left half of the longitudinal cross section aOBcde as it revolves through an angle $\Delta\zeta$ around the pile axis (Fig. 4.3). The three zones ObA, Bac, and acde becomes volumes $aBOa_1$, $aBcc_1a_1$, and $acdee_1d_1c_1a_1$ which will be referred to as volume I, II and III, respectively. Fig. 4.4 shows these volumes separately as free bodies subjected to assumed external forces.

For volume I, the external forces include the weight W_1 of the soil wedge aBOa', the resultant forces R_I and R'_I of earth pressure acting on the tangential plane aBO and a_1BO respectively, the normal force F_N and tangential force F_T acting on the surface aBa_1, and the force ΔQ_p, being the reaction force from the pile tip on the area aOa_1. Volume II, besides its weight W_2, is acted upon by three pairs of normal and tangential forces: (F_N, F_T), (N_1,T_1), and (N',T') on the three surfaces aBa_1, acc_1a_1, and cBc_1, respectively. In addition, the resultant forces R_{II} and R'_{II} acting on the tangential planes aBc and a_1Bc_1, complete the force system on volume II. The soil weight W_3, the resultant R_{III} and R'_{III} of earth pressure on the tangential plane acde and $a_1c_1d_1e_1$, the two pairs of normal and tangential forces $(\Delta E_2, \Delta Q_s)$

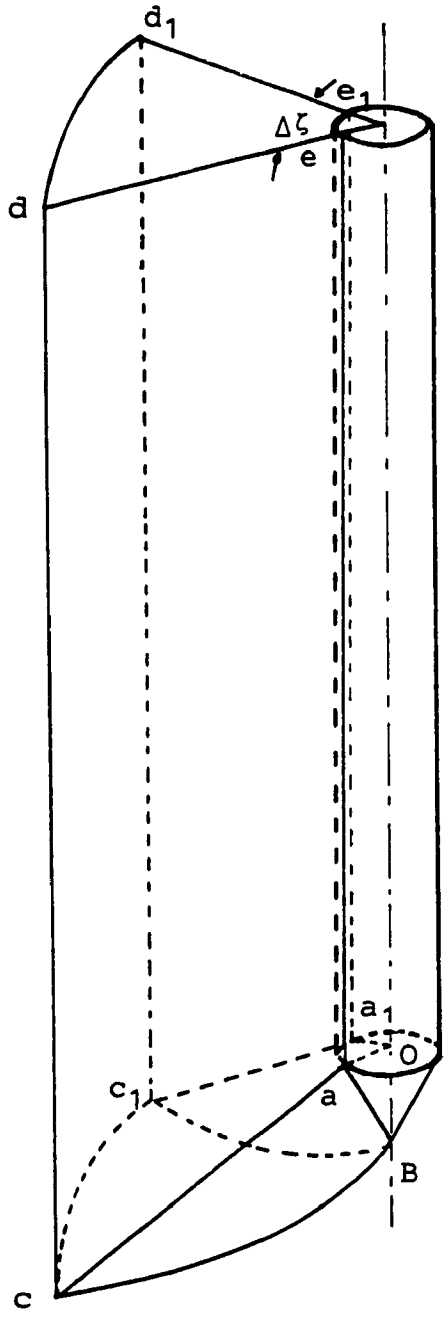

Fig. 4.3 A Volume Generated by a Plane Cross Section Revolving Through a Central Angle $\Delta\zeta$ Around Pile Axis

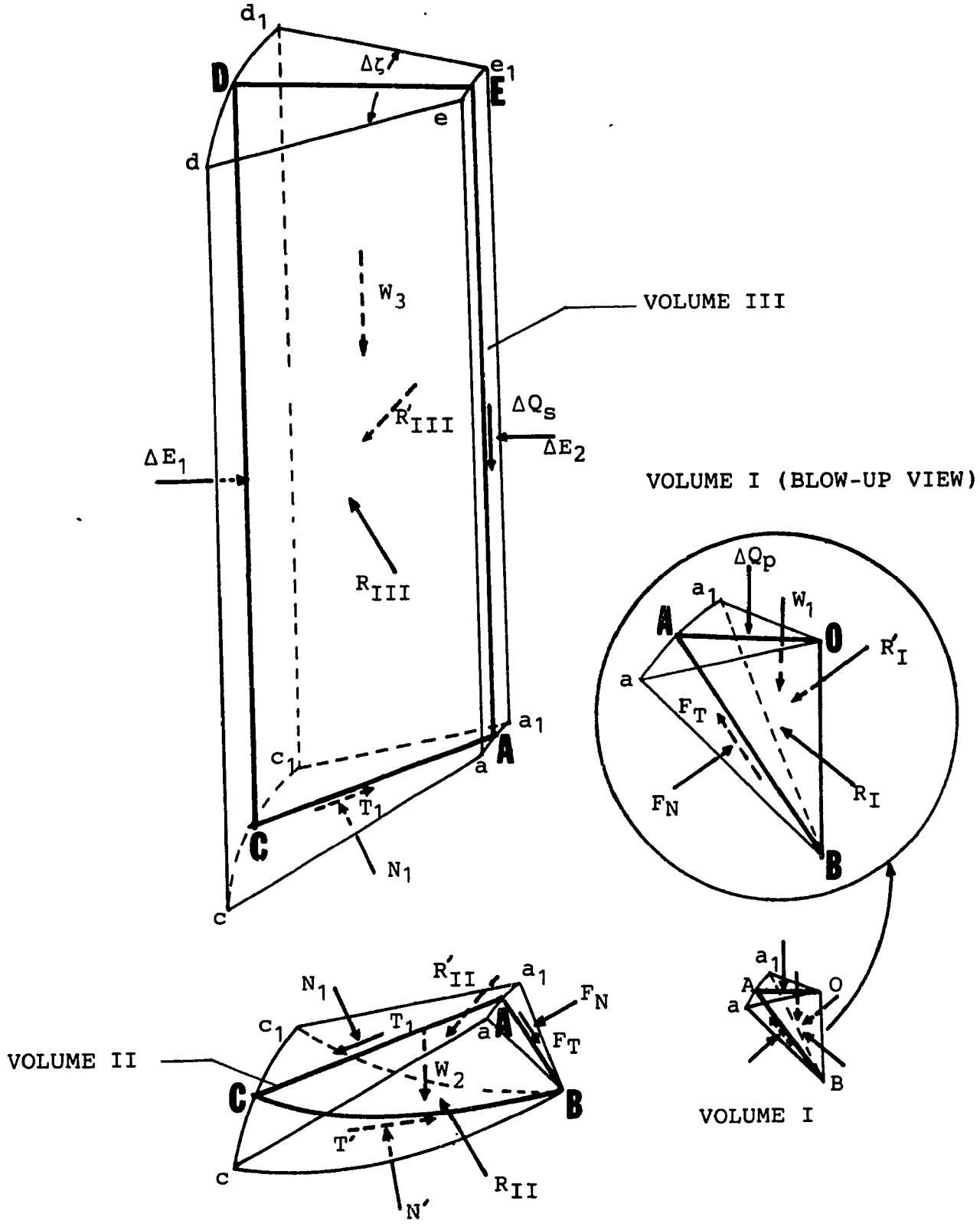

Fig. 4.4 External Forces Acting on Volume I, II, and III

and (N_1, T_1) on the surfaces $acee_1a_1$ and acc_1a_1, and the normal force ΔE_1 on surface cdd_1c_1 constitute the force system acting on volume III. No shear force is assumed to exist on the surface cdc_1d_1 as it is the lateral boundary of the zone of influence. Due to the axisymmetric condition, it is possible to transform the three dimensional analysis of the problem to a two dimensional one. For the three volumes I, II, and III, it can be seen in Fig. 4.5 that all external forces lie in the central plane of symmetry with the exception of those forces acting on the tangential planes, namely R_{III} and R'_{III} in volume III, R_{II} and R'_{II} in volume II, and R_I and R'_I in volume I. Furthermore, as all these forces are normal to the tangential planes, only their components parallel to the plane of symmetry play a role in the overall equilibrium of each volume (i.e., the components normal to the plane of symmetry cancelled each other out in pairs). Once the external forces acting on each volume are identified, a method is proposed to calculate the skin friction Q_s and the point resistance Q_p.

4.3.2 Calculation of Skin Friction Q_s

All assumed external forces acting on volume III are shown in Fig. 4.5. The coplanar force system lies in the plane of symmetry and consists of:

i) The weight W_3 of the soil volume III. This volume is calculated as the product of the area of the trapezoid ACDE and the distance travelled by its centroid around the pile axis over a central angle of rotation equal to $\Delta\zeta$ (i.e., Pappus-Guldinus' theorem).

ii) The force N_1, being normal to AC, and the tangential force T_1 representing the mobilized shear force along the internal surface AC, are related by the expression:

$$T_1 = N_1 \tan \phi_\beta$$

where ϕ_β = the average mobilized angle of shear resistance along AC.

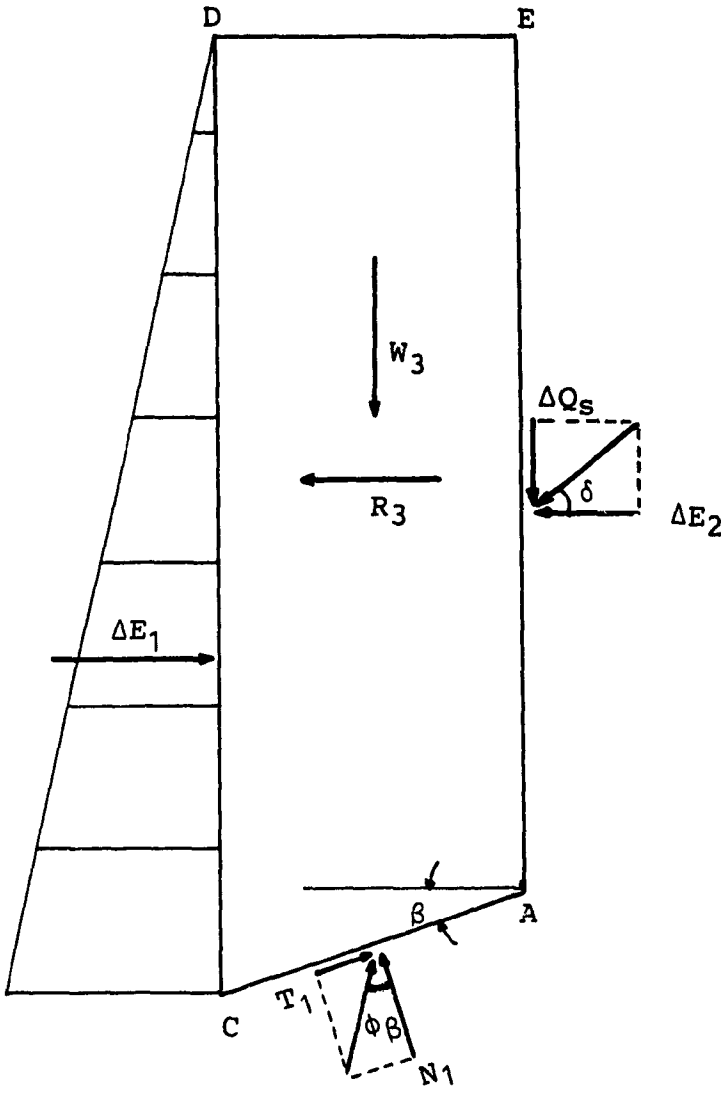

Fig. 4.5 A Free Body Diagram of Zone III

iii) The resultant ΔE_1 of the earth pressure acting on CD (Fig. 4.6) is given by:

$$\Delta E_1 = \frac{1}{2}(K_o \gamma D_1^2) \cdot R \cdot \Delta\zeta \qquad \text{... (4.2)}$$

where

K_o = coefficient of earth pressure at-rest before pile installation

γ = unit weight of sand

D_1 = length of segment CD

R = radius of influence

$\Delta\zeta$ = central angle of rotation (in radian).

iv) The resultant R_3 of the forces R_{III} and R'_{III} can be expressed by:

$$R_3 = R_{IIIx} + R'_{IIIx}$$

$$R_3 = R_{III} \sin\left(\frac{\Delta\zeta}{2}\right) + R'_{III} \sin\left(\frac{\Delta\zeta}{2}\right)$$

$$R_3 = 2R_{III} \sin\left(\frac{\Delta\zeta}{2}\right) = 2R'_{III} \sin\left(\frac{\Delta\zeta}{2}\right) \qquad \text{... (4.3)}$$

in which $R_{IIIx} = R'_{IIIx}$ = components of the forces R_{III} and R'_{III} parallel to the plane of symmetry ACDE.

The nature of the distribution of earth pressure on the tangential planes acde and $a_1c_1d_1e_1$ (See Fig. 4.4) are not known because the stress field around the pile is drastically changed after pile installation. In the analysis, its effect is accounted for by replacing it with an equivalent linear distribution of earth pressure with depth and having a coefficient equal to K_T.

The forces R_{III} or R'_{III} (Fig. 4.4) may be calculated as if it was the hydrostatic force

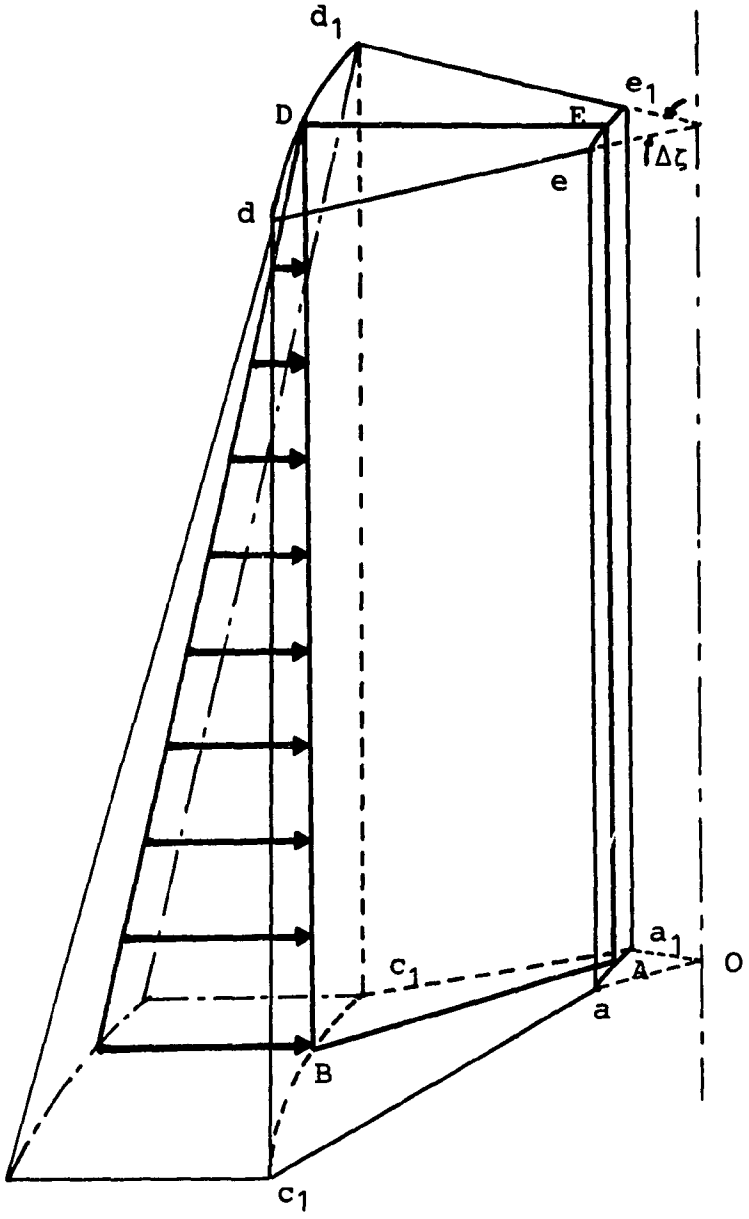

Fig. 4.6 Earth Pressure on Lateral Surface of Zone of Influence

acting on the trapezoid acde submerged in a fluid having its unit weight equivalent to $K_T\gamma$. From Fig. 4.7, it can be seen that:

$$R_{III} = R'_{III} = F_1 + F_2$$

where

F_1 = resultant force of earth pressure acting on rectangle ahde

F_2 = resultant force of earth pressure acting on triangle ahc

Similar to calculating the hydrostatic force acting on a submerged plane area which is computed as the product of the area and the hydrostatic pressure at its centroid, F_1 and F_2 are given by:

$$F_1 = \left(\frac{1}{2} K_T \gamma D\right)(L \cdot R') = \frac{1}{2} K_T \gamma R' D^2$$

$$F_2 = \left[\left(D + \frac{1}{3} R' \tan\beta\right) K_T \gamma\right]\left[\frac{1}{2}(R' \tan\beta)\ R'\right] = \frac{1}{2} K_T \gamma R'\left[R' \tan\beta \left(D + \frac{1}{3} R' \tan\beta\right)\right]$$

$$R_{III} = R'_{III} = \frac{1}{2} K_T \gamma R'\left[D^2 + DR' \tan\beta + \frac{1}{3}(R' \tan\beta)^2\right] \qquad \ldots (4.4)$$

where

$R' = R - \frac{B}{2}$

R = radius of influence

D = pile length

B = pile diameter

β = angle câh (with sign convention: $\beta > 0$ if ac is below the pile tip level).

Although an expression for ΔQ_s may be derived from force equilibrium considerations of the plane area ACDE, it is preferable to introduce here the application of a generalized method of slices, first developed by Sarma (1979), as this method will be used extensively in

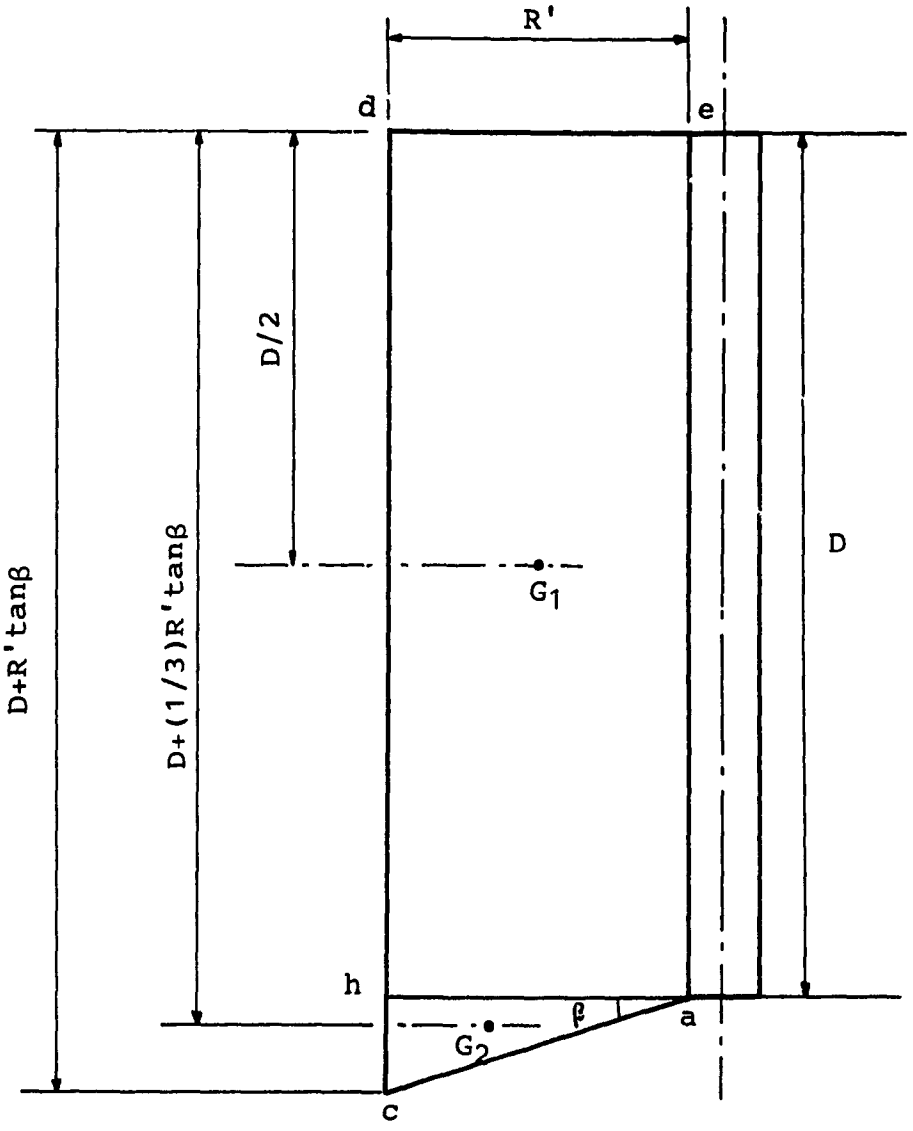

Fig. 4.7 A Diagram Used in Calculation of Total Earth Pressure on Tangential Plane of Volume III

calculating Q_p subsequently. According to Sarma's method of slices, the soil mass enclosed within an assumed plane slip surface is divided into a number of slices. The slices are not required to be vertical or the two sides of any slice to be parallel.

Sarma (1979) derived a recurrence relation between the normal forces E_i and E_{i+1} acting on the left and right sides, respectively, of an arbitrary slice i as follows:

$$E_{i+1} = \frac{\cos(\phi_{Bi} - \alpha_i + \phi_{Si} - \omega_i)\cos\phi_{Si+1}}{\cos(\phi_{Bi} - \alpha_i + \phi_{Si+1} - \omega_{i+1})\cos\phi_{Si}} E_i$$

$$+ \frac{(W_i + FV_i)(\cos\phi_{Si+1})\sin(\phi_{Bi} - \alpha_i)}{\cos(\phi_{Bi} - \alpha_i + \phi_{Si+1} - \omega_{i+1})}$$

$$+ \frac{FH_i(\cos\phi_{Si+1})\cos(\phi_{Bi} - \alpha_i)}{\cos(\phi_{Bi} - \alpha_i + \phi_{Si+1} - \omega_{i+1})} \quad \ldots (4.5)$$

where Fig. 4.8 illustrates the notations and sign conventions used.

E_i, E_{i+1} = normal forces acting on sides of slice i

α_i = basal slope of slice i

ω_i, ω_{i+1} = inclinations of sides of slice i

ϕ_{Bi} = mobilized angle of shearing resistance at mid point of the base of slice i

ϕ_{Si}, ϕ_{Si+1} = average mobilized angles of shearing resistance along sides of slice i

W_i = weight of slice i

F_i = resultant of external forces acting on slice i (other than E_i, E_{i+1}, W_i, N_i and T_i)

FH_i and FV_i = horizontal and vertical components of F_i.

Derivation of Eq. 4.5 is given in Appendix 1.

To calculate the shear force ΔQ_s along AD, Eq. (4.5) can be applied with the number of

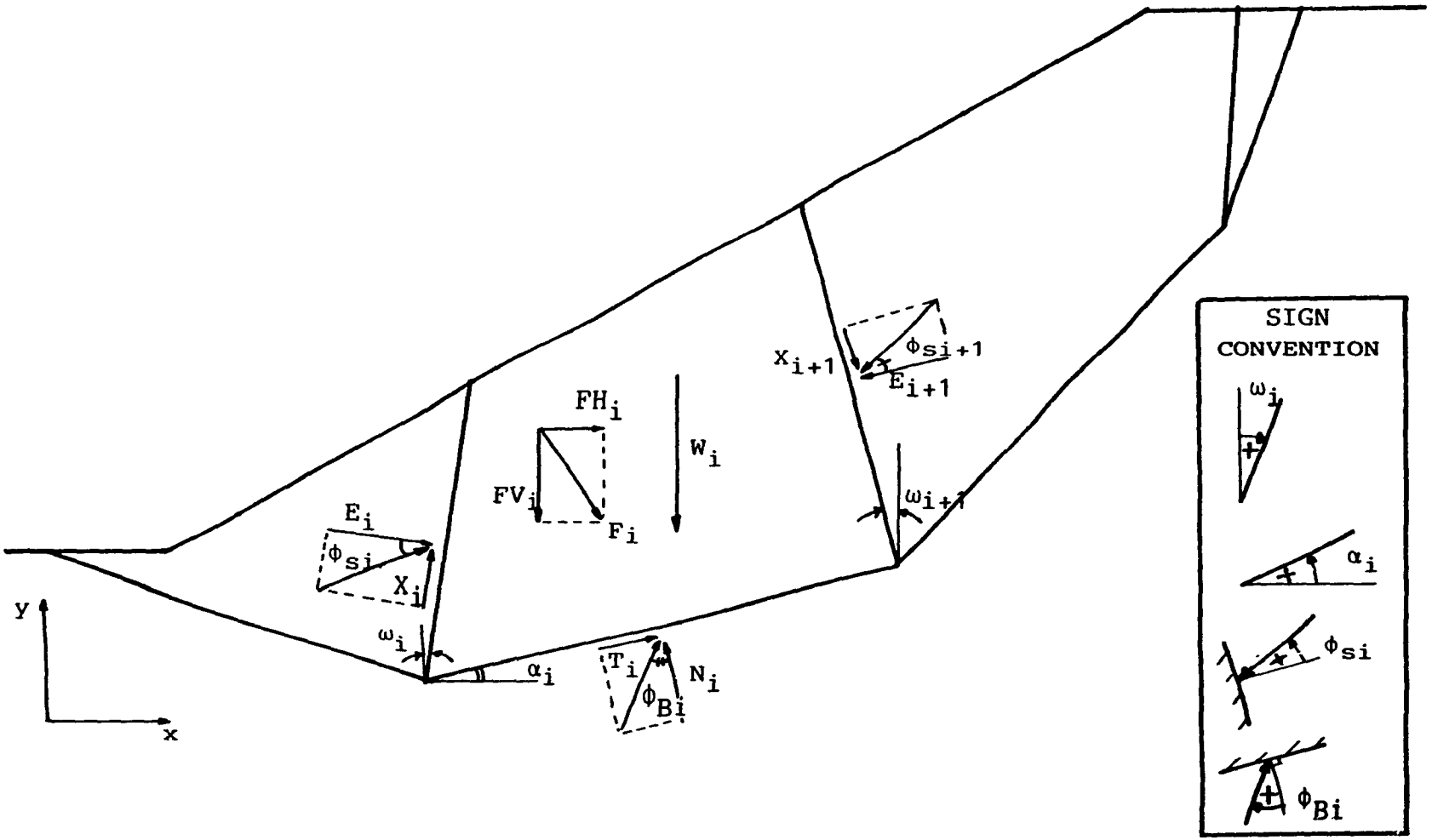

Fig. 4.8 Notations and Sign Conventions Used in Eq. 4.5

slices equal to one and both sides of this slice are vertical ($\omega_i = \omega_{i+1} = 0$). Using the specific symbols previously used for zone ACDE (Fig. 4.5), ΔE_2 is given by:

$$\Delta E_2 = \frac{\Delta E_1 \cos\delta \cos(\phi_\beta - \beta) + W_3 \cos\delta \sin(\phi_\beta - \beta) - R_3 \cos\delta \cos(\phi_\beta - \beta)}{\cos(\phi_\beta - \beta + \delta)} \quad \text{... (4.6)}$$

The shear force ΔQ_s is then given by:

$$\Delta Q_s = \Delta E_2 \tan\delta$$

As ΔQ_s is calculated for a central angle of rotation equal to $\Delta\zeta$, the total skin friction Q_s is computed as:

$$Q_s = \Delta Q_s \left(\frac{2\pi}{\Delta\zeta}\right) = \Delta E_2 \tan\delta \left(\frac{2\pi}{\Delta\zeta}\right) \quad \text{... (4.7)}$$

From the force equilibrium of the zone ACDE (Fig. 4.5), N_1 and T_1 may be calculated as:

$$N_1 = \frac{R_3 + \Delta E_2 - \Delta E_1}{\tan\phi_\beta \cos\beta - \sin\beta} \quad \text{... (4.8-a)}$$

$$T_1 = N_1 \tan\phi_\beta \quad \text{... (4.8-b)}$$

4.3.3 Calculation of Point Resistance Q_p

a. General

To calculate Q_p it is essential to solve first for the normal and tangential forces F_N and F_T, which lie in the plane of symmetry ABC and act on the surface aBa_1 of volume II (Fig. 4.4). Then from equilibrium consideration of forces acting on the volume aa_1OB (i.e., Volume I), the force ΔQ_p is calculated, in which ΔQ_p is the reaction force acting on the area aOa_1 (Fig. 4.4). Finally, the end bearing capacity Q_p is computed by integrating ΔQ_p over a central angle

of rotation of 2π around the pile axis.

b. Calculation of F_N and F_T

The calculation of F_N and F_T starts with the analysis of external forces acting on the volume $aBca_1Bc_1$ (i.e., volume II). As discussed previously in Section 4.3.1, the resultants of all these forces lie on the plane of symmetry ABC (Fig. 4.4).

b.1 Equation of the log spiral BC

The log spiral BC has its pole located at point A, passes through point B, and terminates at point C at a horizontal distance R from the pile axis, where R is the radius of influence. The general equation of a log spiral is given by:

$$r = r_o e^{b\theta} \qquad \text{... (4.9-a)}$$

in which r is the distance from the pole to an arbitrary point on the spiral, r_o is the distance from the pole to a selected reference point also located on the spiral, θ is the angle between these two lines, and b is a constant. Once r_o and b is known, the log spiral can be constructed. For the log spiral BC, its equation may be written as

$$r = (AB)\, e^{b\theta}$$

where AB is chosen as the reference radius r_o. As point C lies on the log spiral BC, AC is given by

$$AC = (AB)\, e^{b\theta} \qquad \text{... (4.9-b)}$$

with θ = Angle $B\hat{A}C$

Then,

$$b = \frac{1}{\theta} \ln\left(\frac{AC}{AB}\right)$$

From the geometry shown in Fig. (4.9):

$$\theta = B\hat{A}C = (\pi - \psi - \beta) \qquad AB = \frac{B}{2\cos\psi} \qquad AC = \frac{R - \frac{B}{2}}{\cos\beta} = \frac{2R-B}{2\cos\beta}$$

where β is the slope of AC. The angle β is considered positive if AC lies below the pile tip level and $\psi = (\pi/4 + \phi/2)$ as assumed previously.

Substitute values of θ, AB and AC into Eq. (4.9-b),

$$b = \frac{1}{(\pi - \psi - \beta)} \ln\left[\frac{2R-B}{B}\left(\frac{\cos\psi}{\cos\beta}\right)\right] \qquad \text{... (4.10)}$$

Hence, the equation of the log spiral BC may be expressed by:

$$r = \left(\frac{D}{2\cos\psi}\right) e^{b\theta} \qquad \text{... (4.11)}$$

in which $\psi = \left(\frac{\pi}{4} + \frac{\phi}{2}\right)$ and b is given by Eq. (4.10).

As it can be seen here that for a given pile diameter B and radius of influence R, b is a function of ϕ and β. If β varies with depth then it is evident that the shape of the log spiral BC will also change as the pile is advanced to a lower depth. This is another distinct assumption made in connection with the postulated failure mechanism. In conventional analysis of pile bearing capacity, the failure surface is usually assumed to be a log spiral having the equation $r = r_o^{b\theta}$ with $b = \tan\phi$, resulting in the shape of the log spiral remaining unchanged with depth (i.e., Meyerhof, 1951; Hu, 1965; Vesic, 1967).

b.2 Application of method of slices for radial shear zone ABC

Once the radial shear zone ABC is clearly defined, the analysis proceeds with the division

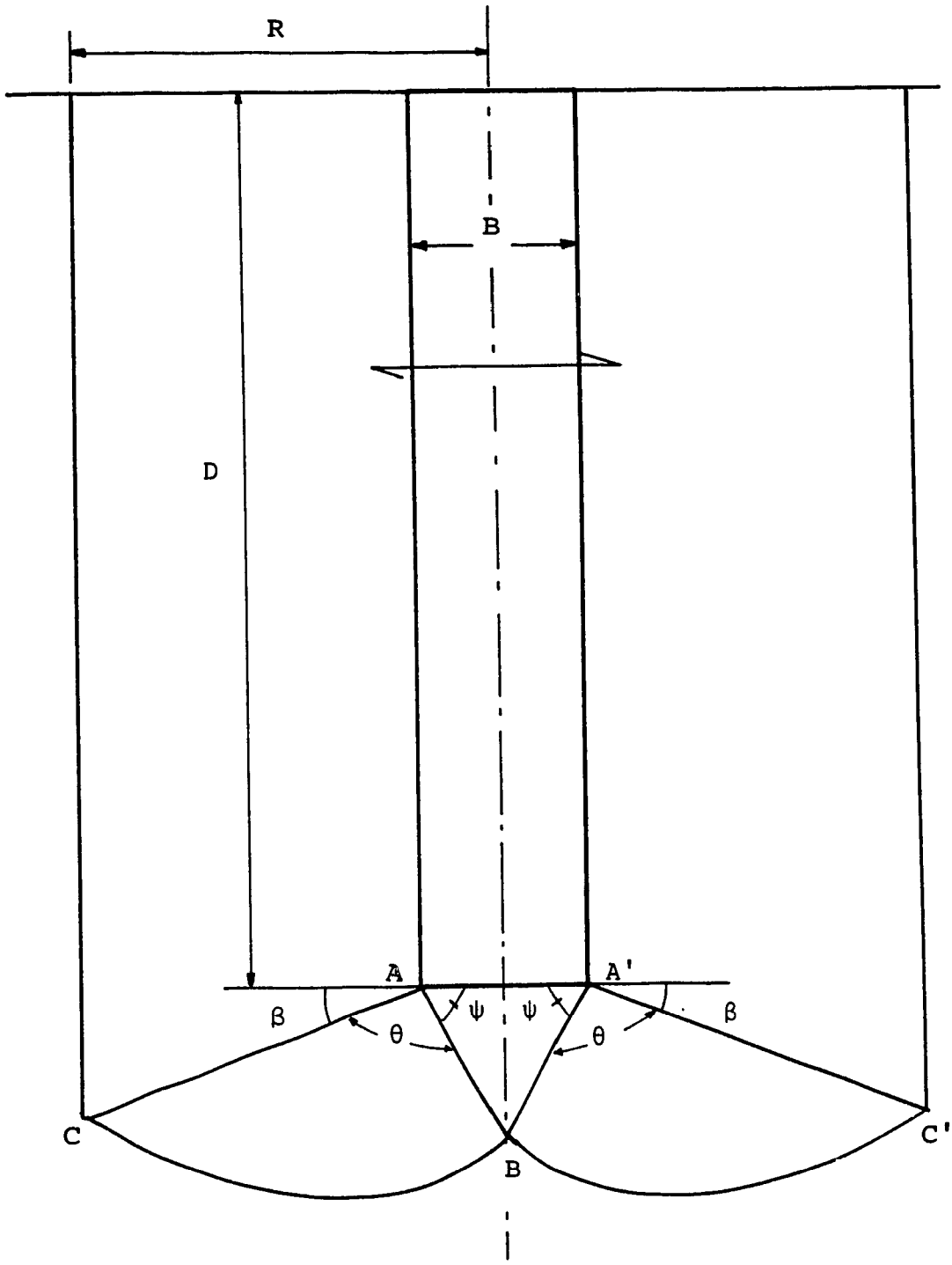

Fig. 4.9 Geometry of a Log Spiral

of this zone into n slices, all sharing the same apex A. Each slice has inclined sides, an apex angle equal to (θ/n) and is subjected to a system of external forces such as shown in Fig. 4.10. These forces consist of:

i) The weight w_i of the slice. Its volume v_i may be calculated as the volume generated by the plane area a_i of the slice revolving around the pile axis. By using the theorem of Pappus-Guldinus, v_i is given by:

$$v_i = a_i \cdot \rho_i \cdot \Delta\zeta$$

where

ρ_i = distance from the pile axis to the centroid of the generating area a_i

$\Delta\zeta$ = central of angle of rotation around the pile axis.

With the volume v_i known, the weight w_i can be easily calculated by: $w_i = \gamma v_i$.

ii) The normal and tangential components of the side forces include N_i, T_i, N_{i+1}, and T_{i+1}, which are related by the expressions:

$$T_i = N_i \tan \phi_{Si}$$

$$T_{i+1} = N_{i+1} \tan \phi_{Si+1}$$

In which ϕ_{Si} and ϕ_{Si+1} are respectively the average mobilized angles of shearing resistance along the left and right sides of the slice i.

It is also assumed that the average mobilized angle of shearing resistance along the side of an arbitrary slice varies linearly with the polar angle measured from AB, between two limiting values: ϕ_β along AC and ϕ along AB (Fig. 4.10). Mathematically, ϕ_{Si} and ϕ_{Si+1}, with $i > 1$, may be expressed by:

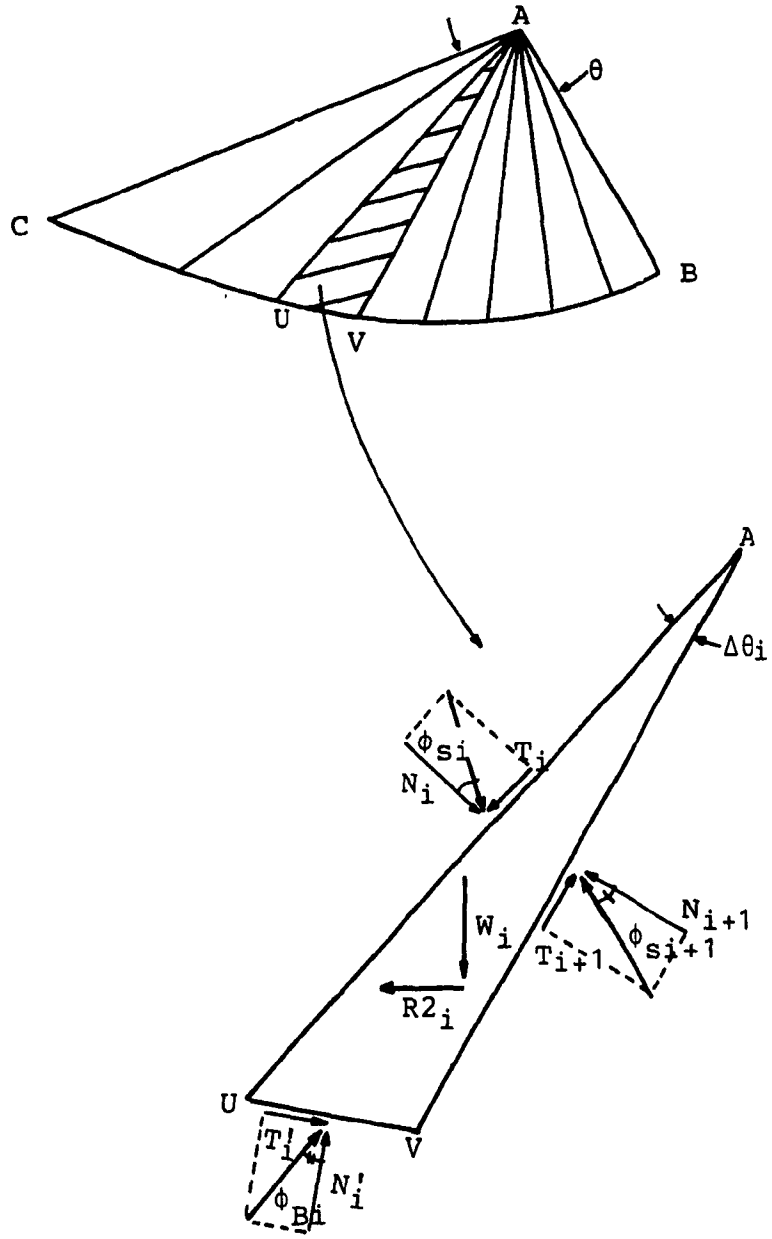

Fig. 4.10 A Free Body Diagram of an Inclined Slice in the Radial Shear Zone

$$\phi_{Si} = \phi_\beta + (\phi - \phi_\beta)\left[\frac{\sum_{k=1}^{i-1} \Delta\theta_k}{\theta}\right] \qquad \text{... (4.12)}$$

$$\phi_{Si+1} = \phi_\beta + (\phi - \phi_\beta)\left[\frac{\sum_{k=1}^{i} \Delta\theta_k}{\theta}\right] \qquad \text{... (4.13)}$$

where

ϕ_β = average mobilized angle of shearing resistance along AC

$\Delta\theta_k$ = apex angle of a slice

θ = Apex angle of radial shear zone BAC

iii) The normal and tangential components N'_i and T'_i of the soil reaction on the slice base are related by:

$$T'_i = N'_i \tan\phi_{Bi}$$

In which ϕ_{Bi}, denoting the mobilized angle of shear resistance at the midpoint of the slice base, may be computed by Eq. 4.1.

iv) R_{IIi} and R'_{IIi} represent the resultant forces of the earth pressure exerting on the area auv and $a_1u_1v_1$ (Fig. 4.11a). The force R_{IIi}, for instance, is then equal to the volume of the truncated pressure prism acting on the area auv (Fig. 4.11b).

$$R_{IIi} = \frac{1}{3}(\text{Area auv})(p_a + p_u + p_v) \qquad \text{... (4.14)}$$

The lateral earth pressure p_a, p_u and p_v at points a, u and v on the tangential plane aBc are given by $K_T \gamma z_a$, $K_T \gamma z_u$, and $K_T \gamma z_v$, respectively; in which z_a, z_u, and z_v are depths of point a, u, and v. The resultant $R2_i$ of the forces R_{IIi} and R'_{IIi} is calculated by:

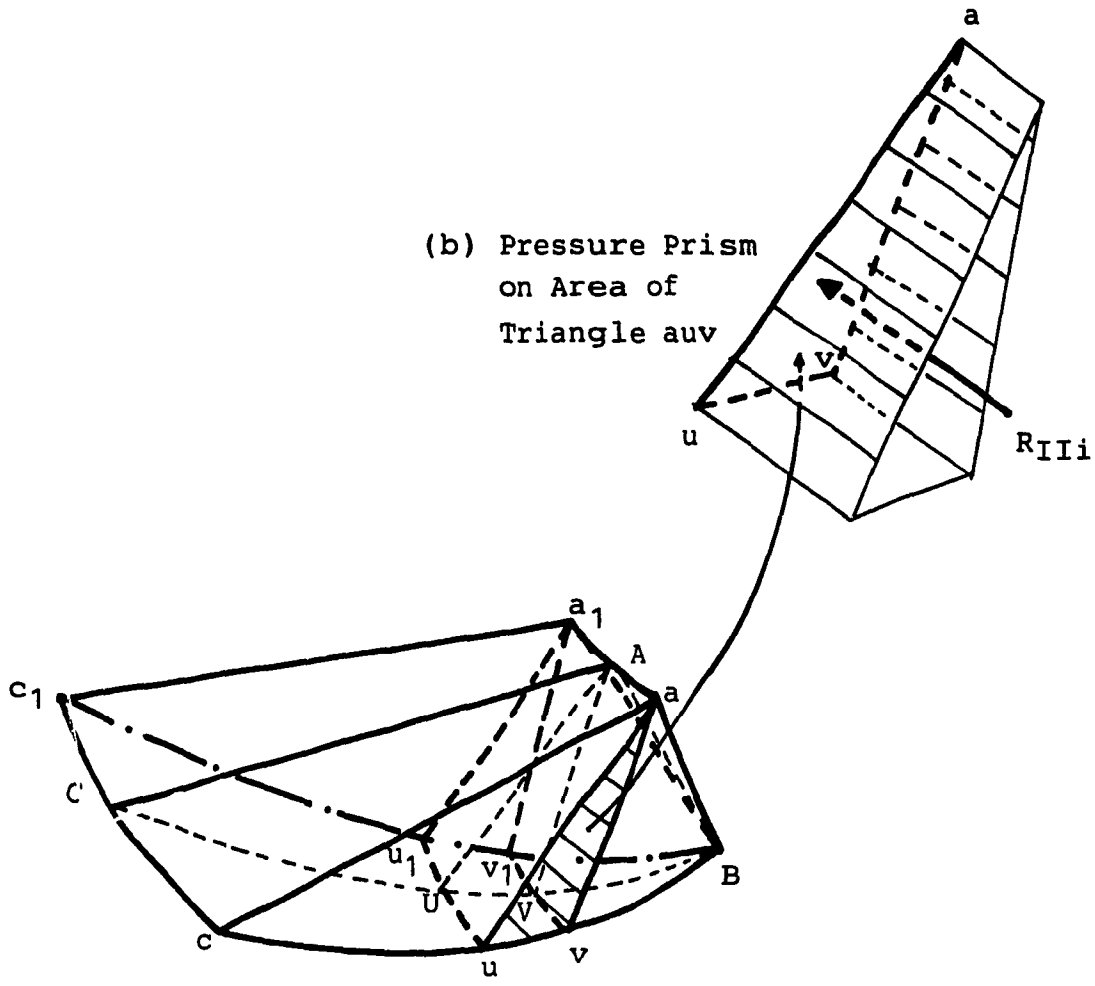

(a) A 3-Dimensional View of an Inclined Slice

Fig. 4.11 Earth Pressure on Tangential Planes of an Inclined Slice

$$R2_i = R_{IIx} + R'_{IIx}$$

$$R2_i = R_{II} \sin\left(\frac{\Delta\zeta}{2}\right) + R'_{II} \sin\left(\frac{\Delta\zeta}{2}\right)$$

$$R2_i = 2R_{II} \sin\left(\frac{\Delta\zeta}{2}\right) = 2R'_{II} \sin\left(\frac{\Delta\zeta}{2}\right) \qquad \text{... (4.15)}$$

in which $R_{IIx} = R'_{IIx}$ = components of the forces R_{II} and R'_{II}, parallel to the plane of symmetry ABC.

For any slice, ϕ_{Si}, ϕ_{Si+1}, and ϕ_{Bi}, $R2_i$ and w_i may be calculated following the procedure just described. If the normal force N_i is known on the left side of the slice, then its counterpart N_{i+1} on the right side may be calculated, using Sarma's recurrence relation (Eq. 4.5). As a result, with N_1, T_1 known from the analysis of volume III (see Fig. 4.4), it is possible to start with the first slice, calculate N_2 then repeat the same procedure to calculate N_3 for the second slice and so on, until the forces $F_N = N_{n+1}$ and $F_T = T_{n+1}$ are computed for the right side of the nth slice.

c. Calculation of point resistance Q_p

In deriving an expression for Q_p, use is made of volume I and its mirror image counterpart with respect to the pile axis (Fig. 4.12a). The triangular area ABA' is subjected to a system of forces shown in Fig. 4.12b. They include a pair of normal and tangential forces F_N and F_T acting along AB, another pair of forces, being the mirror images of F_N and F_T acting along A'B, the weight $2W_1$ of the wedge of sand and the reaction $2\Delta Q_p$ from the pile tip. Due to symmetry, there is no resultant force of the earth pressure acting on the tangential planes aOB, a'OB, a_1OB and a'_1OB. With reference to Fig. 4.12b, the equilibrium of forces in the vertical direction is given by:

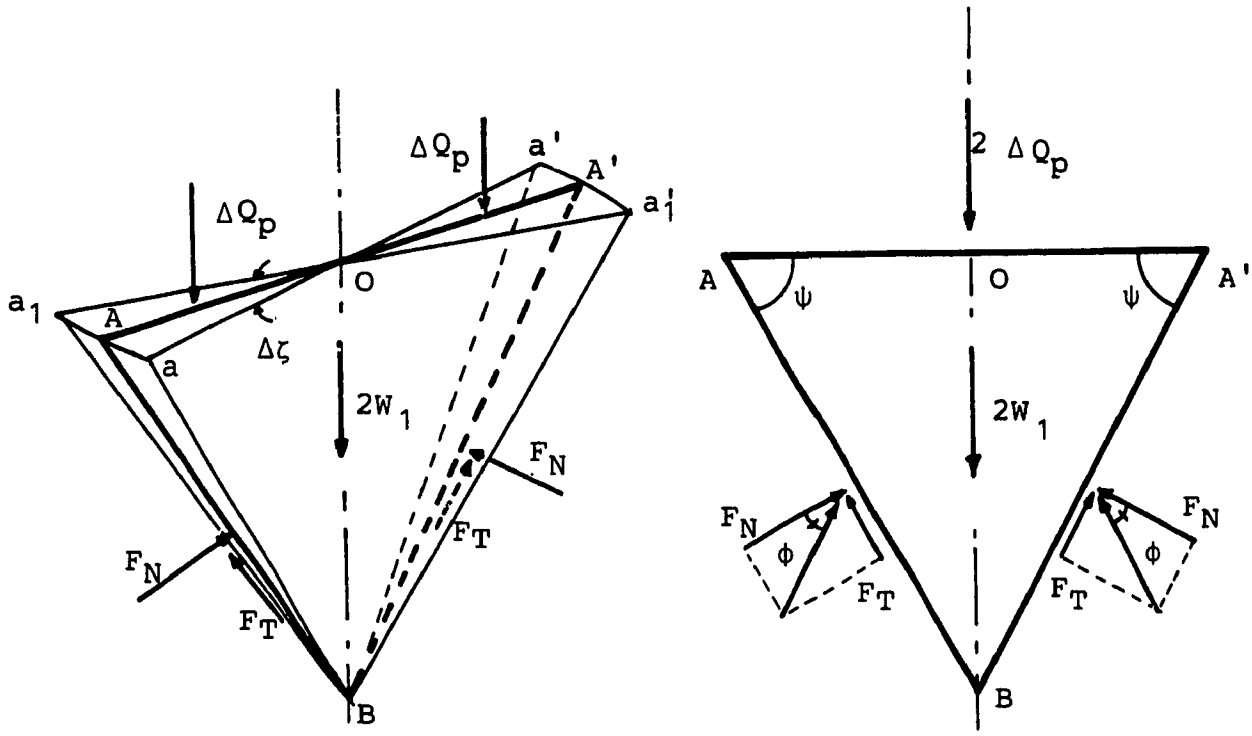

(a) Three Dimensional View Of Volume I and Its Mirror Image

(b) Plane View

Fig. 4.12 A Diagram of Forces Used to Compute Point Resistance Q_p

$$2(F_N \cos\psi + F_T \sin\psi) - 2W_1 - 2\Delta Q_p = 0$$

$$\Delta Q_p = F_N \cos\psi + F_T \sin\psi - W_1 \qquad \text{... (4.16)}$$

in which ΔQ_p = pile load acting on the area aOa_1 of the volume aOa_1B

W_1 = weight of the volume of sand aOa_1B (see Fig. 4.12a)

The point resistance Q_p is then given by:

$$Q_p = \frac{2\pi}{\Delta\zeta} \Delta Q_p \qquad \text{... (4.17)}$$

$$Q_p = \frac{2\pi}{\Delta\zeta} (F_N \cos\psi + F_T \sin\psi) - W_c \qquad \text{... (4.18)}$$

in which W_c = weight of the cone of sand beneath the pile tip.

4.3.4 An Illustrative Example of the Method of Analysis

The method of analysis described in the previous section is demonstrated by an example as shown in Fig. 4.13.

Calculation of skin friction Q_s

The analysis starts with zone III. The weight W_3 of the soil contained in volume III is calculated by:

$$W_3 = \text{Area (ACDE)} \cdot \rho_G \cdot \Delta\zeta \cdot \gamma$$

where

ρ_G = distance from pile axis to centroid of the trapezoid ABCD

$\Delta\zeta$ = central angle of rotation (assume $\Delta\zeta = 1° = \pi/180$ radians in this example).

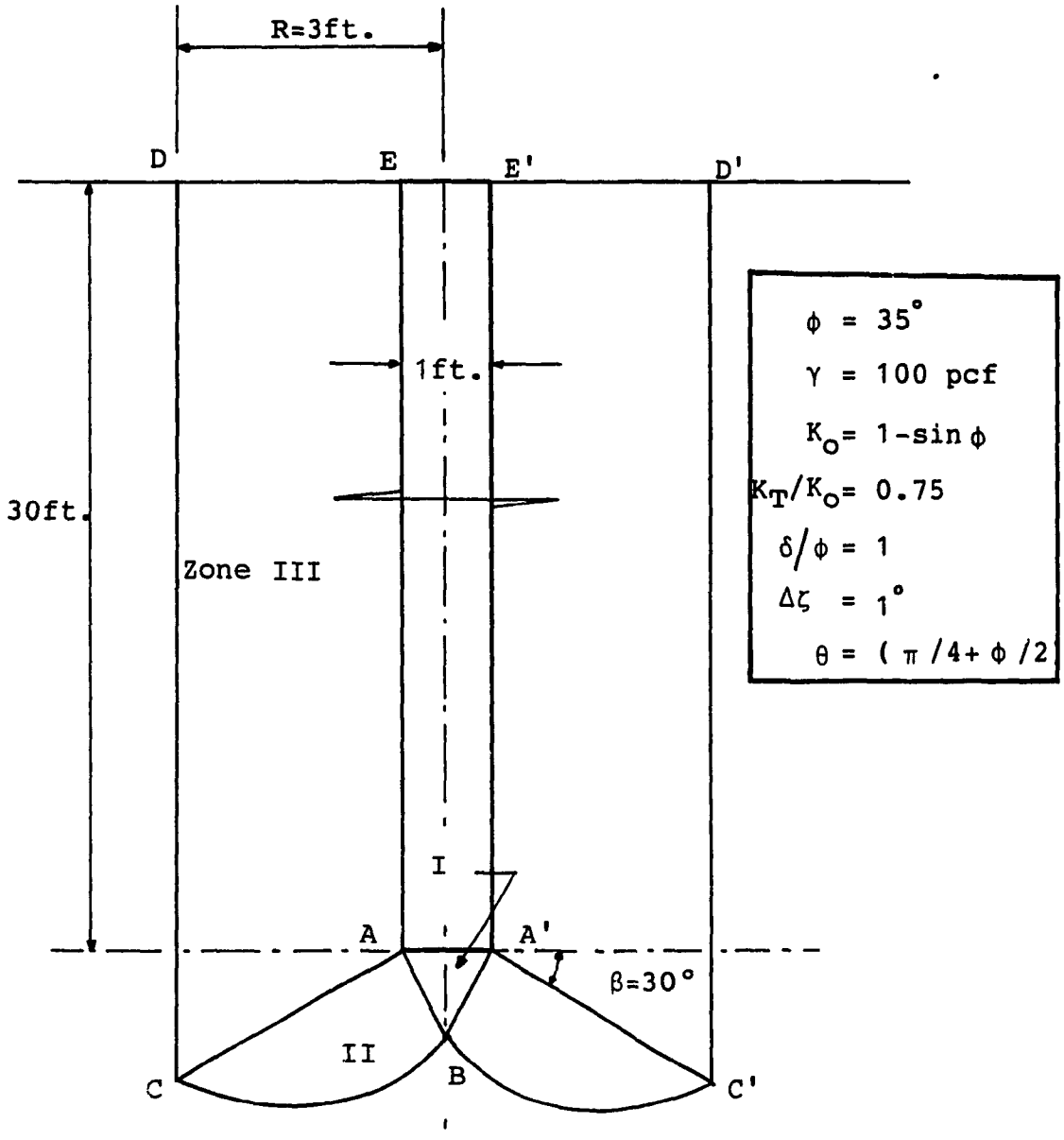

Fig. 4.13 A Numerical Example

From geometry:

AE = embedded pile length = 30 ft

$$DE = R - \frac{D}{2} = 3 - \frac{1}{2} = 2.5 \text{ ft}$$

$$CD = AE + DE \tan\beta = 30 + 2.5 \tan 30° = 31.44 \text{ ft.}$$

$$\rho_G = 1.76 \text{ ft.}$$

$$\text{Area (ACDE)} = \frac{1}{2}(AE + CD)(DE) = \frac{1}{2}(30 + 31.44)(2.5) = 76.80 \text{ ft}^2$$

$$W_3 = (76.80)(1.76)\left(\frac{\pi}{180}\right)(100) = 235.91 \text{ lbs.}$$

The resultant ΔE_1 of the earth pressure acting on the surface cc_1d_1d (Fig. 4.6) is given by Eq. (4.2).

$$\Delta E_1 = \frac{1}{2} K_o \cdot \gamma \cdot CD^2 \cdot R \cdot \Delta\zeta$$

$$\Delta E_1 = \frac{1}{2}(0.4264)(100)(31.44)^2(3)\frac{\pi}{180} = 1103.68 \text{ lbs.}$$

The normal force R_{III} and R'_{III} acting on the tangential plane acde and $a_1c_1d_1e_1$ (Fig. 4.7) can be computed by Eq. (4.4).

$$R_{III} = R'_{III} = \frac{1}{2} K_T \gamma R' \left[D^2 + (R' \tan\beta) D + \frac{1}{3}(R' \tan\beta)^2\right]$$

where

$R' = DE = 2.5$ ft

$D = AE = 30.$ ft

$K_T = (0.75)K_o = 0.75\,(0.4264) = 0.3198$

$\beta = +30°.$

$R_{III} = R'_{III} = \frac{1}{2}(0.3198)(100)(2.5)[30^{\circ} + (2.5 \tan 30°)(30) + (2.5 \cdot \tan 30°)]$

$R_{III} = R'_{III} = 37735.76$ lbs.

The resultant R_3 of R_{III} and R'_{III} is:

$$R_3 = 2R_{III} \sin\left(\frac{\Delta\zeta}{2}\right) = 2R'_{III} \sin\left(\frac{\Delta\zeta}{2}\right)$$

$$R_3 = (2)(37735.76) \sin\left(\frac{1°}{2}\right) = 658.61 \text{ lbs.}$$

The force ΔE_2 is calculated by Eq. (4.6):

$$\Delta E_2 = \frac{\Delta E_1 \cos\delta \cos(\phi_\beta - \beta) + W_3 \cos\delta \sin(\phi_\beta - \beta) - R_2 \cos\delta \cos(\phi_\beta - \beta)}{\cos(\phi_\beta - \beta + \delta)}$$

where

$\phi_\beta = \frac{35°}{2} = 17.5°$

$\delta = 35°$

$\beta = +30°$

$$E_2 = \frac{\cos(17.5° - 30°)\cos 35°}{\cos(17.5° - 30° + 35°)}(1103.68)$$

$$+ \frac{\cos 35° \sin(17.5° - 30°)}{\cos(17.5° - 30° + 35°)}(235.91)$$

$$- \frac{\cos 35° \cos(17.5° - 30°)}{\cos(17.5° - 30° + 35°)}(658.61)$$

$\Delta E2 \simeq 340.0$ lbs.

The normal and tangential components N_1 and T_1 of the force acting on the terminal radial surface AC may be calculated by Eqs. (4.8) and (4.9):

$$N_1 = \frac{R_3 + \Delta E_2 - \Delta E_1}{\tan \phi_B \cos \beta - \sin \beta} = \frac{658.61 + 340 - 1103.68}{\tan (17.5°) \cos 30° - \sin 30°} = 463.0 \text{ lbs.}$$

$$T_1 = N_1 \tan \phi_B = 463.0 \cdot \tan (17.5°) = 146.0 \text{ lbs.}$$

The skin friction Q_s is given by Eq. (4.7):

$$Q_s = \frac{2\pi}{\Delta\zeta} \cdot \Delta E_2 \tan \delta = \frac{360}{1} (340) \tan (35°) = 85705. \text{ lbs.}$$

Calculation of point resistance Q_p

For demonstration purposes, only four slices are used in the radial shear zone ABC (Fig. 4.14). These slices have the same apex angles equal to:

$$\Delta\theta = \frac{\theta}{4} = \frac{B\hat{A}C}{4} = \frac{87.5°}{4} = 21.875°$$

The equation of the log spiral BC is given by Eq. (4.11):

$$r = \frac{B}{2 \cos \psi} e^{b\theta}$$

where

B = pile diameter = 1.0 ft

$$\psi = \frac{\pi}{4} + \frac{\phi}{2} = 45° + \frac{35°}{2} = 62.5°$$

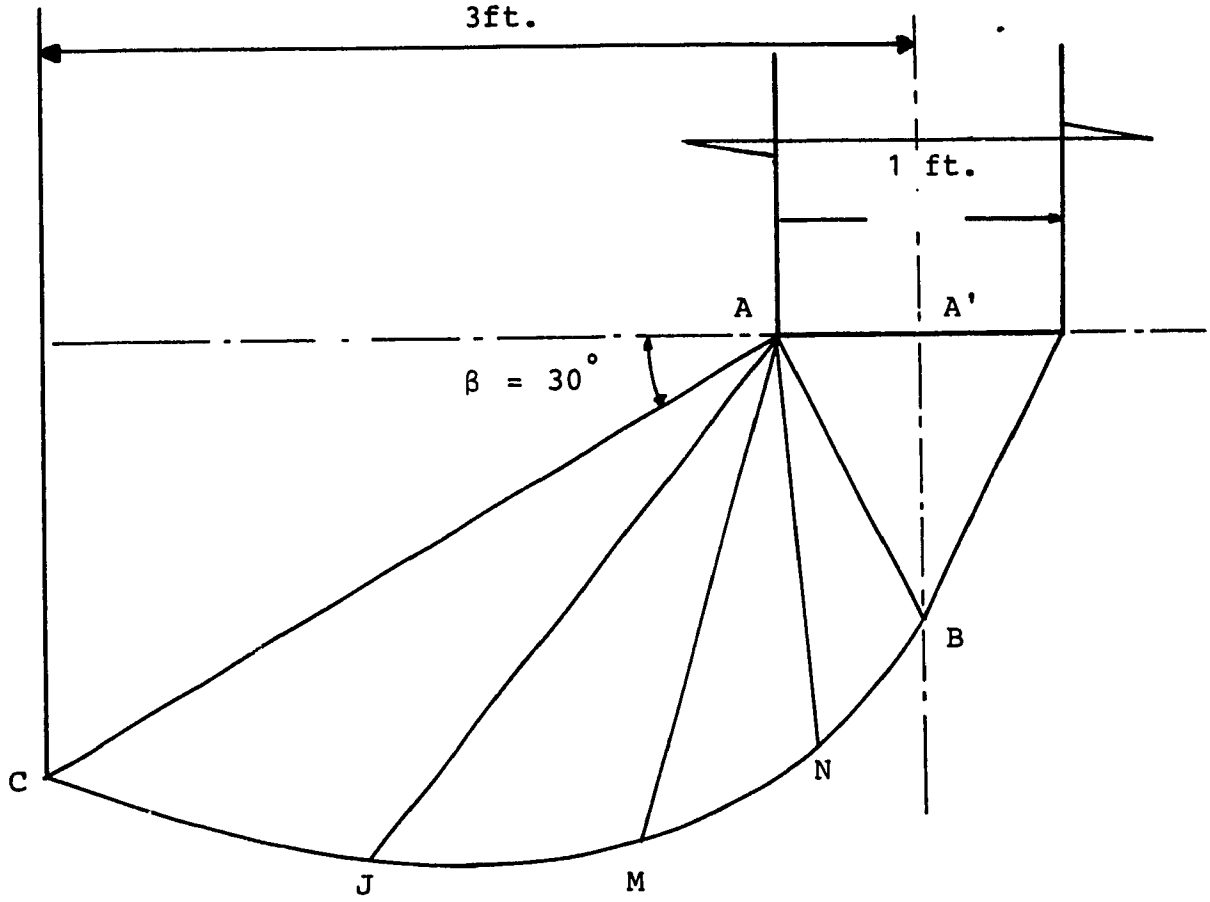

Fig. 4.14 A Division of a Radial Shear Zone into Four Inclined Slices

$$b = \frac{1}{(\pi - \psi - \beta)} \ln\left[\frac{2R-B}{B}\left(\frac{\cos\psi}{\cos\beta}\right)\right]$$

$(\pi - \psi - \beta) = 180° - 62.5° - 30° = 87.5° = 1.527$ Radians

$R = 3$ ft

$$b = \frac{1}{1.527} \ln\left[\frac{(2)(3)-1}{1} \cdot \left(\frac{\cos 62.5°}{\cos 30°}\right)\right] = 0.64214$$

Numerically, the equation of the log spiral BC is:

$$r = (1.0828) \cdot e^{(0.64214)\theta}$$

To calculate the normal component N_{i+1} of the side force on the right side of the i slice, the following parameters must be known: N_i, w_i, ω_i, w_{i+1}, α_i, ϕ_{Si}, $\phi_{S,i+1}$, ϕ_{Bi} and $R2_i$, i.e., Eq. (4.5)

Only a detailed sample computation for the first slice is shown herein because the same calculation procedure applies for all slices.

Area of slice No.1 (Fig. 4.14):

$$\text{Area (ACJ)} = \frac{1}{2}(AC)(AJ)\sin(\hat{SCJ})$$

$AC = 1.0828\,[e^{(0.64214)\theta}]$ where $\theta = B\hat{A}C = 87.5° = 1.527$ Radians

$$AC = 1.0828\ [e^{(0.64214)\cdot 1.527}] = 2.887 \text{ ft}$$

$$AJ = 1.0828\ [e^{(0.64214)\theta}] \text{ where } \theta = B\hat{A}J = 65.625° = 1.145 \text{ radians}$$

$$AJ = 1.0828\ [e^{(0.64214)\cdot 1.145}] = 2.259 \text{ ft}$$

$$\text{Area (ACJ)} = \frac{1}{2}\,(2.887)\,(2.2590 \sin (21.875°) = 1.215 \text{ ft}^2$$

The distance ρ_1 from the pile axis to the centroid of the area ACJ is equal to 1.797 ft. from geometry.

The weight of slice No. 1 is:

$$w_1 = \text{Area (ACJ)}\ \rho_1\ \Delta\zeta \cdot \gamma$$

$$w_1 = (1.215)\,(1.797)\,\frac{\pi}{180}\,(100) = 3.810 \text{ lbs.}$$

By geometry, the inclinations of AC and AC_1 with respect to the vertical are found to be:

$$\omega_1 = + 62.5°$$
$$\omega_2 = + 38.125$$

The slope of the base CJ with the horizontal is:

$$\alpha_i = - 16.81°$$

The average mobilized angles of shear resistance ϕ_{S1} along AC and ϕ_{S2} along AJ are calculated

using Eq. (4.12):

$$\phi_{S1} = -\phi_\beta = -\frac{35°}{2} = -17.5°$$

$$\phi_{S2} = \phi_\beta + (\phi - \phi_\beta) \cdot \frac{C\hat{A}J}{B\hat{A}C}$$

$$\phi_{S2} = -17.5° + [(35° - (-17.5°)] \cdot \frac{21.875}{87.5} = -4.375°$$

In calculating ϕ_{Si} for any i slice, the following sign convention should be carefully observed: ϕ_{Si} is positive if the side force is measured counter-clockwise from the normal.

The mobilized angle of shear resistance ϕ_{B1} along the base c_1 of slice No. 1 is:

$$\phi_{B1} = \left[1. - \frac{0.5 \cdot (B\hat{A}C + B\hat{A}J)}{B\hat{A}C}\right] \cdot \phi$$

$$\phi_{B1} = \left[1. - \frac{0.5 \cdot (87.5 + 65.625)}{87.5}\right] \cdot 35. = 4.375°$$

The resultant forces R_{III} and R'_{III} of the earth pressure acting on the tangential planes are calculated using Eq. (4.15).

$$R_{III} = R'_{III} = \frac{1}{3} \text{ Area (ACJ) } (z_A + z_C + z_J) K_T \gamma$$

where

z_A, z_C and z_J are depths of point A, C and J

$$R_{III} = R'_{III} = \frac{1}{3} (1.215) (30 + 31.44 + 31.78) (0.3198) 100 = 1207.38 \text{ lbs.}$$

The horizontal component $R2_1$ of R_{III} and R'_{III} combined, is given by Eq. (4.15).

$$R2_1 = 2\,R'_{111}\sin\left(\frac{\Delta\zeta}{2}\right) = 2\,(1207.38)\sin\left(\frac{1^\circ}{2}\right) = 21.07 \text{ lbs.}$$

The normal force N_2 acting of the right side of the slice No. 1 can be calculated using Eq. (4.5).

$$N_2 = \frac{\cos(\phi_{B1} - \alpha_1 + \phi_{S1} - \omega_1)\cos\phi_{S2}}{\cos(\phi_{B1} - \alpha_1 + \phi_{S2} - \omega_2)\cos\phi_{S1}} N_1$$

$$+ \frac{\cos\phi_{S2}\sin(\phi_{B1} - \alpha_1)}{\cos(\phi_{B1} - \alpha_1 + \phi_{S2} - \omega_2} W_1$$

$$- \frac{\cos\phi_{S2}\cos(\phi_{B1} - \alpha_1)}{\cos(\phi_{B1} - \alpha_1 + \phi_{S2} - \omega_2)} R2_1$$

$$N_2 = \frac{\cos[4.375^\circ - (-16.81^\circ) + (-17.5^\circ) - 60.^\circ]\cdot\cos(-4.375^\circ)}{\cos[4.375^\circ - (-16.81^\circ) + (-4.375^\circ - 38.125^\circ)]\cdot\cos(-17.5^\circ)} \cdot 463.$$

$$+ \frac{\cos(-4.375^\circ)\sin[4.375^\circ - (-16.81^\circ)]}{\cos[4.375^\circ - (-16.81^\circ) + (-4.375^\circ) - 38.125^\circ]} \cdot 3.183$$

$$- \frac{\cos(-4.375^\circ)\cos(21.185^\circ)}{\cos[4.375^\circ - (-16.81^\circ) + (-4.375^\circ) - 38.125^\circ]} \cdot 21.07$$

$$N_2 = 288.18 + 1.475 - 21.03 = 268.62 \text{ lbs.}$$

The same procedure is used to calculate N_3, N_4 and N_5 for slice No. 2, No. 3, and No. 4 respectively. Numerical values of relevant parameters used in the computation and the results obtained for each slice are tabulated in Table 4.1. From this table, it is seen that:

$F_N = N_5 = 235.05$ lbs.

$F_T = F_N \tan 35^\circ = 235.05 \tan 35^\circ = 164.58$ lbs.

Table 4.1: Significant Results From An Illustrative Example of The Method of Analysis.

i (Slice No.)	$W2_i$ (lbs.)	α_i (deg.)	ϕ_{Bi} (deg.)	ω_i (deg.)	ω_{i+1} (deg.)	ϕ_{Si} (deg.)	ϕ_{Si+1} (deg.)	N_i (lbs.)	N_{i+1} (lbs.)
1	3.810	-16.81	4.375	62.500	38.125	-17.50	-4.375	463.00	268.62
2	1.463	5.07	13.125	38.125	16.250	-4.375	8.750	268.62	207.11
3	0.491	26.93	21.885	16.250	-5.620	8.750	21.870	207.11	197.52
4	0.140	48.82	30.625	-5.620	-27.500	21.870	35.000	197.52	235.05

The point resistance Q_p is given by Eq. (4.18):

$$Q_p = \frac{2\pi}{\Delta\zeta}(F_N \cos\psi + F_T \sin\psi) - W_c$$

in which W_c is the weight of the cone of sand ABA'.

$$W_c = \left(\frac{1}{3}\right)\frac{\pi\ 1^2}{4}(1)\sin 62.5°\ (100) = 23.22 \text{ lbs.}$$

$$Q_p = \frac{360}{1}\ (235.05 \cos 62.5° + 164.58\ \sin 62.5°) - 23.22 = 91600.4 \text{ lbs.}$$

4.3.5 Computer program implementation

A computer program, entitled TEMPO, was written to facilitate the tedious computation procedure. In addition, a sensitivity study was also conducted because in the computer implementation of the proposed model, it became apparent that the number of slices used in the radial shear zone (i.e. zone II in Fig. 4.2), and the magnitude of the central angle of rotation $\Delta\zeta$ (see Fig.4.3) did affect the accuracy of the computed results. For this purpose, the example in Fig. 4.13 was again adopted to demonstrate typical findings. In the computation, the central angle of rotation $\Delta\zeta$ was kept constant at one degree while the percentage error was computed on the basis of the Q_u value corresponding to the case involving 50 slices. Figure 4.15 shows that the percentage error of the computed pile bearing capacity Q_u decreases sharply then levels off as the number of slices increases, leading to the conclusion that using more than 20 slices hardly improves the computation accuracy.

To illustrate the effect of the central angle of rotation $\Delta\zeta$, the same example was used in another series of computer runs with $\Delta\zeta$ ranging from 0.001 degree to 100 degrees, and the number of slices set equal to 20. It can be seen from Fig. 4.16 that the percentage error of Q_u, computed on the basis of the Q_u value corresponding to $\Delta\zeta = 0.001°$, starts to increase as $\Delta\zeta$ exceeds about 1°. From this sensitivity study, it is concluded that excellent accuracy may be

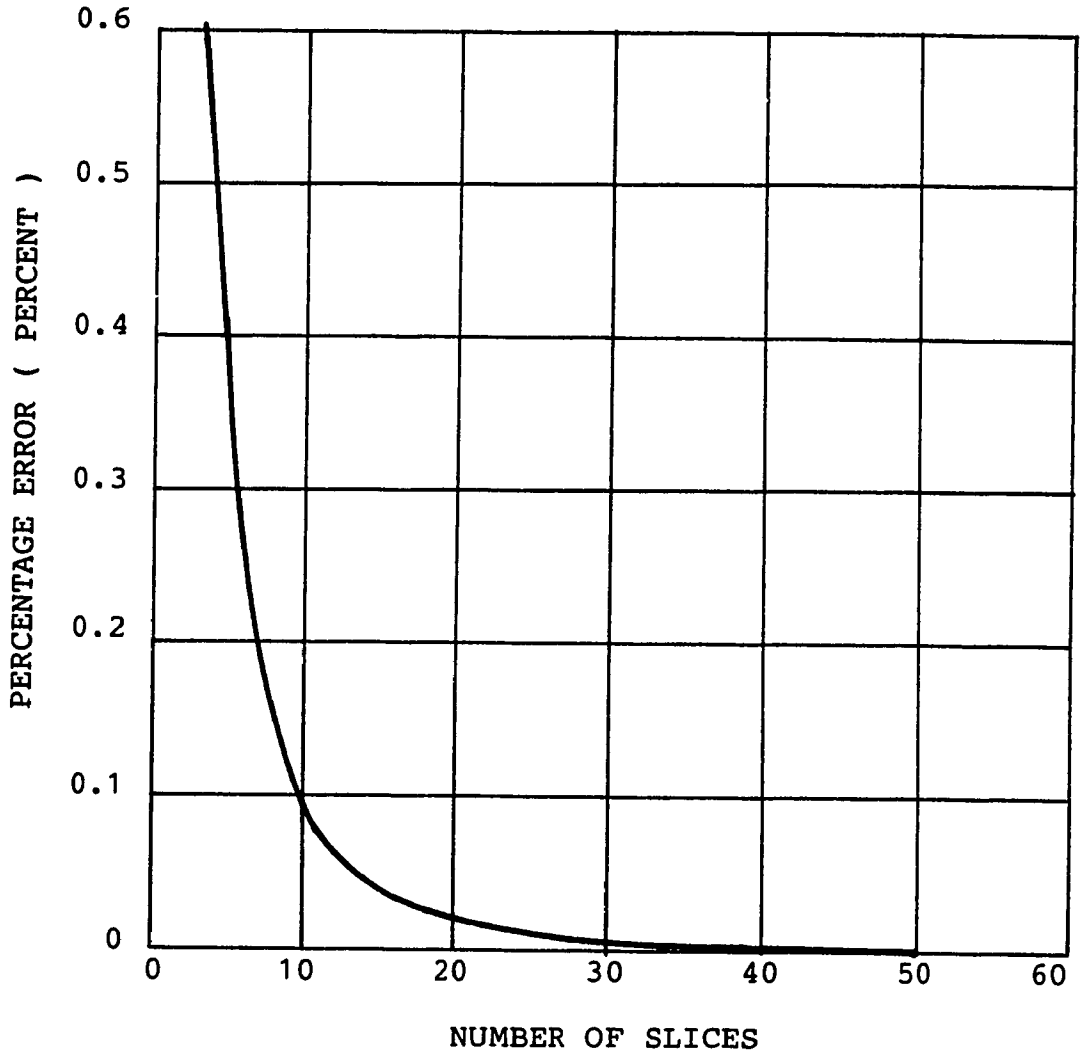

Fig. 4.15 Influence of Number of Slices on Computation Accuracy

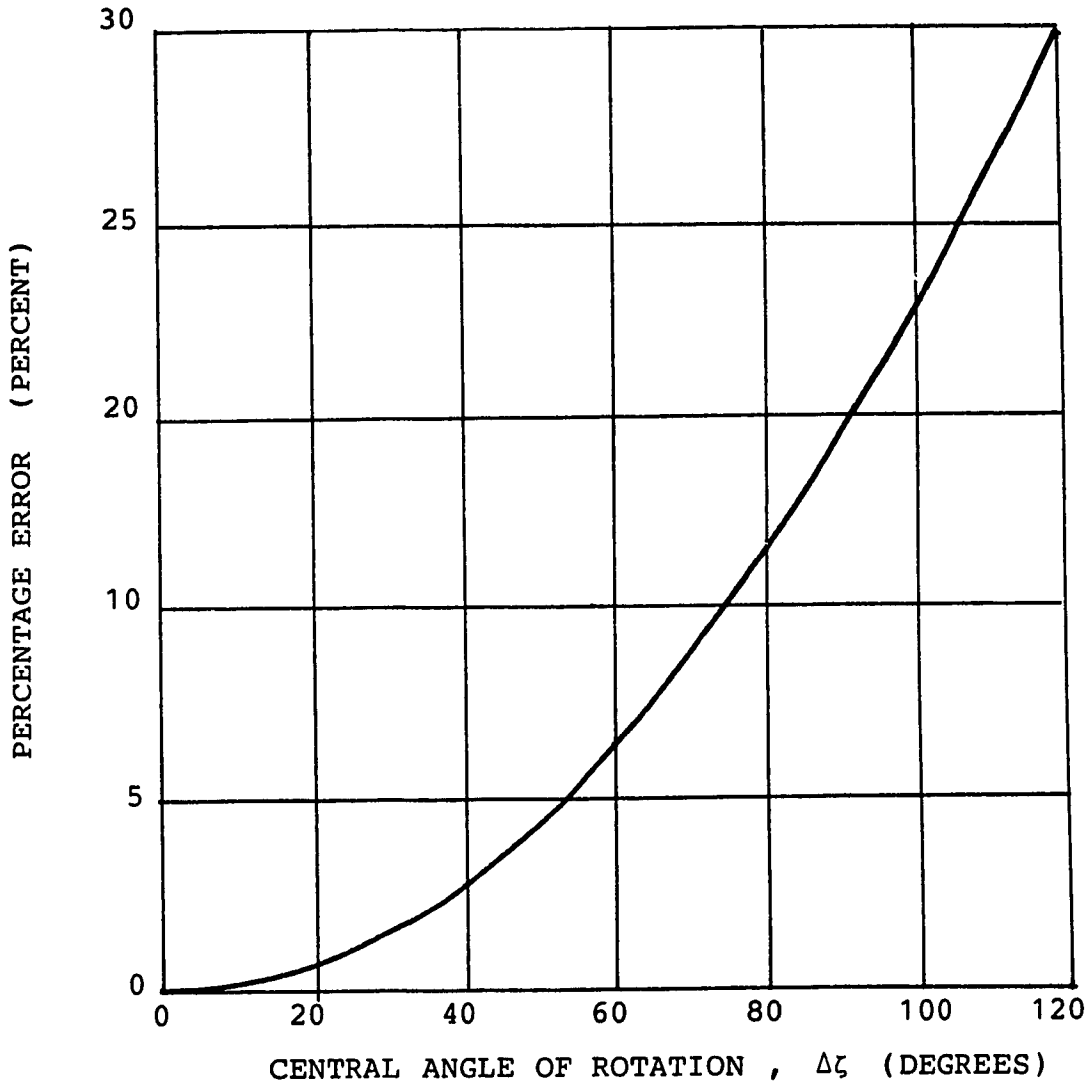

Fig. 4.16 Influence of Central Angle of Rotation on Computation Accuracy

expected from the computer program TEMPO, using 20 slices for the radial shear zone and selecting $\Delta\zeta = 1°$.

4.3.6 Direction of shear on the terminal radial surface

In the present model, the direction of shear along the terminal radial surface AC in the radial shear zone ABC is assumed to be from A to C (i.e., away from the pile tip, see Fig. 4.4). This assumption needs an explanation since it differs from its counterpart in previous bearing capacity theories. As discussed in the literature review in Chapter 2, almost all conventional pile bearing capacities adopt the general shear failure mode which includes the terminal radial surface as part of its failure boundary. On the other hand, the terminal radial surface in the present model is treated as an internal surface. Consequently, the direction of shear along this surface in the case of punching shear is not necessarily identical to that dictated by the kinematics of the radial shear zone ABC at failure in the general shear failure mode. The more crucial requirement, however, demands that the selected direction of shear must not result in inconsistencies when the force equilibrium of the mixed shear zone is considered (i.e., zone ACDE in Fig. 4.5).

The effect of the assumed direction of shear on the point resistance and skin friction of a single pile in sand may be demonstrated by using the computer program TEMPO to analyse a simple example involving a 12 in. diameter concrete pile driven into a homogeneous, dry sand deposit with $\phi = 35°$ and $\gamma = 100$ lbs/ft^3. Other pertinent assumed data include: R/B = 3; $K_T/K_A = 0.75$; $K_o = 1\text{-}\sin\phi$, and $\delta/\phi = 1$, in which R = radius of influence; K_T = coefficient of earth pressure on the tangential plane; K_A = coefficient of active earth pressure, K_o = coefficient of earth pressure at-rest; and δ = angle of friction between pile shaft and sand. In the first case, the direction of shear was selected from A to C in the radial shear zone ABC (i.e., case 1). In the second case, this direction was reversed (i.e., case 2). Results of the analysis of both cases were presented in Fig. 4.17 and Fig. 4.18 where the equivalent bearing

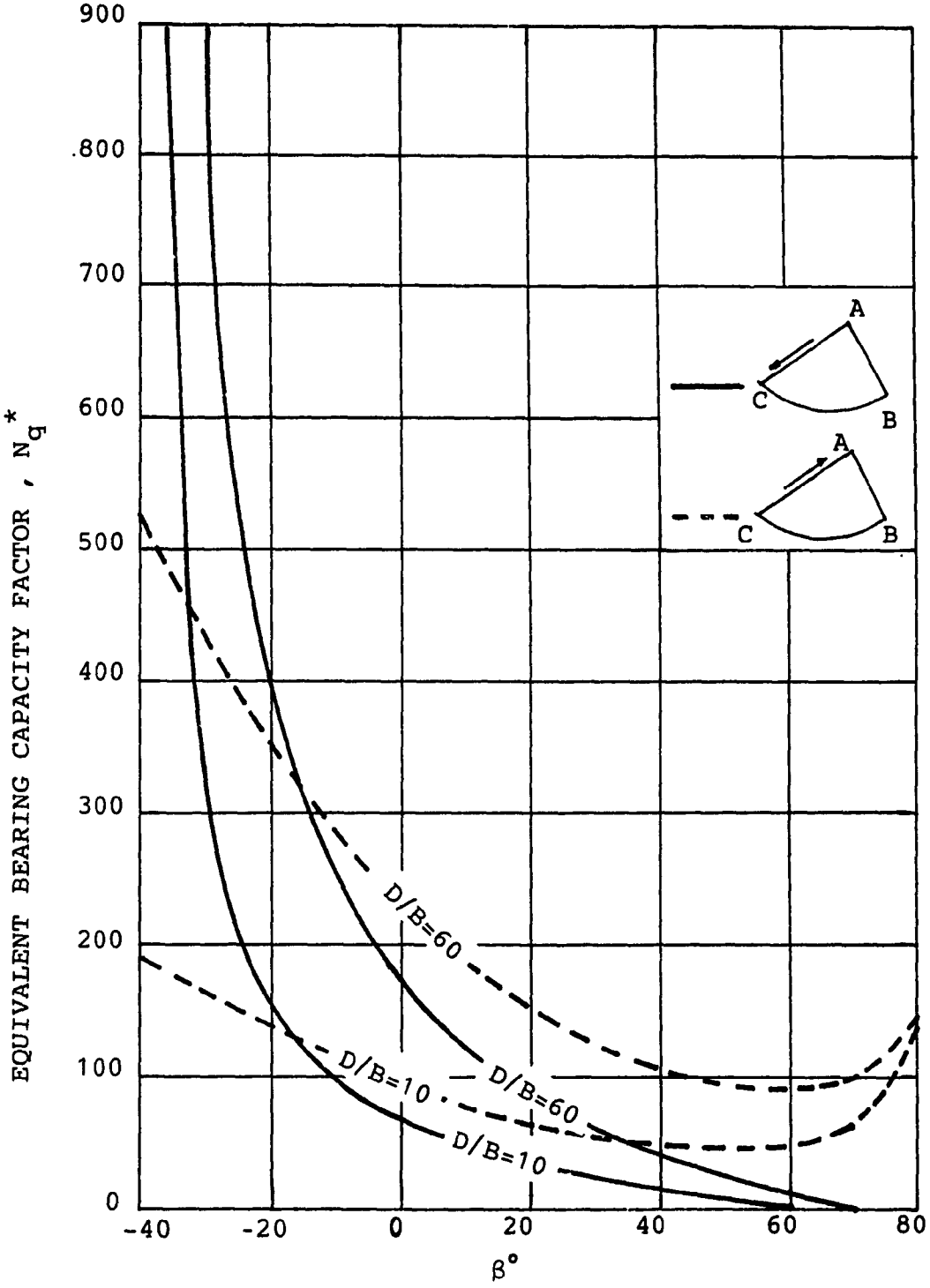

Fig. 4.17 Effect of Assumed Direction of Shear Force on Point Resistance

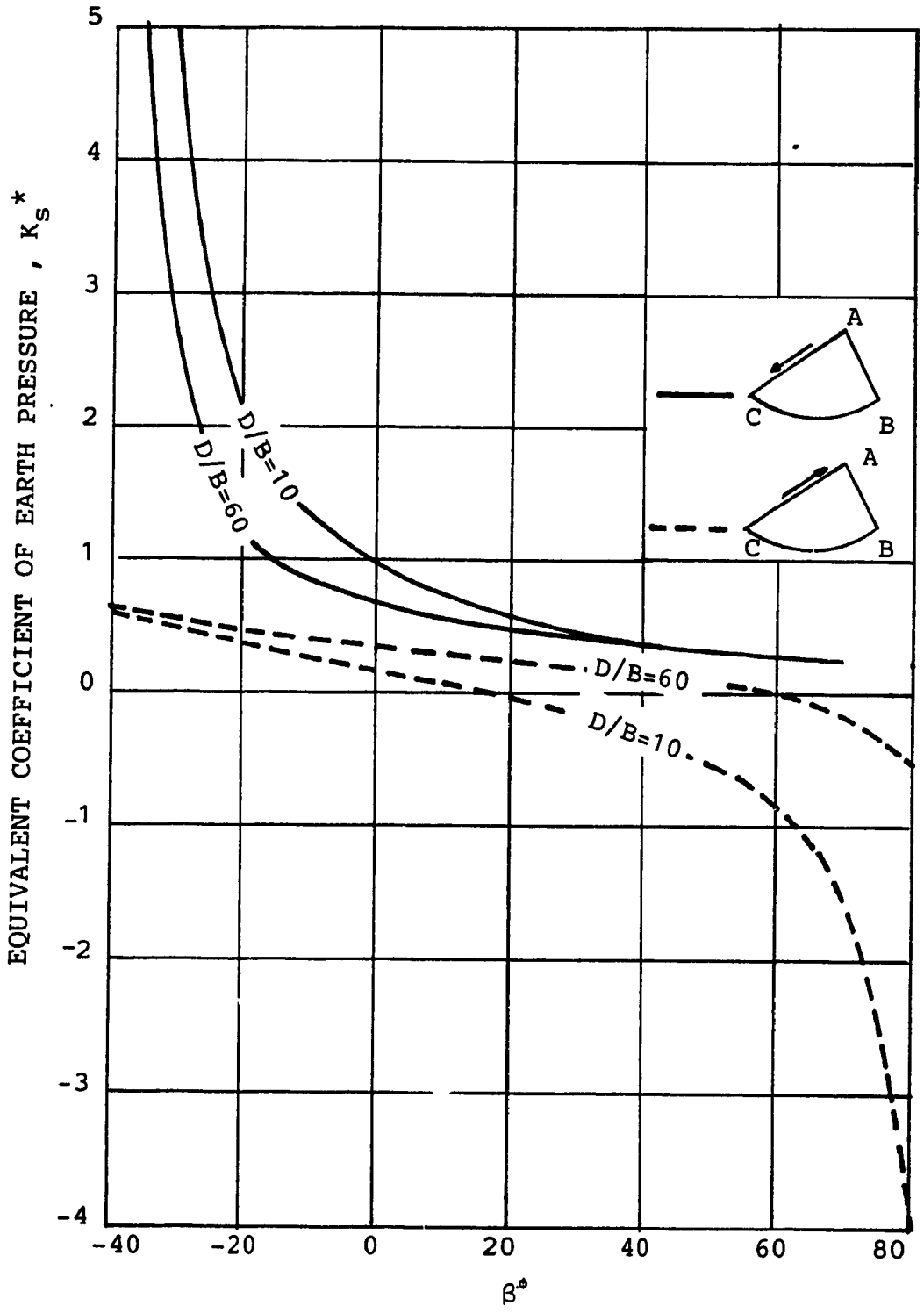

Fig. 4.18 Effects of Assumed Direction of Shear Force on Skin Friction

capacity N^*_q and the equivalent coefficient of earth pressure K^*_s on the pile shaft (i.e. Eqs. 4.18 and 4.19) were plotted against the slope β of the terminal radial surface for two relative depths D/B = 10 and 60. In general, the reversal of the direction of shear along the terminal radial surface results in an increase or a decrease in N^*_q, depending on the angle β (Fig. 4.17). The skin friction, however, is greatly reduced, regardless of β. It can be seen in Fig. 4.18 that for $-30° < \beta < +70°$, the coefficient of earth pressure K^*_s on the pile shaft in case 2 is either consistently lower than its counterpart in case 1 or becoming negative in certain range of β, indicating a negative skin friction and, thus, an unacceptable situation. From this perspective, the direction of shear assumed in case 1 is evidently more logical. This assumption is amply justified in later sections, where verifications of the proposed model show good agreement between predicted and measured pile bearing capacities from several laboratory and field load tests.

In previous bearing capacity theories, the state of stresses on the terminal radial surface is either postulated as principal stresses (Berezantzev, 1961; Janbu, 1974; etc...) or derived from an earth pressure distribution prescribed on the pile shaft (Meyerhof, 1951; Hu, 1965; Durgonoglu and Mitchell, 1973). While the skin friction is not considered in the former approach, the latter apparently implies a unilateral influence of skin friction on the point resistance, leading to the barren consequence that the earth pressure at the pile shaft must still be evaluated empirically.

4.4 PARAMETRIC STUDY

4.4.1 General

The proposed theoretical model to study the bearing capacity of a single pile in sand involves 8 variables, namely: ϕ, D, B, δ, K_o, R, K_T and β, where

ϕ = angle of shearing resistance of sand

D = embedded length of pile

B = pile diameter

δ = angle of friction between pile shaft and sand (i.e., shaft friction angle)

K_o = coefficient of lateral earth pressure at-rest

K_T = coefficient of earth pressure acting on the tangential plane

β = slope of the terminal radial surface

R = radius of influence.

The first five variables may be considered as intrinsic parameters while the remaining three variables β, K_T, and R are strictly model parameters related to the failure mechanism assumed in the model. In the following section, a parametric study is presented to investigate the effects of each of these parameters on the point resistance Q_p and the skin friction Q_s of an axially loaded pile driven in a homogeneous sand. The study is further simplified by combining D and B into the dimensionless relative depth D/B, and expressing δ, K_T and R in terms of dimensionless ratios δ/ϕ, K_T/K_o, and R/B. The basic parameters now reduce to: ϕ, D/B, δ/ϕ, K_o, β, K_T/K_o, and R/B.

The computation of Q_p and Q_s was carried out utilizing the computer program TEMPO. For simplicity and especially for easy graphical comparison purposes, it is preferred here to adopt the dimensionless equivalent bearing capacity factor N^*_q and the equivalent coefficient of lateral earth pressure at the pile shaft K^*_s rather than Q_p and Q_s in studying the influences of a particular parameter. The following expressions for N^*_q and K^*_s will be used:

$$N^*_q = \frac{Q_p}{\gamma' D A_p} \qquad \text{... (4.19)}$$

$$K^*_s = \frac{2Q_s}{\gamma' D (\tan \delta) A_s} \qquad \text{... (4.20)}$$

where

γ' = effective unit weight of sand

D = pile embedment length

A_p = cross section area of pile tip

δ = friction angle between pile shaft and sand

A_s = surface area of pile shaft.

4.4.2 Effect of Angle of Shearing Resistance ϕ

The variation of N^*_q with ϕ is presented in Figs. 4.19, 4.20, and 4.21 for D/B = 10, 30, and 60 with other parameters kept constant: $K_o = 0.5$, $\delta/\phi = 1$, $K_T/K_o = 0.75$, and R/B = 3. It can be seen that N^*_q increases with ϕ for a given relative depth D/B, and for a selected value of β. It is also evident from these figures that for a given set of ϕ and D/B, the rate of increase in N^*_q is significantly affected by the angle β, especially in cases where $\beta < 0$ (i.e., the terminal radial surface moves up towards the pile shaft).

The corresponding variation of K^*_s with ϕ is shown in Figs. 4.22, 4.23, and 4.24. In these example curves, K^*_s also increases with ϕ for a given angle β. As β becomes more positive (i.e., the terminal radial surface moves downwards from the pile tip level), the effect of ϕ on K^*_s diminishes rapidly.

4.4.3 Effect of Relative Depth D/B

The effect of the relative depth D/B on N^*_q is demonstrated by example curves shown in Figs. 4.25, 4.26, 4.27, and 4.28 for ϕ = 30°, 35 °, 40 °, and 45 °, while other parameters are kept constant: $\delta/\phi = 0.5$, $K = 1 - \sin\delta$, $K_T/K_o = 0.75$, and R/B = 3. It can be seen that N^*_q increases linearly with the relative depth D/B at a decreasing rate as angle β becomes more positive (i.e., the terminal radial surface moves downwards from the pile tip level). On the other hand, K^*_s is found to decrease with D/B at a decreasing rate for a given angle β as illustrated in Figs. 4.29, 4.30, 4.31 and 4.32. As the terminal radial surface dips further

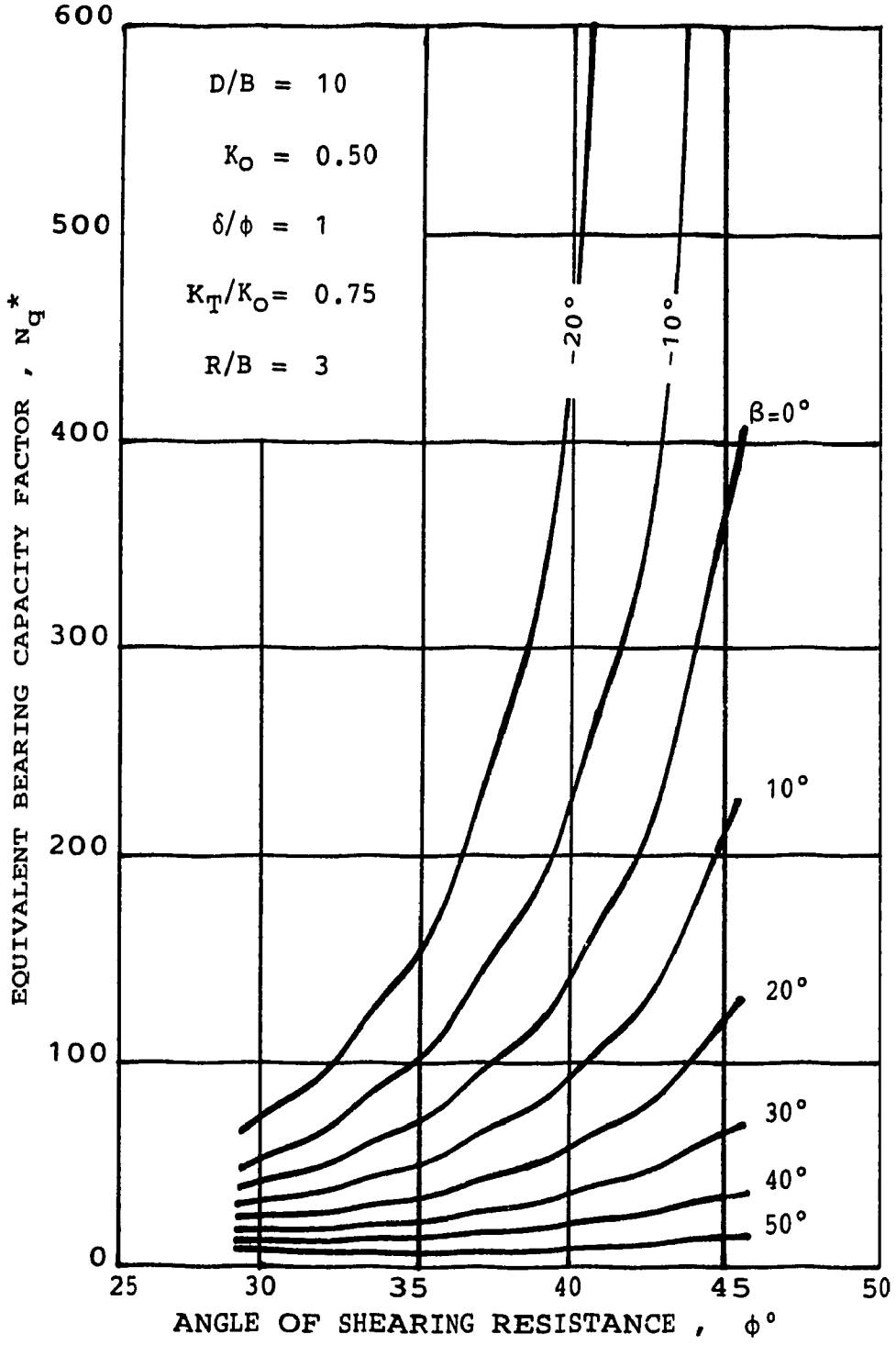

Fig. 4.19 Effect of φ on Point Resistance (D/B=10)

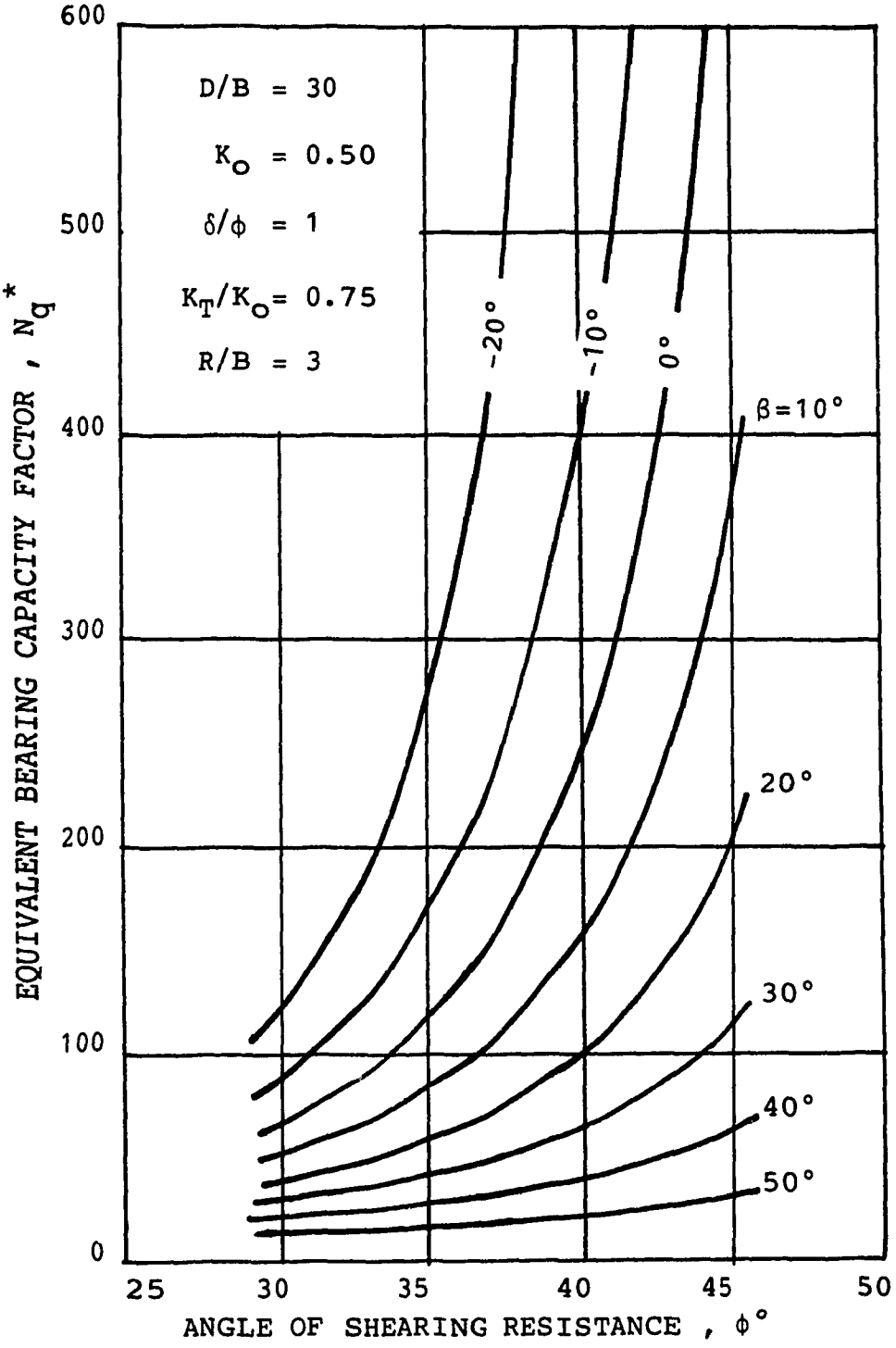

Fig. 4.20 Effect of ϕ on Point Resistance (D/B=30)

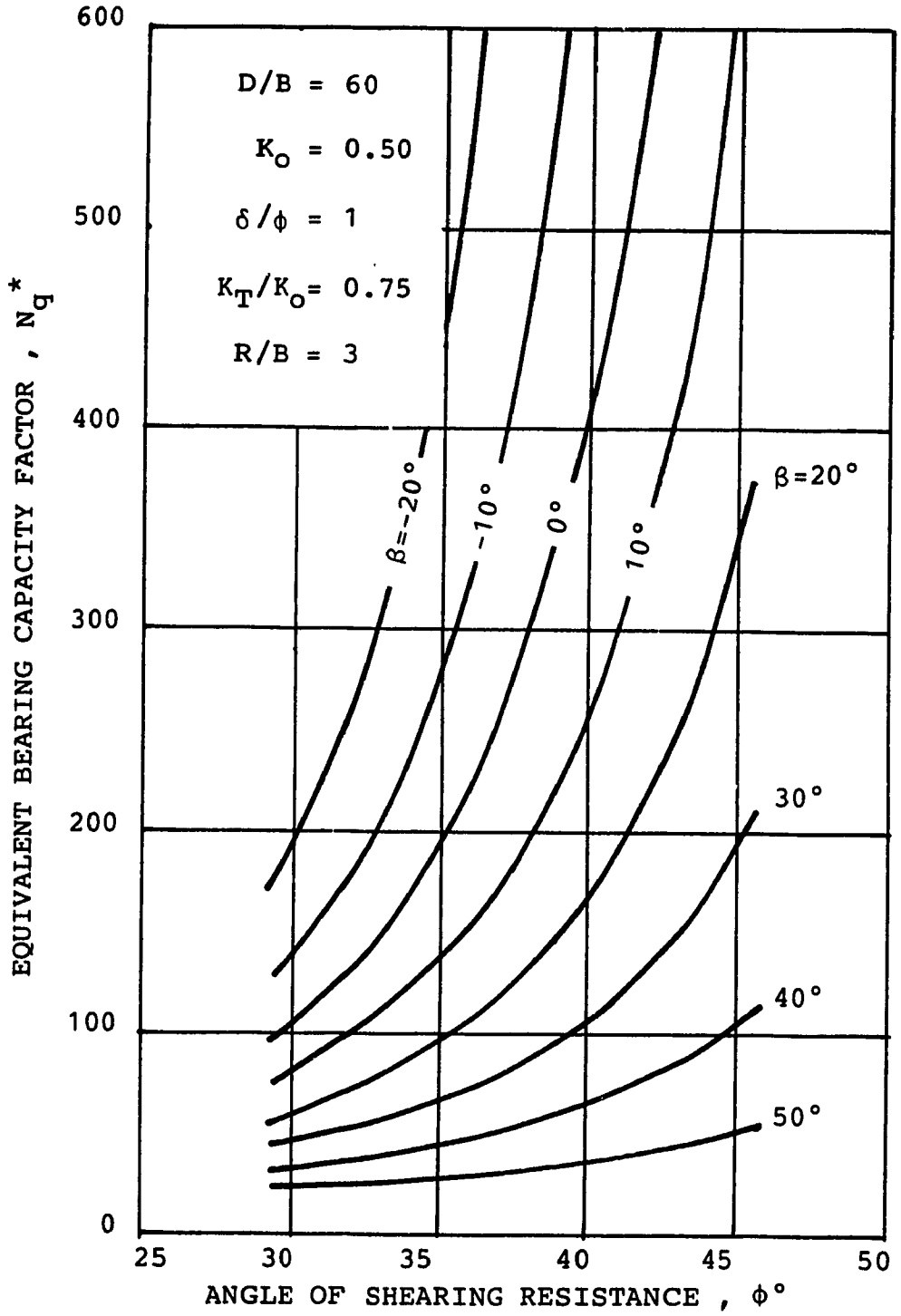

Fig. 4.21 Effect of ϕ on Point Resistance (D/B=60)

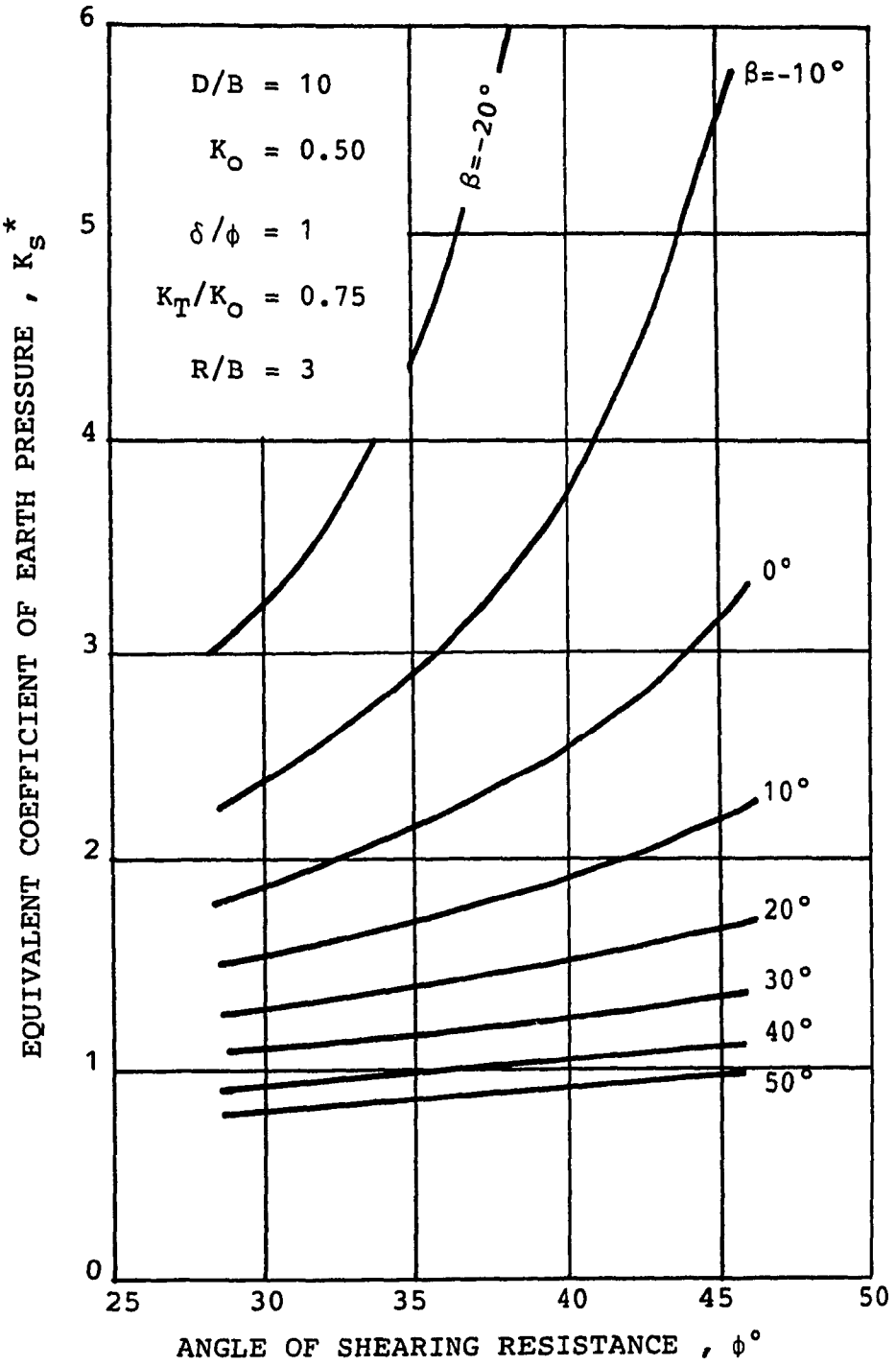

Fig. 4.22 Effect of φ on Skin Friction (D/B=10)

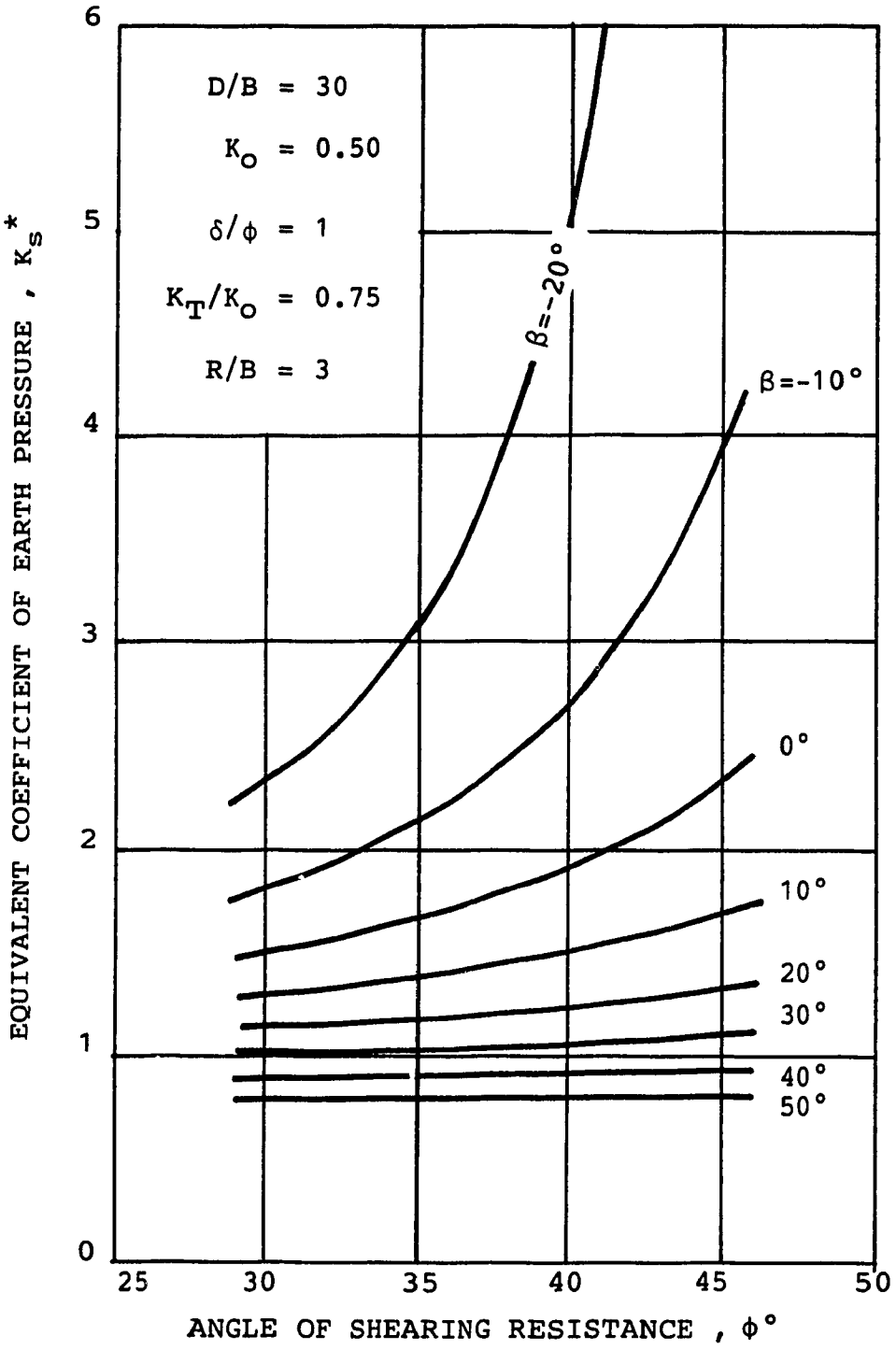

Fig. 4.23 Effect of φ on Skin Friction (D/B=30)

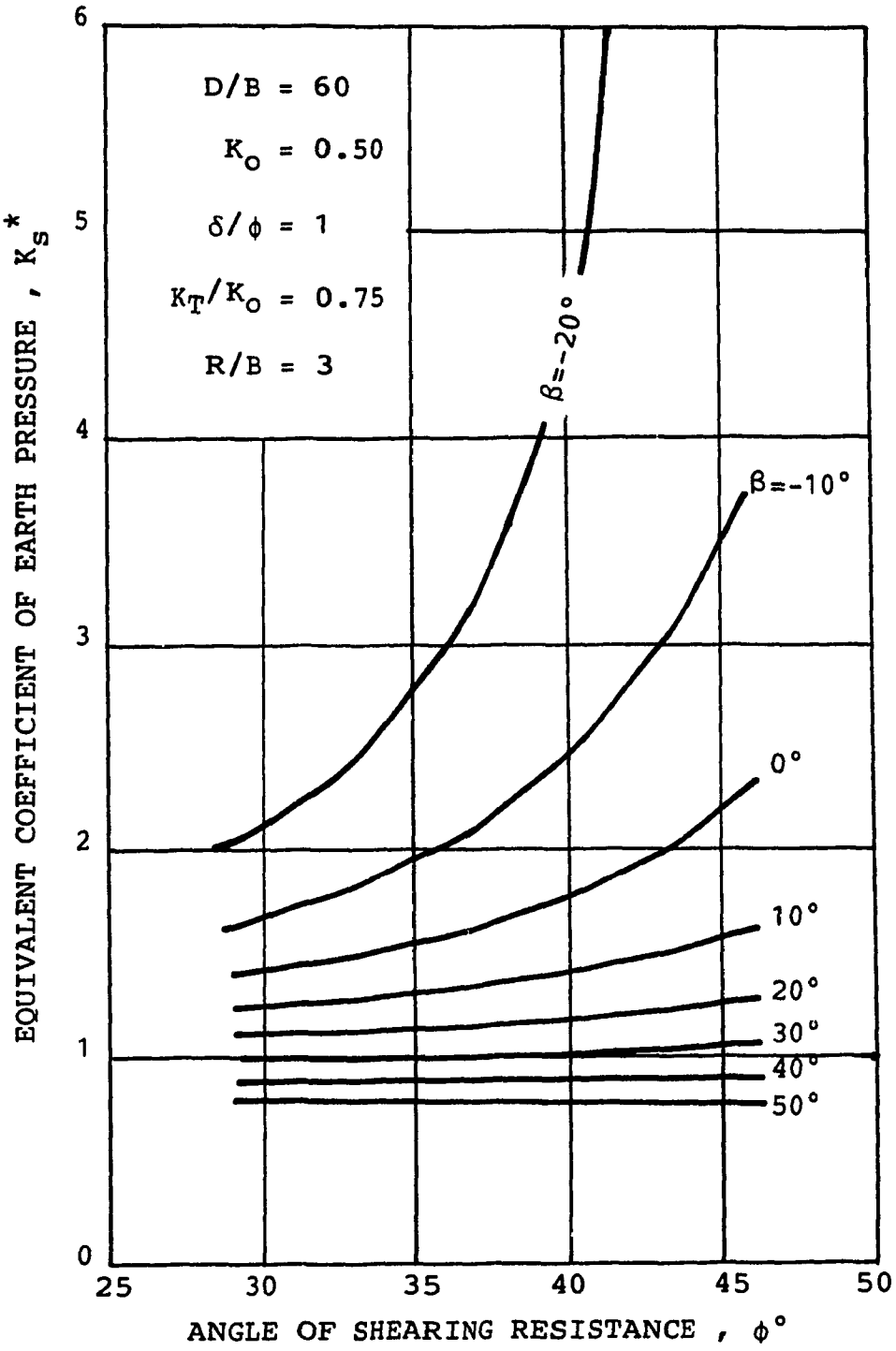

Fig. 4.24 Effect of φ on Skin Friction (D/B=60)

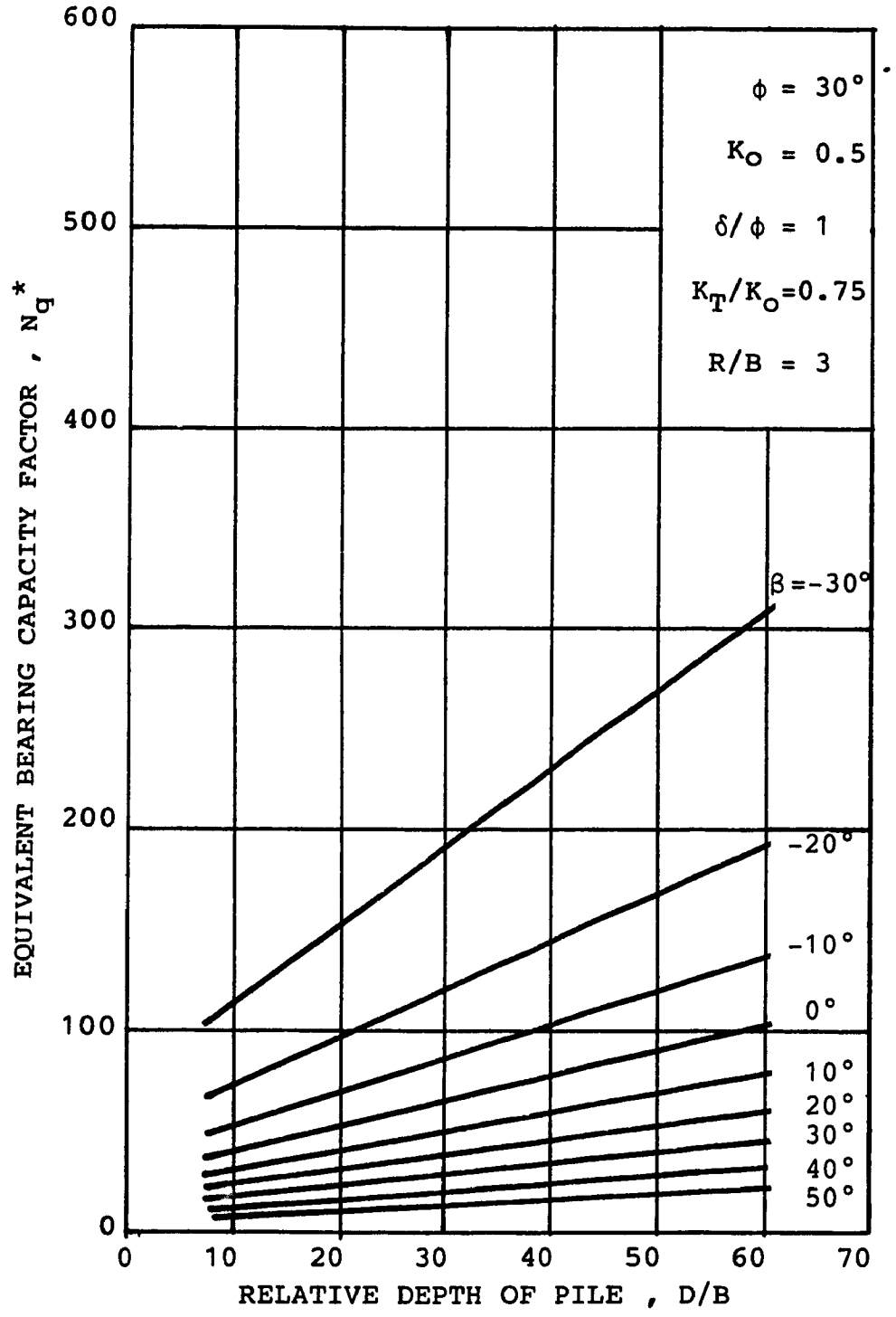

Fig. 4.25 Effect of Relative Depth on Point Resistance (ϕ=30°)

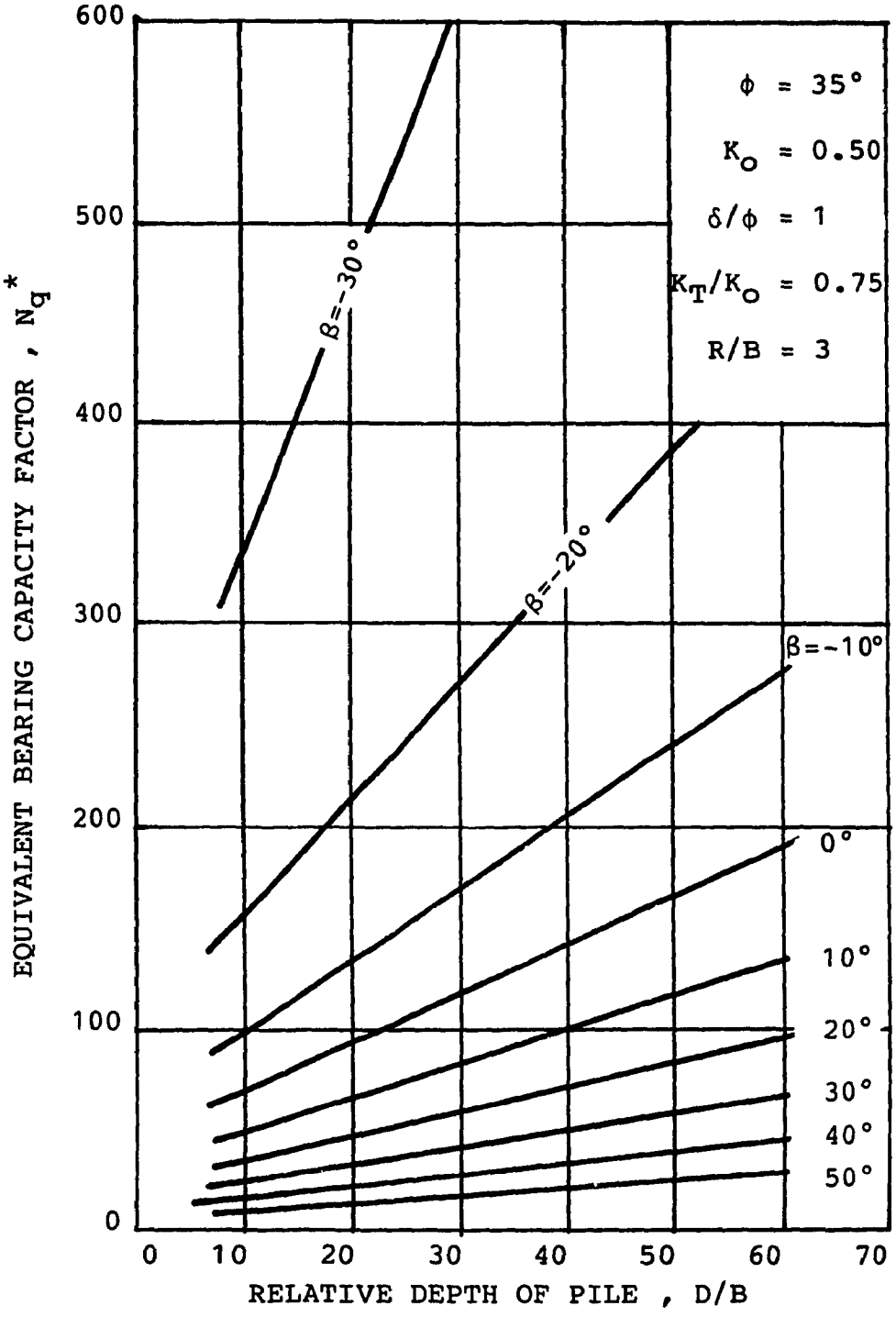

Fig. 4.26 Effect of Relative Depth on Point Resistance (ϕ=35°)

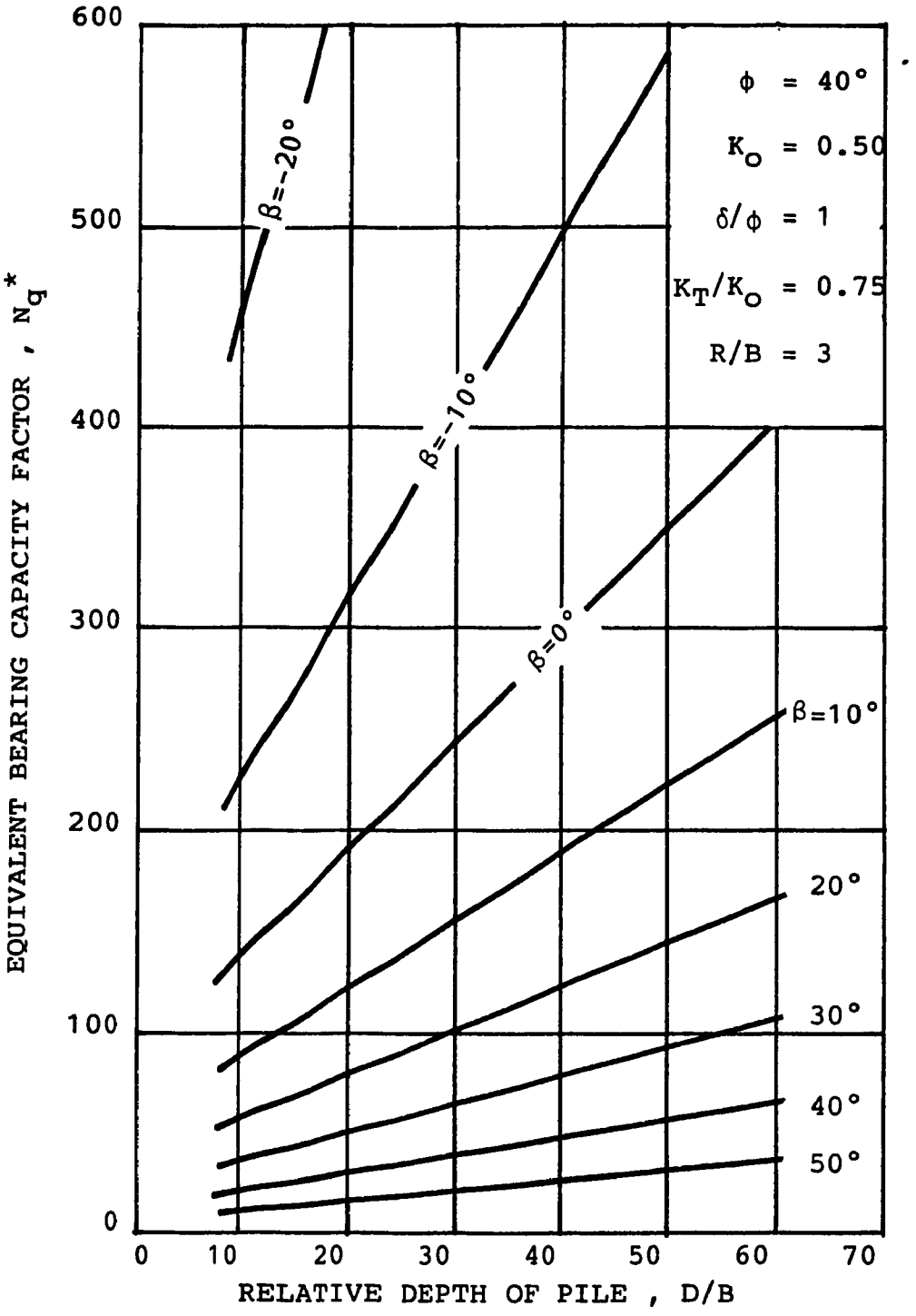

Fig. 4.27 Effect of Relative Depth on Point Resistance (ϕ=40°)

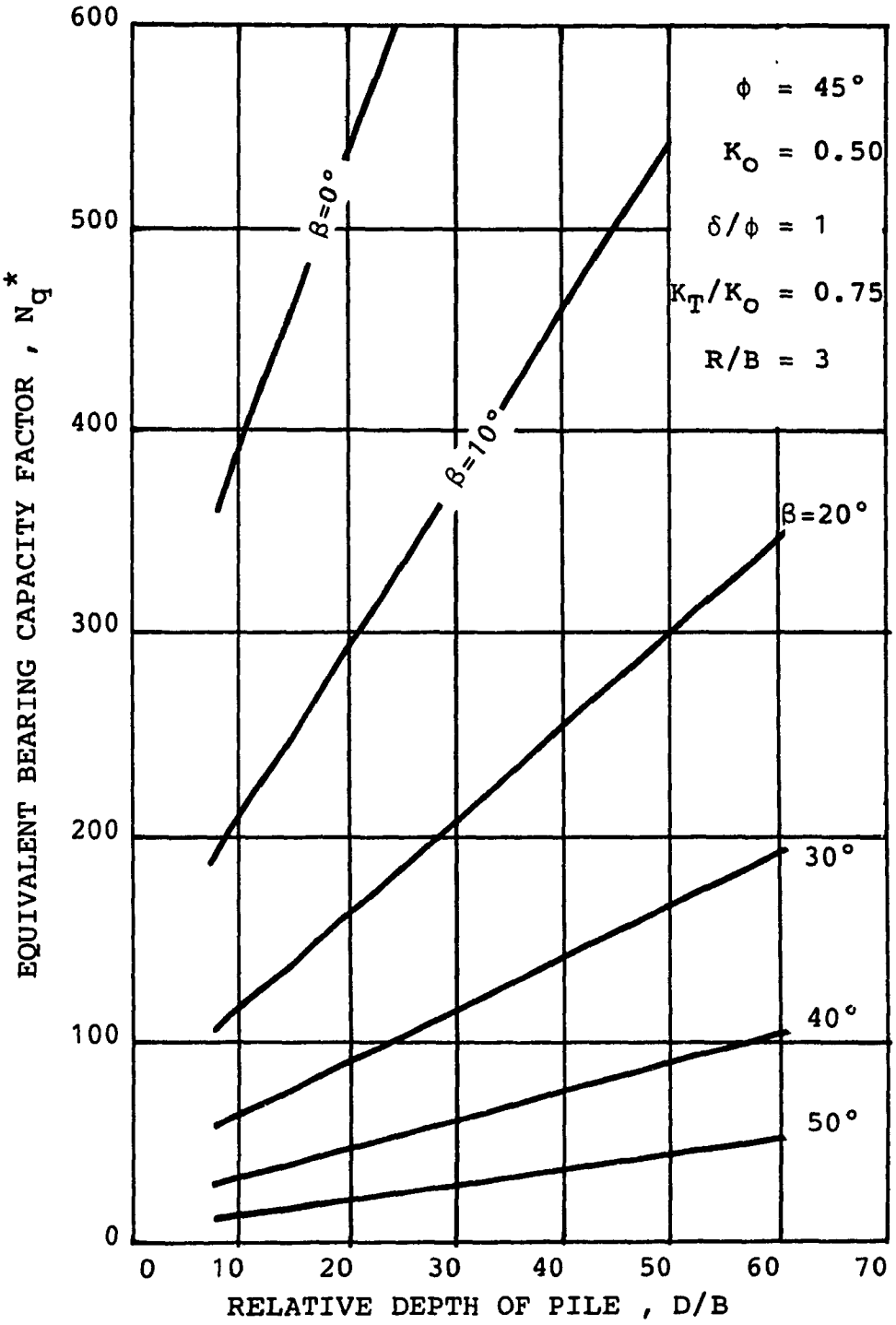

Fig. 4.28 Effect of Relative Depth on Point Resistance (ϕ=45°)

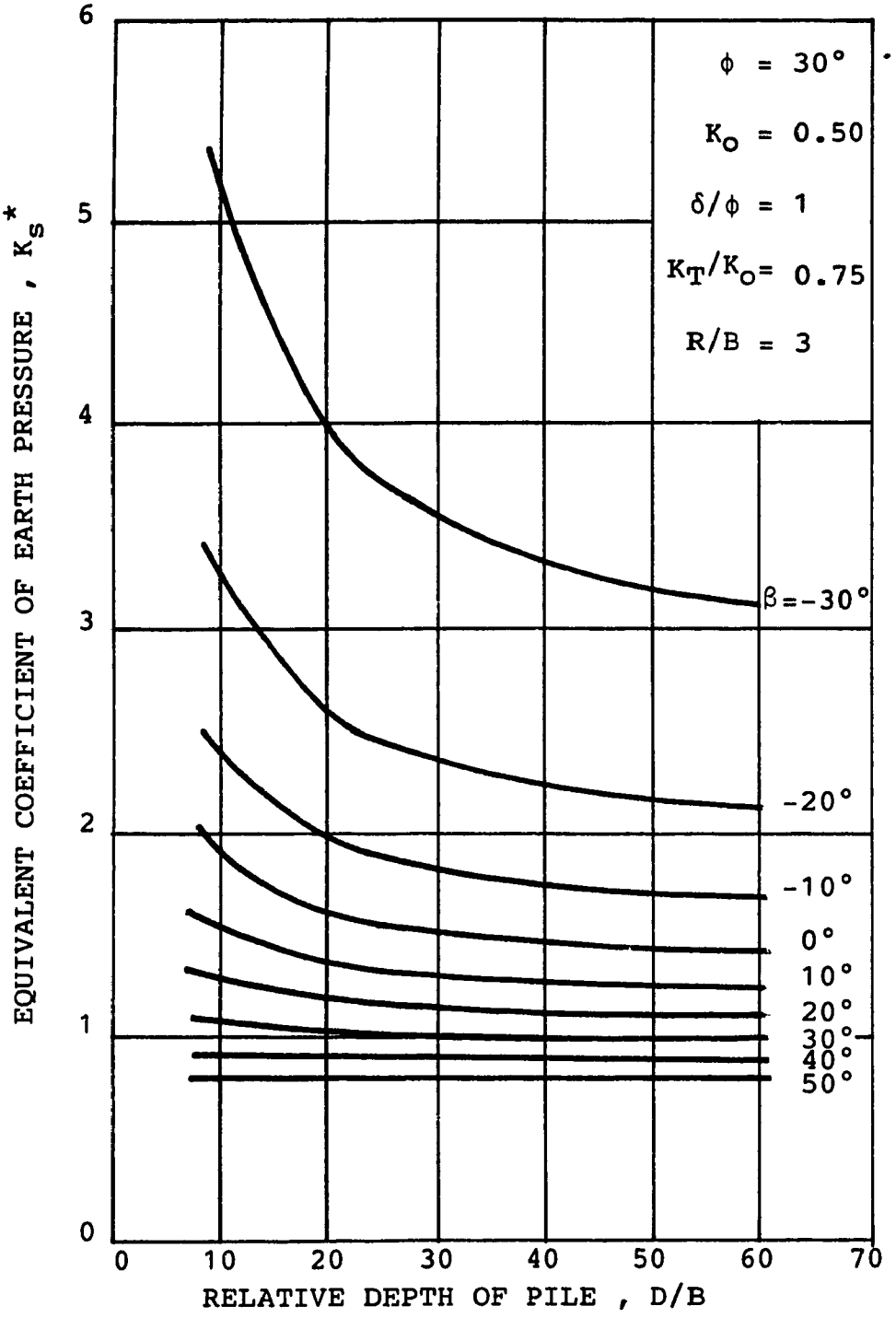

Fig. 4.29 Effect of Relative Depth on Skin Friction (ϕ=30°)

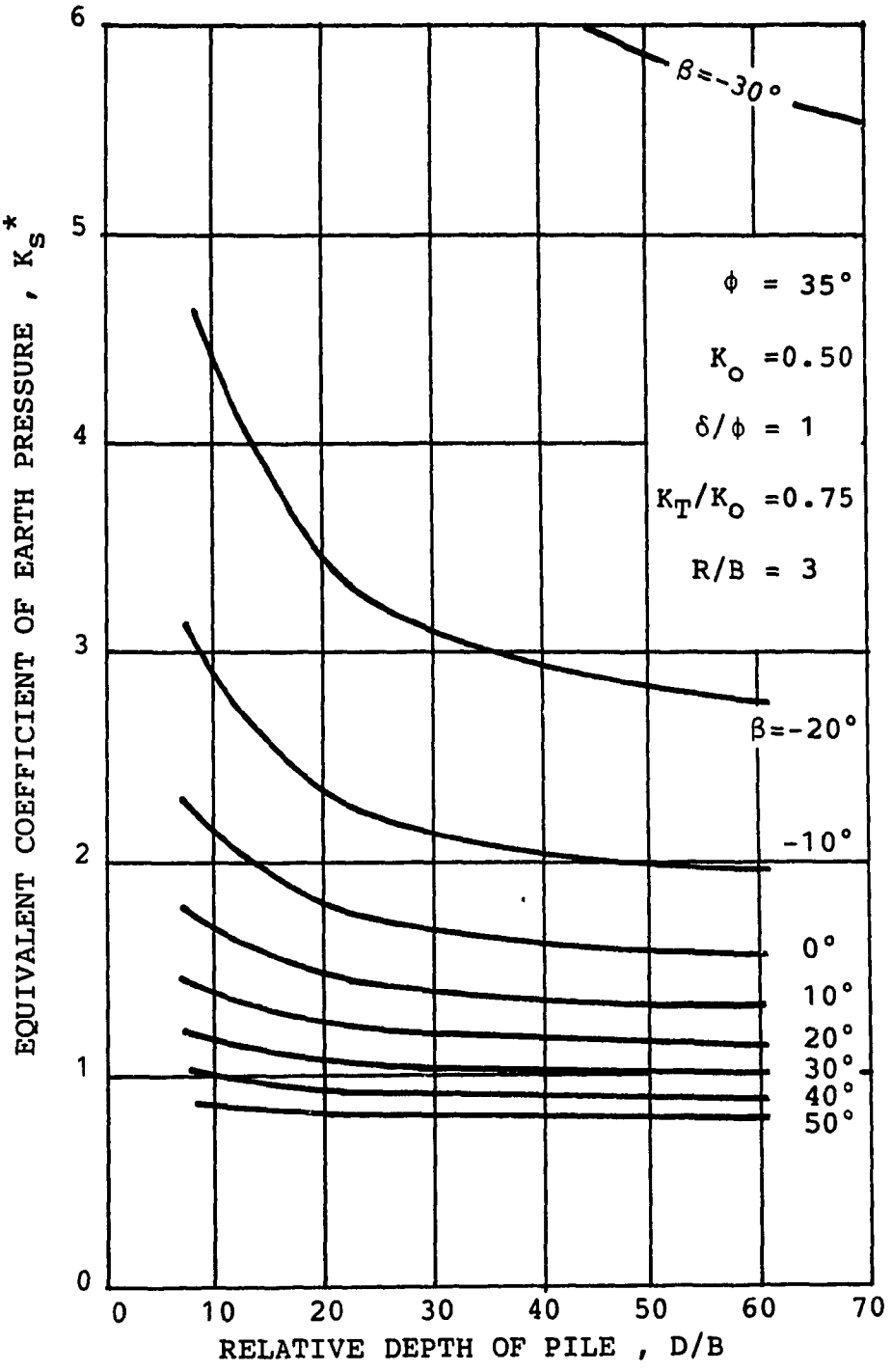

Fig. 4.30 Effect of Relative Depth on Skin Friction (ϕ=35°)

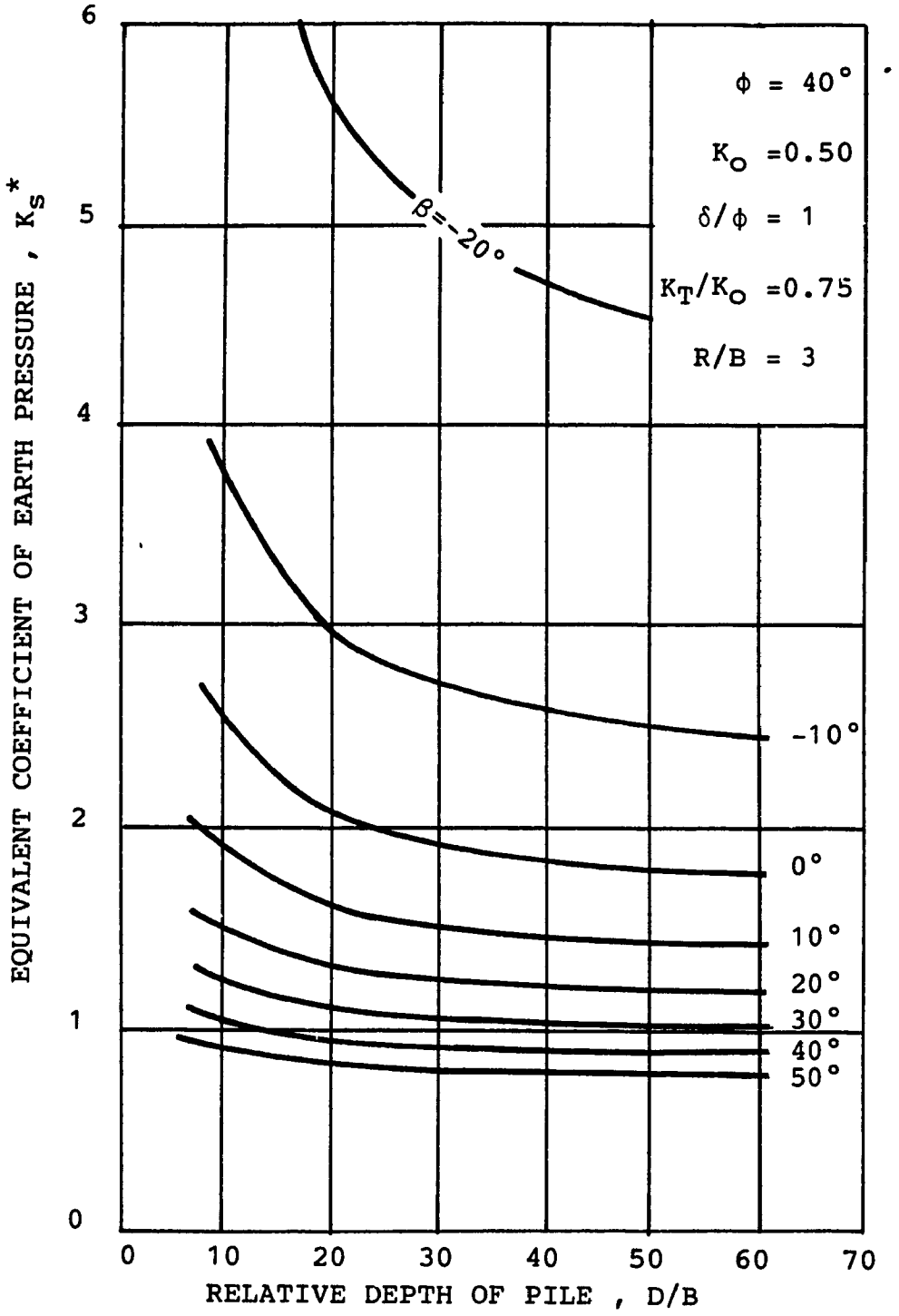

Fig. 4.31 Effect of Relative Depth on Skin Friction (ϕ=40°)

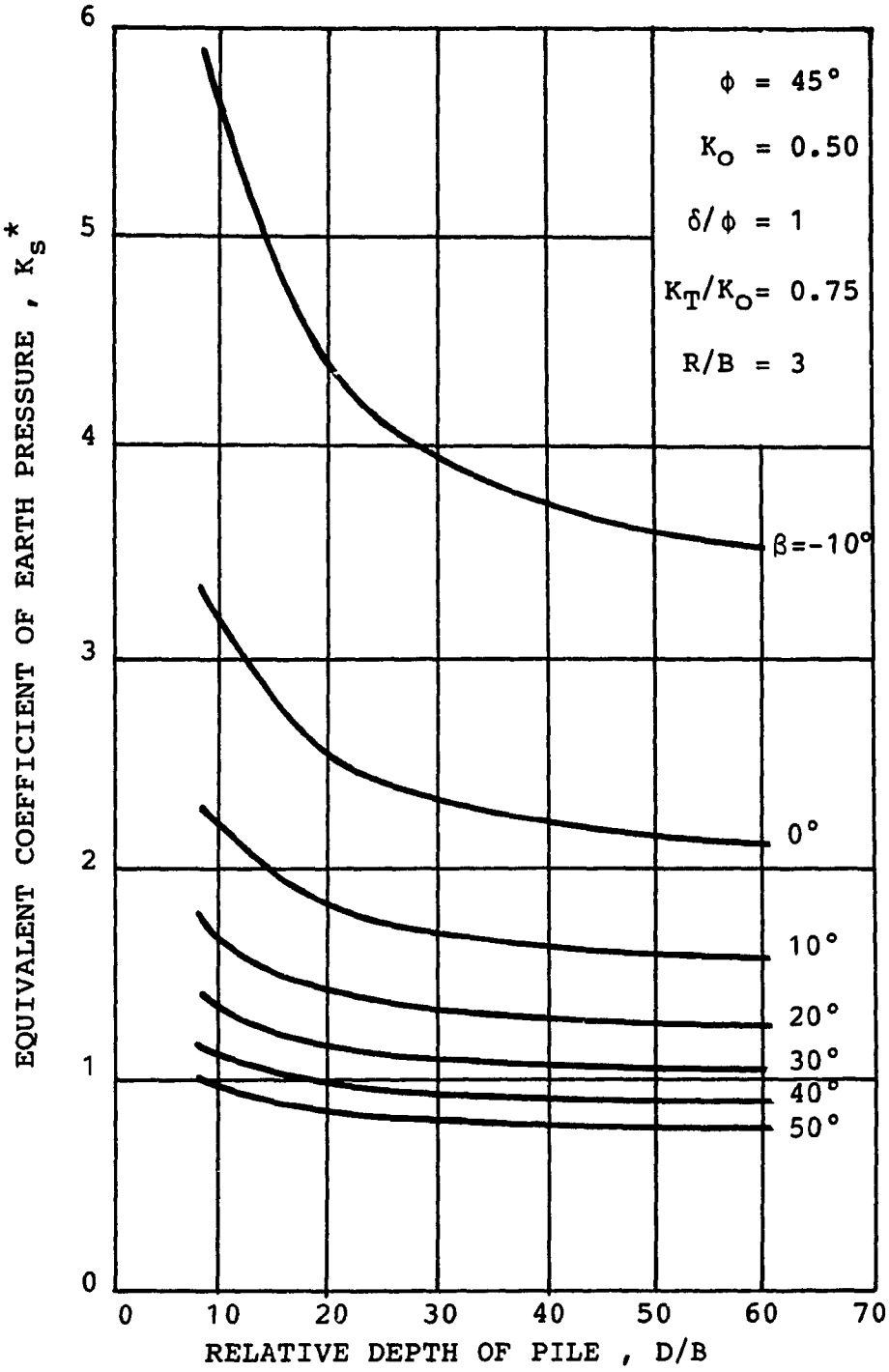

Fig. 4.32 Effect of Relative Depth on Skin Friction (ϕ=45°)

downwards from the pile tip level (i.e., $\beta > 0$), the relative depth D/B has negligible effect on K^*_s.

4.4.4 Effect of Coefficient of Earth Pressure At-Rest K_o

The variation of N^*_q with the coefficient of earth pressure at-rest K_o is found to be linear as indicated in Figs. 4.33, 4.34, and 4.35 where example curves show N^*_q versus K_o at three different relative depths D/B = 10, 30, and 60 for $\phi = 35°$, $\delta/\phi = 1$, $K_T/K_o = 0.75$, and R/B = 3. The effect of K_o is specially important for cases in which the terminal radial surface lies above the pile tip level (i.e., $\beta < 0$). However, this effect reduces considerably as the terminal radial surface sweeps downwards below the pile tip level (i.e. $\beta > 0$).

A similar trend is observed for K^*_s in Figs. 4.36, 4.37, and 4.38. It can be seen that while K^*_s increases linearly with K_o for a given angle β, its rate of change appears to be affected by β and the relative depth D/B.

4.4.5 Effect of Pile Shaft Roughness δ/ϕ

The bearing capacity factor N^*_q is found to increase with the pile shaft roughness δ/ϕ as shown in Figs. 4.39, 4.40, and 4.41 for three different relative depths D/B = 10, 30, and 60. In theses example curves, other parameters are held constant: $\phi = 35°$, $K_o = 1 - \sin\phi$, $\delta/\phi = 1$, $K_T/K_o = 0.75$, and R/B = 3.

As for K^*_s, Figs. 4.42, 4.43, 4.44 show that it may increase or decrease linearly with δ/ϕ, depending on the angle β. The values of N^*_q and K^*_s for a given intermediate roughness can be well approximated by linear interpolation between perfectly smooth and perfectly rough values (i.e., $\delta/\phi = 0$ and $\delta/\phi = 1$, respectively) for $\beta \geq 0$. The linear approximation, however, should not be used for $\beta < 0$ since the variation of N^*_q and K^*_s with δ/ϕ are nonlinear in this range.

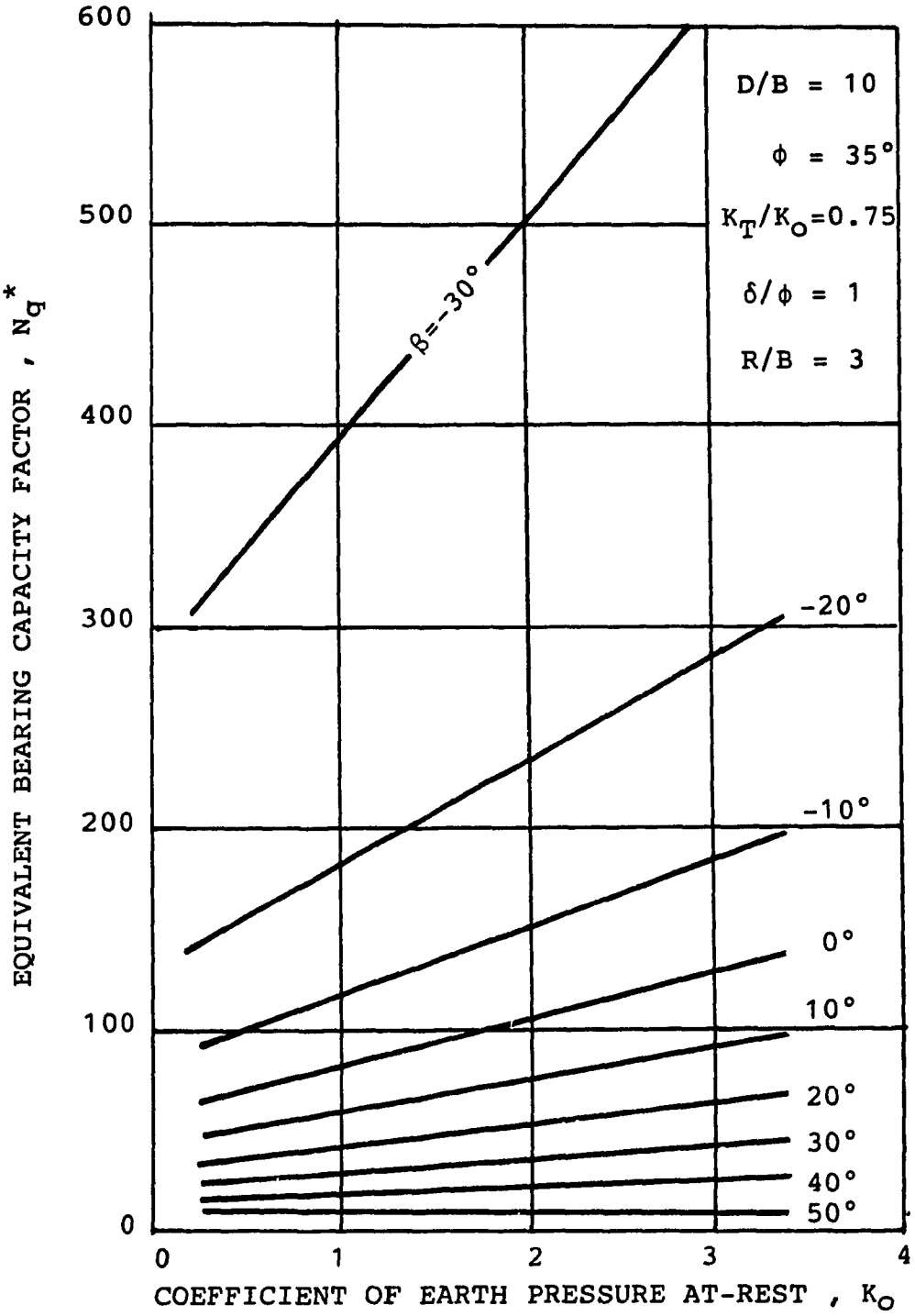

Fig. 4.33 Effect of Lateral Earth Pressure on Point Resistance (D/B=10)

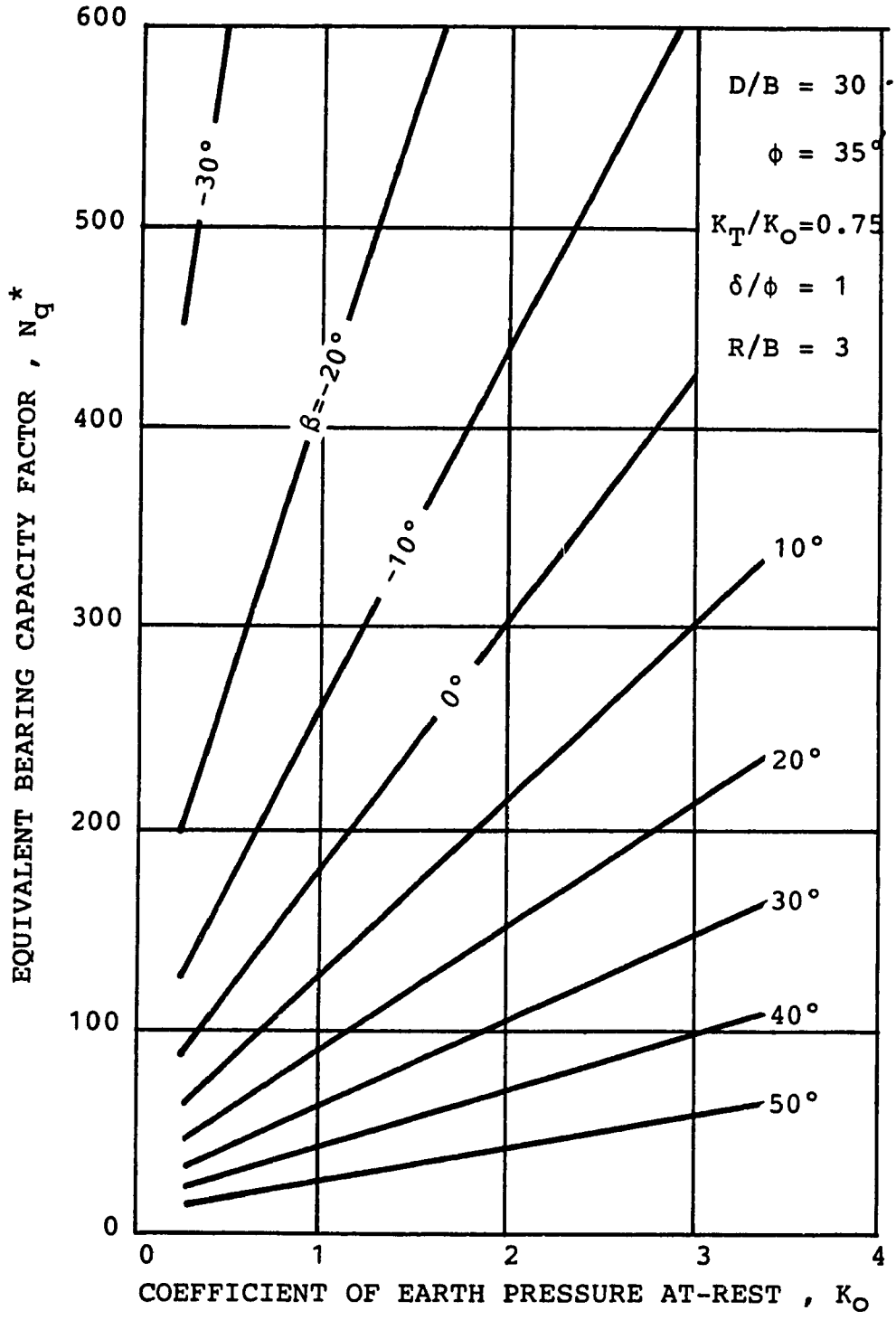

Fig. 4.34 Effect of Lateral Earth Pressure on Point Resistance (D/B=30)

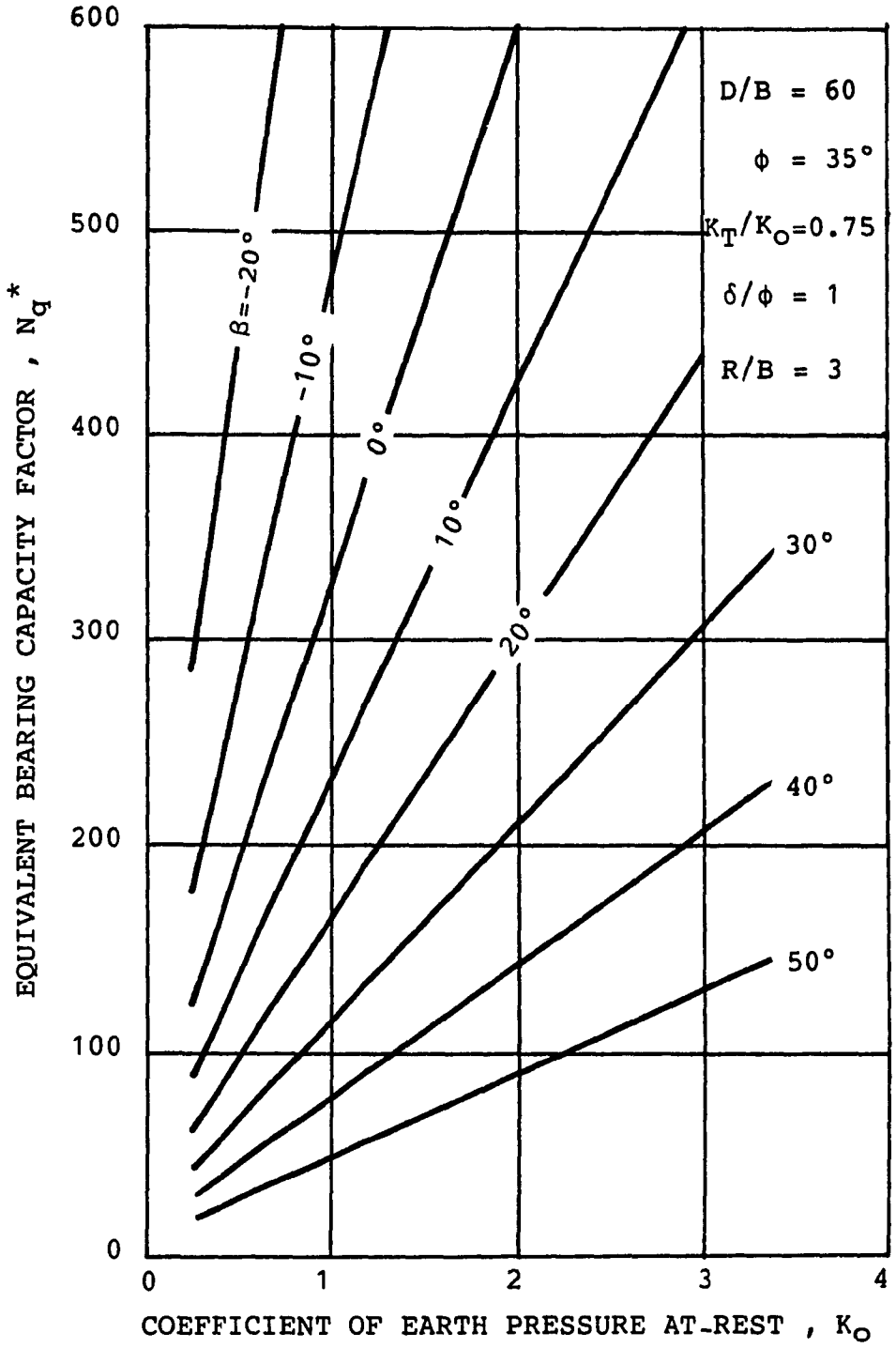

Fig. 4.35 Effect of Lateral Earth Pressure on Point Resistance (D/B=60)

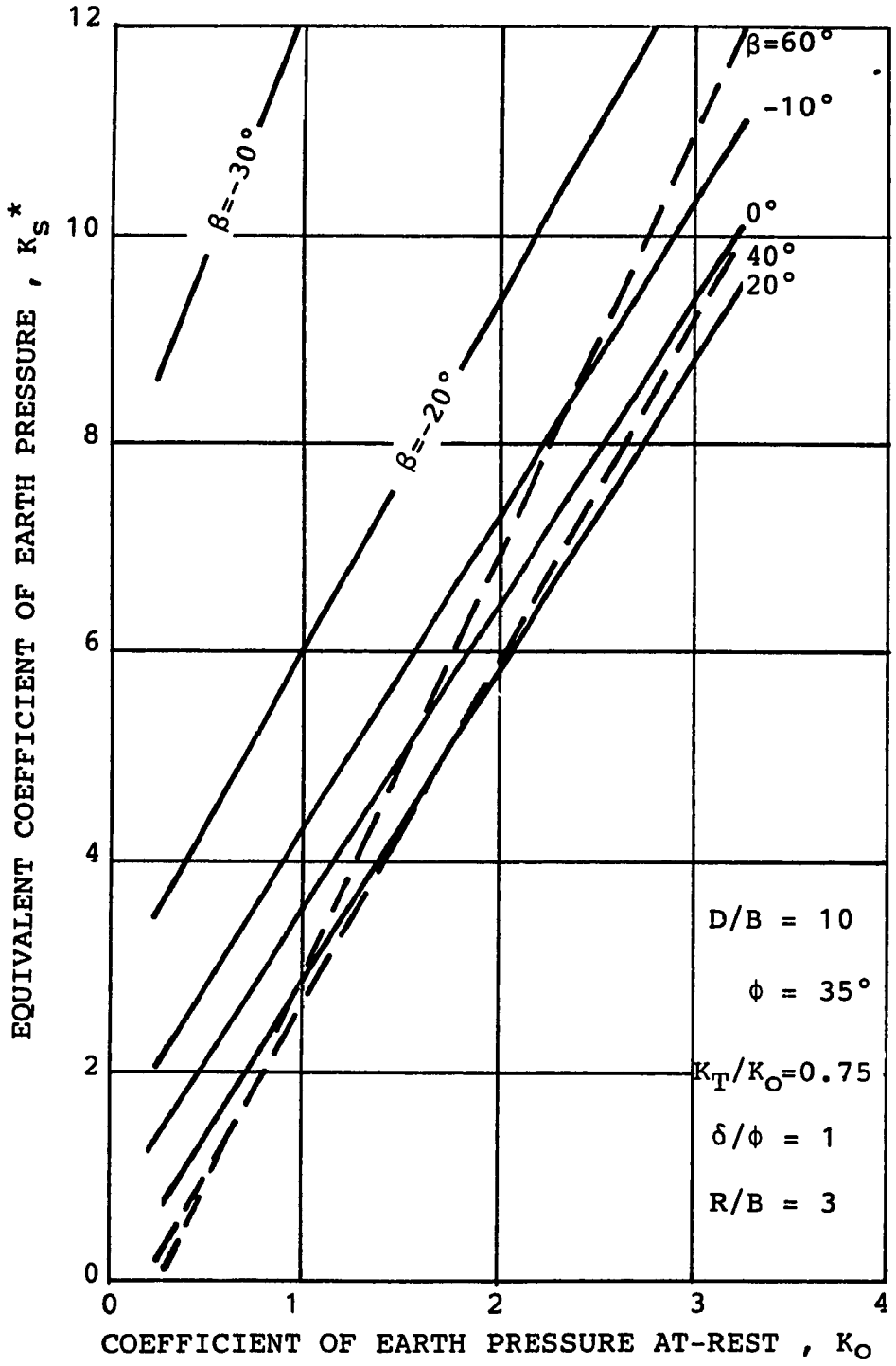

Fig. 4.36 Effect of Lateral Earth Pressure on Skin Friction (D/B=10)

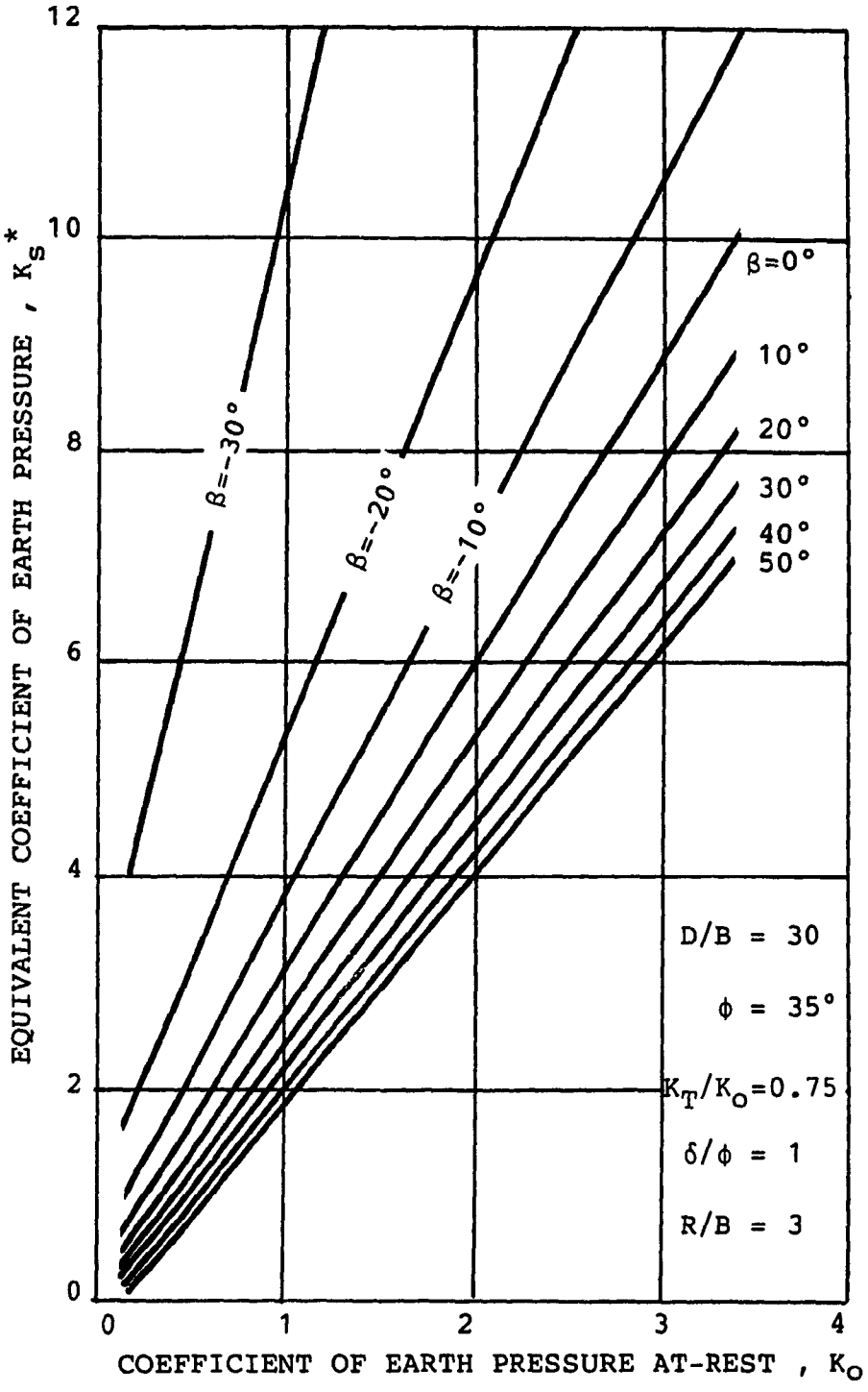

Fig. 4.37 Effect of Lateral Earth Pressure on Skin Friction (D/B=30)

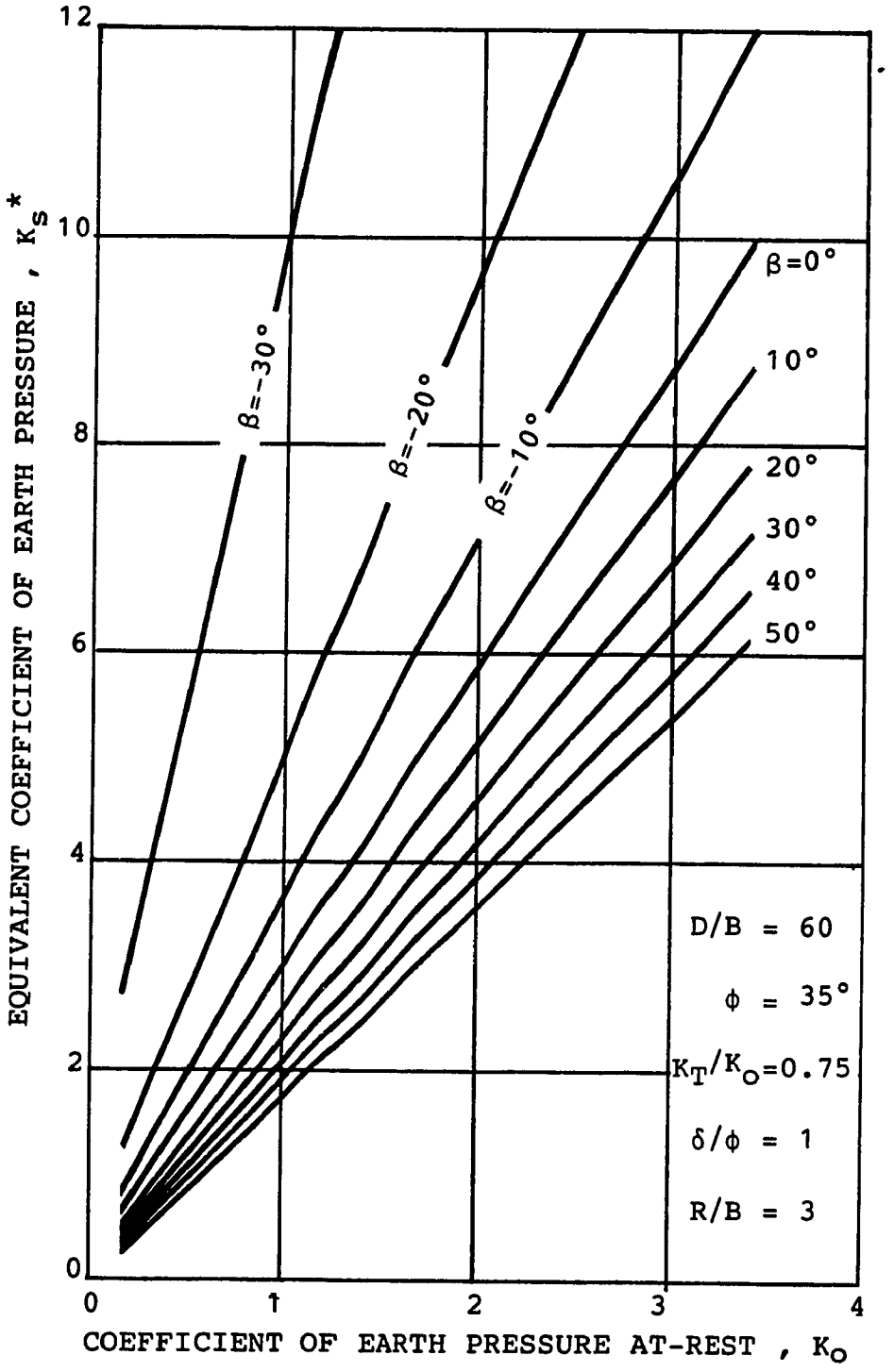

Fig. 4.38 Effect of Lateral Earth Pressure on Skin Friction (D/B=60)

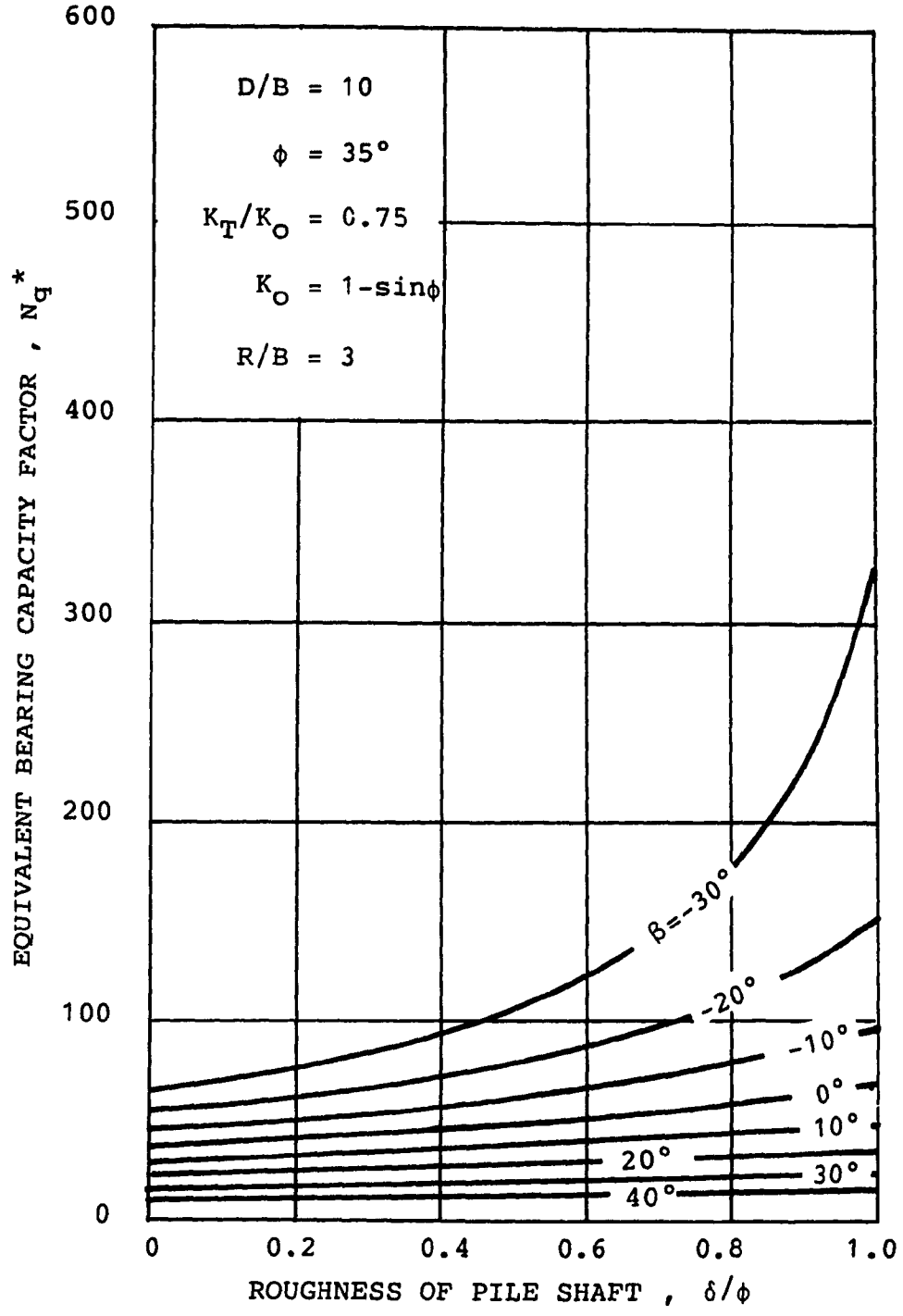

Fig. 4.39 Effect of Pile Roughness on Point Resistance (D/B=10)

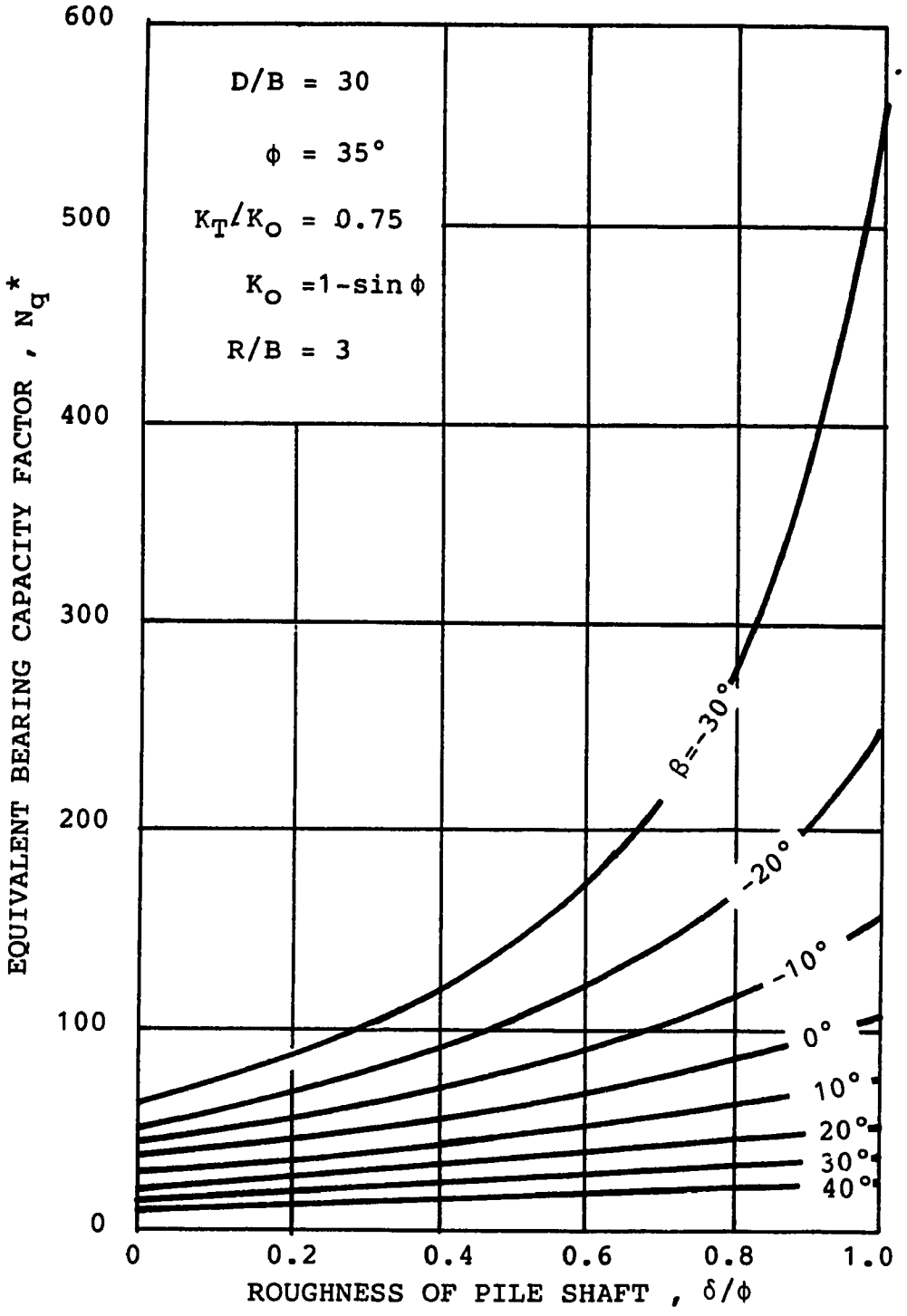

Fig. 4.40 Effect of Pile Roughness on Point Resistance (D/B=30)

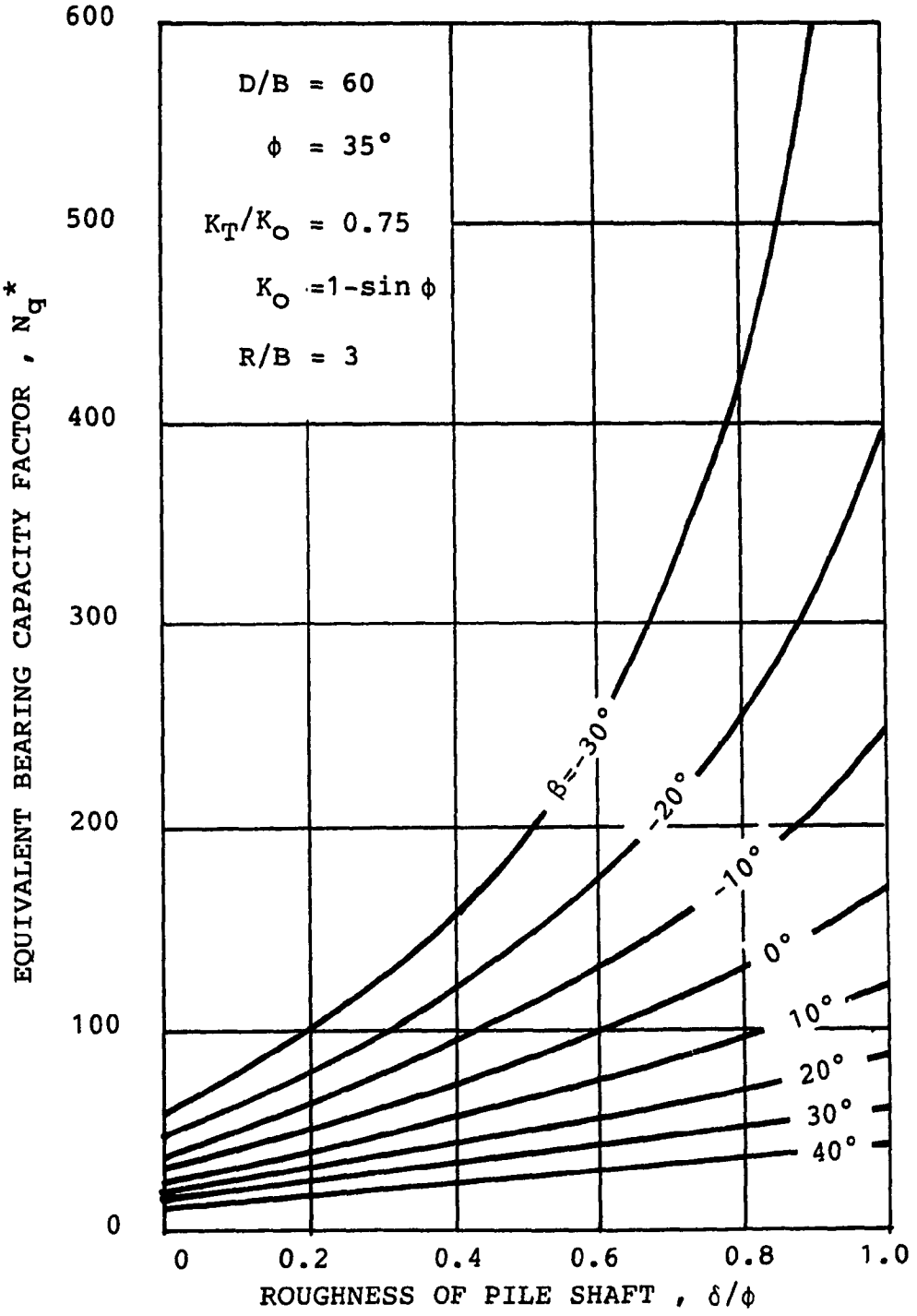

Fig. 4.41 Effect of Pile Roughness on Point Resistance (D/B=60)

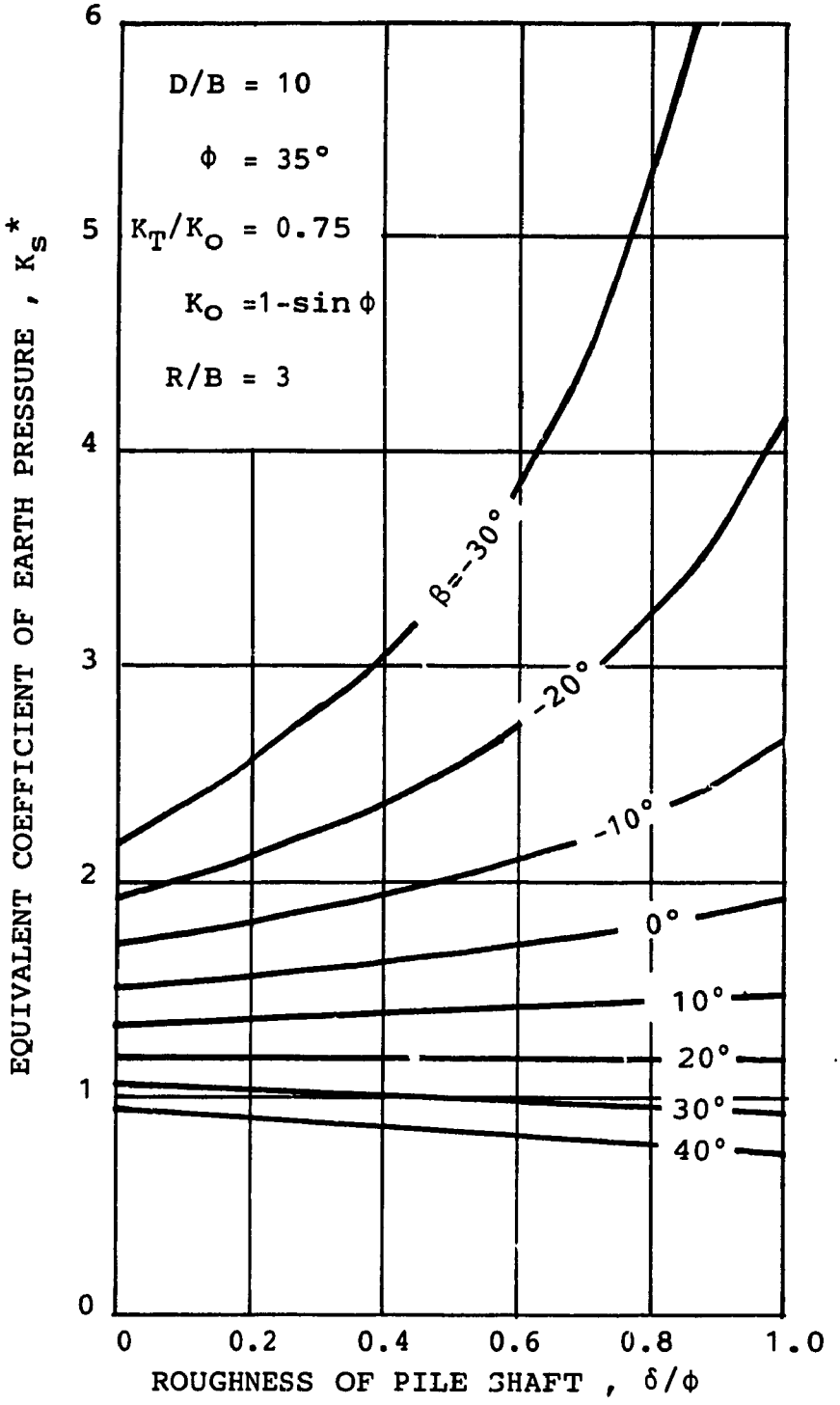

Fig. 4.42 Effect of Pile Roughness on Skin Friction (D/B=10)

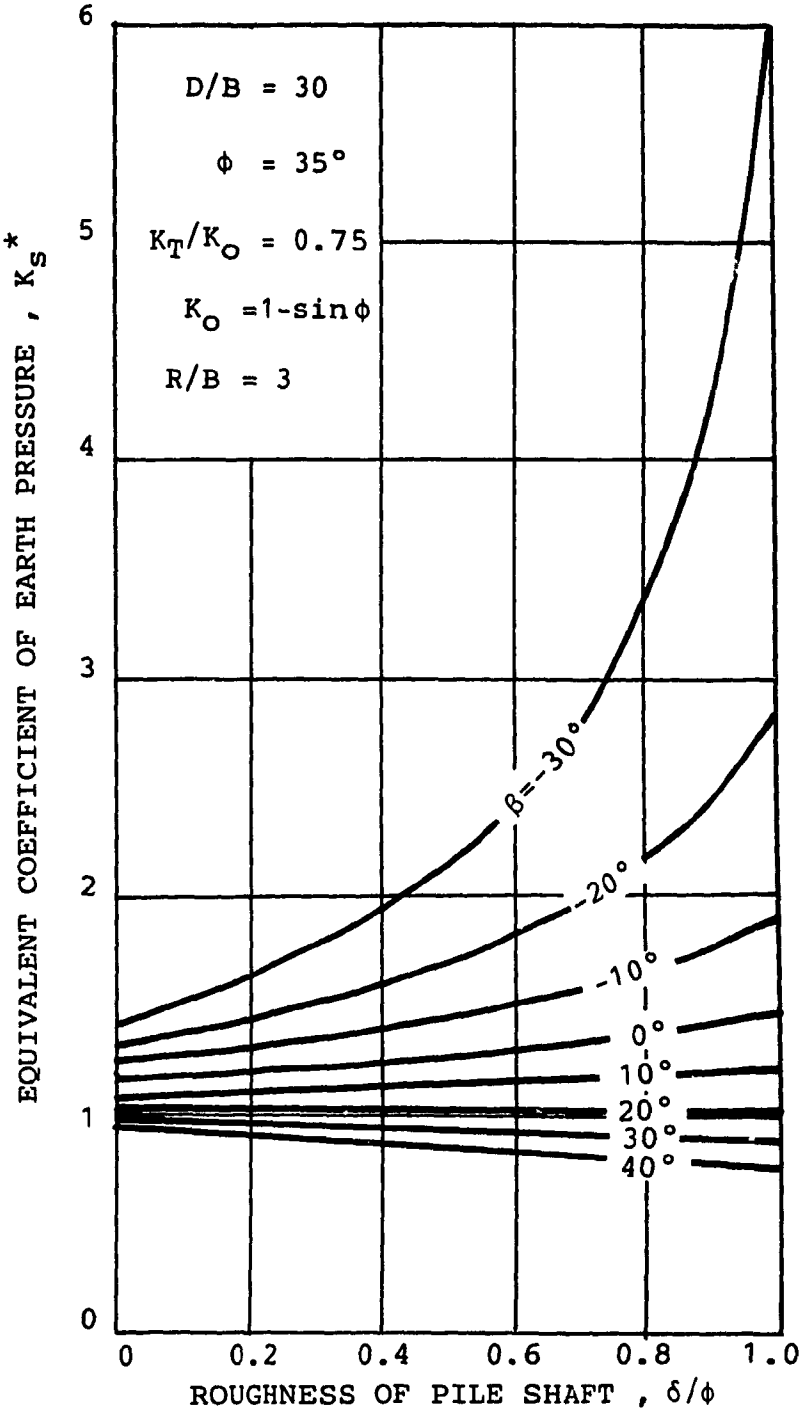

Fig. 4.43 Effect of Pile Roughness on Skin Friction(D/B=30)

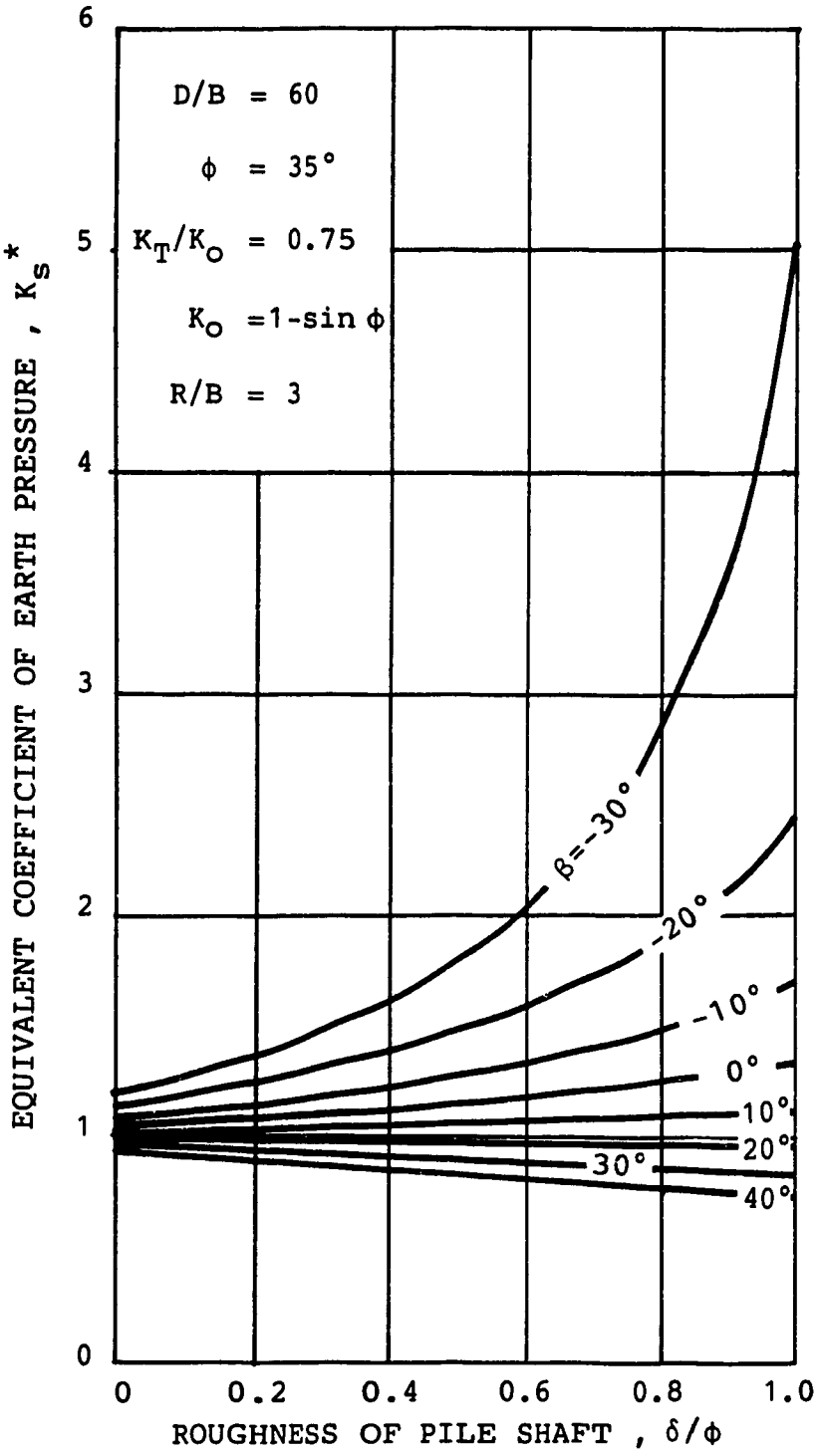

Fig. 4.44 Effect of Pile Roughness on Skin Friction(D/B=60)

4.4.6 Effect of Earth Pressure on Tangential Plane

The variation of N^*_q with K_T/K_o for three different relative depths D/B = 10, 30, and 60 are shown in Figs. 4.45, 4.46, and 4.47 where $\phi = 35^o$, $K_o = 1 - \sin\delta$, $\delta/\phi = 1$, and R/B = 3. For any given angle β, it can be seen that N^*_q decreases linearly with increasing ratio K_T/K_o. As β becomes more positive, the influence of K_T/K_o on N^*_q diminishes considerably.

The decrease of K^*_s with increasing K_T/K_o, shown in Figs. 4.48, 4.49, and 4.50, may be explained from Figs. 4.4 and 4.5 : an increase in the pressure on the tangential plane results in a larger force R_3 which reduces the effect of E_1, leading to a reduction in the earth pressure exerting on the pile shaft. Almost all previous studies of pile shaft friction based on two dimensional models and thus neglected the effect of the earth pressure on the tangential plane, which exits only if a three dimensional model is used.

4.4.7 Effect of radius of influence R

The effect of the radius of influence R on N^*_q is demonstrated at three relative depths D/B = 10, 30, and 60, while keeping other parameters constant: $\phi = 35°$, $K_o = 1 - \sin\phi$, $\delta/\phi = 1$, and $K_T/K_o = 0.75$. It can be seen in Figs. 4.51, 4.52, and 4.53 that N^*_q decreases with increasing β and passes through minimum values for certain range of β as R/B increases.

On the other hand, K^*_s tends to increase with increasing R/B as seen in Figs. 4.54, 4.55, and 4.56. The increase of R/B results in an increase in the surface area of the cylindrical boundary of the zone of influence contained within the central angle of rotation $\Delta\zeta$ (See Fig.4.6) . As the total earth pressure acting on this surface area increases , it becomes a dominant factor in augmenting the earth pressure on the pile shaft , especially for $\beta < 0$ (i.e. the terminal radial surface is above the pile shaft level).

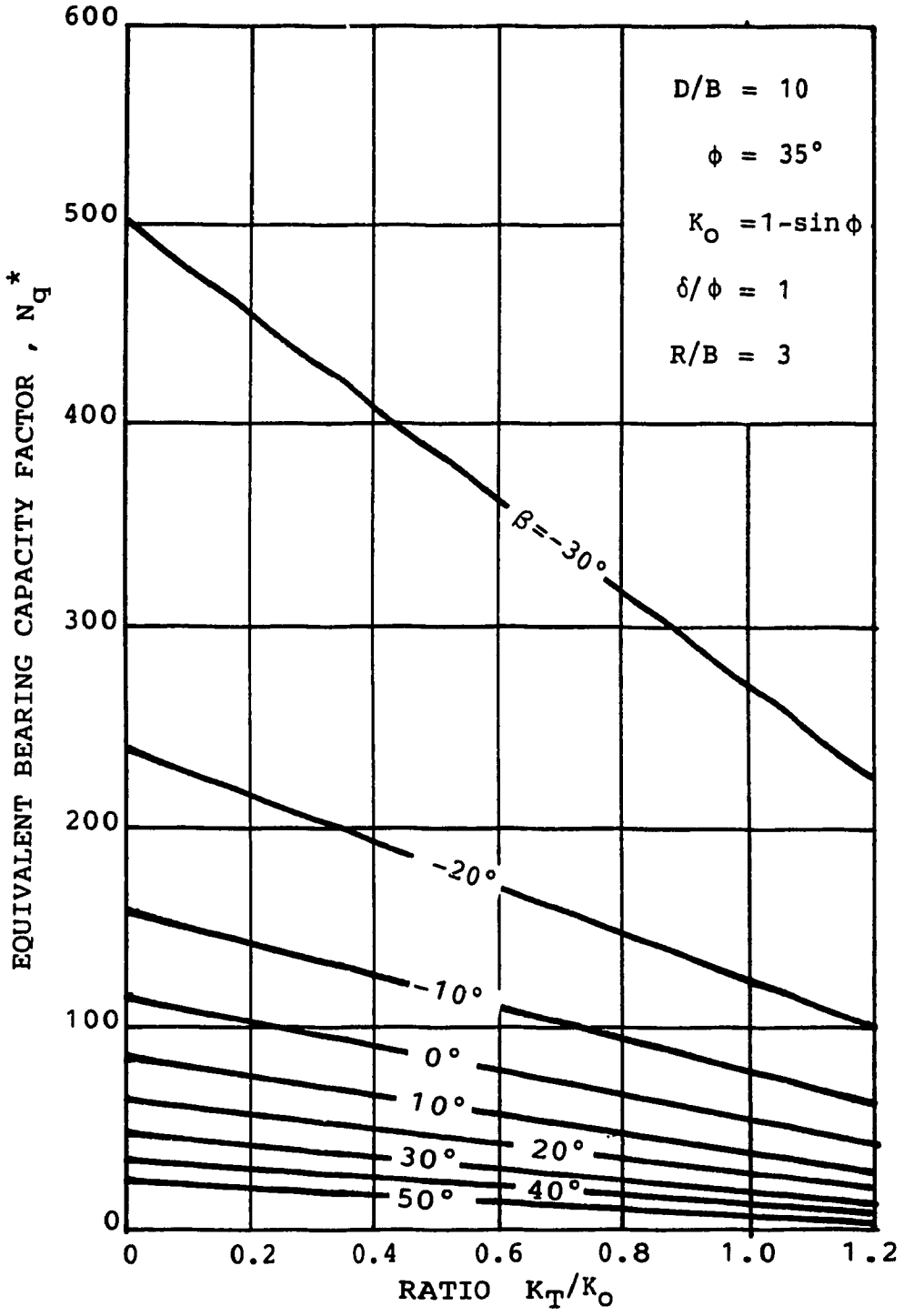

Fig. 4.45 Effect of Assumed K_T/K_0 Ratio on Point Resistance (D/B=10)

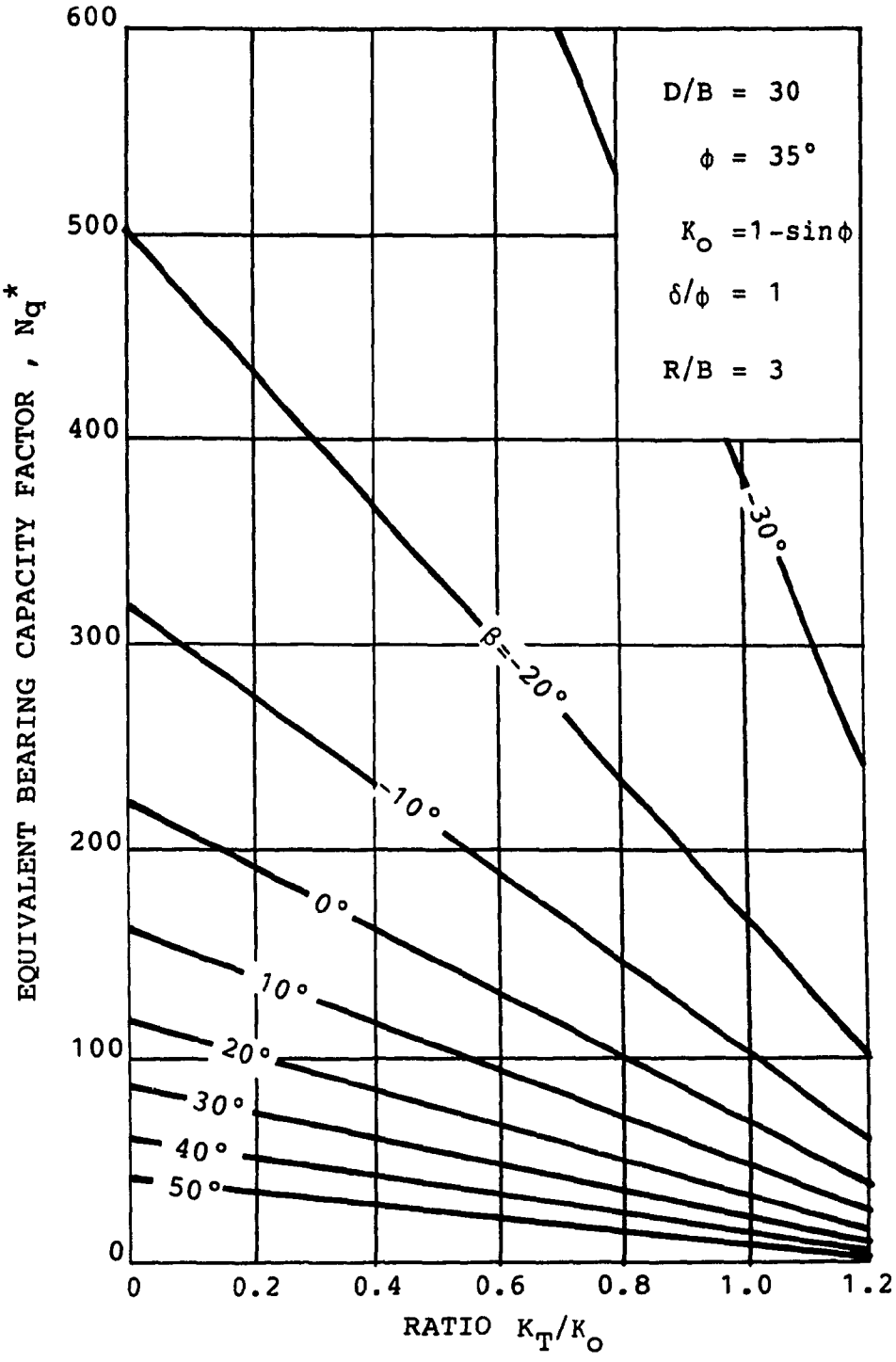

Fig. 4.46 Effect of Assumed K_T/K_o Ratio on Point Resistance (D/B=30)

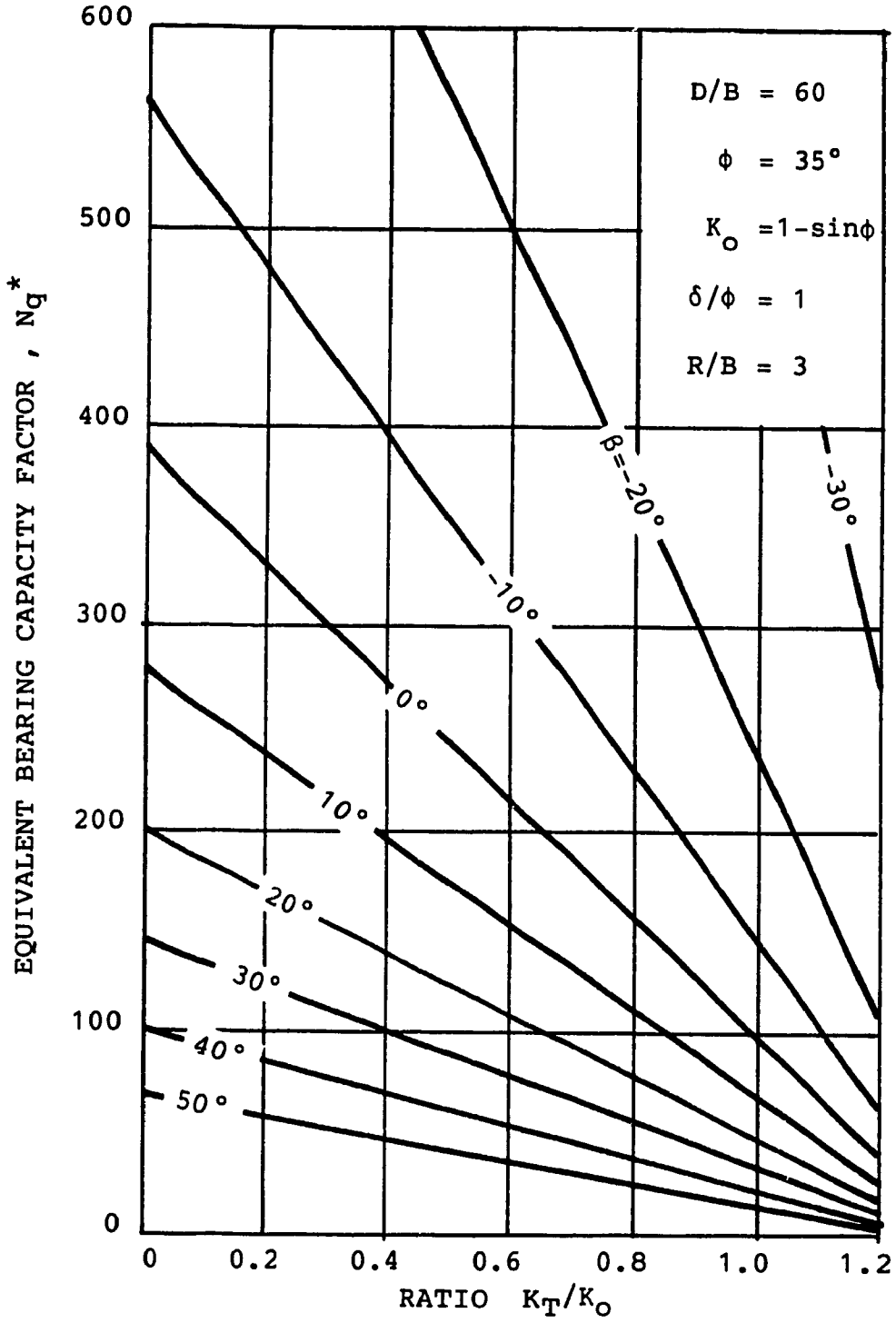

Fig. 4.47 Effect of Assumed K_T/K_o Ratio on Point Resistance (D/B=60)

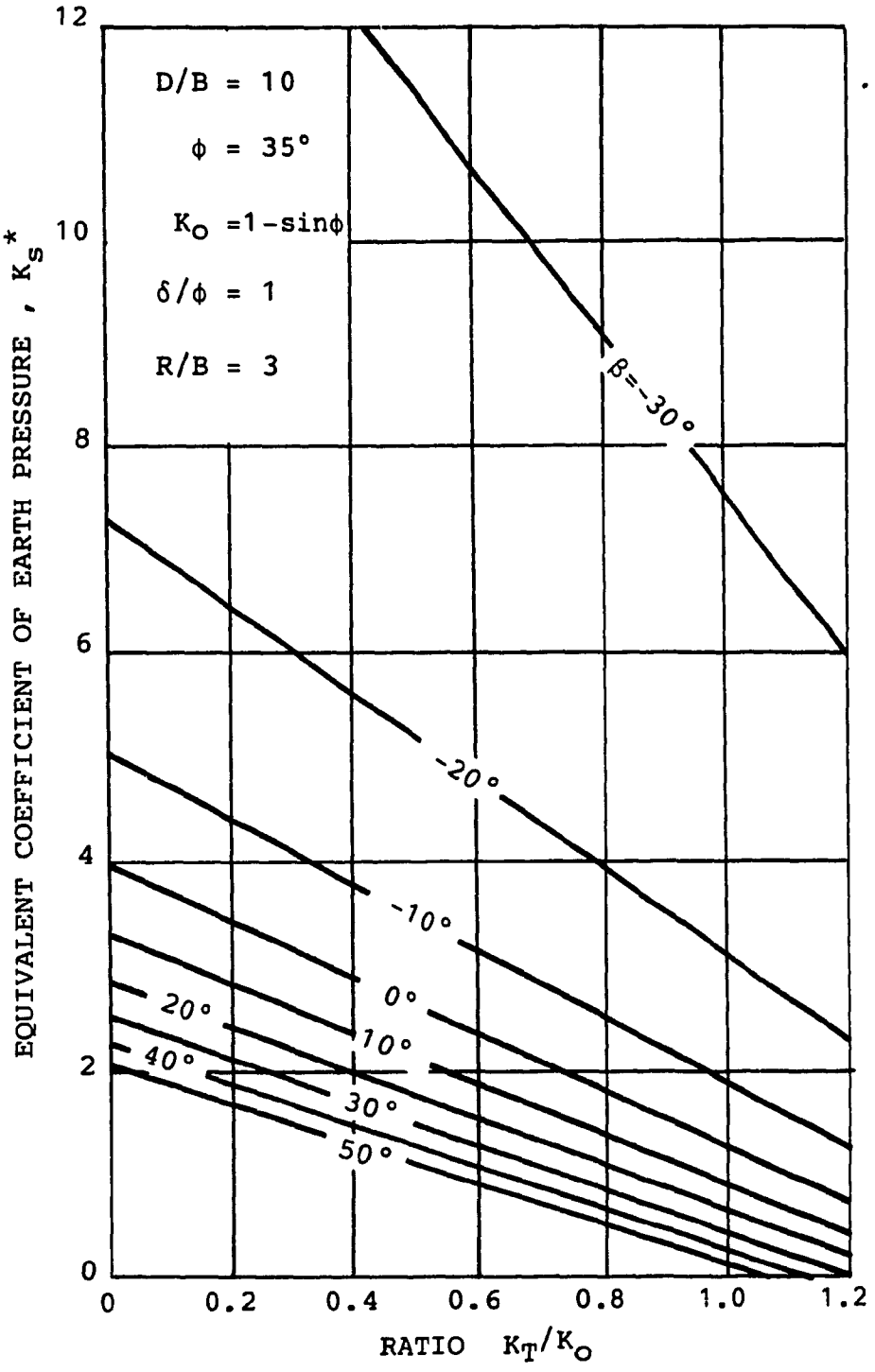

Fig. 4.48 Effect of Assumed K_T/K_o Ratio on Skin Friction (D/B=10)

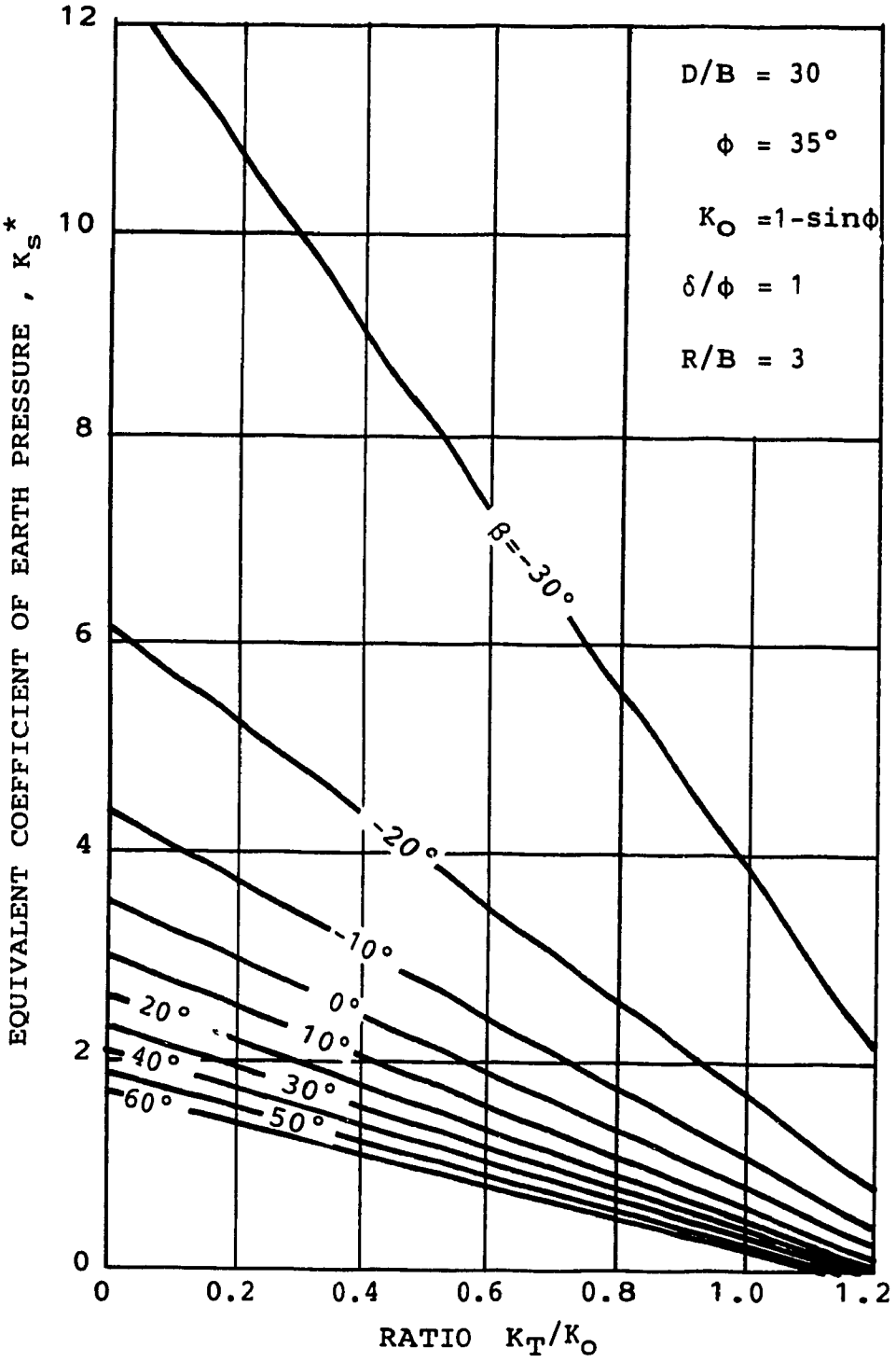

Fig. 4.49 Effect of Assumed K_T/K_0 Ratio on Skin Friction (D/B=30)

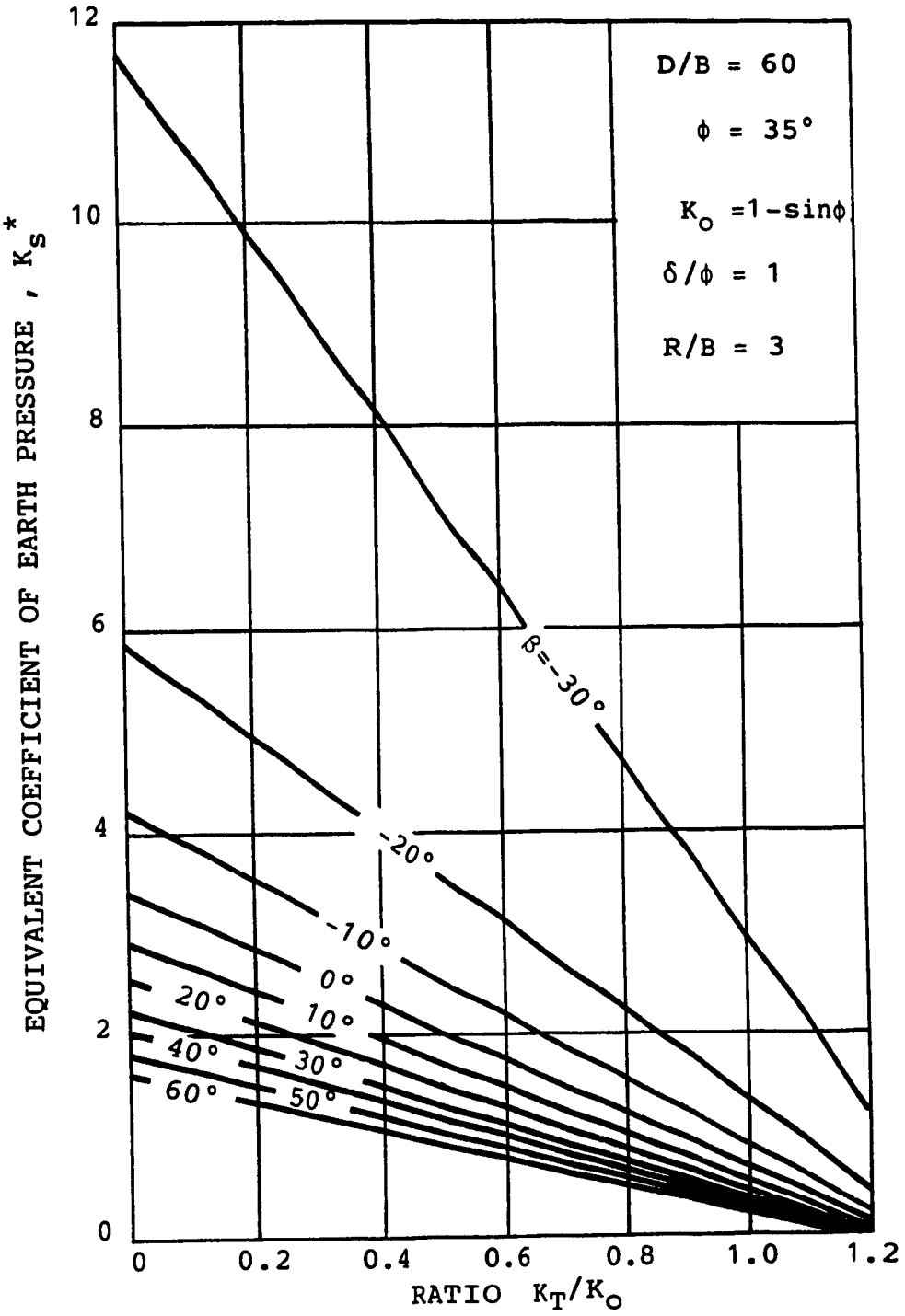

Fig. 4.50 Effect of Assumed K_T/K_o Ratio on Skin Friction (D/B=60)

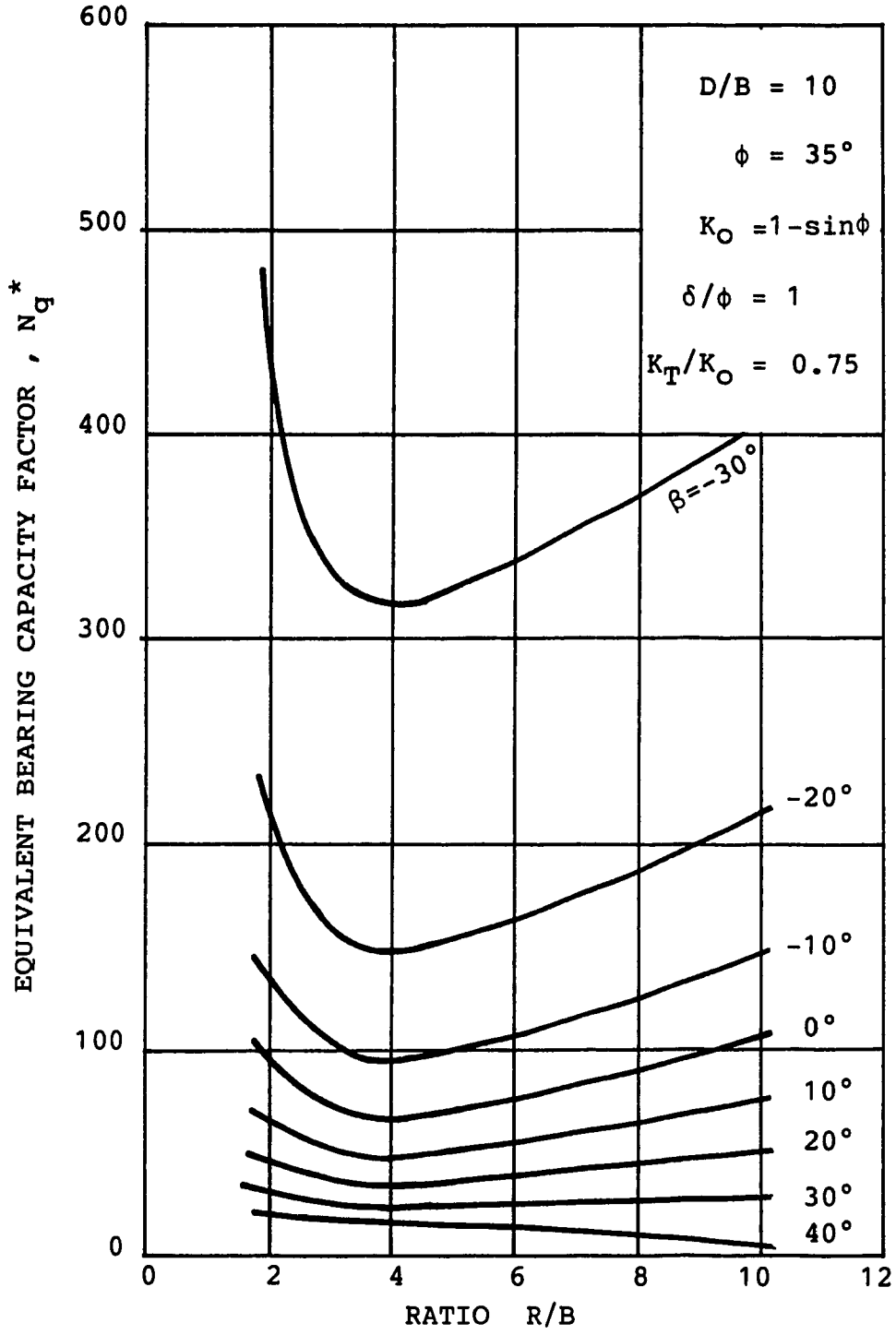

Fig. 4.51 Effect of Radius of Influence on Point Resistance (D/B=10)

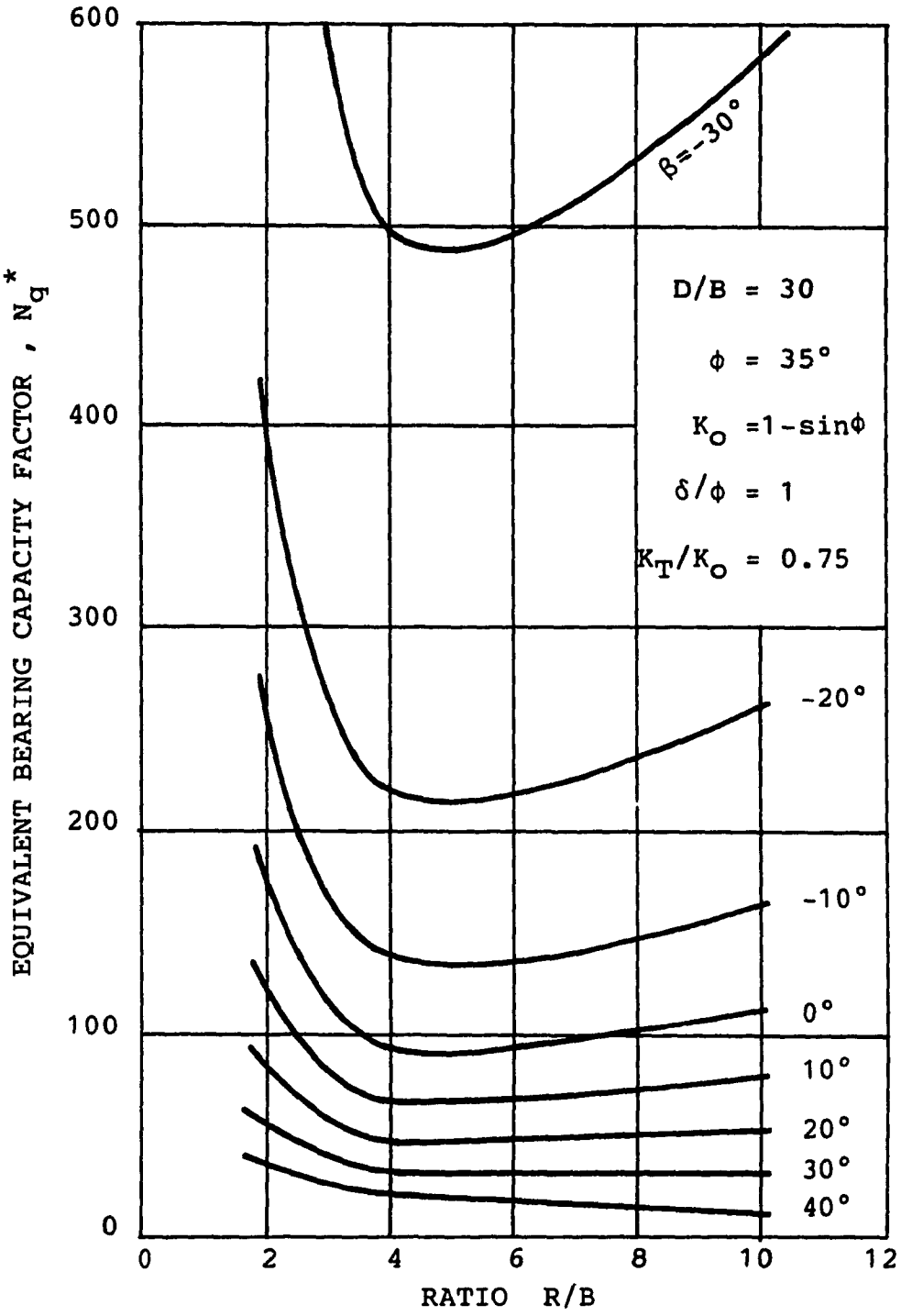

Fig. 4.52 Effect of Radius of Influence on Point Resistance (D/B=30)

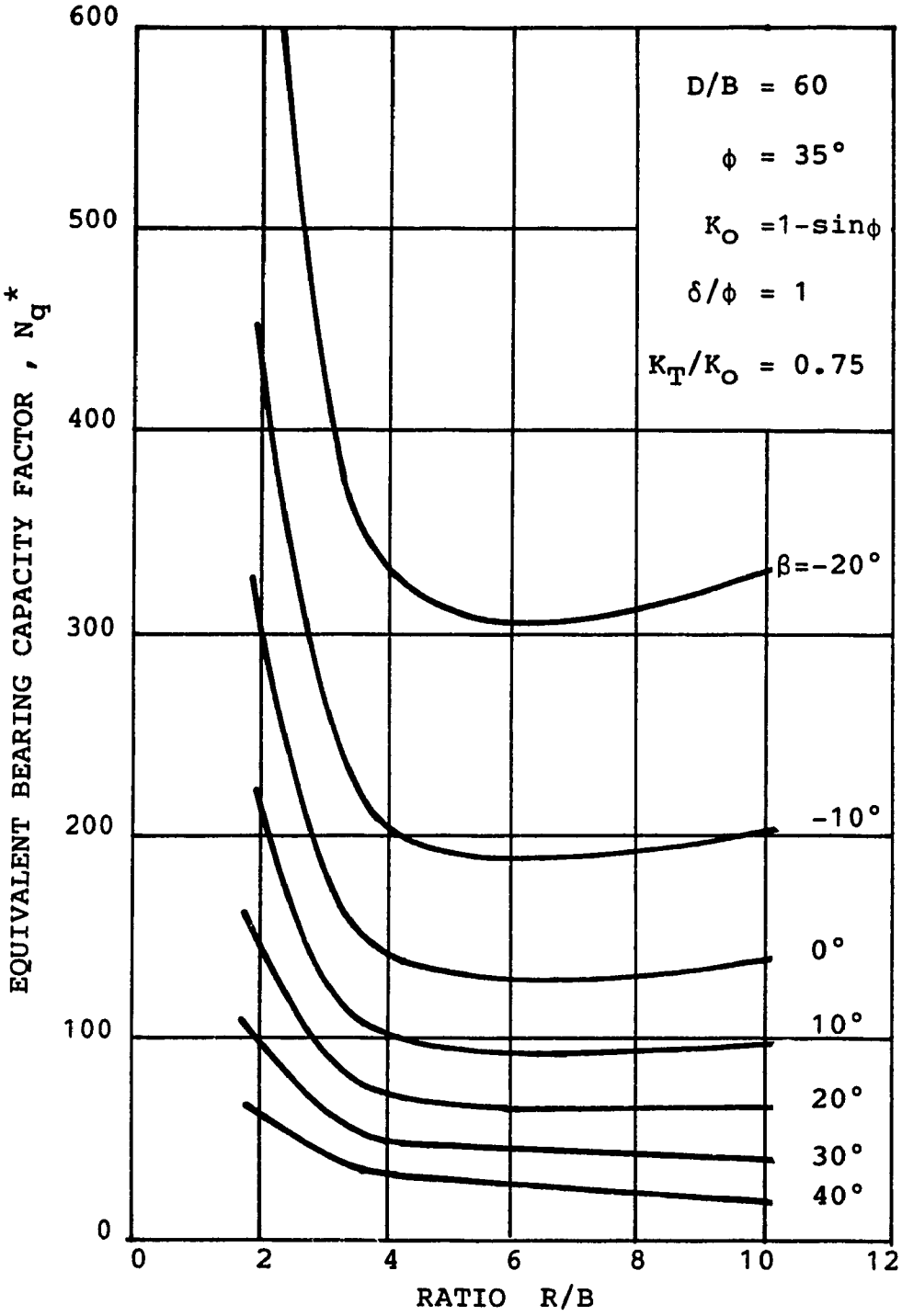

Fig. 4.53 Effect of Radius of Influence on Point Resistance (D/B=60)

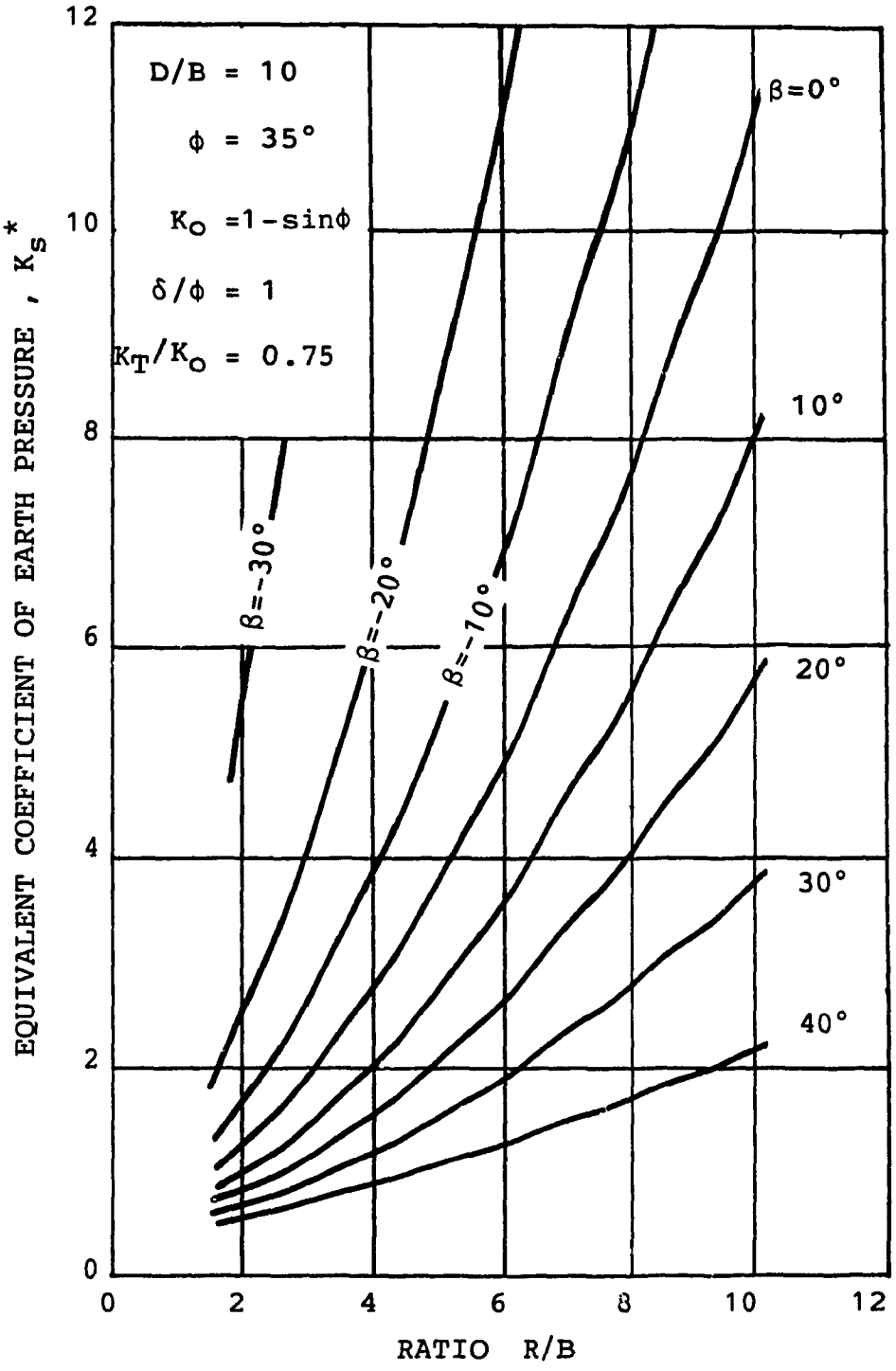

Fig. 4.54 Effect of Radius of Influence on Skin Friction (D/B=10)

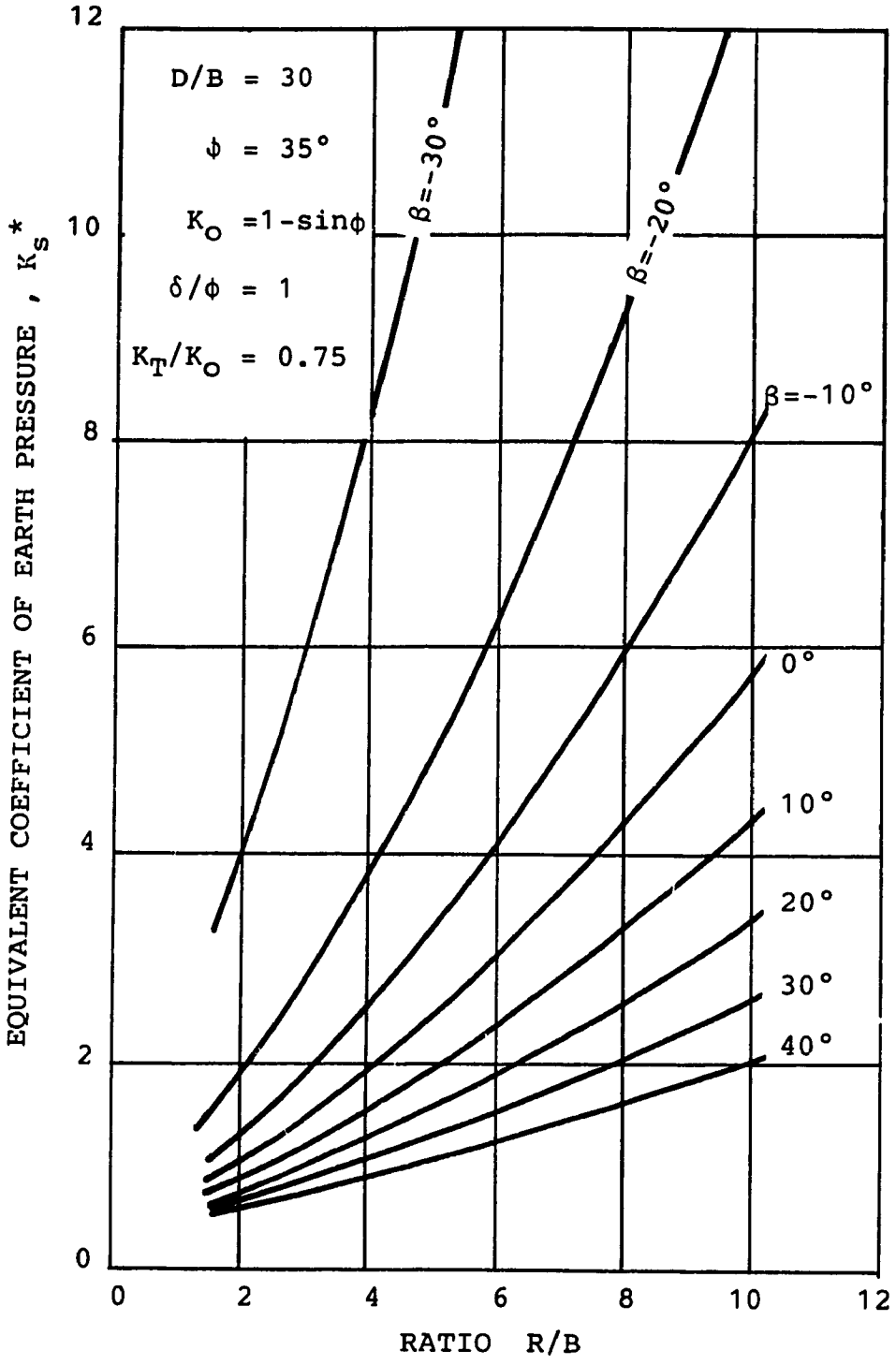

Fig. 4.55 Effect of Radius of Influence on Skin Friction (D/B=30)

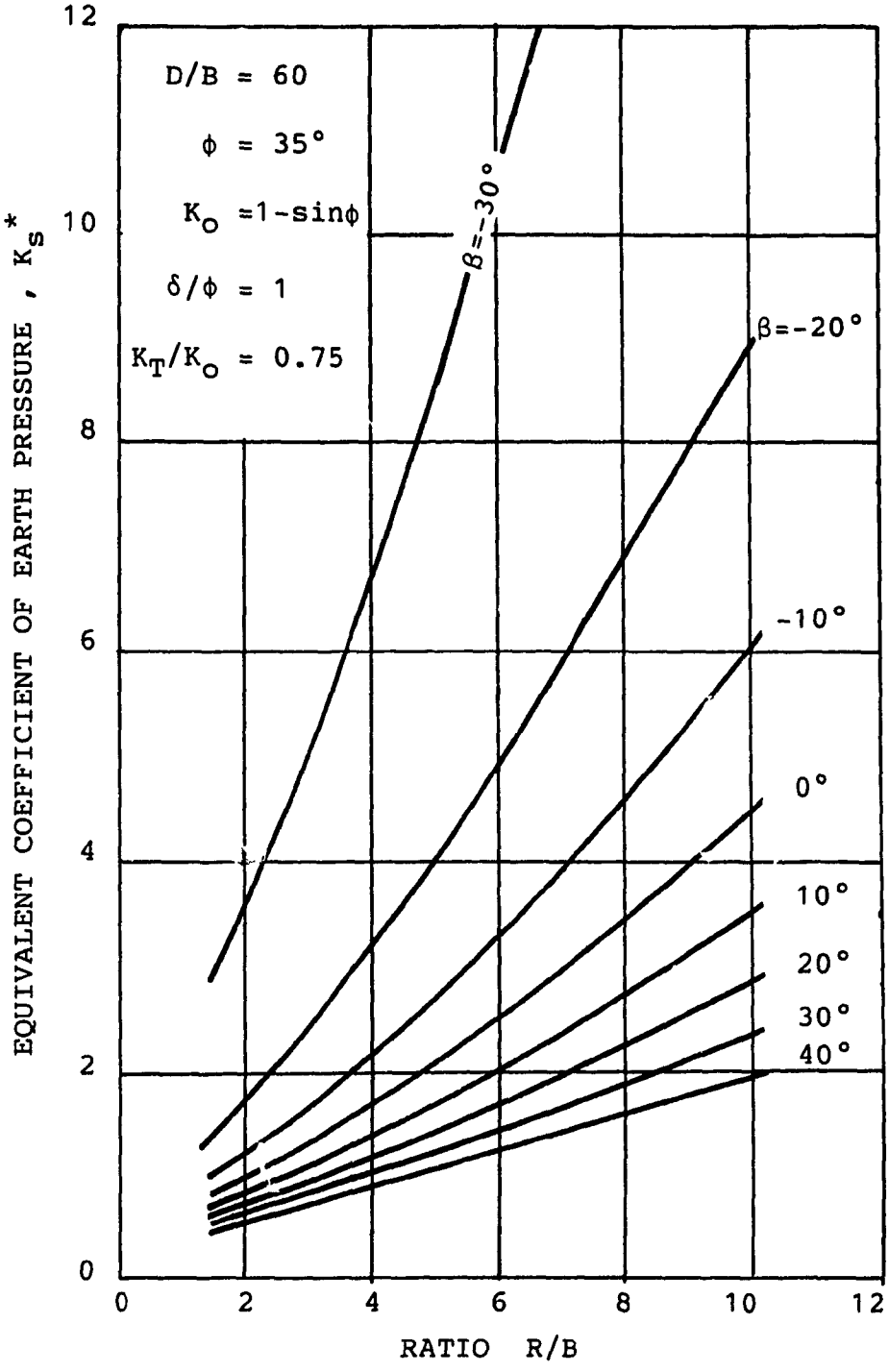

Fig. 4.56 Effect of Radius of Influence on Skin Friction (D/B=60)

4.5 EFFECT OF SLOPE OF TERMINAL RADIAL SURFACE β

4.5.1 General

So far, the effect of β on N^*_q and K^*_s was shown with each of the parameters ϕ, D/B, K, δ/ϕ, K_T/K_o and R/B . It can be seen that regardless of the parameter involved, N^*_q and K^*_s decrease as β becomes more positive (i.e., the terminal radial surface moves downwards from the pile tip level). The significance of this trend will be further studied in details in subsequent sections.

4.4.2 Equivalent bearing capacity factors N^*_q

The unit point resistance q_p of a single pile in sand is conventionally expressed as:

$$q_p = \sigma'_o \; N_q \qquad \text{... (4.21)}$$

In Eq. (4.21), q_p is expressed in the form of a product of two factors; the first factor σ'_o having the unit of pressure, indicates the effective vertical stress at the level of the pile tip. The second factor, N_q, is dimensionless and referred to as the bearing capacity factor. The expression for q_p may exist in alternate forms such as in Meyerhof's theory (1951):

$$q_p = \left(\frac{1}{2}\gamma B\right) N_{\gamma q} \qquad \text{... (4.22)}$$

or in Hu's (1965) and Durgunoglu and Mitchell's (1973):

$$q_p = (\gamma B)\, N_{\gamma q} \qquad \text{... (4.23)}$$

where

B = foundation width

$N_{\gamma q}$ = a resultant bearing capacity factor, combining N_q and N_γ

Or in Vesic's theory (1977):

$$q_p = \sigma_m N_\sigma \qquad \ldots (4.24)$$

where

$\sigma_m = \left(\frac{1 + 2K_o}{3}\right)\sigma'_o$ = mean normal ground stress

N_σ = a bearing capacity factor.

In addition, with the introduction of the critical depth concept (Kerisel, 1961; Vesic, 1967), the effective stress σ'_o in Eq. (4.21) was postulated as constant below a certain relative depth, depending on the relative density of sand (Poulos and Davis, 1980; Canadian Foundation Engineering Manual, 1985). As a result, care must be exercised when comparing bearing capacity factors from different theories. In order to avoid confusion and develop a meaningful comparison among numerous bearing capacity factors, it is proposed here to adopt an equivalent form of Eq. (4.19) as a common definition of the unit point resistance q_p of a single pile in sand.

$$q_p = \sigma'_o N^*_q \qquad \ldots (4.25)$$

where

$\sigma'_o = \gamma D$ = effective overburden pressure at the pile tip level

N^*_q = an equivalent bearing capacity factor.

From Eq. (4.25):

$$N^*_q = \frac{q_p}{\sigma'_o} \qquad \ldots (4.26)$$

The equivalent bearing capacity factor N^*_q may be deduced, for instance, from

Meyerhof's theory (1951) as:

$$N_q^* = \frac{1}{2}\frac{N_{\gamma q}}{\left(\frac{D}{B}\right)} \qquad \text{... (4.27)}$$

or from Hu's (1965) and Durgunoglu and Mitchell's (1973) theories as:

$$N_q^* = \frac{N_{\gamma q}}{\left(\frac{D}{B}\right)} \qquad \text{... (4.28)}$$

In the case of Vesic's theory (1977), N^*_q is given by:

$$N_q^* = \left(\frac{1 + 2K_o}{3}\right) N_\sigma \qquad \text{... (4.29)}$$

On the basis of Eq. (4.19) or (4.25), N^*_q can be also calculated from available semi-empirical design recommendations or empirical correlation charts (Meyerhof, 1976; Poulos and Davis, 1980; Canadian Foundation Engineering Manual, 1985; Coyle and Castello, 1981).

4.5.3 Modes of variation of N^*_q with depth

Table 4.2 presents a classification of important bearing capacity theories based on the trend of variation of N^*_q with the relative depth D/B. It can be seen that three major groups emerge, depending on whether their calculated values of N^*_q increase, decrease, or remain constant with D/B. It is important to observe that most recent theories and design charts, as found in group III, indicate N^*_q decreases with the relative depth D/B. Furthermore, except for Berezantzev's theory and the empirical correlation chart of Coyle and Castello, authors in group III took into account the effect of critical depths (Meyerhof, 1976; Poulos and Davis, 1980; Canadian Foundation Engineering Manual, 1985) or the soil compressibility in their theories (Vesic, 1977). These two factors are conspicuously absent from theories in group I

Table 4.2: Classification of Bearing Capacity Theories Based on Mode of Variation of N_q^* with Depth

N_q^*	AUTHOR	β (degrees)	
GROUP I: N_q^* is constant with D/B	TERZAGHI (1943)	0	Sign Convention for β 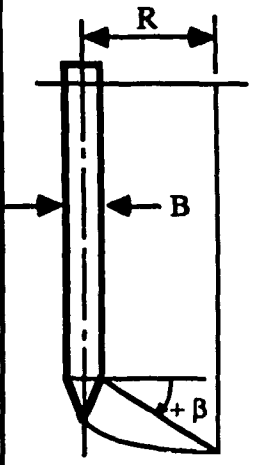
	VESIC (1967)	135–2.4ϕ	
	JANBU (1974)	−15→+15	
GROUP II: N_q^* increases with D/B	MEYERHOF (1951)	0→−90	
	SKEMPTON ET AL. (1953)	0	
	HU (1965)	0→−ϕ	
	DURGUNOGLU & MITCHELL (1973)	0→−ϕ	
GROUP III: N_q^* decreases with D/B	BEREZANTZEV ET AL. (1961)	0	REMARK * = β is not available due to empirical or semi-empirical approach
	MEYERHOF (1976)	*	
	VESIC (1977)	+90	
	POULOS & DAVIS (1980)	0	
	COYLE & CASTELLO (1981)	*	
	CANADIAN FOUNDATION ENGINEERING MANUAL (1985)	0	

and group II (Table 4.2). A review of basic assumptions used by authors in these two groups also revealed that for a given angle of shearing resistance ϕ, the assumed failure surfaces are either unchanged with depth (i.e., group I) or allowed to vary such that the terminal radial plane moves upwards toward the foundation shaft (i.e., group II). In addition, the shearing resistance along the failure surfaces are assumed fully mobilized (i.e., a general shear failure). Is it possible that these two basic assumptions, shared by all theories in group I and group II, result in N^*_q values either constant or increasing with depths, a trend contradicting those obtained by authors in group III? This question will be dealt with in the next section, using the proposed three dimensional model.

4.5.4 Justification for Model Parameters

As described in details in Section 4.3, the proposed model is capable of simulating the punching shear failure by incorporating a variable failure mechanism with depth and a variable degree of shearing resistance mobilization along the assumed critical shear surfaces. Theoretically, it can predict both the point resistance, Q_p, and skin friction, Q_s, for a single pipe pile driven in a homogeneous sand deposit if the following 8 parameters are known, namely: ϕ, B, D, δ, K_o, R, K_T, and β (see Section 4.4 for definitions). Apart from the first four parameters, which are commonly encountered in conventional bearing capacity theories of deep foundations and relatively easy to estimate, the coefficient of earth pressure at rest K_o may be difficult to evaluate, requiring appropriate field measuring techniques (i.e., pressure meters). The two parameters R and K_T are introduced into the model to allow the skin friction Q_s to be calculated simultaneously with point resistance Q_p in the same failure mechanism. Their numerical values are assumed based on the following justifications:

a. Assumption on radius of influence R

The radius of influence usually denotes the radius, measured from the central axis of the pile, of the cylindrical envelope which delineates the boundary between the disturbed and

undisturbed soil surrounding the pile. This radius of influence R was found to depend on the pile size, the initial density of the sand, pile installation methods, and pile roughness (Meyerhof, 1959; Robinsky and Morrison, 1964; Broms, 1966). Table 4.3 summarizes some typical measured values of the radius of influence R. The zone of influence generally extends laterally to a distance ranging from 2B to 6B from the pile axis, and longitudinally downwards from 2B to 5B from the level of the pile tip. On the other hand, the radius of influence inferred from conventional bearing capacity theories are mostly found to be either a function of the angle of internal friction ϕ or, in a few cases, a function of ϕ and the relative depth D/B above certain depths (see Table 4.4). The inferred values of R/B from various theories were plotted in Fig. 4.57. As Berezantzev's bearing capacity theory has been extensively verified by field load tests (Norlund, 1963; Vesic, 1967) and gained wide acceptance among practical foundation designers (Poulos and Davis, 1980; Tomlinson, 1986), it is logical to adopt Berezantzev's theoretical expression for the ratio R/B as followed:

$$\frac{R}{B} = \frac{1}{2}\left(1 + \frac{\sqrt{2}\, e^{\left(\frac{\pi}{2}-\frac{\phi}{2}\right)\tan\frac{\phi}{2}}}{\sin\left(\frac{\pi}{4}-\frac{\phi}{2}\right)}\right) \qquad \text{... (4.30)}$$

Obviously, Eq. 4.30 represents only an approximation. In reality, the radius of influence probably diminishes with depth under increasing confining pressure. Further research is clearly needed to address the important effect of lateral earth pressure on the development of the zone of influence.

b. Assumption on equivalent coefficient of earth pressure K_T

The spatial distribution of lateral earth pressure acting on the tangential plane is generally unknown due to the complex behaviour of the sand surrounding the advancing pile tips. In case of vertical retaining walls which are curved in plane, Mackey (1966) assumed the earth

Table 4.3: Typical Values of Radius of Influence.

AUTHOR	$\frac{R}{B}$	$\frac{R_T}{B}$	D_R (%)	B (in.)
SCHULTZE (1952)	2	2	–	–
MEYERHOF (1959)	3→4	5	<30	–
SZÉCHY (1960)	2	–	–	–
KÉRISEL (1961)	2.5	1.75	94	12.6
ROBINSKY & MORRISON (1964)	3.3	3.3	17	1.16
	4.5	4.5	37	1.16
	2.5→3	2.5→3	17	1.42
	3.6→4	2.5→3	37	1.42
BROMS (1966)	3.5→6	3→5	–	–

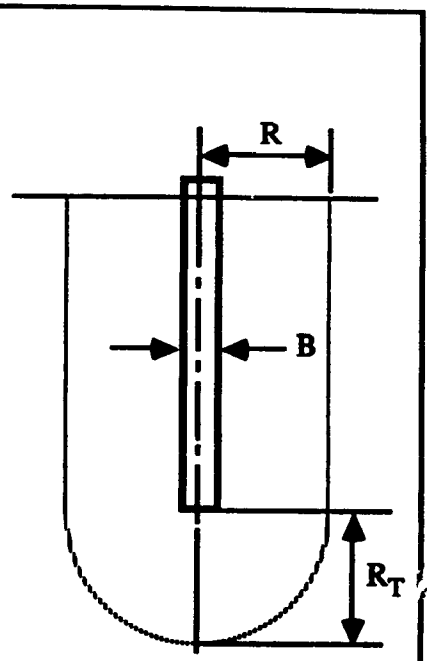

D_R = Relative density of sand

Table 4.4: Radius of Influence Inferred From Various Theories.

AUTHOR	β (degrees)	ϕ (degrees)			
		30	35	40	45
		R/B			
TERZAGHI (1943)	0.0	3.9	5.1	6.9	9.8
BISHOP ET AL. (1953)	0.0	2.0	-	-	4.5
BEREZANTZEV (1961)	0.0	2.5	2.8	3.1	3.5
HU (1965)	- ϕ	4.4	6.2	9.3	14.9
DURGONOGLU & MITCHELL (1973)	- ϕ	4.4 (D/B>2.3)	6.2 (D/B>4.0)	9.3 (D/B>7.4)	14.9 (D/B>44.8)
MEYERHOF (1951)	- ϕ	4.4 (D/B>8.3)	6.2 (D/B>13.7)	9.3 (D/B>23.8)	14.9 (D/B>44.8)
VESIC (1967)	135-2.4 ϕ	1.3	2.0	3.3	5.7
JANBU (1976)	-15 +15	5.3 4.1	7.2 5.1	10.1 6.7	15.1 9.1

Sign Convention for β

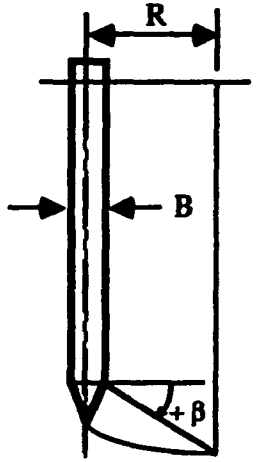

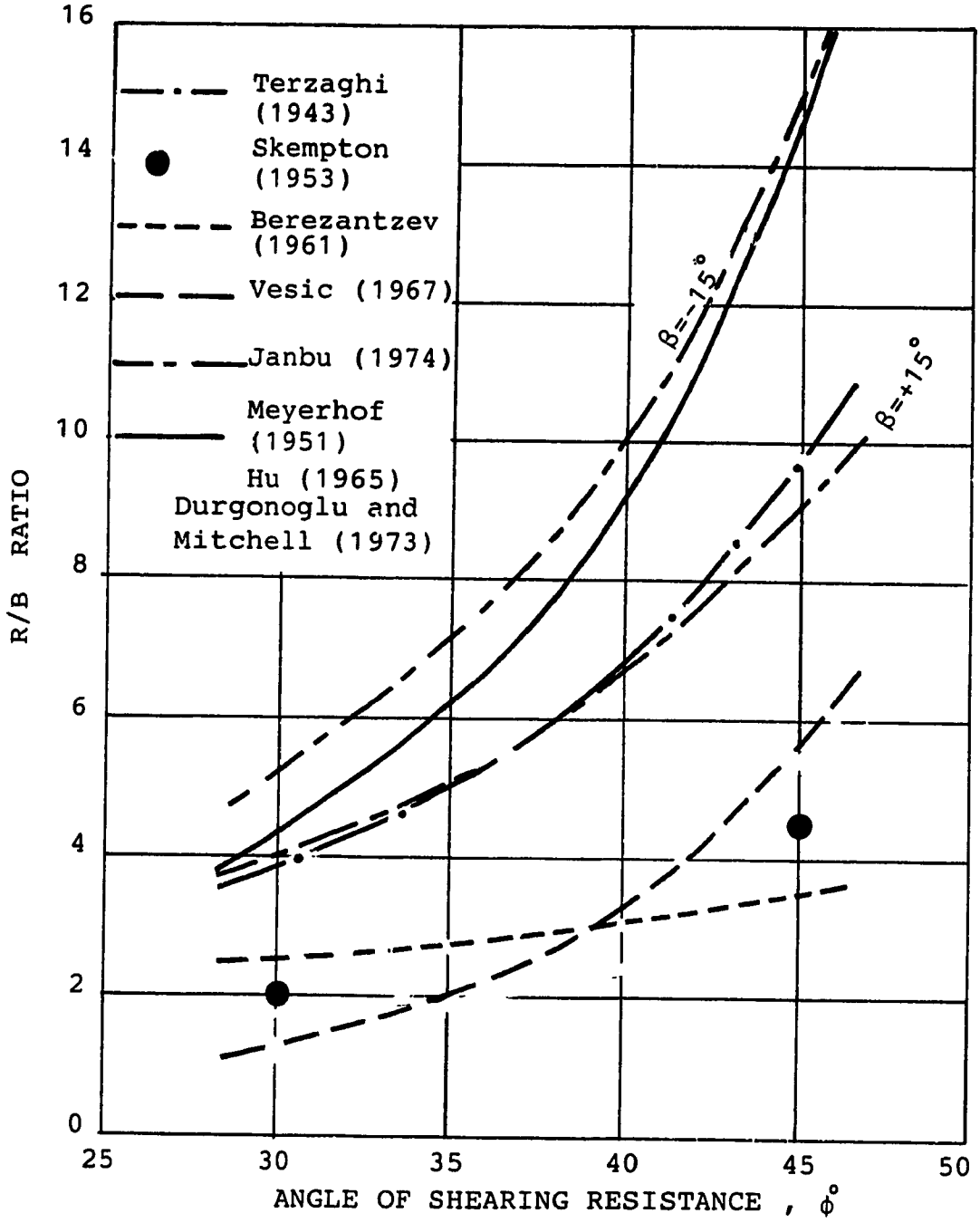

Fig. 4.57 A Comparison of Radius of Influence Inferred from Various Theories

pressure acting on the tangential plane varies linearly with depth, and has its coefficient equal to K_o. The situation, however, is quite different for a pile being driven into sand because, in this case, both lateral and vertical movements of sand occur within the zone of influence. According to Al-Awkati (1975), the sand flows around the pile shaft and "undergoes considerable extensional strains and unloading" as the pile is driven into a sand deposit. It can be qualitatively interpreted from Al-Awkati's conclusion that the earth pressure acting on the tangential plane may indeed decrease to an even lower magnitude than the at-rest condition.

Consequently, it is herein assumed that the effect of the earth pressure acting on the tangential plane may be replaced by an equivalent linear distribution of earth pressure with depth and having its coefficient K_T equal to the active coefficient of earth pressure K_A.

$$K_T = K_A = \frac{1 - \sin \phi}{1 + \sin \phi} \qquad \text{... (4.31)}$$

c. Assumption on slope β of terminal radial surface

The parametric study in Section 4.4 indicates that the angle β is a major factor affecting the magnitude of Q_p and Q_s. Except for the theories of Meyerhof (1951), Hu (1965) and Durgonoglu and Mitchell (1973), it can be seen in Table 4.2 that conventional bearing capacity theories mostly assume β to be a unique function of the angle of shearing resistance ϕ.

In Meyerhof's failure mechanism, β increases from 0° to the maximum value -90° as the foundation penetrates the soil from the ground surface to greater depths. Meanwhile, the variation of β with depths in Hu's and Durgunoglu and Mitchell's models also follow a similar trend as that in Meyerhof's, except that it varies in a narrower range from 0° to -ϕ°. The relationship between β, ϕ, and D/B in Meyerhof's model was demonstrated graphically by Scott (1963) and reproduced with some adaptations in Fig. 4.58. The same kind of relationship in Hu's and Durgonoglu and Mitchell's theories was plotted in Fig. 4.59. The construction of this figure was based on Eq. (4.31), derived from Hu's failure mechanism:

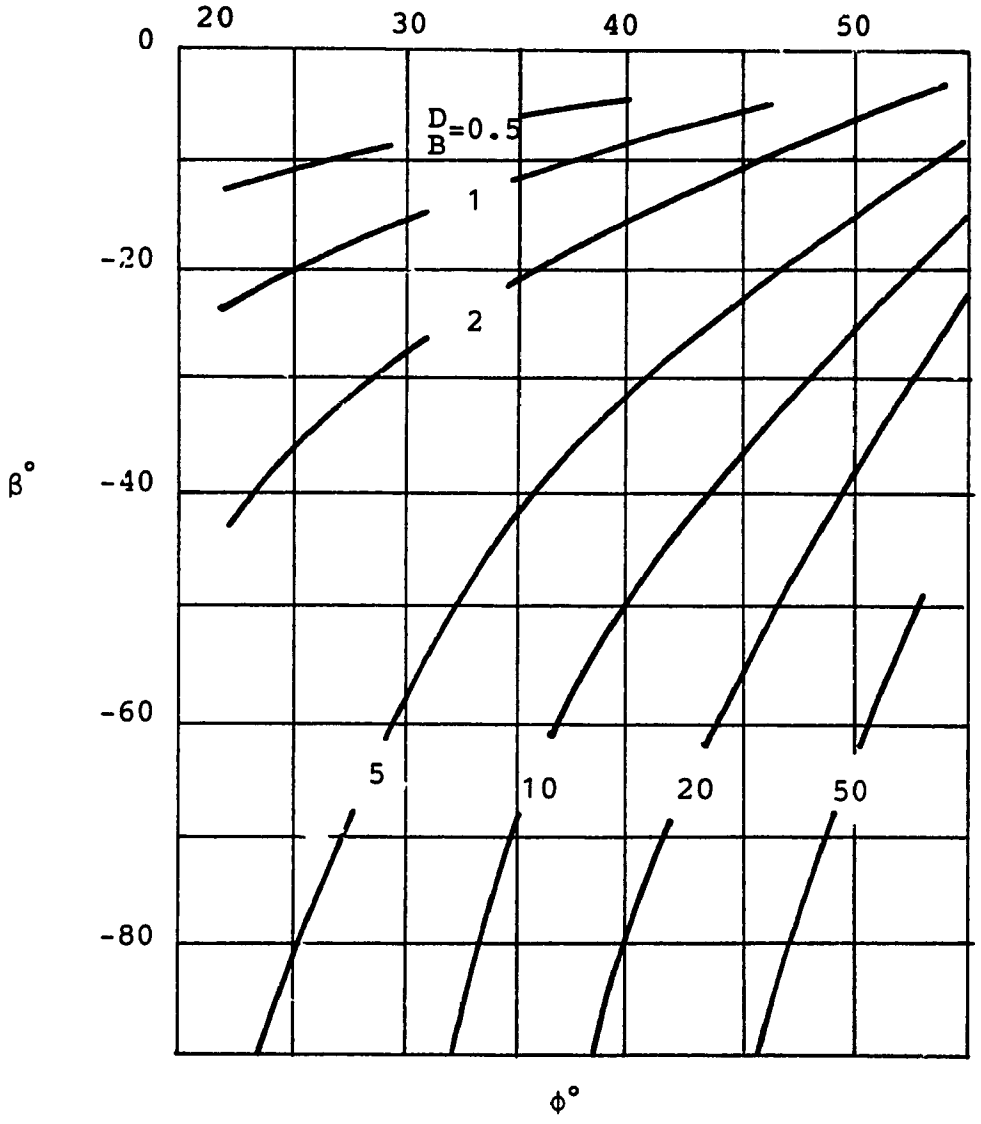

Fig. 4.58 Variation of β with Relative Depth and Angle of Shearing Resistance in Meyerhof's Theory (After Scott, 1963)

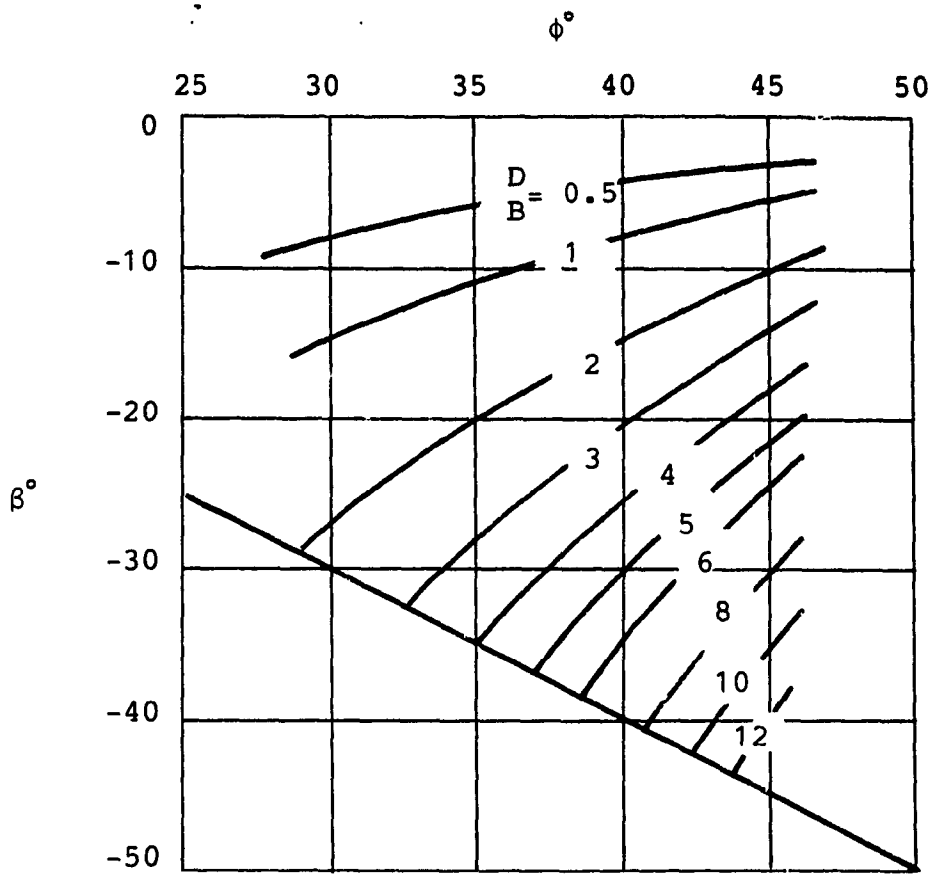

Fig. 4.59 Variation of β with Relative Depth and Angle of Shearing Resistance in Hu's Theory (Hu, 1965)

$$\sin\beta\, e^{\beta\tan\phi} = 2\left(\frac{D}{B}\right)\frac{\cos\left(\frac{\pi}{4}+\frac{\phi}{2}\right)}{e^{\left(\frac{3\pi}{4}-\frac{\phi}{2}\right)}} \qquad \ldots (4.32)$$

In the failure mechanisms proposed by Meyerhof, Hu, and Durgonoglu and Mitchell, the angle β becomes constant below a certain relative depth D/B which depends on the angle of shearing resistance ϕ. Once β is constant, the shape and the extent of the assumed failure surface remain unchanged with depth.

It is of interest to examine a few examples of the trend of variation with ϕ and D/B of β values deduced from recent theories, empirical and semi-empirical design recommendations for bearing capacity of piles in sands. This deduction of β was performed using the computer program TEMPO. The deduction procedure for each set of values of ϕ and D/B starts with running the program TEMPO, allowing β varying from -30.° to +80.° at 1.° interval. The angle β deduced from a given N^*_q can be found by linear interpolations among the N^*_q values computed from the computer run. In the examples, the following conditions were assumed:

- the sand deposit is homogeneous, dry with a unit weight equal to 100. lbs./ft.^{3}
- the pile diameter is 1.0 ft.
- $K_o = 1 - \sin\phi$
- the radius of influence R is given by Eq. (4.30)
- $K_T = K_A = \dfrac{1-\sin\phi}{1+\sin\phi}$
- $\delta/\phi = 1.$

The variation with ϕ and D/B of β deduced from N^*_q values of different authors, were shown in Figs. 4.60, 4.61, and 4.62. It can be seen from these figures that, for a given ϕ, the

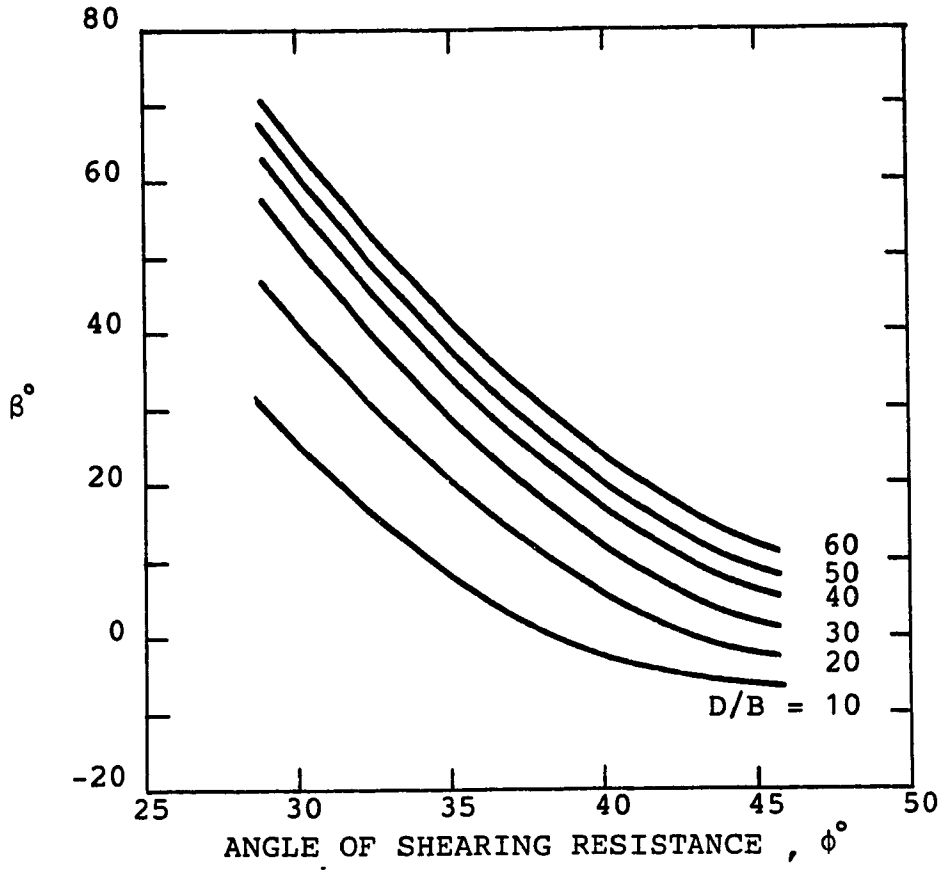

Fig. 4.60 Typical Variation of Deduced β with Relative Depth and Angle of Shearing Resistance (Based on Berezantsev, 1961)

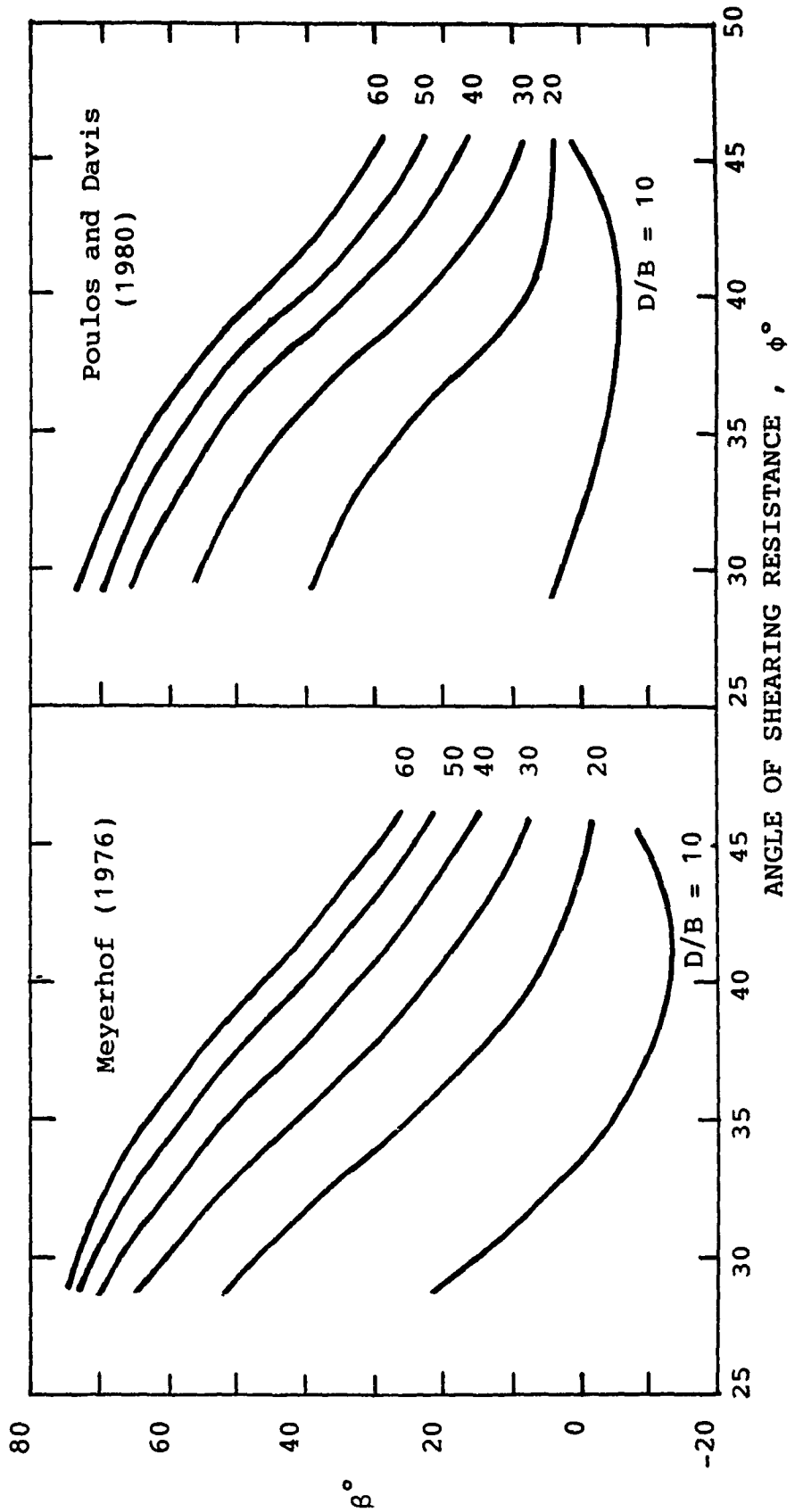

Fig. 4.61 Typical Variation of β with Relative Depth and Angle of Shearing Resistance (Deduced from Semi-Empirical Procedures)

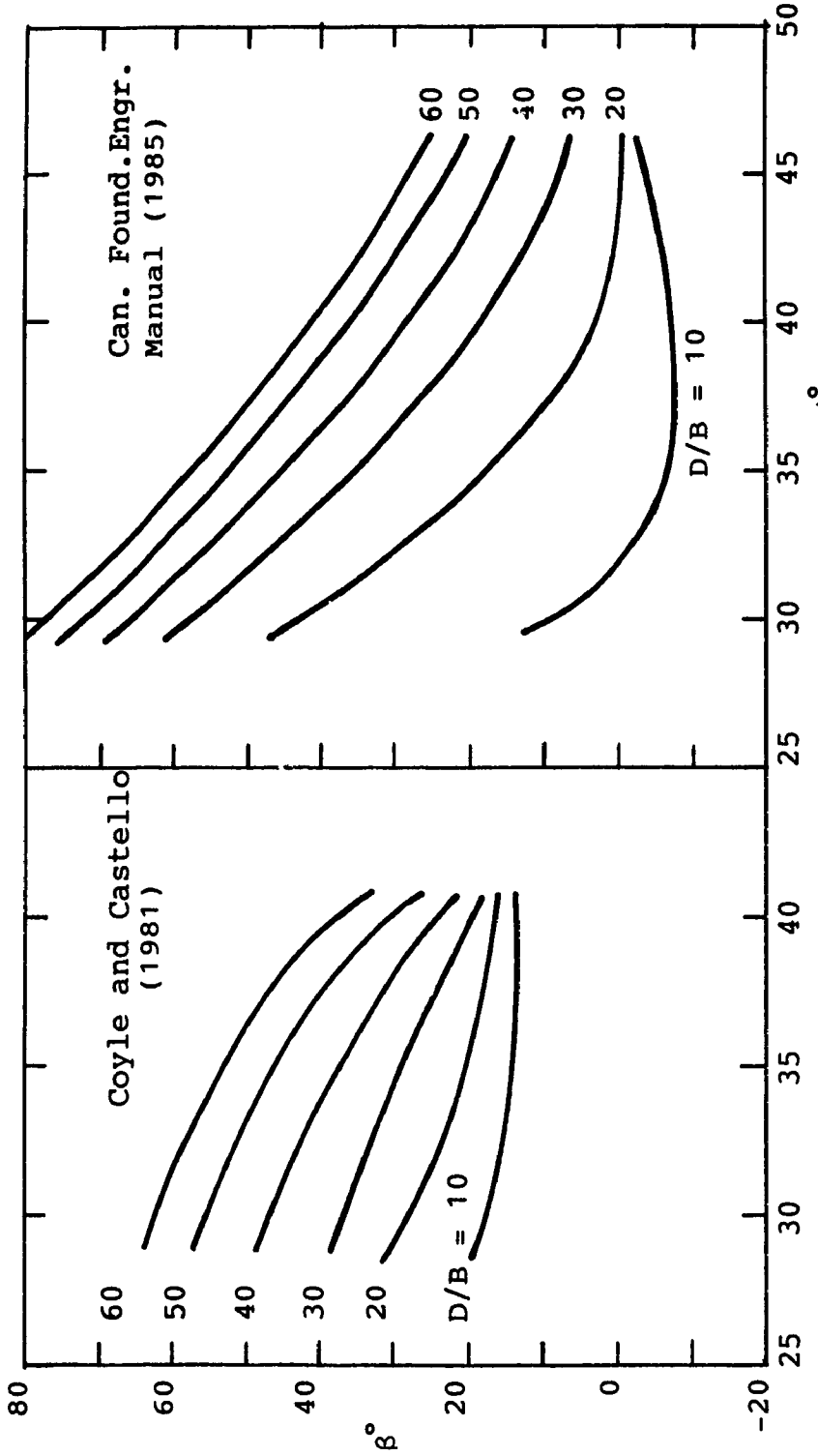

Fig. 4.62 Typical Variation of β with Relative Depth and Angle of Shearing Resistance (Deduced from Empirical and Semi-Empirical Procedures)

angle β increases positively with the relative depth D/B, indicating that the terminal radial surface moves downwards with respect to the pile tip level as the pile is driven to lower depths. This variation trend of β with the relative depth D/B is clearly in direct contrast to that postulated by Meyerhof (1951), Hu (1964), and Durgunoglu and Mitchell (1973), which indicates the terminal radial plane reverts upward towards the pile shaft.

Furthermore, experimental investigations into the shear failure mechanism of model piles by Vesic (1967) and Al-Awkati (1975) lent no support to the types of failure patterns assumed by Meyerhof (1951), Hu (1965), and Durgunoglu and Mitchell (1973). In fact, as the lateral confining pressure increases with depth, it is difficult to justify why the shear failure surfaces can remain exactly the same at all depths or revert upwards from the pile tip level. A more logical assumption is schematically illustrated in Fig. 4.63. As the pile is driven to different depths, the angle β becomes more positive (i.e., the terminal radial surface AC dips further downwards). The compressibility of sand under high confining pressure at lower depths is believed to be responsible for containing the "plasticised zone" development within a more restricted space below the pile tip (Janbu, 1974). On the whole, arguments from both theoretical and physical view points strongly support the assumption of a downward movement of the terminal radial surface from the pile tip level as the pile is advanced to lower depth in a homogeneous sand deposit.

Theoretically, it appears plausible to envisage the position of the terminal radial surface depends not only on ϕ and D/B, but also on the shaft angle of friction δ and the coefficient of earth pressure at-rest K_o of the sand deposit. Although it is conceivable to establish an explicit relationship relating β to ϕ, D/B, δ and K_o from extensive experimental investigations and the application of the proposed model, such a grand scheme is beyond the scope of this study. On the other hand, β may be deduced from the point resistance Q_p (or its equivalent bearing capacity factor N^*_q) using the proposed model, which subsequently allows the

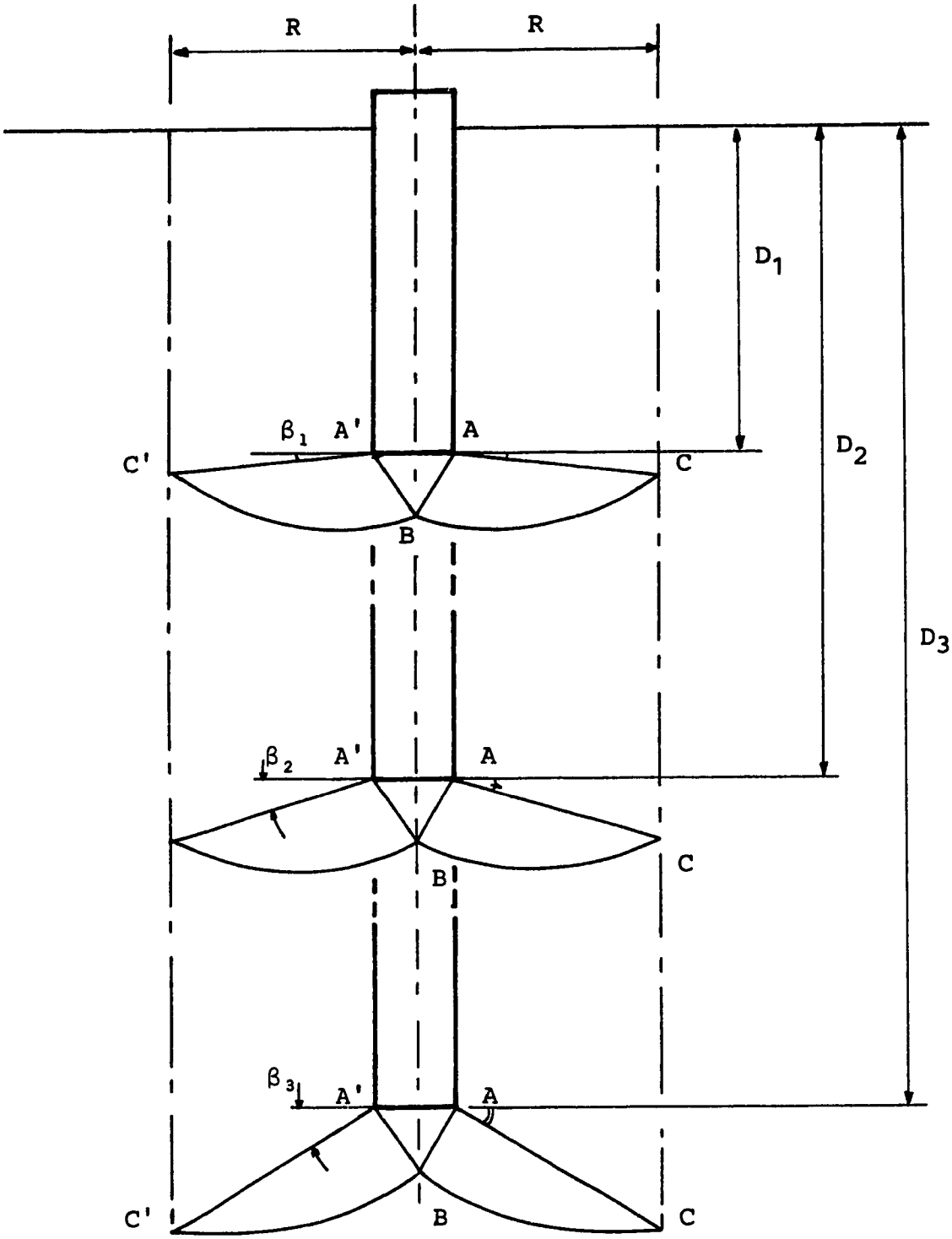

Fig. 4.63 A Proposed Mode of Variation of β with Depth

calculation of the skin friction Q_s once β is known. This approach of computing Q_s based on Q_p signifies a distinct departure from existing empirical methods. As a result, its validity as a rational method to estimate the skin friction will be carefully examined by applying the proposed model to seven representative pile load test series totaling up to 35 individual tests. They include two test series on model piles from this present study, three others from Vesic's investigation (Vesic, 1967) and two field load test series from Vesic (1967) and Tavenas (1971), respectively.

4.6 VERIFICATION OF MODEL

The verification process for each pile load test consists of the following steps:

1. Calculate the equivalent bearing capacity factor N^*_q from the measured tip load Q_p, using Eq. (4.19).

2. Run the computer program Tempo with the angle β varying from -40° to +80° at 2° intervals. Numerical values for intrinsic parameters used in the analysis are obtained from pertinent experimental and field data. These parameters include the pile embedment length D, the pile diameter B, the angle of shearing resistance ϕ of the soil, the angle of friction δ between the pile shaft and the soil, and the coefficient of earth pressure at-rest K_o. As for the model parameters K_T and R (i.e., the coefficient of earth pressure on the tangential plane and the radius of influence), they are given by equation 4.31 and 4.32, respectively.

3. Corresponding to the N^*_q value computed in step 1, the angle β and the equivalent coefficient of earth pressure K^*_s at the pile shaft, may be evaluated from the computer output by linear interpolations.

4. Finally, the skin friction Q_s can be calculated by Equation 4.20.

4.6.1 Verification Using Load Tests on Model Piles

Present Study

Back ground information on the two test series performed on 1.5 in. and 3. in. diameter model piles were detailed in chapter 3. Table 4.5 summarizes a typical set of numerical values used in the analysis and the computed skin friction Q_s at different depths for both model piles. As the value of the coefficient of lateral earth pressure K_o was unknown, the computation of Q_s at each depth was repeated with various assumed values starting with $K_o = 1 - \sin \phi$. The influence of K_o on the skin friction Q_s of both model piles at various pile embedment lengths were shown in Fig. 4.64. It can be seen in Fig. 4.65 that most data points lie within a narrow band of ± 10 percent deviation from the computed values of Q_s corresponding to $K_o = 0.45$ for both piles. This magnitude of K_o appears entirely congruent with the fact that due to the employed sand placement technique of raining sand from a height of at least 44 in., the sand deposit is not expected to remain in a normally consolidated condition, which may exist if the height of fall of sand is only a few inches. In addition. the validity of the present model is further strengthened because the deduced values of K_o were found essentially the same in both load test series (i.e., $K_o = 0.45$) where identical sand placement techniques were strictly adhered to.

The movement of the failure mechanism downward from the pile tip level, indicated by the angle β increasing positively with further pile penetration, is schematically shown in Fig. 4.66. The predicted earth pressure distribution also shows good agreement with measured values in pile test No. B-2 , as indicated in Fig. 4.67. Each experimental data point plotted in this figure represents an average value measured by a pair of pressure transducers located at about the same level on the pile shaft. As for pile test No. B-1, measurements of the upper pressure transducers No. 4 and No. 5 (see Table 3.5) appears in errors. This discrepancy was possibly due to a very slight tilting of the pile during the load test, in which it was unsupported over half of its length.

Table 4.5: Analysis of Load Tests on 1.5 in. and 3 in. Diameter Model Piles.

Type of Model Pile	Pile Test No.	Nominal Depth, D (in.)	Relative Depth D/B	Measured Point Resistance, Q_p (lbs.)	Equivalent Bearing Capacity Factor, N_q^*	Deduced Angle β (Deg.)	Computed Skin Friction, Q_s (lbs.)
1.5 in. Diameter	A-1	15	10	300	196.4	-4.0	105
	A-2	30	20	625	204.6	3.1	287
	A-3	45	30	965	210.6	8.6	535
	A-4	60	40	1320	216.0	13.0	848
3.0 in. Diameter	B-1	30	10	1408	115.2	8.4	575
	B-2	60	20	2681	109.7	18.0	1664

REMARK:

i) Numerical values used in the analysis:

D_R=65.3%
ϕ =39.3 °(From Fig. 3.11 for e = 0.668)
γ =99.6 pcf
δ =42 ° (From Fig. 3.11 for e = 0.668)
K_o=0.45 (Assumed)
K T=0.244 (Eq. 4.31)
R/B=3.06 (Eq. 4.30)

ii) For 1.5 in. diameter pile, measured values of Q_p were obtained from best fitted curve in Fig. 3.24.

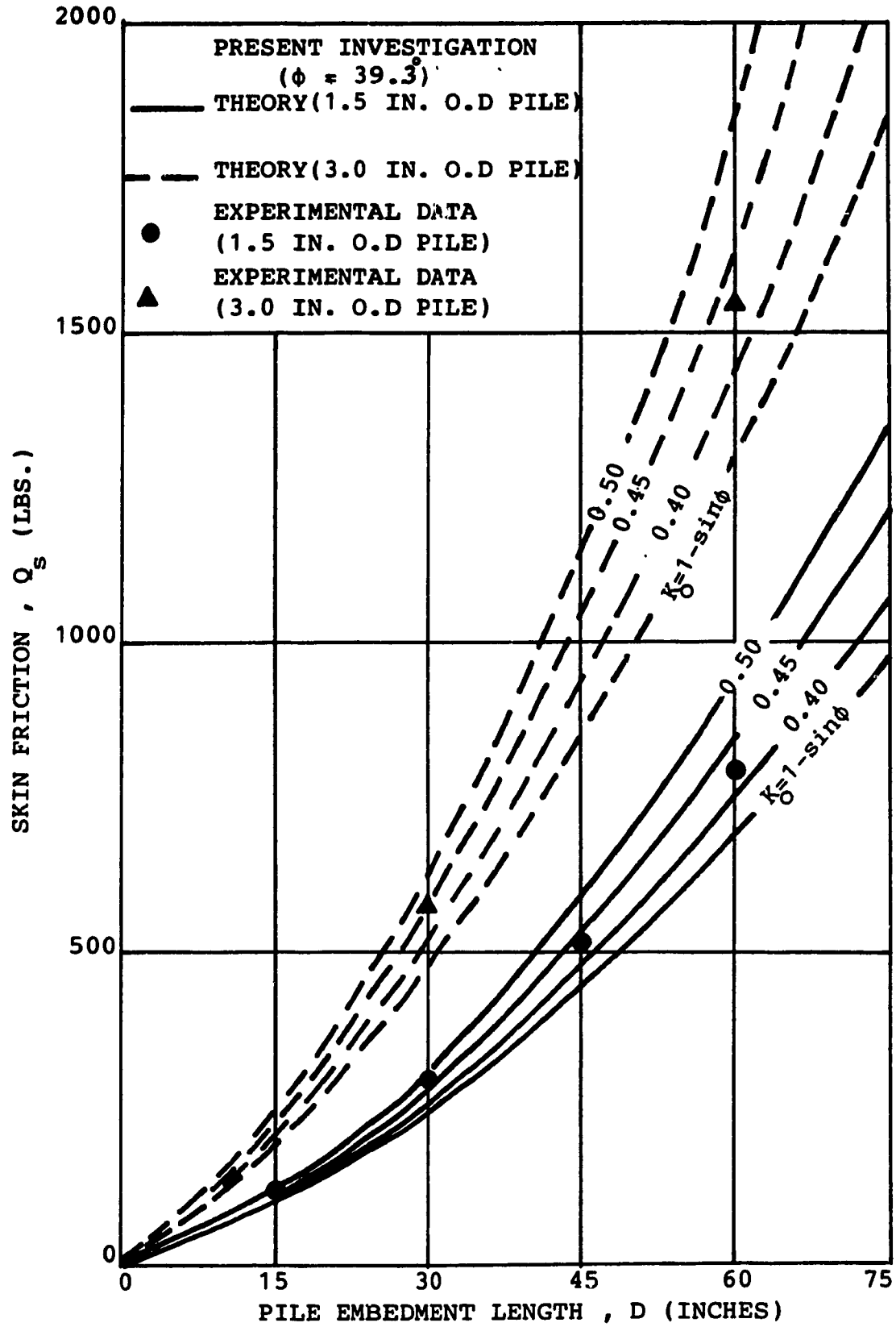

Fig. 4.64 Effect of K_o in Analysis of Skin Friction (Present Study)

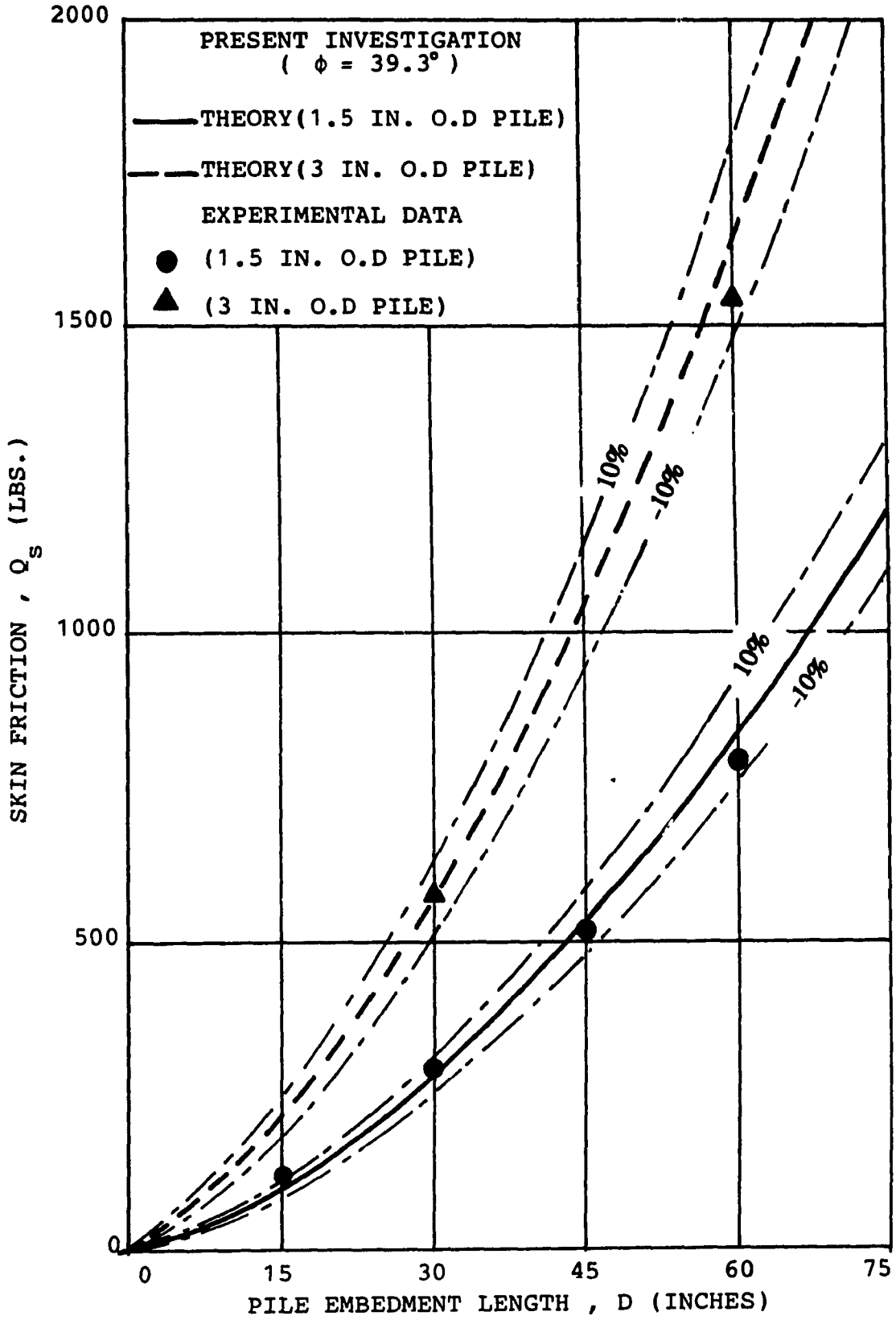

Fig. 4.65 Results of Analysis of Skin Friction (Present Study)

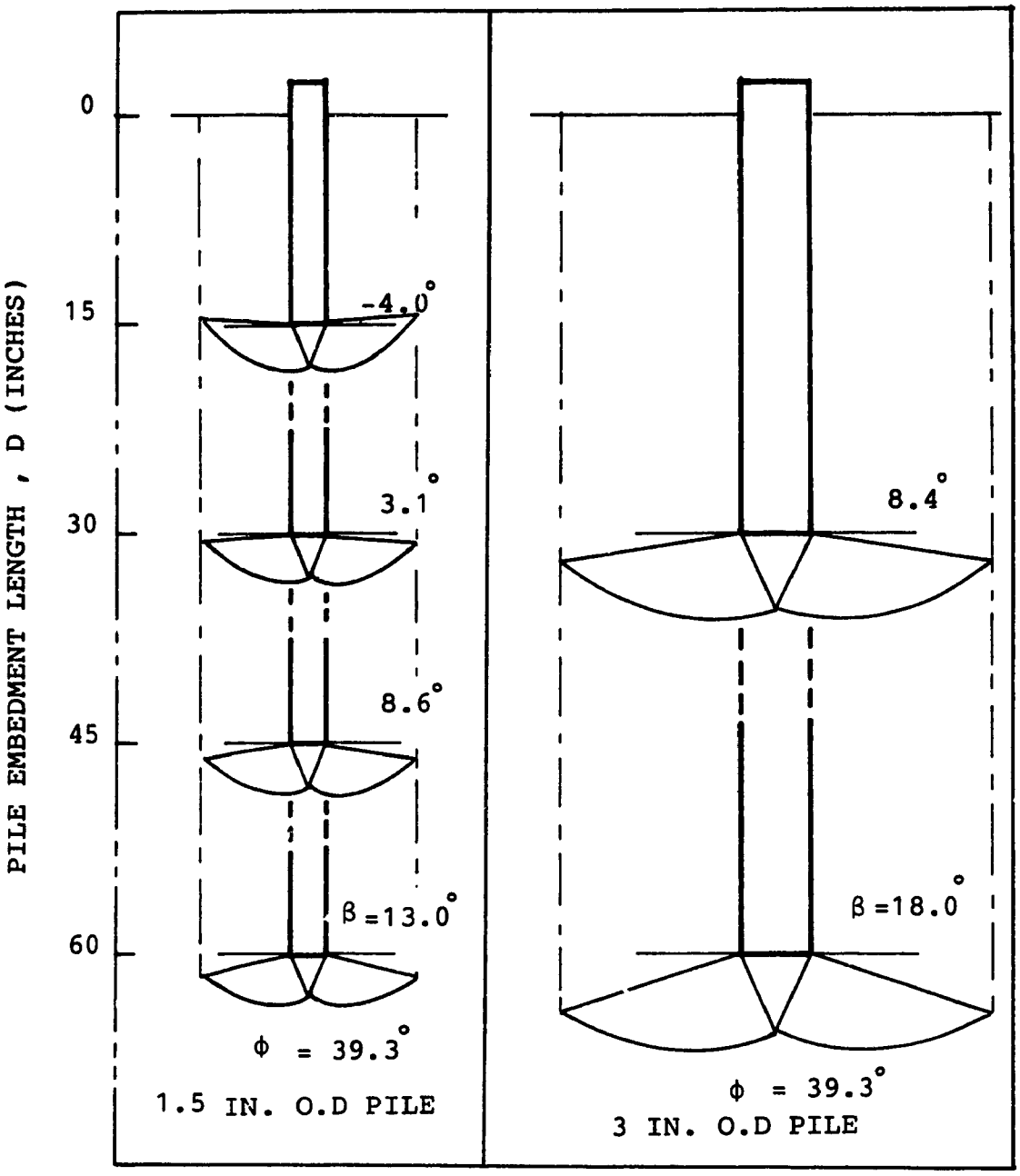

Fig. 4.66 Predicted Movement of Failure Mechanism of Model Piles (Present Study)

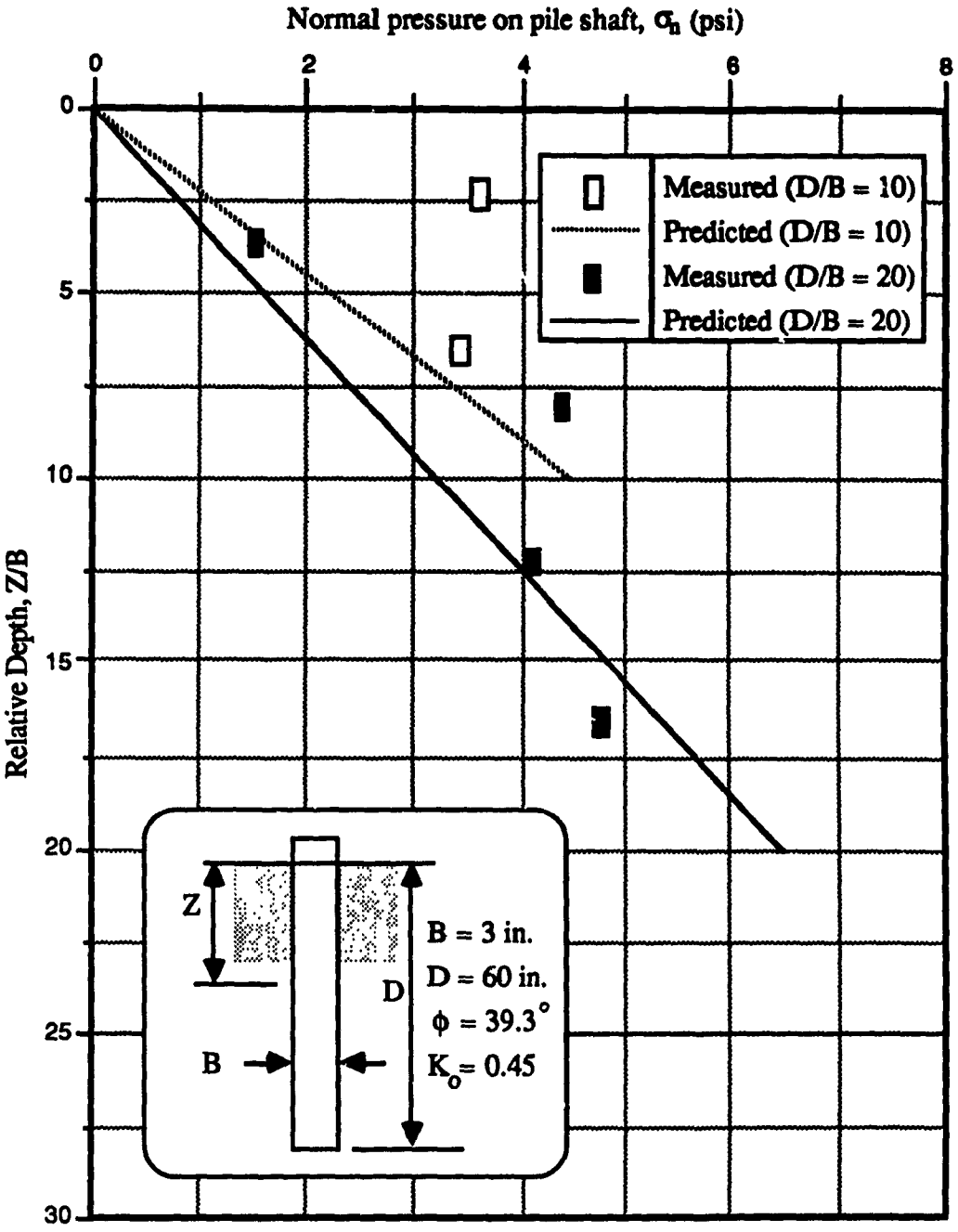

Fig. 4.67 Analysis of Earth Pressure on Pile Shaft

Vesic's Study (Vesic, 1967)

As the present experimental program was carried out only at one relative density, it is of interest to confirm whether similar findings may be discovered with another type of sand prepared at different states of compaction. For this purpose, Vesic's results obtained from load tests on a 4 in. diameter model pile were used. Three series of load tests were performed in air-dried Chattahoochee river sand, prepared at three relative densities: D_R = 31.2, 59.8 and 83.1%, respectively. In each test series, the model pile was driven and tested at six depths ranging approximately from 20 in. to 120 in. Three separate loading stages were performed similar to stages of operation of a conventional cone penetrometer: tip loading, shaft loading and loading of the whole assembly. Further details of Vesic's 4 in. diameter model pile, testing procedures, physical properties of Chattahoochee river sand, and load test results may be found in Appendix 3. It is important to note also that critical depths were observed in all three test series (i.e., the unit point resistance and the average unit skin friction remain relatively constant below certain depth).

Numerical values for parameters used in the analysis were presented in Table 4.6. The deduced values of Q_s were plotted in Figs. 4.68, 4.69, and 4.70 as a function of pile embedment length D for different values of earth pressure K_o. Measured values of the skin friction Q_s were also superimposed in corresponding figures for comparison purposes. In loose sand, most data points are located more or less close to the curve corresponding to K_o = 1 - sin ϕ (Fig. 4.68), within a band of less than ±15 percent deviation from computed values as shown in Fig. 4.71. This result agrees well with the fact that for this sand density, the sand deposit was essentially normally consolidated as it had been formed by raining sand from a height of only 1.5 in. For medium sand, it can be seen in Figs. 4.69 and 4.72 that the first four data points lie reasonably close to the curve corresponding to K_o = 0.45, within a band of about ±10 percent deviation from calculated values. The last two data points show considerable scattering, indicating most probably experimental irregularities. Agreement between deduced

Table 4.6: Analysis of Vesic's Load Tests on 4 in. Diameter Model Pile.

Type	Sand Characteristics	Pile Test No.	Nominal Depth, D (in.)	Relative Depth D/B	Measured Point Resistance, Q_p (lbs.)	Equivalent Bearing Capacity Factor, N_q^*	Deduced Angle β (Deg.)	Computed Skin Friction, Q_s (lbs.)
Loose Sand	D_R =31.2% ϕ =34.9° γ =85.0 pcf δ =32° K_o =0.428 K_T =0.273 R/B=2.78	G-11	20	5	716	57.9	2.7	186
		G-12	40	10	926	37.4	21.0	406
		G-13	60	15	926	25.0	36.4	682
		G-14	80	20	926	18.7	46.4	1050
		G-15	100	25	926	15.0	53.1	1511
		G-16	120	30	926	12.5	57.8	2064
Medium Dense Sand	D_R =59.8% ϕ =38.8° γ =91.5 pcf δ =32° K_o =0.45 K_T =0.229 R/B=3.02	G-21	20	5	1495	112.4	-3.7	329
		G-22	40	10	1949	73.3	13.3	719
		G-23	60	15	2149	53.9	24.8	1263
		G-24	80	20	2149	40.4	36.4	1886
		G-25	100	25	2149	32.3	44.0	2670
		G-26	120	30	2149	26.9	49.8	3588
Dense Sand	D_R =83.1% ϕ =43.0° γ =97.6 pcf δ =32° K_o =0.55 K_T =0.189 R/B=3.34	G-31	20	5	3814	268.8	-10.3	654
		G-32	40	10	6022	212.2	1.0	1597
		G-33	60	15	7936	186.4	8.9	2895
		G-34	80	20	9519	167.7	15.3	4521
		G-35	100	25	10714	151.0	21.0	6438
		G-36	120	30	11144	130.9	27.1	8539

Remark: Values of Q_p were obtained from curves in Fig. A 3.3, Appendix 3.

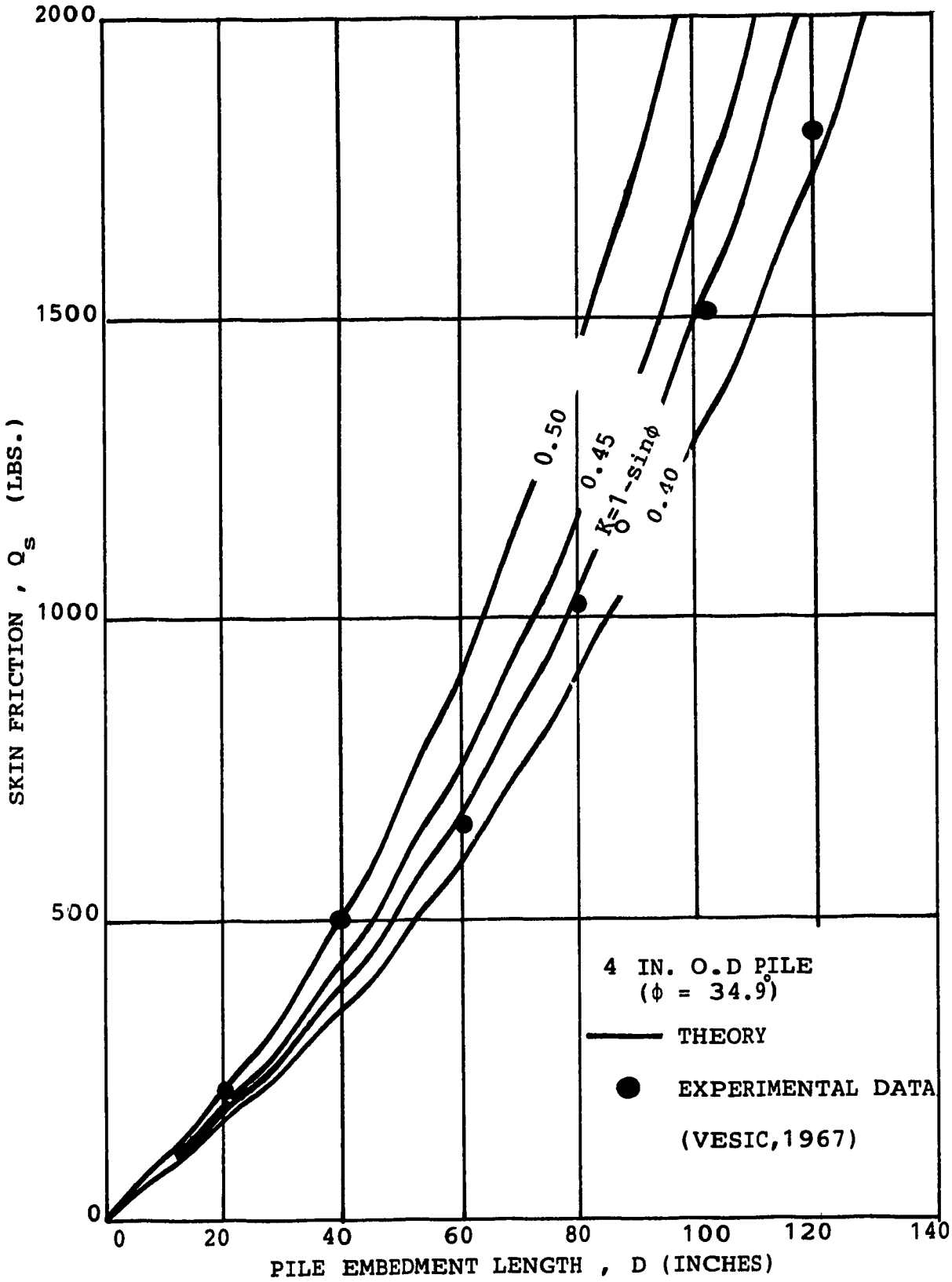

Fig. 4.68 Effect of K_o in Analysis of Skin Friction (Loose Sand, Vesic's Study)

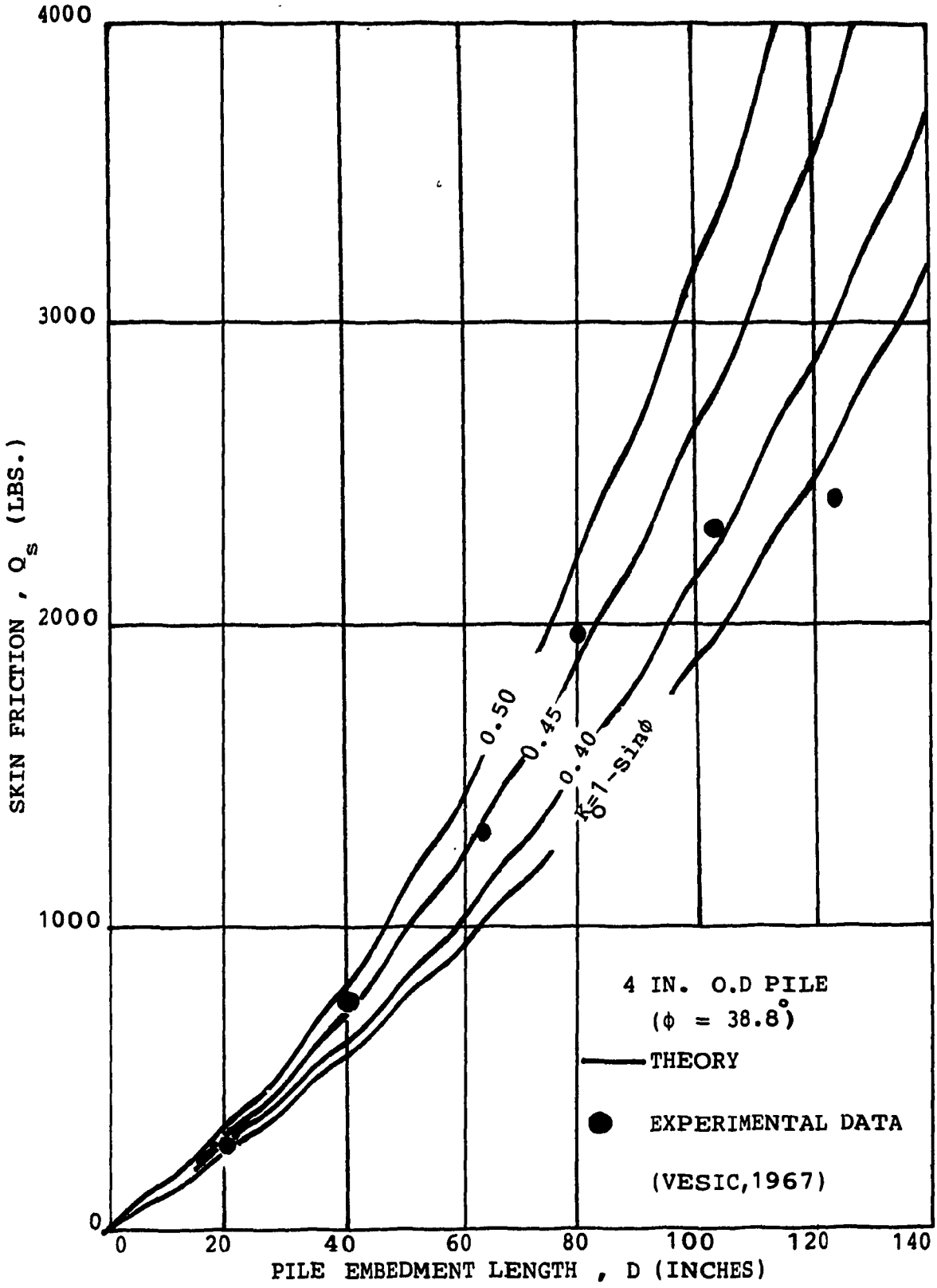

Fig. 4.69 Effect of K_o in Analysis of Skin Friction (Medium Dense, Vesic's Study)

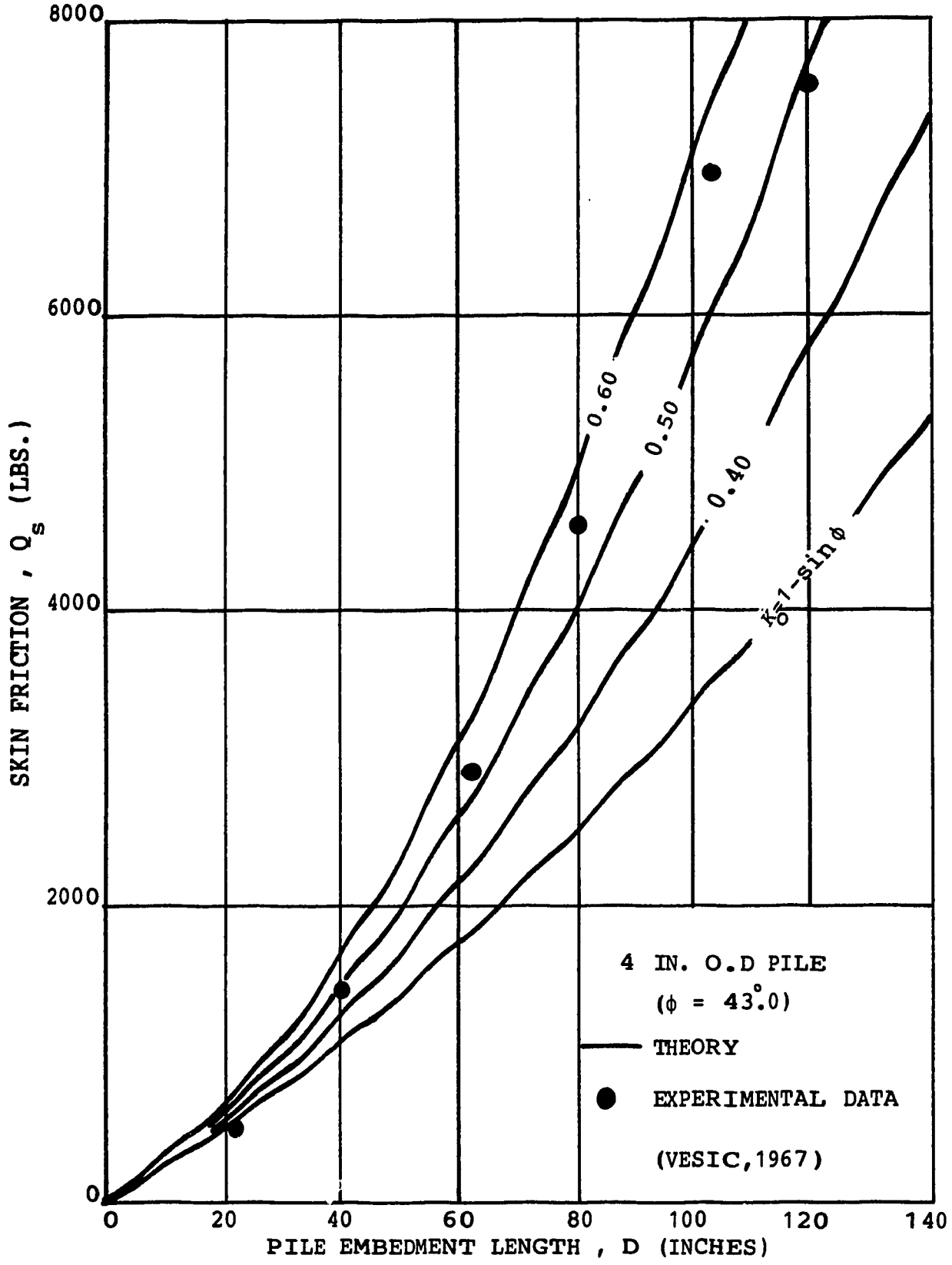

Fig. 4.70 Effect of K_o in Analysis of Skin Friction (Dense Sand, Vesic's Study)

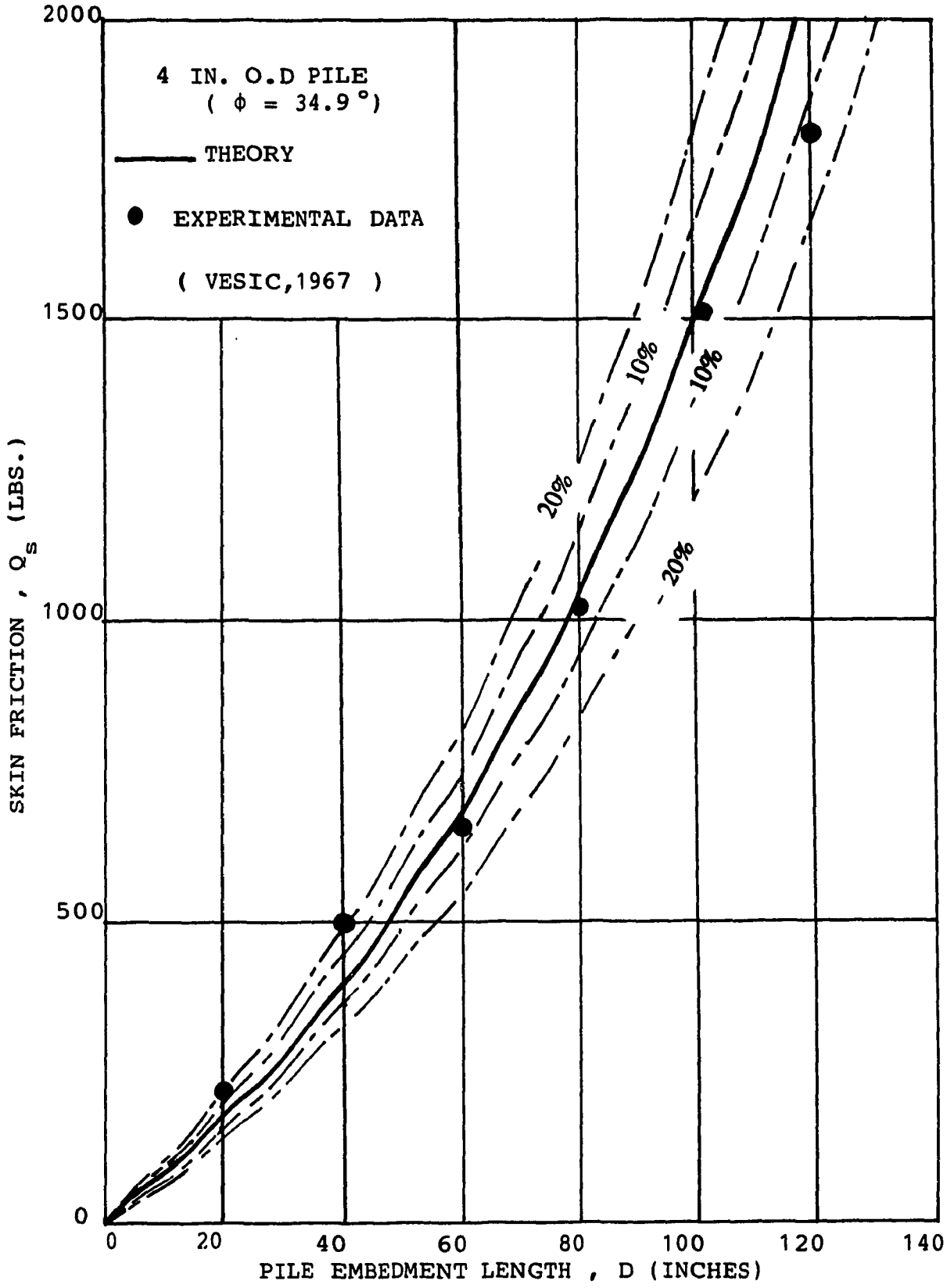

Fig. 4.71 Result of Analysis of Skin Friction (Loose Sand, Vesic's Study)

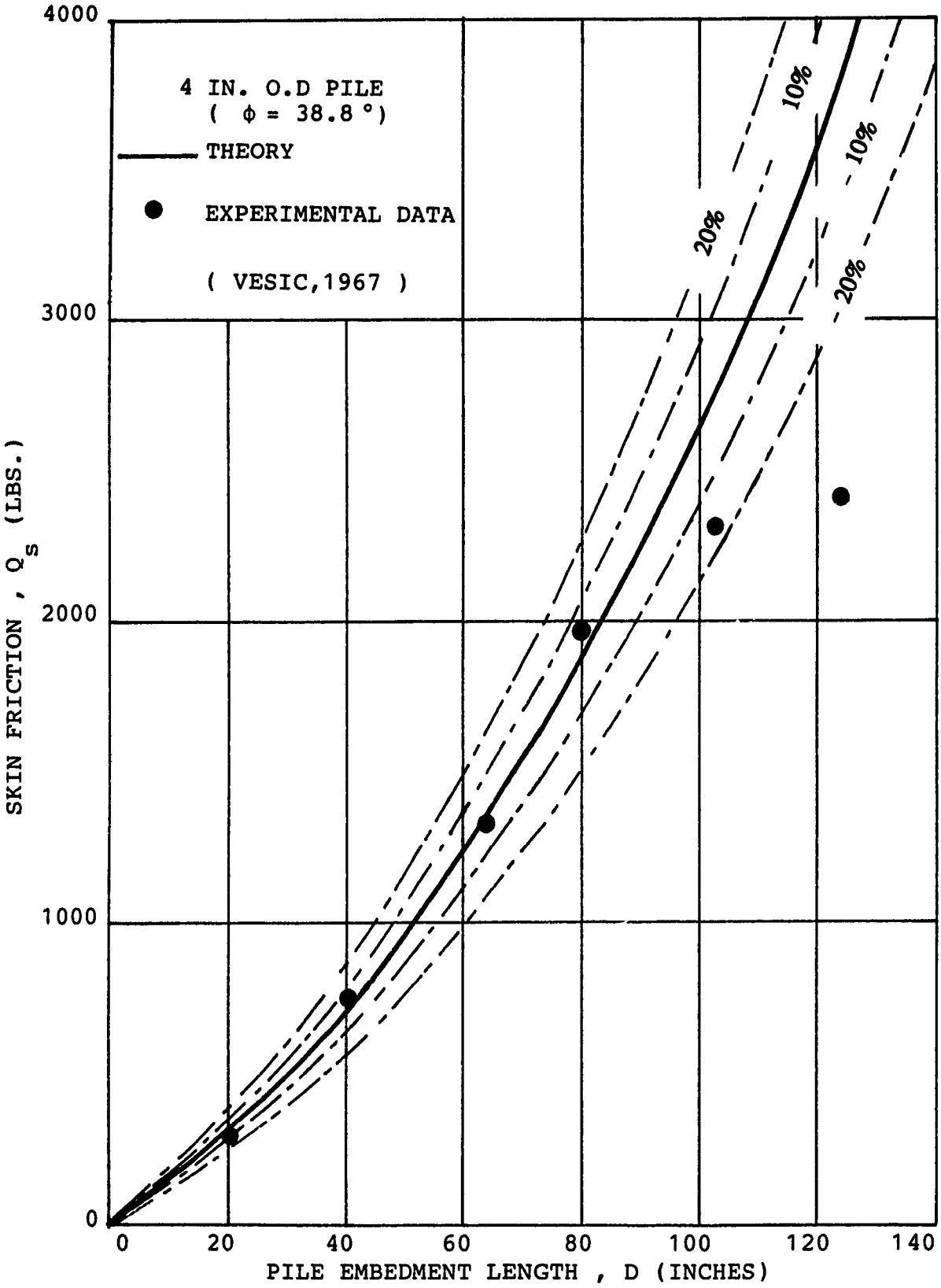

Fig. 4.72 Result of Analysis of Skin Friction (Medium Dense, Vesic's Study)

and measured values of skin friction proves much better in case of dense sand, as indicated in Fig. 4.70 and Fig. 4.73 where almost all data points are distributed favorably well along the curve corresponding to $K_o = 0.55$ within a band of approximately ±10 percent deviation from calculated values. With the exception of Vesic's load test series in loose sand where a normally consolidated condition is believed to prevail due to the low height of fall of sand (i.e., only 1.5 in.), exact values of K_o were unknown in other test series. However, all deduced K_o in these cases are higher than their counterparts estimated by Jaky's formula (i.e., $K_o = 1 - \sin \phi$), indicating a trend consistent with the employed sand placement technique of raining sand from appropriate heights (or in combination with additional surface vibration), which tends to produce various degrees of overconsolidation. In future model pile testing, it is highly desirable to monitor K_o by installing pressure transducers at different elevations both on the wall of the testing tank and inside the sand deposit.

Figure 4.74 shows schematically the positions of the terminal radial surface implied from the model at different relative depths in all three test series. It can be seen that in all these cases, this surface moves downward from the pile tip level as the pile is tested at greater depths. From this perspective, the change of the failure mechanism with depth appears to be responsible for the critical depth phenomenon observed in these tests.

4.6.2 Verification Using Field Load Tests

While the proposed model works very well with model pile test results, it is essential to further investigate its merit under field conditions. For this purpose, two sets of field test data were studied in detail. They were selected from studies by Vesic (1967) and Tavenas (1971) due to the following reasons:

(i) The geotechnical profiles of both test sites are simple and the sand deposits in both cases exist in relatively homogeneous condition to justify meaningful applications of the proposed

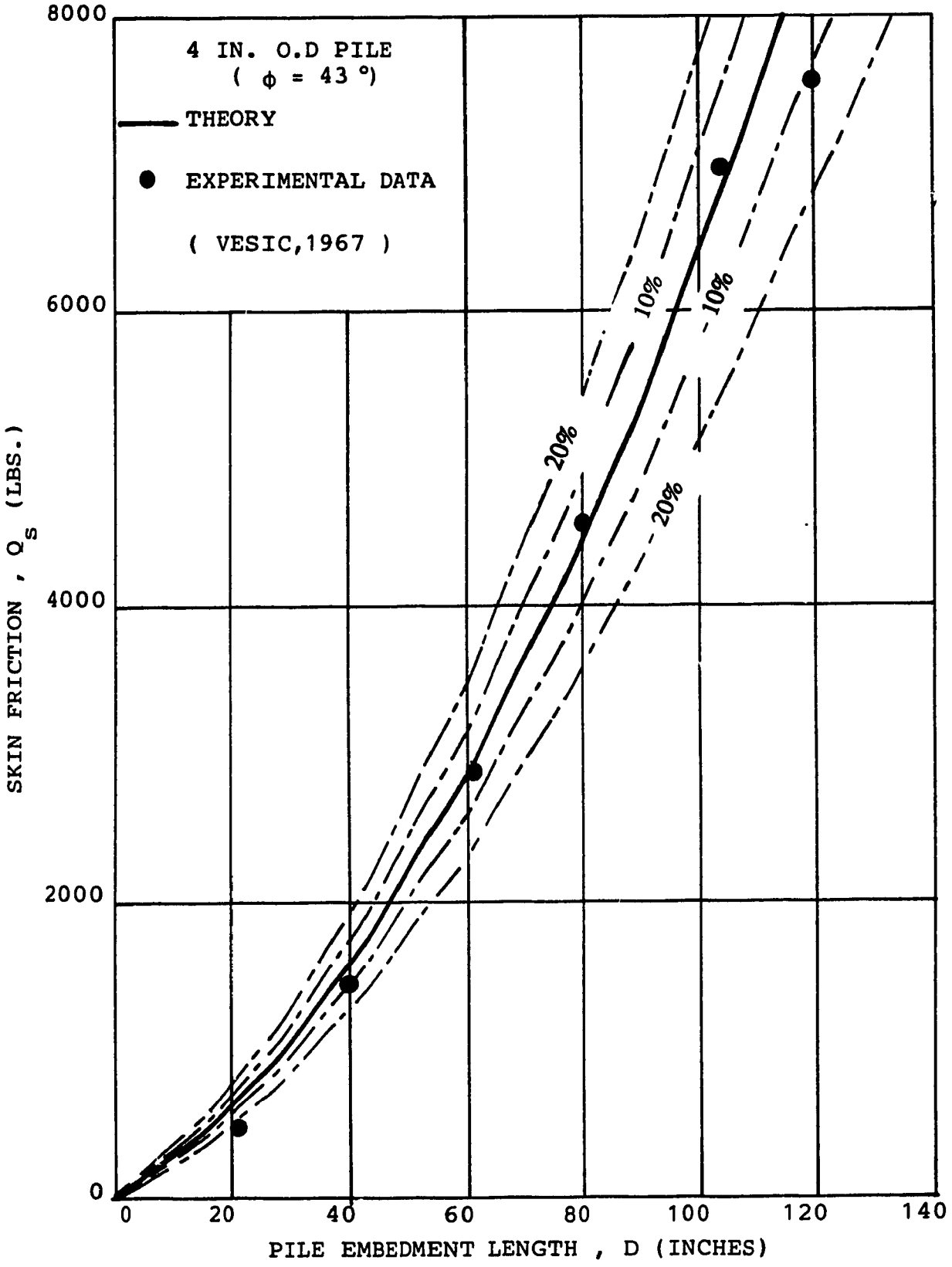

Fig. 4.73 Result of Analysis of Skin Friction (Dense Sand, Vesic's Study)

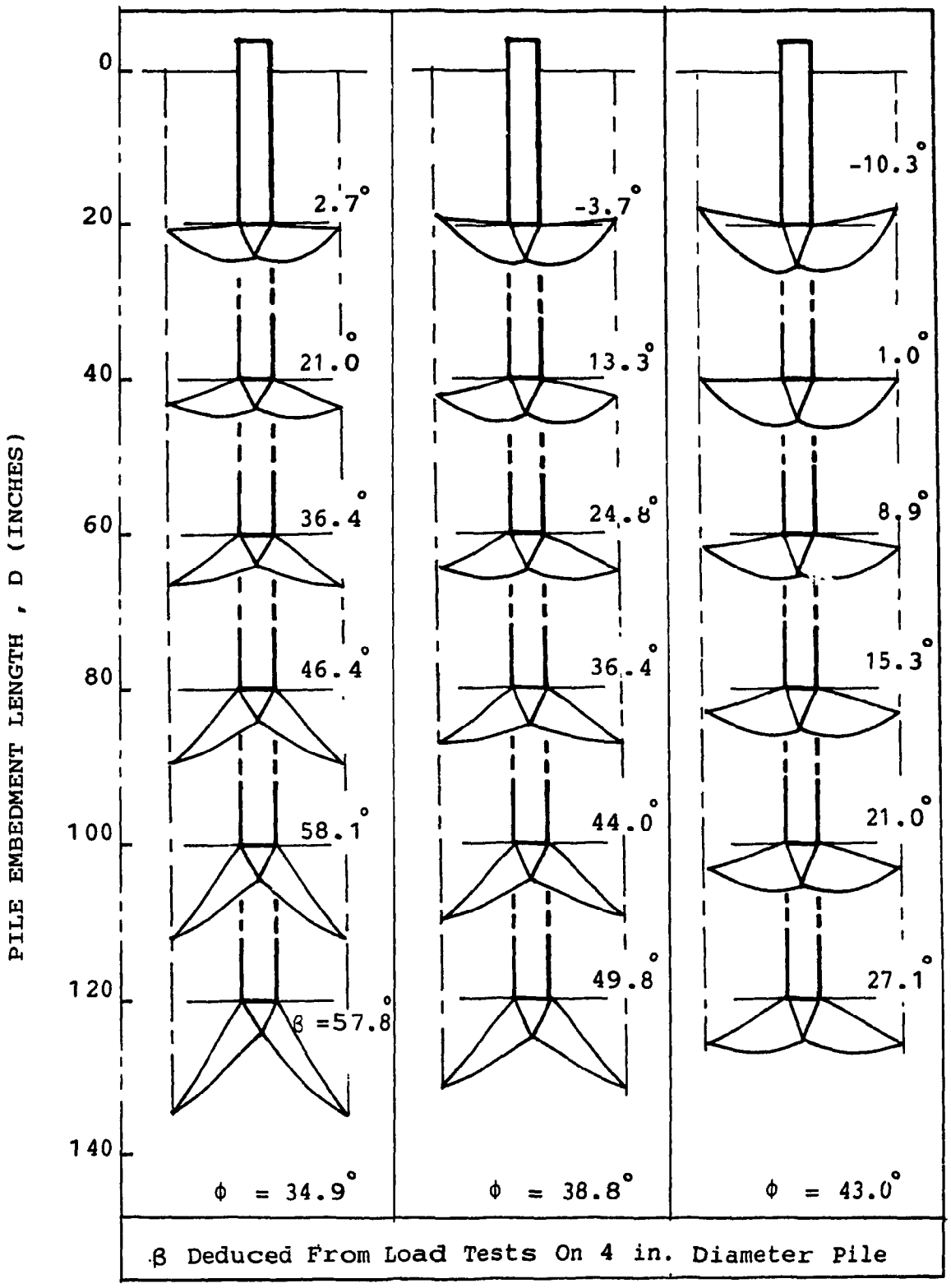

Fig. 4.74 Predicted Movement of Failure Mechanism of Model Pile (Vesic's Study)

model.

ii) In both test series, the critical depth phenomenon was observed.

iii) Tavenas' tests are particularly important because they are among rare cases where the coefficient of earth pressure K_o at the test site was evaluated.

Significant results from these two test series are summarized in Table 4.7.

Vesic's Field Tests:

Load tests were carried out at the site of the future Ogeechee River bridge on Interstate Highway 16, in Effingham County, about 18 miles West of Savanah, Georgia state, U.S.A. The site condition was characterized as consisting of a silty sand layer down to about 12 ft., underlain by a fine to medium sand deposit. Figure 4.75a shows an idealized geotechnical profile at the test site, together with its pertinent soil properties. The test pile was an 18 in. diameter, closed end steel pipe pile, driven in five sections approximately 10 ft. long each and tested at nominal depths of 10, 20, 30, 40 and 50 ft. Strain gauges were installed on the internal walls of the pile sections to measure axial loads in the pile shaft at various depths.

To account for the two-layered soil system, additional simplifying assumptions were made in the analysis as follows:

i) The model parameters K_T and R were calculated based on the average angle of shearing resistance $\bar{\phi}$, defined by:

$$\bar{\phi} = \frac{\phi_1 D_1 + \phi_2 D_2}{D_1 + D_2} \qquad \text{... (4.33)}$$

Table 4.7: Significant Results From Field Load Tests By Vesic (1967) and Tavenas (1971).

Author	Type of Pile	Pile Test No.	Pile Embedment Depth, D (ft.)	Ultimate Bearing Capacity, Q_u (ton)	Point Resistance, Q_p (ton)	Skin Friction, Q_s (ton)
Vesic (1967)	Steel Pipe Pile (B = 1.50 ft.)	H-11	9.9	76.0	61.0	15.0
		H-12	20.1	232.0	173.0	59.0
		H-13	29.1	297.0	212.0	85.0
		H-14	39.3	347.0	214.0	133.0
		H-15	49.3	421.0	258.0	163.0
Tavenas (1971)	Precast Concrete Herkules Pile (B = 1.06 ft.)	J-1	19.0	40.0	32.2	7.8
		J-2	29.0	55.0	32.6	23.4
		J-3	39.0	77.0	39.7	37.7
		J-4	49.0	95.0	41.0	54.0
		J-5	59.0	107.5	41.0	66.5
		J-6	69.0	120.0	39.3	80.7

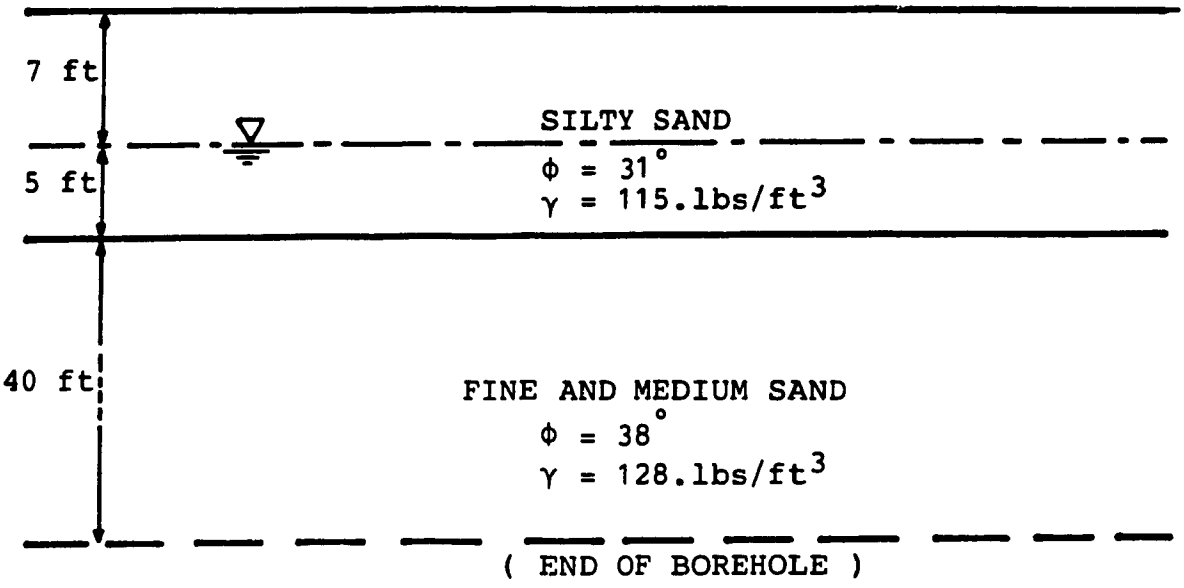

(a) Vesic's Test Site

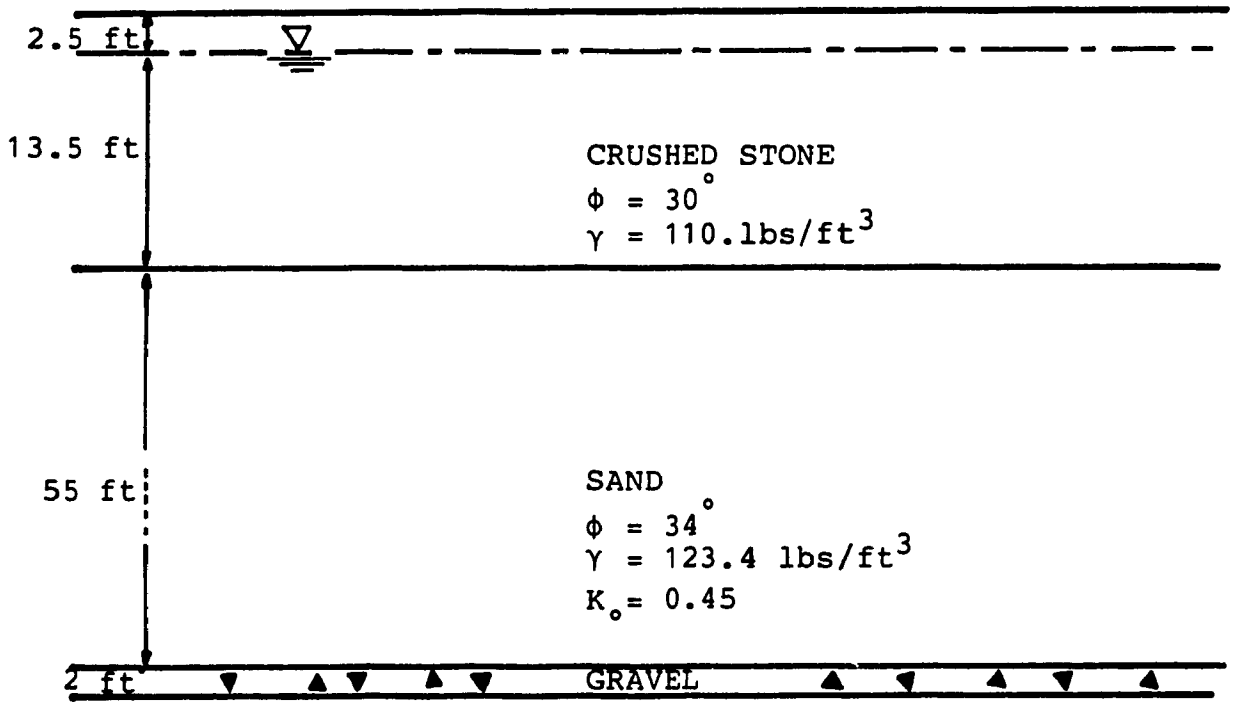

(b) Tavenas' Test Site

Fig. 4.75 Idealized Geotechnical Profile of Vesic's and Tavenas' Test Sites

where ϕ_1, D_1, and ϕ_2, D_2 denote angles of shearing resistance and pile embedment lengths in soil layers 1 and 2, respectively.

ii) All other parameters were unaffected.

For the assumed values of $\bar{\phi} = 25°$ and $K_o = 0.55$, good agreements between computed and measured values of the average unit skin friction f_s are evident in Figure 4.76c which shows most data points lie within a ± 20 per cent error band of the computed f_s values. The variation of β with D/B is also schematically shown in Fig. 4.76b, indicating a downward movement of terminal radial surface as the test pile was driven to lower depths.

Tavenas' Field Tests:

Tavenas (1971) performed a series of six load tests on a Herkules H800 precast concrete pile as part of an extensive testing program to determine the type of pile best suited for the embankment project of the St. Charles River in Quebec City, Quebec, Canada. The idealized geotechnical profile of the test site and physical properties of the dominant layers were shown in Figure 4.75b. The Herkules pile, consisting of one 20 ft. section and five 10 ft. sections, was driven and tested at six depths of 19, 29, 39, 49, 59 and 69 ft., respectively. Axial loads were monitored by deformation gauges installed inside the pile shaft. Although all pile load tests were performed with the pile point located in the sand stratum, the first 16 ft. of the test pile was embedded in a loose crushed stone layer which had been dumped uncompacted under water. In the analysis, the same procedure was followed as in Vesic's case to account for the layering effects. The angle of shaft friction δ was estimated by $\delta = (2/3)(\bar{\phi} + 5)$ as suggested by Tavenas. The calculated values of the average unit skin friction f_s at various relative depths D/B were presented in Table 4.8 and plotted in Figure 4.77c, which indicates almost all data points lie within an error band of ± 20 per cent of the computed values. The downward movement of the terminal radial surface with depth is also clearly shown in Fig. 4.77b.

Table 4.8: Analysis of Field Load Tests exhibiting Critical Depths.

Author	Type of Pile	Pile Test No.	D (ft.)	Significant Input Data								Computed Values	
				σ'_o (Tsf)	ϕ (deg.)	$\bar{\phi}$ (deg.)	δ (deg.)	K_o	K_T	R/B	N_q^*	β (deg.)	Unit Skin Friction f_s(Tsf)
Vesic (1967)	Steel Pipe Pile (B = 1.50 ft.)	H-11	9.9	0.498	34+	31.0	25.0	0.55	0.320	2.56	69.3	-19.8	0.323
		H-12	20.1	0.831	38	33.8	25.0	0.55	0.285	2.71	117.8	-2.0	0.495
		H-13	29.1	1 127	38	35.0	25.0	0.55	0.271	2.78	106.5	+7.2	0.600
		H-14	39.3	1.461	38	35.9	25.0	0.55	0.261	2.87	82.9	+20.2	0.692
		H-15	49.3	1.788	38	36.3	25.0	0.55	0.256	2.86	81.7	+24.9	0.819
Tavenas (1971)	Precast Concrete Herkules Pile (B = 1.06 ft.)	J-1	19.0	0.538	34	30.6	23.7	0.45	0.325	2.54	67.9	-2.2	0.165
		J-2	29.0	0.843	34	31.8	24.5	0.45	0.310	2.60	43.9	+21.5	0.205
		J-3	39.0	1.148	34	32.4	24.9	0.45	0.302	2.63	38.8	+31.6	0.264
		J-4	49.0	1.453	34	32.7	25.1	0.45	0.299	2.65	32.0	+41.5	0.312
		J-5	59.0	1.758	34	32.9	25.3	0.45	0.296	2.66	26.5	+49.6	0.357
		J-6	69.0	2.063	34	33.1	25.4	0.45	0.294	2.67	21.6	+56.3	0.400

Remark: (+) ϕ was corrected for layering effect.

4.7 CRITICAL DEPTH

It can be seen in Figs. 4.74, 4.76b, and 4.77b that the angle β deduced from measured unit point resistances q_p becomes more and more positive, indicating the terminal radial surface (i.e., AC and A'C') dip further downwards from the pile tip level as the pile is driven to lower depths. According to the model, this movement results in a reduced value of the computed equivalent bearing capacity factor N^*_q. The unit point resistance q_p, being the product of the effective overburden pressure at the pile tip level σ'_o and N^*_q with the former increasing while the latter decreasing with depth, may become relatively constant if the two opposite tendencies neutralize each other over certain range of depth. The analysis of Vesic's and Tavenas' field tests clearly confirms this explanation of the critical depth. Whether the unit point resistance q_p continues to maintain its quasi-constant status at greater depth than encountered herein (i.e. D/B > 70), it is an interesting matter for experimentalists to settle. In either case, the present model is flexible enough to accommodate further modifications because it has clearly identified 8 vital parameters and thus offer advantageous terrains to manoeuver in the analysis. In the case of skin friction, however, the critical depth concept appears much less viable. As can be seen in Figs. 4.76c and 4.77c, almost all measured values of the average unit skin friction f_s deviate less than ± 20 per cent from their computed counterparts. Experimentally, this magnitude of deviations certainly permits alternative interpretations for the variation trend of f_s with depth such as those already advocated by Coyle and Castello (1981) and Kulhawy (1984): the average unit skin friction does not become constant below a certain depth but it continues to increase with depth.

4.8 MODEL APPLICATION

4.8.1 An Approximate Method for Pile Bearing Capacity

It is recalled that the use of the proposed model in estimating pile bearing capacity necessitates a total of eight parameters which include five intrinsic parameters, namely: D, B, ϕ, K_o and δ, and three model parameters: β, K_T and R (See Section 4.4.1 for definitions). All

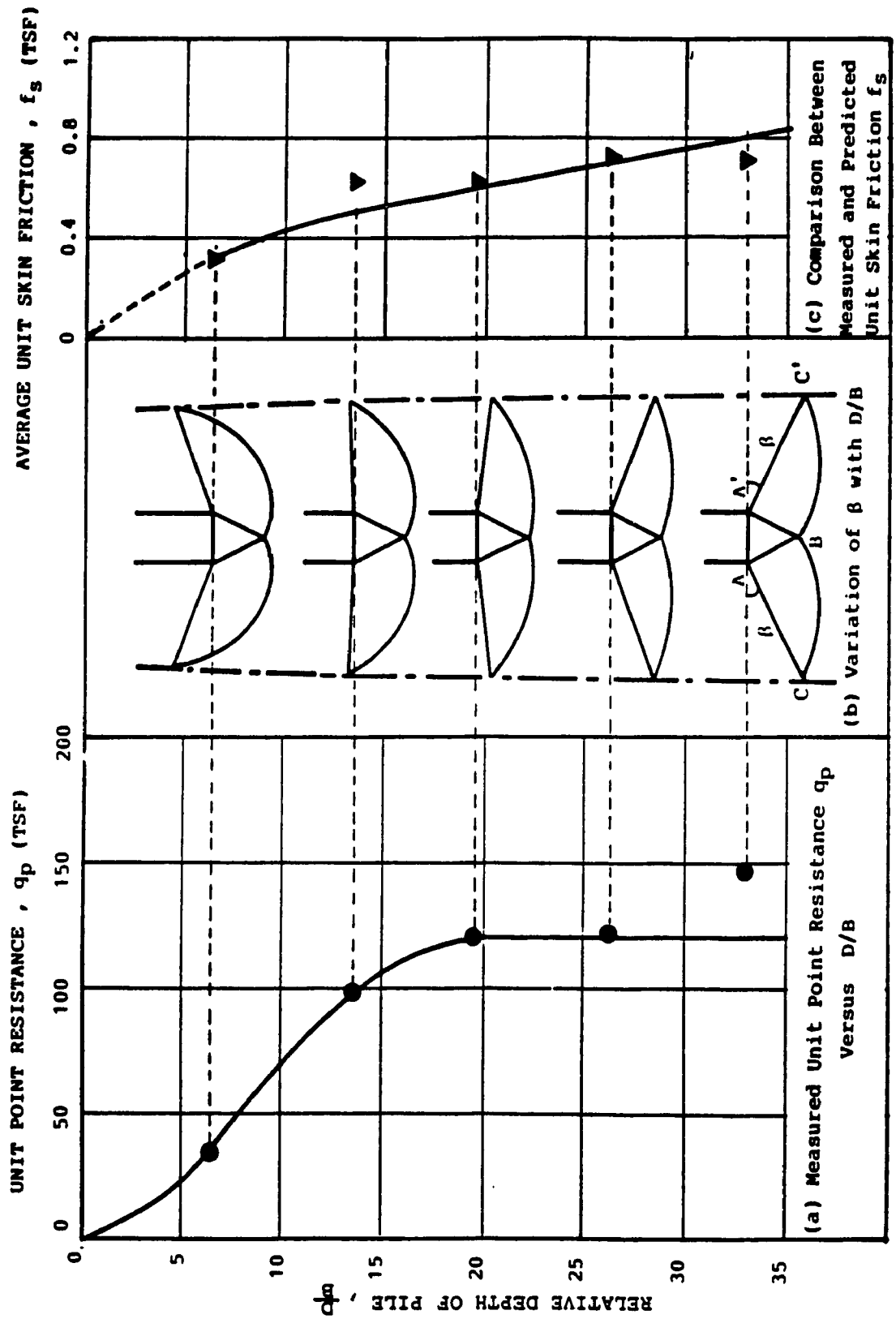

Fig. 4.76 Analysis of Vesic's Field Load Tests

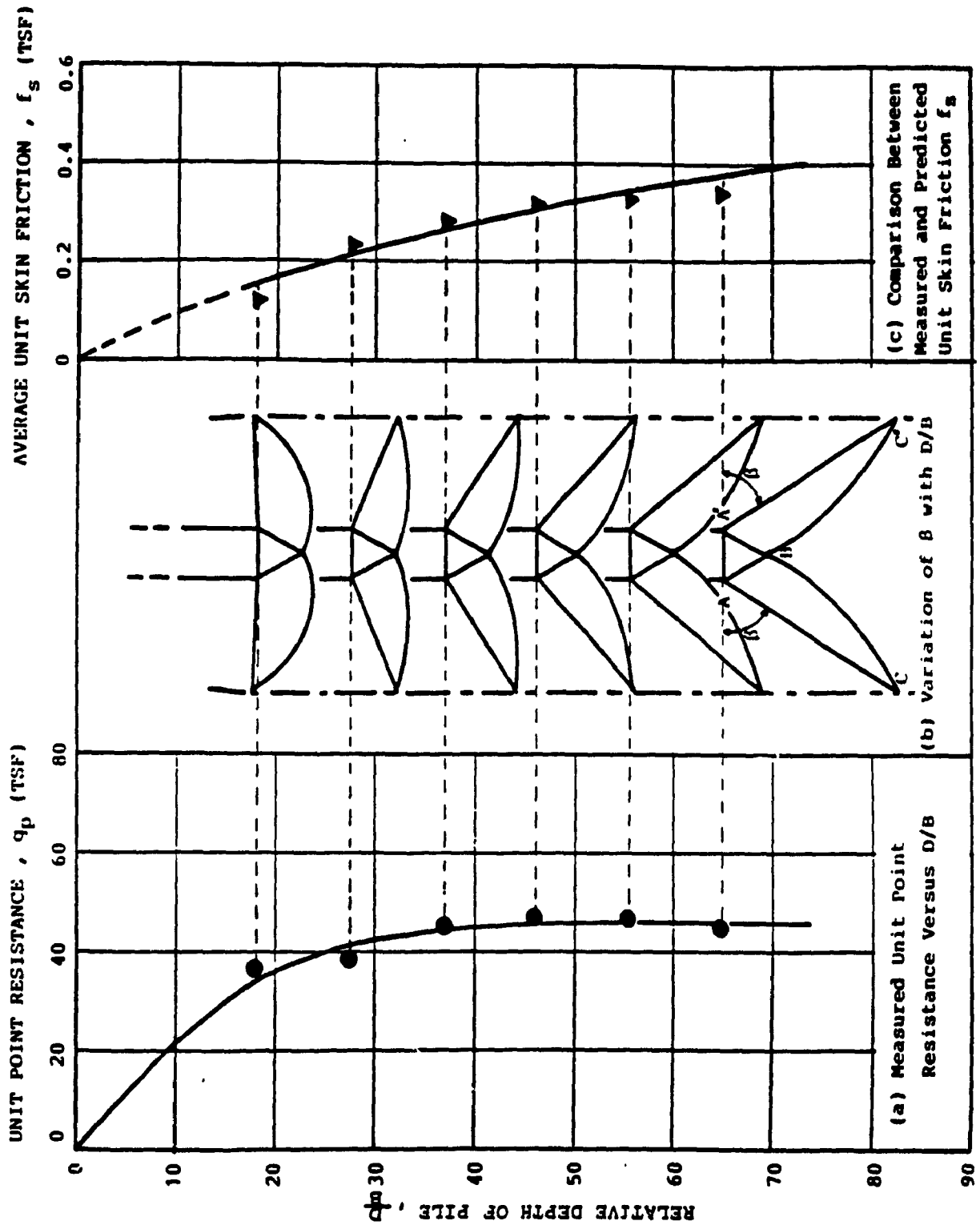

Fig. 4.77 Analysis of Tavenas' Load Tests (Herkulus Pile)

required parameters, except for the angle β, can be either estimated directly from laboratory and field data or logically assumed as explained in Section 4.5. The unknown angle β, fortunately, may not necessarily disallow an approximate method to evaluate pile bearing capacity. It has been clearly demonstrated in Section 4.6 that if the point resistance Q_p is known then by computing its equivalent bearing capacity factor N^*_q and applying the proposed model, the angle β may be deduced, leading to a good estimate of the skin friction Q_s. As Berezantzev's bearing capacity factor N^*_q was found reliable in predicting point resistances for single piles in sand (i.e. Norlund, 1969: Vesic, 1967), its adoption in the proposed model may provide a mean to deduce the angle β, which subsequently allows a rational approach to calculate the skin friction Q_s. This process constitutes an approximate method for estimating the ultimate bearing capacity Q_u of driven piles in sand. The computation procedure consists of the following steps:

1) Estimate the angle of shearing resistance ϕ of sand and the shaft friction angle δ as established by laboratory and/or field tests.

2) Calculate the coefficient of earth pressure at-rest by $K_o = 1 - \sin \phi$ (i.e., assume the sand deposit is normally consolidated).

3) Evaluate Berezantzev's bearing capacity factor N^*_q based on ϕ and the pile relative depth D/B (See Fig. A.2.1 for values of Berezantzev's N^*_q).

4) Calculate the model parameters K_T and R/B using Equations 4.31 and 4.30, respectively.

5) Run the computer program TEMPO with the angle β varying from -40° to 80° at 2° intervals.

6) Compute the angle β and the equivalent coefficient of earth pressure K^*_s at the pile shaft

by linear interpolation using Berezantzev's N^*_q and results obtained in Step 5.

7) The pile bearing capacity Q_u is then computed as the sum of Q_p and Q_s, which are given by equations 4.19 and 4.20, respectively.

From a practical point of view, it is of great interest to investigate the validity of applying this approximate method in predicting pile bearing capacity in field situations.

4.8.2 Verification of Approximate Method

To assess the merit of the proposed approximate method, a total of 30 well-documented field load tests were analysed, which include:

i) Five load tests performed on a steel pipe pile by Vesic (1967).

ii) Two load test series consisting of six tests each carried out by Tavenas (1971) on a precast concrete Herkules pile and a steel H-pile, respectively.

iii) Seven load tests from the Arkansas River Project (Mansur and Hunter, 1970).

iv) Seven load tests performed at the site of the low-sill structure, Old River, Louisiana (Mansur and Kaufman, 1958).

Vesic's Tests on Steel Pipe Pile

Vesic's load tests on the 18 in. diameter steel pipe pile had been previously analysed in Section 4.6.2, using equivalent bearing capacity factors deduced from measured point resistances Q_p. The same procedure was followed herein except that this time Berezantzev's bearing capacity factors were used instead. Details of the idealized geotechnical profile for

Vesic's test series may be found in Fig. 4.75a. As it can be seen in Tables 4.9 and 4.10, which summarize numerical values assumed and results obtained from the analysis, the computed pile bearing capacities in these five tests show good agreement with their measured counterparts, incurring errors ranging from -1.4 to -22.2 percent.

Tavenas' Tests on Herkules Pile

By adopting the same analysis procedure as applied in Vesic's tests just mentioned above, Tavenas' tests on the precast concrete Herkules pile were reanalyzed, using the same geotechnical profile described in Section 4.6.2. Tables 4.9 and 4.10 show results of the analysis together with its assumed numerical values. Reasonable agreements between computed and measured pile bearing capacities were observed, indicating errors ranging from -28.8 to +24.6 percent.

Tavenas' Tests on H-Pile

In addition to load tests performed on the Herkules pile at the test site of the embankments project of the St. Charles River in Quebec, Tavenas also carried out another load test series on a steel H-pile (type 12BP74), driven at about 12 ft from the Herkules pile. This steel H-pile which consisted of one 20 ft section and five 10 ft sections, was driven and tested at six depths of 18, 28, 38, 48, 58 and 68 ft, respectively. In the analysis, the same idealized geotechnical profile used to analyze the Herkules pile (see Fig. 4.75b) was assumed valid for the H-pile. Tables 4.9 and 4.10 summarize numerical values of pertinent parameters utilized in the analysis and the obtained results. It can be seen that fairly good agreements between computed and measured bearing capacities occurred for pile test Nos. H-2, H-3, H-4 and H-6, with errors ranging from +4.3 percent to +25.8 percent. Errors exceeding +40 percent, however, were encountered in pile test Nos. H-1 and H-5. The incomplete formation of soil plugs between the flanges of the H-pile is believed responsible for the low measured bearing

Table 4.9: Significant Input Data Used in Analysis of 30 Field Tests.

Pile Test No.	Type of Pile	D (ft.)	B (ft.)	σ'_o (Tsf)	D_1 (ft.)	D_2 (ft.)	ϕ_1 (deg.)	ϕ_2 (deg.)	$\bar{\phi}$ (deg.)	δ (deg.)	K_o	K_T	R/B	N_q^*
Vesic														
H-11	Steel pipe	9.9	1.50	0.498	9.9	0.0	31	38	31.0	25.0	0.485	0.320	2.56	55.1
H-12		20.1	1.50	0.831	12.0	8.0	31	38	33.8	25.0	0.444	0.285	2.71	99.6
H-13		29.1	1.50	1.127	12.0	17.1	31	38	35.0	25.0	0.426	0.271	2.78	94.7
H-14		39.3	1.50	1.461	12.0	27.3	31	38	35.9	25.0	0.414	0.261	2.87	92.1
H-15		49.3	1.50	1.788	12.0	37.3	31	38	36.3	25.0	0.408	0.256	2.86	90.7
Tavenas														
J-1	Precast Concrete	19.0	1.06	0.538	16.0	3.0	30	34	30.6	23.7	0.491	0.325	2.54	43.7
J-2		29.0	1.06	0.843	16.0	13.0	30	34	31.8	24.5	0.473	0.310	2.60	40.6
J-3		39.0	1.06	1.148	16.0	23.0	30	34	32.4	24.9	0.464	0.302	2.63	39.3
J-4		49.0	1.06	1.453	16.0	33.0	30	34	32.7	25.1	0.460	0.299	2.65	38.7
J-5		59.0	1.06	1.758	16.0	43.0	30	34	32.9	25.3	0.457	0.296	2.66	38.2
J-6		69.0	1.06	2.063	16.0	53.0	30	34	33.1	25.4	0.454	0.294	2.67	37.8
Tavenas														
H-1	Steel H-pile	18.0	1.14	0.507	16.0	2.0	30	34	30.4	23.8	0.494	0.328	2.52	44.8
H-2		28.0	1.14	0.812	16.0	12.0	30	34	31.7	24.9	0.475	0.311	2.60	41.3
H-3		38.0	1.14	1.117	16.0	22.0	30	34	32.3	25.4	0.466	0.303	2.63	39.7
H-4		48.0	1.14	1.422	16.0	32.0	30	34	32.7	25.7	0.460	0.298	2.65	38.9
H-5		58.0	1.14	1.727	16.0	42.0	30	34	32.9	25.9	0.457	0.296	2.66	38.5
H-6		68.0	1.14	2.032	16.0	52.0	30	34	33.1	26.1	0.454	0.294	2.68	38.0
Arkansas														
1	Steel Pipe	53.1	1.20	1.580	53.1	0.0	35	35	35.0	25.0	0.426	0.271	2.78	47.6
2		52.8	1.50	1.540	52.8	0.0	34	34	34.0	25.0	0.441	0.283	2.72	39.5
3		53.0	1.70	1.575	53.0	0.0	35	35	35.0	25.0	0.426	0.271	2.78	48.9
10		53.0	1.42	1.543	53.0	0.0	34	34	34.0	25.0	0.441	0.283	2.72	39.3
4	Conc.	40.2	1.50	1.184	40.2	0.0	35	35	35.0	30.0	0.426	0.271	2.78	49.7
7	H	52.1	1.34	1.532	52.1	0.0	34	34	34.0	28.5	0.441	0.283	2.72	39.1
Low-Sill														
1	H	81.0	1.33	2.198	49.0	32.0	28	36	31.2	21.8	0.482	0.318	2.57	47.8
2	Pipe	65.0	1.75	1.800	48.0	17.0	28	36	30.1	21.1	0.498	0.332	2.50	59.1
3	H	71.0	1.33	1.900	52.0	19.0	28	36	30.1	21.6	0.498	0.332	2.50	58.1
4	Steel pipe	66.0	1.42	1.830	48.0	18.0	28	36	30.8	21.6	0.488	0.323	2.55	58.5
5		45.0	1.42	1.260	45.0	0.0	28	36	28.0	19.6	0.531	0.361	2.41	21.0
6		65.0	1.58	1.795	50.0	15.0	28	36	29.8	20.9	0.503	0.336	2.49	58.7
7		65.0	1.50	1.781	47.0	18.0	28	36	30.2	21.1	0.497	0.331	2.51	58.6

Remarks on Table 4.9

i) Average angle of shearing resistance, $\bar{\phi}$

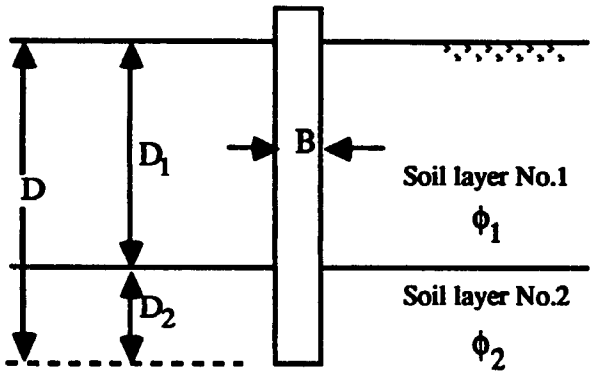

$$\bar{\phi} = \frac{D_1 \phi_1 + D_2 \phi_2}{D_1 + D_2}$$

$\bar{\phi}$ is used to calculate K_T, K_o, and R only

ii) Correction for layering effect

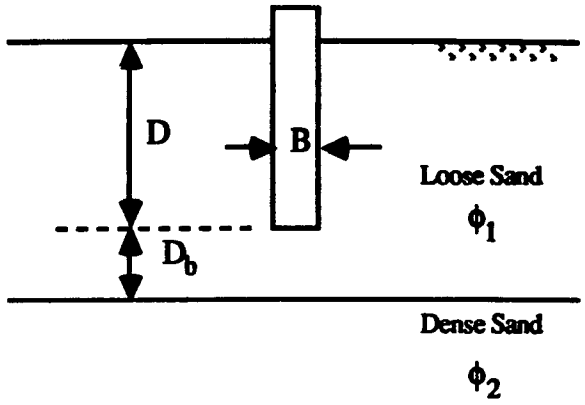

$$\phi_{Cor.} = \phi_1 + 0.5\left(1 - \frac{D_b}{10\,B}\right)(\phi_1 - \phi_2)$$

Vesic's test No. H-11 and Low-Sill test No. 5 were corrected for layering effect.

capacity in pile test No. H-1 (i.e., only 20 tons compared to 40 tons in case of the Herkules pile test No. J-1 at approximately the same depth). In the analysis, the H-pile was explicitly assumed to be fully plugged and replaced by an equivalent circular pile having the same cross section area. If the flanges of the H-pile was only partially plugged with soil then this assumption would lead to an overestimation of Q_u. The situation in pile test No. H-5 appears different because in this case, the discrepancy is more likely resulted from the conservative evaluation of the measured bearing capacity. For these reasons, pile test Nos. H-1 and H-5 will be excluded from a subsequent correlation study.

Arkansas Test Piles

The pile testing program for the Arkansas river navigation project was initiated to develop design criteria for the construction of pile foundations to support locks and dams on sand, located on the east bank of the Arkansas river, about 20 miles downstream from Pine Bluff in Arkansas state, U.S.A. Preparations of the test area included a 20 ft deep excavation down to the top of the 100 ft thick sand stratum. The standard penetration resistances generally increased with depth, varying from 20 to 40 blows per foot with an average of about 20 blows per foot after site excavation. The ground water table was kept about 2 to 3 feet below the ground surface by a dewatering system installed around the test area. A total of 21 test piles were driven at the site and subjected to a variety of tests which included compression, lateral, tension and cyclic tests. Only six test piles were considered relevant for use in the analysis which idealized the test site as a single layer deposit, having average physical properties summarized in Table 4.9. It can be seen in Table 4.10 that the calculated bearing capacity Q_u of the six selected test piles agreed well with their measured counterparts, incurring errors ranging only from about -21 percent to +14 percent.

Low-Sill Test Piles

The pile testing program for the Old River control project was undertaken at the site for

Table 4.10: Results of Analysis of 30 Field Tests.

Pile Test No.	Predicted Q_u (ton)	Measured Q_u (ton)	Error E_R (%)	Reference for Measured Q_u
Vesic				
H-11	60.0	76.0	-21.0	
H-12	180.0	232.0	-22.4	Vesic (1967)
H-13	246.0	297.0	-17.2	[Table 19, p. 51]
H-14	327.0	347.0	-6.1	
H-15	415.0	421.0	-1.4	
Tavenas				
J-1	28.5	40.0	-28.8	
J-2	54.0	55.0	-1.8	
J-3	77.5	77.0	+0.6	Tavenas (1971)
J-4	98.0	95.0	+3.2	[Table 2, p. 19]
J-5	126.0	107.5	+17.2	
J-6	149.5	120.5	+24.6	
Tavenas				
H-1	33.0	20.0	+65.0	
H-2	57.0	50.0	+14.0	
H-3	85.0	80.0	+6.3	Tavenas (1971)
H-4	117.0	93.0	+25.8	[Table 3, p. 21]
H-5	153.0	105.0	+45.7	
H-6	193.0	185.0	+4.3	
Arkansas				
1	163.0	172.0	-5.8	i) Hunter & Davisson (1969)
2	202.0	242.0	-16.5	[Table 2, p. 19]
3	294.0	272.0	+8.1	
10	185.0	242.0	-23.6	ii) Coyle & Castello (1981)
4	178.0	200.0	-11.0	[Table 3, p. 972-973]
7	174.0	243.0	-28.4	
Low-Sill				
1	336.0	292.0	+15.1	Mansur and
2	402.0	296.0	+35.8	Kaufman (1958)
3	273.0	151.0	+80.7	[Table 3, p. 730]
4	291.0	361.0	-19.4	
5	88.0	117.0	-24.8	
6	336.0	329.0	+2.1	
7	304.0	317.0	-4.1	

the low-sill structure, which is a controlled spillway located on the west bank of the Mississippi River, 35 miles south of Natchez, Mississippi, U.S.A. Compression or compression/tension tests were performed on two 14 in. steel H-piles, one of which was fitted with a steel bottom plate, and five steel pipe piles having diameters ranging from 16 to 20 inches. The soil profile beneath the low-sill structure generally consists of 50 to 60 ft of alternating strata of silts, sandy silts and silty sands overlying a clean sand stratum of varying thickness from 40 to 60 ft, which is in turn underlain by stiff clays. The analysis was carried out following the general procedure outlined previously in Section (4.6.2). The only exception occurred with test pile No. 5 where the angle of shearing resistance ϕ_1 of the silt layer was corrected to account for the stiffening effect of the stronger sand layer located only 4 ft below the interface of the two layers. The procedure for this correction as well as for other numerical values used in the analysis can be found in Table 4.9. Computed values showed good agreement with measured bearing capacity Q_u for pile Nos. 1, 4, 5, 6, and 7, as indicated in Table 4.10, with errors ranging from -24.8 to +15.1 percent. More serious errors, however, were encountered in cases of pile No. 2 and No. 3. For pile No. 2, its measured bearing capacity Q_u appeared inconsistent with those of pile No. 4 and pile No. 6. As these three piles were driven about 30 ft apart and to the same depth, pile No. 2 was expected to have higher bearing capacity than the others due to its larger size (i.e., B = 1.75 ft compared to B = 1.42 ft and 1.58 ft, respectively, for pile No. 4 and pile No. 6). In reality, pile No. 2 had the lowest bearing capacity. This inconsistancy is believed most likely due to local variations in soil conditions and/or measurement irregularities. As for pile No. 3, the significant discrepancy between computed and measured bearing capacities may be clearly attributed to the 3/4 in. thick square plate welded onto the bottom of the H-pile. The bottom steel plate creates a zone of loose materials between the flanges of the H-pile, resulting in a significant reduction of skin friction. This explanation is fully supported by test data of pile No. 1 and No. 3. Although these two piles were both made from 14BP73 steel H-pile, differed only 10 ft in length and driven less than 30 ft apart, the measured bearing capacity of pile No. 3 (i.e., the shorter pile

with bottom plate) was only about 50 percent of that of pile No. 1 (i.e., the longer pile with no bottom plate).

Figure 4.78 presents an analysis based on predicted bearing capacities for 26 of the 30 pile load tests analyzed above. The remaining four load tests (i.e., two tests from Tavenas' test series on H-piles and two tests from the Low-Sill piles) were considered inappropriate to be included in this error analysis. Explanations for these exclusions were fully provided in the section dealing with their analysis. It can be seen in Fig. 4.78 that all bearing capacities were predicted within an error band of ± 30 percent, with the majorities of them (i.e., 73 percent) lying within a ± 20 percent error band.

4.8.3 Design Charts

From this analysis, the approximate method is recommended as a rational approach for estimating pile bearing capacity of single piles driven vertically in sands. The computation procedure, however, appears cumbersome in routine, preliminary design situations involving homogeneous sand deposits. For these conditions, it is much more efficient to rely on design charts rather than performing computer analysis anew each time. For instance, the skin friction Q_s may be quickly estimated based on charts which show the results of analysis in dimensionless quantity such as the combined factor $K_s\tan\delta$ versus the relative depth D/B, covering practical ranges of ϕ and δ. The heavy solid lines in Figures 4.79, 4.80, and 4.81 provide typical examples of such design charts. For further comparison purposes , results obtained from six recent empirical and semi-empirical methods for estimating skin friction of single piles in sand were also superimposed on the same figures . These methods included recommended procedures from Vesic (1970), Meyerhof (1976), Tomlinson (1977), Poulos and Davis (1980), Coyle and Castello (1981) and The Canadian Foundation Engineering Manual (1985). The values of $K^*_s\tan\delta$ deduced from these methods were based on Equation 4.20.

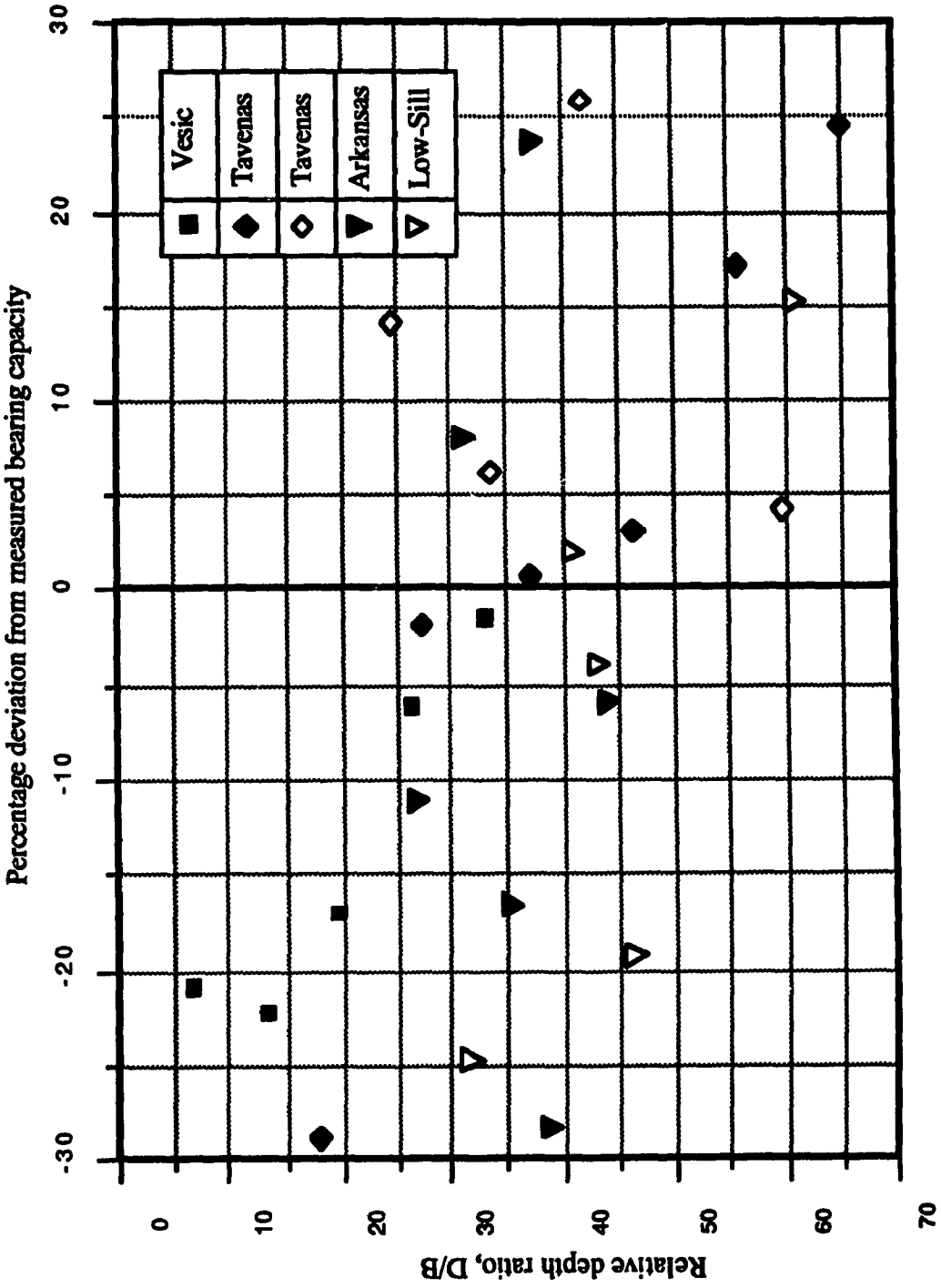

Fig. 4.78 Comparison Between Measured and Predicted Bearing Capacities

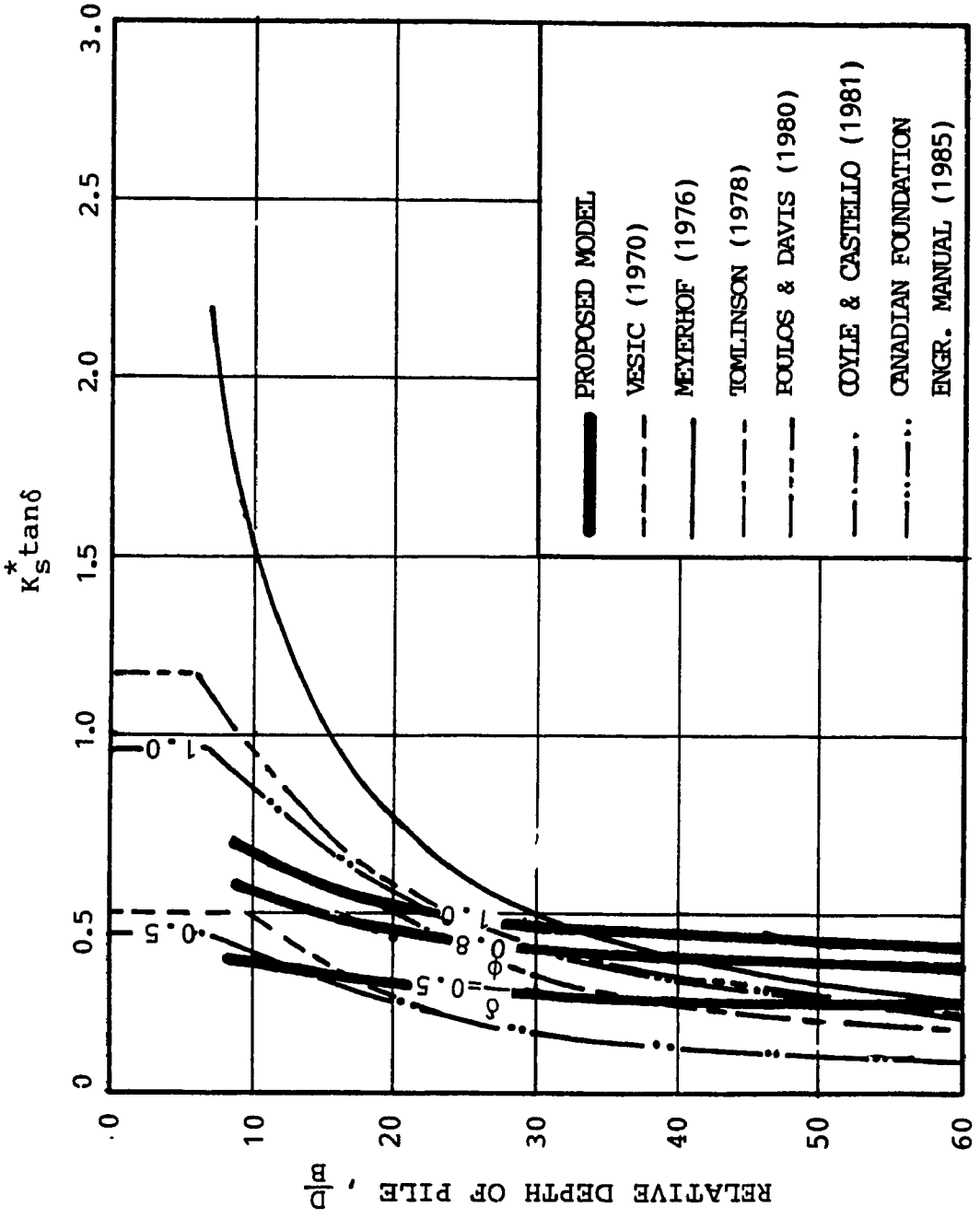

Fig. 4.79 Combined Factor $K^*_s \tan\delta$ Versus Relative Depth D/B ($\phi = 30°$)

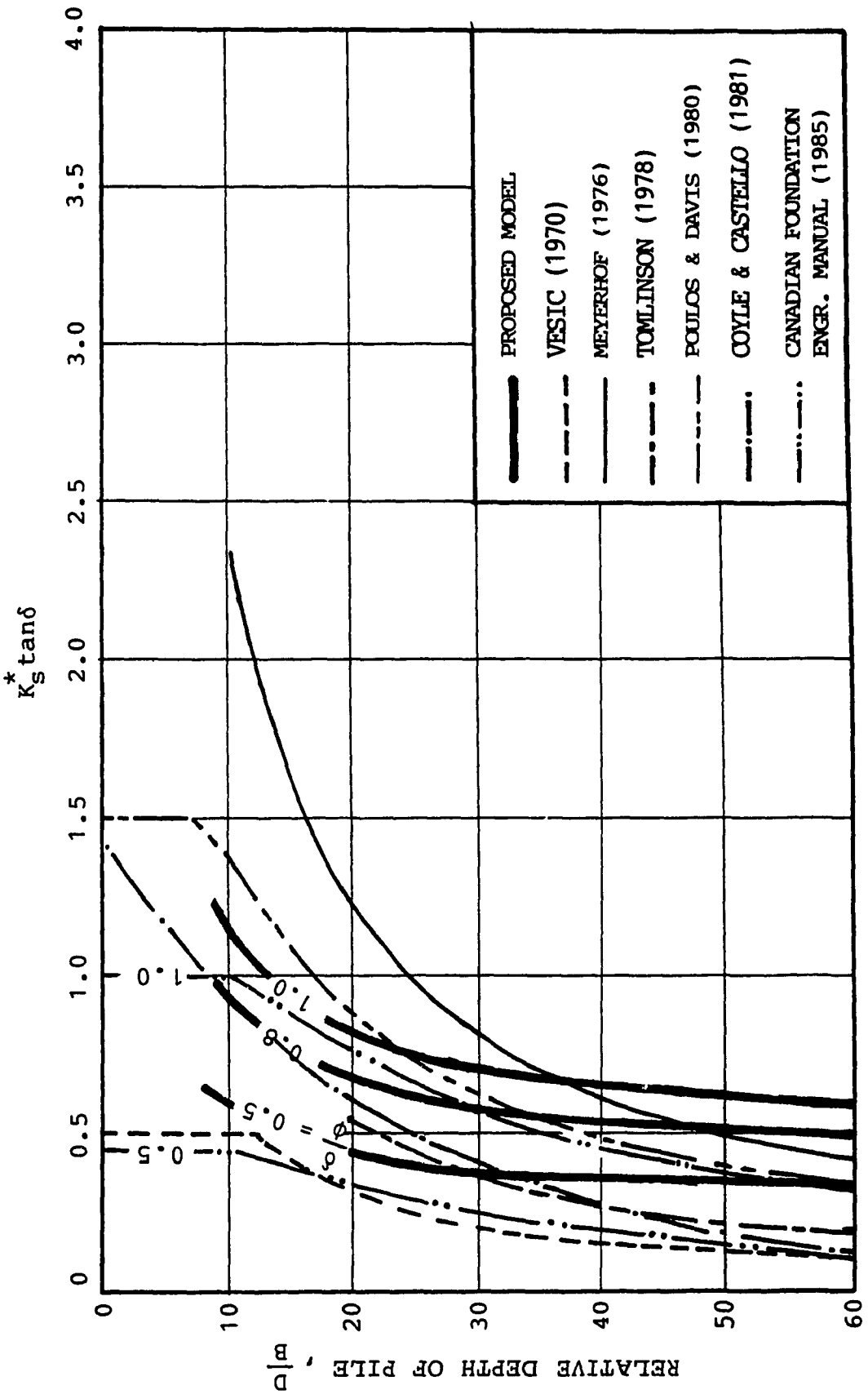

Fig. 4.80 Combined Factor $K^*_s \tan\delta$ Versus Relative Depth D/B ($\phi = 35°$)

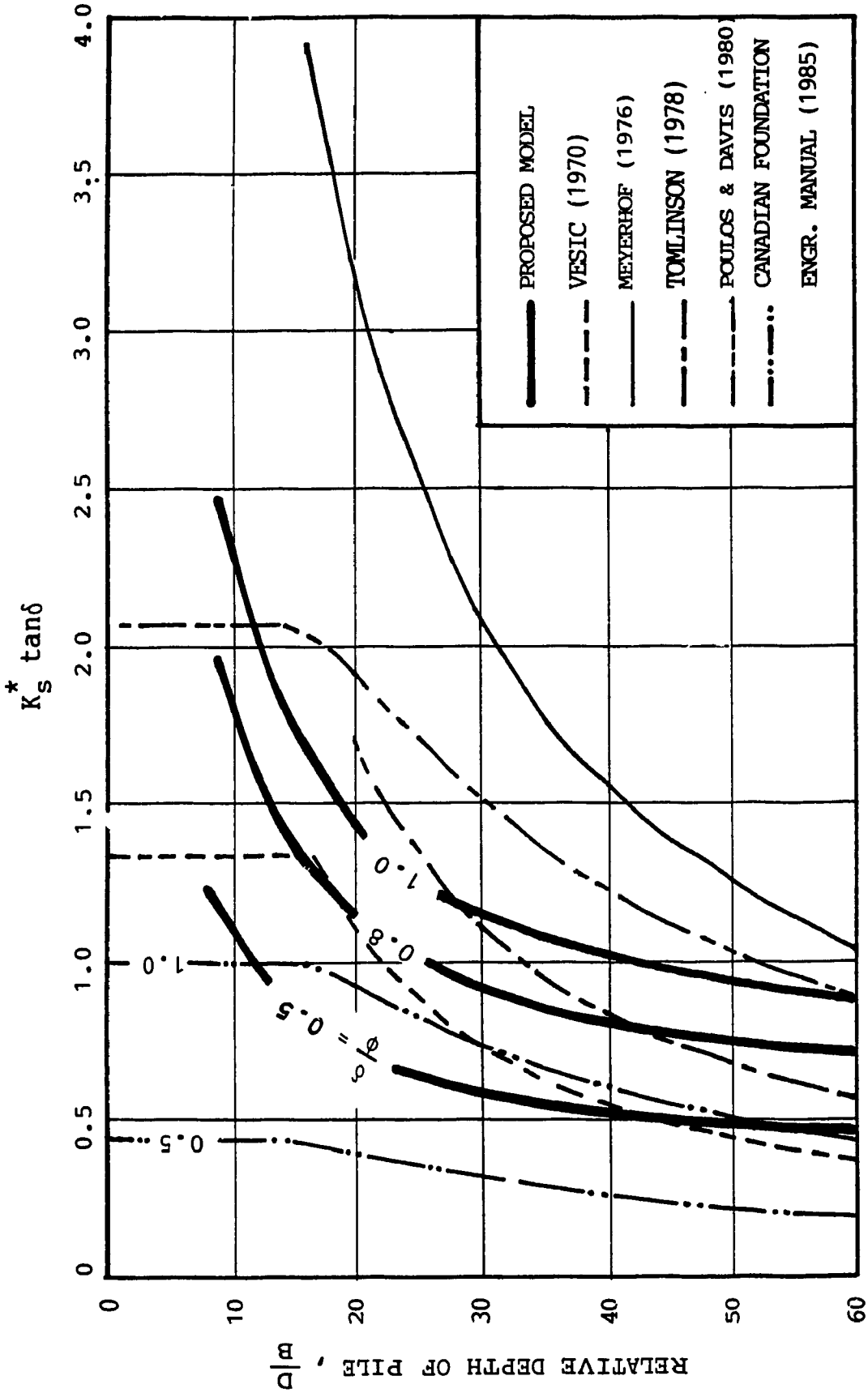

Fig. 4.81 Combined Factor $K^*_s \tan\delta$ Versus Relative Depth D/B ($\phi = 40°$)

The following example is used as the basis for the comparison: A 12 in. diameter pipe pile is driven into a homogeneous sand deposit, having a unit weight of 60 lbs/ft^3 (assume: ground water table is at ground level, and $K_o = 1 - \sin \phi$). It is desirable to estimate $K^*_s \tan\delta$ for this pile under specified conditions as follows:

ϕ = 30°, 35°, 40°

D/B = 10, 20, 30, 40, 50, 60

δ/ϕ = 0.5, 0.8, 1

It can be seen from Fig. 4.79 , 4.80 and 4.81 that values of the combined factor $K^*_s \tan\delta$ computed from the proposed model generally fit well within the range of variations of their counterparts from other authors. In particular, the proposed model is capable of theoretically predicting the common variation trend of $K^*_s \tan\delta$ with D/B as indicated by the empirical and semi-empirical methods.

4.9 RECOMMENDED DESIGN PROCEDURE

On the basis of the present investigation, the recommended procedure to estimate the ultimate bearing capacity of a single vertical pile driven in sands may be summarized as follows:

1. From the angle of shearing resistance ϕ of sand and the relative depth D/B of the pile, calculate the point resistance Q_q using Berezantzev's bearing capacity factor in Eq . 4.19.
2. The skin friction Q_S may be computed by Eq. 4.20 in which the combined factor $K^*_s \tan\delta$ is estimated from the design charts , typified in Figs. 4.79, 4.80, and 4.81. Linear interpolation based on these figures may provide reasonable estimates of $K^*_s \tan\delta$ values within practical ranges of ϕ, D/B and δ.
3. The ultimate bearing capacity Q_u is then given by the sum of Q_p and Q_s.
4. In case a more detailed calculation is preferred , the computer program TEMPO may be

used in computing the ultimate bearing capacity , following the procedure outlined in section 4.7.

5. For piles driven into a two-layered sand , the same procedure as in step 4 applies, except that in this case K_o, K_T and R should be estimated on the basis of an average angle of shearing resistance $\bar{\phi}$, defined by Eq. 4.33.

The recommended procedure described above is subjected to the following limitations:

i. It is not applicable for very short piles (i.e. D/B<10). In these cases the assumption of punching shear failure is not strictly valid. According to Vesic (1967), the failure mode under a foundation experiences a gradual transformation from a general shear failure near the ground surface to local shear failure, and finally punching shear failure as the foundation is advanced to lower depth.

ii. For very deep pile (i.e. D/B>70) field tests are needed to validate the suggested procedure.

iii. For piles driven in overconsolidated sand deposits,the procedure results in a conservative estimate of pile bearing capacity. Further research into the effect of K_o on point resistance and skin friction may lead to a more economical design.

iv. Bored piles are not suited for this recommended procedure because in its present state of development, the proposed model is amenable basically to cases in which an increase in earth pressure on the pile shaft is expected after pile installation. Consequently, only driven displacement piles fall into this catagories. As for H-piles, as long as the complete plugging of the pile flanges are ascertained, the recommended procedure seems equally applicable.

CHAPTER 5

CONCLUSIONS AND RECOMMENDATIONS

5.1 GENERAL

The important conclusions drawn from the present investigation are summarized in this concluding chapter which includes suggestions for further work.

5.2 CONCLUSIONS

1. The present investigation results in a theoretical model capable of incorporating three important features previously unaccounted for in most conventional bearing capacities of deep foundations, namely: treating the pile bearing capacity problem under axisymmetric conditions; adopting punching shear failure as the principal failure mode; and taking into account the interdependence between point resistance and skin friction.

2. In implementing the variable shearing resistance mobilized along critical shear surfaces, Sarma's method of slices was found particularly effective, especially with inclined slices which are easily adopted in the radial shear zone, and amenable to computerized techniques.

3. Findings from the parametric study indicate that the slope of the terminal radial surface (i.e., angle β) appears to be a major parameter affecting the bearing capacity factor N^*_q and the coefficient of earth pressure at the pile shaft K^*_s.

4. Within the context of analyzed load test results, the model suggests an alternative

explanation for the critical depth concept. The combined effects of a variable failure mechanism, in which the terminal radial surface moves gradually downward from the pile tip level, and a variable shearing resistance mobilized along critical surfaces result in a decrease of the bearing capacity factor N^*_q with depth. This tendency is counter balanced by the increasing overburden pressure at the pile tip level. Consequently, relatively constant point resistance may persist when these two opposite trends neutralize each other over certain range in depth. As for the skin friction, the proposed model seems to support recent findings indicating that the average unit skin friction does not become constant below certain depth but continues to increase with depth.

5. The model clearly demonstrates that a realistic estimate of skin friction is possible if the angle β is known by deduction from the point resistance, and the shearing resistance mobilized on the terminal radial surface is assumed to vary linearly with the distance from the pile shaft. This conclusion is verified by results of load tests performed on the 1.5 in. and 3. in. diameter model piles used in this present investigation. In addition, the predicted earth pressures along the pile shaft also show good agreement with normal pressures measured in the 3. in. diameter pile. Other available laboratory and field load tests provide further solid support for this conclusion.

6. The above conclusion forms the theoretical basis for a design procedure to estimate the ultimate bearing capacity of a single pile driven in sand. Accordingly, it is suggested that the point resistance computed on the basis of Berezantzev's bearing capacity factor, may be used in the model to calculate skin friction. Ultimate bearing capacities estimated according to this design procedure show good agreement with field load test results, attested by the fact that more than 70 percent of these tests were predicted within ±20 percent of their

measured counterparts in a correlation study involving 26 well documented field tests.

7. The estimation of ultimate bearing capacity of piles driven in two-layered sands seems possible using the present model with minor corrections for the layering effect.

5.3 RECOMMENDATIONS FOR FUTURE STUDIES

Many aspects of the bearing capacity problem as anticipated on the proposed model need further research. Among these, the following appear to be the most important:

1. The extent of the zone of influence around a circular pile driven in sand should be investigated experimentally, focusing on the effects of density of the sand, size, depth and surface roughness of the pile, and especially the confining pressure.

2. Futher investigation should be done to study the lateral earth pressure effects on bearing capacity of piles in sand within the theoretical frame work of the present investigation. It is speculated once the relationship between the coefficient of earth pressure at-rest K_o and the radius of influence R is established experimentally, the model appears to be easily modified to incorporate these new findings.

3. It is recommended to extend the present study to clays and homogeneous soils possessing both cohesion and friction.

4. The proposed model holds potential promise in the study of bearing capacity of piles in layered soils since it has been formulated on the basis of the method of slices, a technique particularly suitable for stratified soil conditions.

REFERENCES

1. Al-Awkati, A.Z. (1975), "On Problems of Soil Bearing Capacity at Depth", Ph.D. Thesis, Duke University, North Carolina, U.S.A.

2. Awad, A. and Petrasovits, G. (1968), "Consideration on the Bearing Capacity of Vertical and Batter Piles Subjected to Forces Acting in Different Directions", Proc. 3rd Budapest Conf. Soil Mech. and Found. Engr., Akadémiai Kiado, pp. 483-497.

3. Berezantzev, V.G. et al. (1961), "Load Bearing Capacity and Deformation of Piled Foundations", Proc. 5th Int. Conf. Soil Mech. and Found. Engr., Vol. II, pp. 11-15.

4. Berezantzev, V.G. (1965), "Design of Deep Foundations", Proc. 6th Int. Conf. Soil Mech. and Found. Engr., Vol IV, pp. 234-237.

5. Bishop, R.F. et al. (1945), "The Theory of Indeptation and Hardness Test", Proc. of the Physical Society, Vol. 57, pp. 147-159.

6. Broms, B.B. and Silberman, J.O. (1964), "Skin Friction Resistance for Piles in Cohesionless Soils", Sols-Soils, No. 10, pp. 33-43.

7. Broms, B.B. (1966), "Methods of Calculating the Ultimate Bearing Capacity of Piles: A summary", Sols-Soils, No. 18, pp. 21.

8. Coyle, H.M. and Castello, R.M. (1981), "New Design Correlations for Piles in Sand", Jnl. Geot. Engr. Div., ASCE, Vol. 107, No. GT7, pp. 965-986.

9. Coyle, H.M. and Sulaiman, I.H. (1967), "Skin Friction for Steel Piles in Sand", Jnl. Soil Mech. Found. Div., ASCE, Vol. 93, SM6, pp. 261-278.

10. Canadian Foundation Engineering Manual (1985), Second Edition, Canadian Geotechnical Society, Technical Committee on Foundations.

11. D'Appolonia, E. and Romualdi, J.P. (1963), "Load Transfer in End Bearing Steel H

Piles", Jnl. Soil Mech. Found. Div., ASCE, Vol. 89, SM2, pp. 1-25.

12. Durgunoglu, H.T. and Mitchell, J.K. (1973), "Static Penetration Resistance of Soils", Space Sciences Laboratory, Series 14, Issue 24, University of California, Berkeley, CA.

13. Gibson, R.E. (1950), Discussion, Jnl. Institution of Civil Engr., Vol. 34, p. 382.

14. Habib, P. (1953), "Essais de Charge Portante de Pieux en Modèle Reduit", Annales de l'Institut Technique du Bâtiment et des Travaux Publics, No. 63-64, pp. 361-366.

15. Hanna, T.H. and Tan, R.H.S. (1973), "The Behavior of Long Piles Under Compressive Loads in Sand", Can. Geot. Jnl., Vol. 10, pp. 311-340.

16. Hu, G. (1965), "Bearing Capacity of Foundations with Overburden Shear", Sols-Soil, No. 13, pp. 11-18.

17. Jaky, J. (1948), "On the Bearing Capacity of Piles", Proc. 2nd Int. Conf. Soil Mech. and Found Engr., Vol. I, pp. 100-103.

18. Janbu, N. and Senneset, K. (1974), "Effective Stress Interpretation of In-Situ Static Penetration Tests", Proc. European Symposium on Penetration Testing, Stockholm, Vol. 2.2, pp. 181-193.

19. Janbu, N. (1976), "Static Bearing Capacity of Friction Piles", Proc. 6th European Conf. Soil Mech. and Found. Engr., Vol. 1.2, pp. 479-488.

20. Kérisel, J. (1961), "Fondations Profondes en Milieux Sableux: Variation de la Force Portant Limit en Fonction de la Densité, de la Profondeur, du Diametre et de la Vitesse d'Enfoncement", Proc. 5th Int. Conf. Soil Mech. and Found. Engr., Vol. 2, pp. 73-83.

21. Kérisel, J. (1964), "Deep Foundations: Basic Experimental Facts", Proc. North American Conf. on Deep Foundations, Mexico City, Vol. I, pp. 5-44.

22. Kérisel, J. et al. (1965), "Point Resistance in Cohesionless Media at Various Densities", Proc. 6th Int. Conf. Soil Mech. and Found. Engr., Vol. III, pp. 265-269.

23. Kulhawy, F.H. (1984), "Limiting Tip and Side Resistance: Fact or Fallacy", Proc. Analysis and Design of Pile Foundations, Meyer J.R. Editor, ASCE, pp. 80-98.

24. L'Herminier, R. (1953), "Remarques sur le Poinçonnement Continue des Sables et Graviers", Annales de l'Institut Technique du Bâtiment et des Travaux Publics, No. 63-64, pp. 377-386.

25. Ladanyi, B. (1961), "Étude Théorique et Expérimentale de l"Expansion dans un Sol Pulvérulent d'une Cavité Présentant une Symétrie Sphéricale ou Cylindrique", Annales des Travaux Publics de Belgique, Vol. 62, pp. 105-148, pp. 365-406.

26. Ladanyi, B. (1963), "Expansion of Cavities in a Saturated Clay Medium", Jnl. Soil Mech. Found. Div., ASCE, Vol. 90, No. SM4, pp. 127-161.

27. Ladanyi, B. (1969), "Use of the Deep Penetration Test in Sensitive Clays", Proc. 7th Int. Conf. on Soil Mech. and Found. Engr., Vol. I, pp. 225-230.

28. Mackey, R.D. (1966), "Active and Passive Pressures on Curved Surfaces", Sols-Soil, No. 17, pp. 31-40.

29. Mansur, C.E. and Kaufman, R.I., " Pile Tests, Low-Sill Structure, Old River, Louisiana", Transactions, ASCE, Vol. 123, pp. 715-748.

30. McClelland, B. et al. (1967), "Problems in Design and Installation of Heavy Loaded Pipe Piles", Proc. Conf. Civil Engr. in the Oceans, ASCE, pp. 601-634.

31. Meyerhof, G.G. (1951), "The Ultimate Bearing Capacity of Foundations", Geotechnique, Vol. 2, pp. 301-322.

32. Meyerhof, G.G (1959), "Compaction of Sands and Bearing Capacity of Piles", Jnl. Soil Mech. and Found. Engr., ASCE, Vol. 85, No. SM6, pp. 1-29.

33. Meyerhof, G.G. (1976), "Bearing Capacity and Settlement of Pile Foundations", Jnl. Geot. Engr. Div., ASCE, Vol. 102, No. GT3, pp. 195-228.

34. Mohan, D. et al. (1963), "Load Bearing Capacity of Piles", Geotechnique, Vol. 13, pp.

76-86.

35. Norlund, R.L. (1963), "Bearing Capacity of Piles in Cohesionless Soils", Jnl. Soil Mech. Found Div., ASCE, Vol. 89. SM3, pp. 1-35.

36. Potyondy, J.G. (1961), "Skin Friction Between Soils and Various Construction Materials", Geotechnique, Vol. XI, No. 4, pp. 339-353.

37. Poulos, H.G. and Davis, E.H. (1980), "Pile Foundation Analysis and Design", John Wiley, New York.

38. Prandtl, L. (1920), "Uber die Harte Plastisher Korper", Nachirichten Kon. Gesell. des Wissenschafften, Bottingen, Math. Phys. Klasse, pp. 74-85.

39. Ranjan, G. (1970), "The Bearing Capacity of Batter Piles under Inclined Loads in Sand", Ph.D Thesis, Nova Scotia technical College, Halifax, Nova Scotia, Canada.

40. Reissner, H. (1924), "Zum Erdolruckproblem", Proc. 1st Int. Conf. Appl. Mech., Delft, Holland, pp. 295-311.

41. Robinsky, E.I. and Morrison, C.F. (1964), "Sand Displacement and Compaction Around Model Friction Piles", Can. Geot. Jnl., Vol. I, No. 2, pp. 81-93.

42. Robinsky, E.I. et al. (1964), "Effect of Shape and Volume on the Capacity of Model Piles in Sand", Can. Geot. Jnl., Vol. 1, No. 4, pp. 189-204.

43. Sarma, S.K. (1979), "Stability Analysis of Embankments and Slopes", Jnl. Geot. Engr. Div., ASCE, Vol. 105, No. GT12, pp. 1511-1524.

44. Schultze, E. (1953), "État Actuel des Methodes d"Evaluation de la Force Portant des Pieux en Aleemagne", Annales de l"Institut Technique du Bâtiment et des Travaux Publics, No. 63-64, pp. 305-312.

45. Skempton, A.W. et al (1953), "Théorie de la Force Portante des Pieux", Annales de l'Institut Technique du Bâtiment et des Travaux Publics, No. 63-64, pp. 285-289.

46. Széchy, C. (1960), "A New Pile Bearing Formula for Friction Piles in Cohesionless Sands", Symposium on Pile Foundations, Stockholm, pp. 73-76.

47. Tavenas, F.A. (1971), "Load Tests Results on Friction Piles in Sand", Can. Geot. Jnl., No. 8, pp. 7-22.

48. Terzaghi, K. (1943), "Theorectical Soil Mechanics, Wiley, New York, N.Y.

49. Tomlinson, M.J. (1977), "Pile Design and Construction Practice", Cement and Concrete Association, London.

50. Tomlinson, M.J. (1986), "Foundation Design and Construction", 5th Edition, Longman Scientific and Technical, Essex, England.

51. Vesic, A.S. (1963), "Bearing Capacity of Deep Foundations in Sand", Highway Research Record, No. 39, pp. 112-153.

52. Vesic, A.S. (1967), "A Study of Bearing Capacity of Deep Foundations", Final Report, Project B-189, Georgia Institute of Technology, Atlanta, Georgia, U.S.A.

53. Vesic, A.S. (1977), "Design of Pile Foundations", Synthesis of Highway Practice No. 42, Transporation Research Board, National Research Council, Washington, U.S.A.

APPENDIX 1

NOTES ON SARMA'S METHOD OF SLICES

In Sarma's method of slices (Sarma, 1979), the soil mass enclosed within an assumed plane slip suface is divided into a number of slices which are not required to have vertical sides. The geometric of and forces acting on a typical slice is shown in Fig. A 1.1

The equilibrium of horizontal and vertical forces give the following two equations:

$$E_i \cos \omega_i + X_i \sin \omega_i - E_{i+1} \cos \omega_{i+1} - X_{i+1} \sin \omega_{i+1} + FH_i + T_i \cos \alpha_i - N_i \sin \alpha_i = 0 \quad \text{... (A 1.1)}$$

$$E_i \sin \omega_i + X_i \cos \omega_i + E_{i+1} \sin \omega_{i+1} - X_{i+1} \cos \omega_{i+1} - FV_i - W_i - T_i \sin \alpha_i + N_i \cos \alpha_i = 0 \quad \text{... (A 1.2)}$$

In Eq. A1 and A2, replace S_i, S_{i+1}, and T_i, respectively, by:

$$X_i = E_i \tan \phi_{Si}$$

$$X_{i+1} = E_{i+1} \tan \phi_{Si+1}$$

$$T_i = N_i \tan \phi_{Bi}$$

After simplification, we obtain:

$$E_i = \left[\frac{\cos (\phi_{Si} - \omega_i)}{\cos \phi_{Bi}}\right] - E_{i+1}\left[\frac{\cos (\phi_{Si+1} - \omega_{i+1})}{\cos \phi_{Si+1}}\right] + FH_i$$

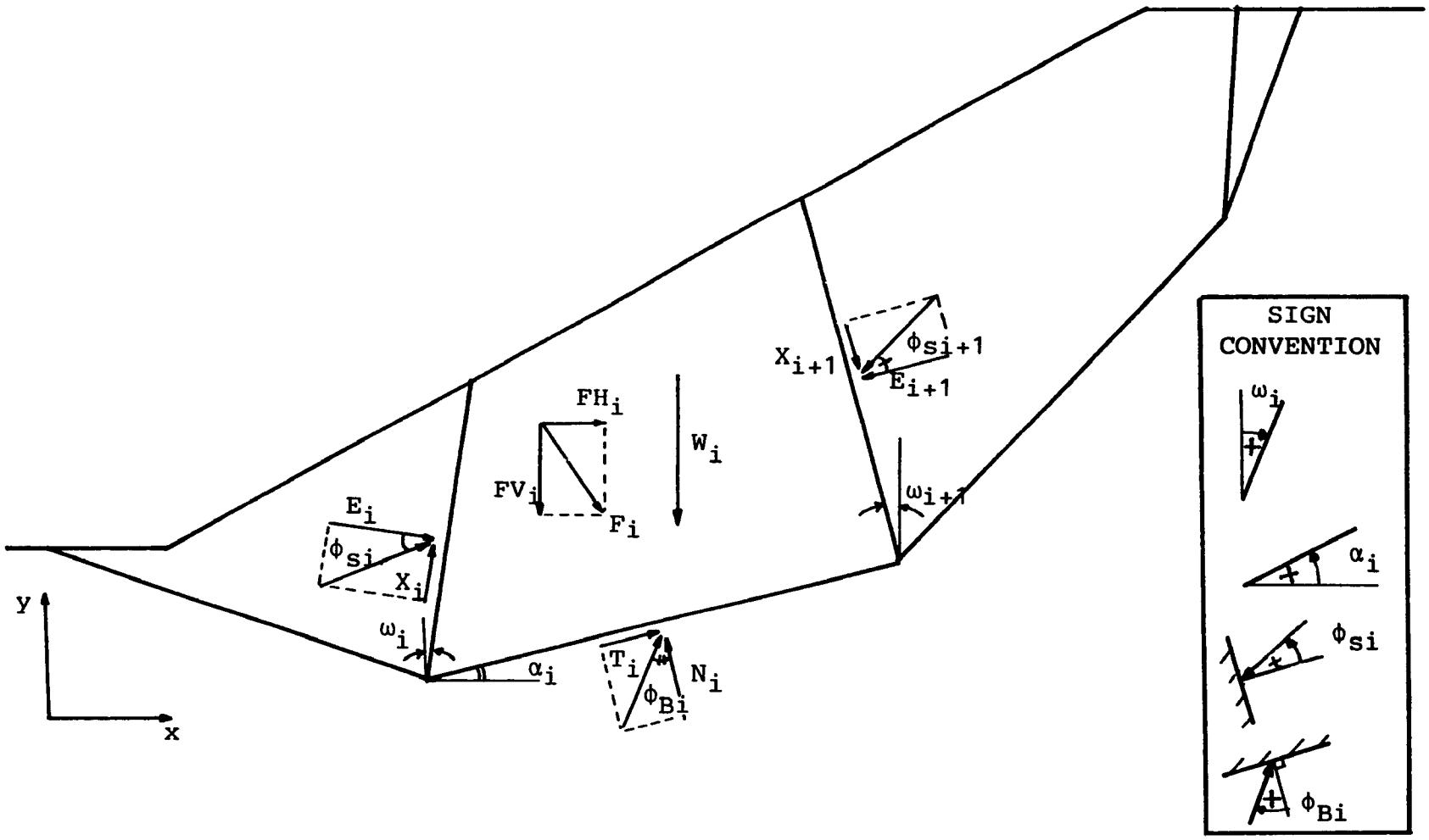

Fig. A 1.1 Forces Acting on a Typical Slice in Sarma's Method of Slices

$$- N_i \left[\frac{\sin (\phi_{Bi} - \alpha_i)}{\cos \phi_{Bi}} \right] = 0 \qquad \text{... (A 1.3)}$$

$$E_i \left[\frac{\sin (\phi_{Si} - \omega_i)}{\cos \phi_{Si}} \right] - E_{i+1} \left[\frac{\sin (\phi_{Si+1} - \omega_{i+1})}{\cos \phi_{Si+1}} \right] - FV_i - W_i$$

$$+ N_i \left[\frac{\cos (\phi_{Bi} - \alpha_i)}{\cos \phi_{Bi}} \right] = 0 \qquad \text{... (A 1.4)}$$

Eliminating N_i from Eq. A 1.3 and A 1.4,

$$E_i \cos (\phi_{Bi} - \alpha_i + \phi_{Si} - \omega_i) \cos \phi_{Si+1}$$

$$- E_{i+1} \cos (\phi_{Bi} - \alpha_i + \phi_{Si+1} - \omega_{i+1}) \cos \phi_{Si}$$

$$+ FH_i \cos \phi_{Si+1} \cos \phi_{Si} \cos (\phi_{Bi} - \alpha_i)$$

$$+ FV_i \cos \phi_{Si+1} \cos \phi_{Si} \sin (\phi_{Bi} - \alpha_i)$$

$$+ W_i \cos \phi_{Si+1} \cos \phi_{Si} \sin (\phi_{Bi} - \alpha_i) = 0$$

Finally, we obtain:

$$E_{i+1} = \frac{\cos (\phi_{Bi} - \alpha_i + \phi_{Si} - \omega_i) \cos \phi_{Si+1}}{\cos (\phi_{Bi} - \alpha_i + \phi_{Si+1} - \omega_{i+1}) \cos \phi_{Si}} E_i$$

$$+ \frac{(W_i + FV_i) (\cos \phi_{Si+1}) \sin (\phi_{Bi} - \alpha_i)}{\cos (\phi_{Bi} - \alpha_i + \phi_{Si+1} - \omega_{i+1})}$$

$$+ \frac{FH_i (\cos \phi_{Si+1}) \cos (\phi_{Bi} - \alpha_i)}{\cos (\phi_{Bi} - \alpha_i + \phi_{Si+1} - \omega_{i+1})} \qquad \text{... (4.5)}$$

APPENDIX 2

BEREZANTZEV'S BEARING CAPACITY FACTORS

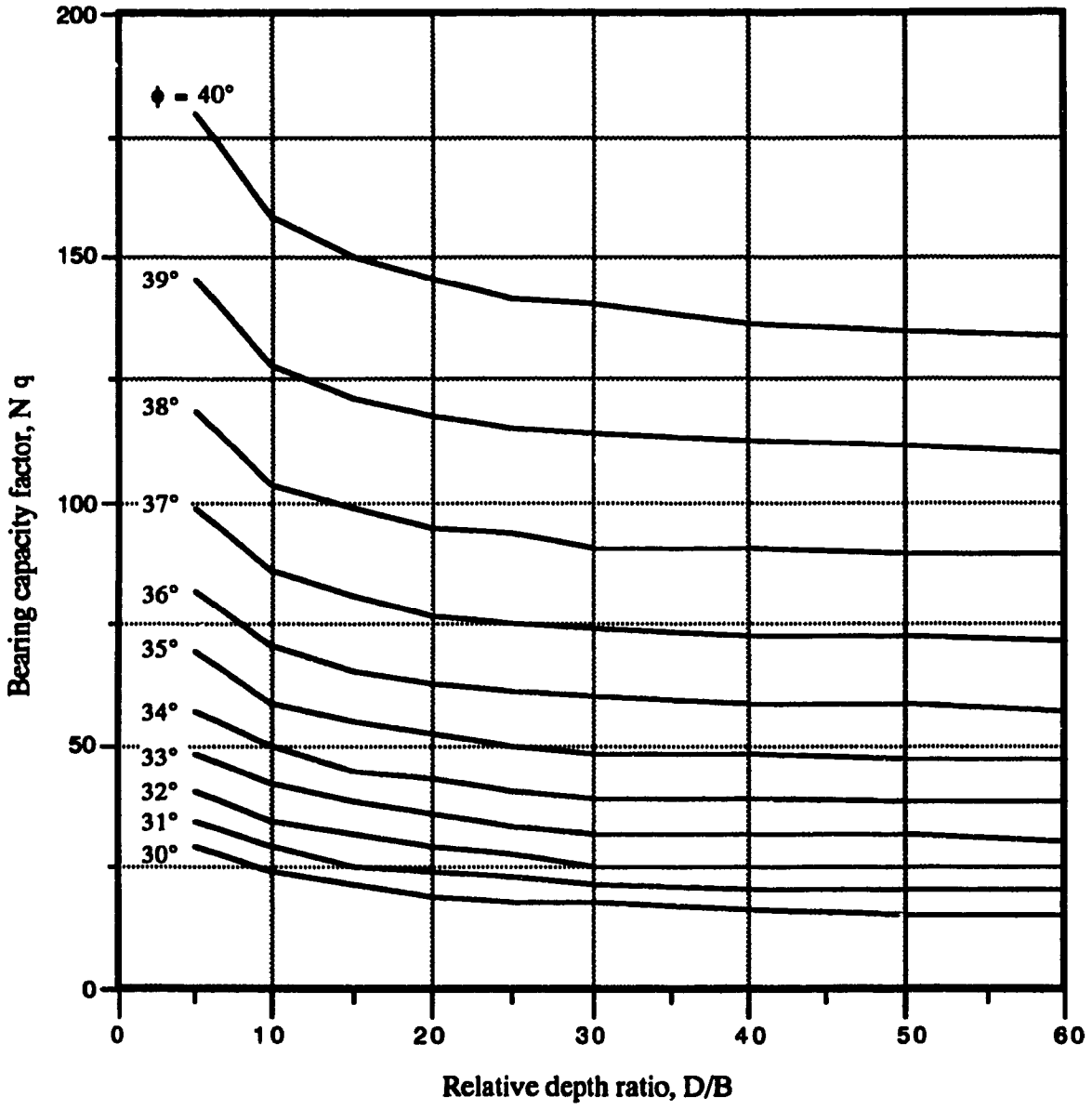

Fig. A 2.1 Berezantzev Bearing Capacity Factors (After Berezantzev, 1961)

APPENDIX 3

DETAILS OF VESIC'S LOAD TESTS ON 4 IN. DIAMETER MODEL PILE

Vesic's three test series on a 4 in. diameter steel model pile were performed with air dried Chattahoochee River Sand, contained in large cylindrical test pit, 8.3 ft. in diameter and 22 ft deep (Fig. A3.1a). The model pile was constructed on a similar principle to that of a deep cone penetrometer (Fig. A3.1b,. The main characteristics of Chattahoochee sand were summarized in Fig. A3.2, which also showed the relationship between its angle of shearing resistance ϕ and the void ratio e. This relationship was obtained by analyzing Vesic's original triaxial test data summarized in Table A3.1. The angle of friction δ between the pile shaft and Chattahoochee River sand was also estimated by Vesic to be about 32°, regardless of sand density.

The sand placement technique consisted of raining sand from a container with perforated bottom to produce a desired density. For relative density larger than 70 percent, every 4 in. thick sand layer which had been formed by raining sand from a height of 30 inches was compacted by means of an electrical vibrator.

A summary of Vesic's original load test results was presented in Table A3.2. However, due to some scattering in the original test data, Vesic's curves, reproduced in Fig. A3.3 and showing the variation of the unit point resistance q_p with depth, were used in computing the point load Q_p and equivalent bearing capacity factor N^*_q in Table 4.6.

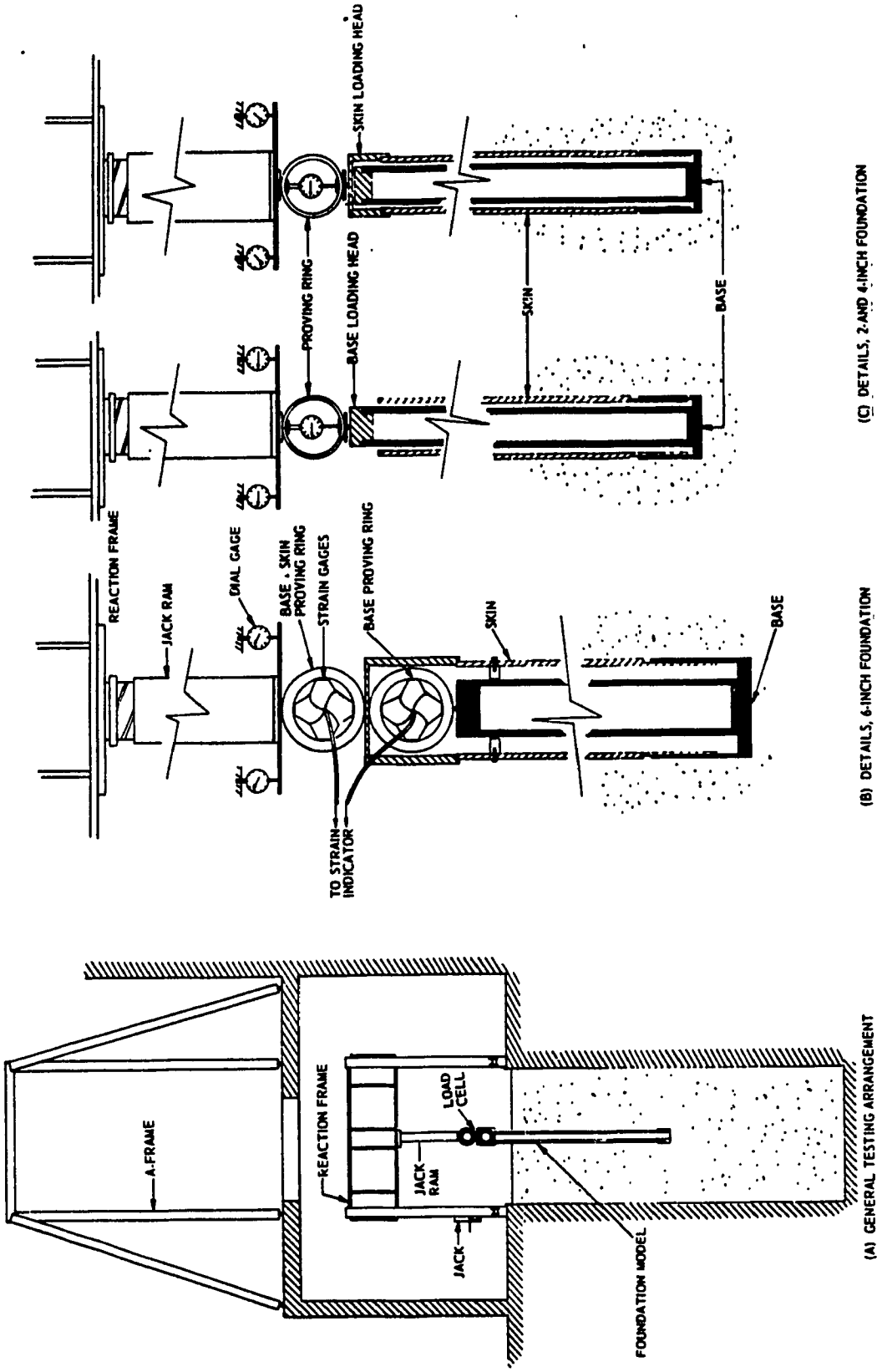

Fig. A3.1 Vesic's Experimental study (Vesic, 1967)

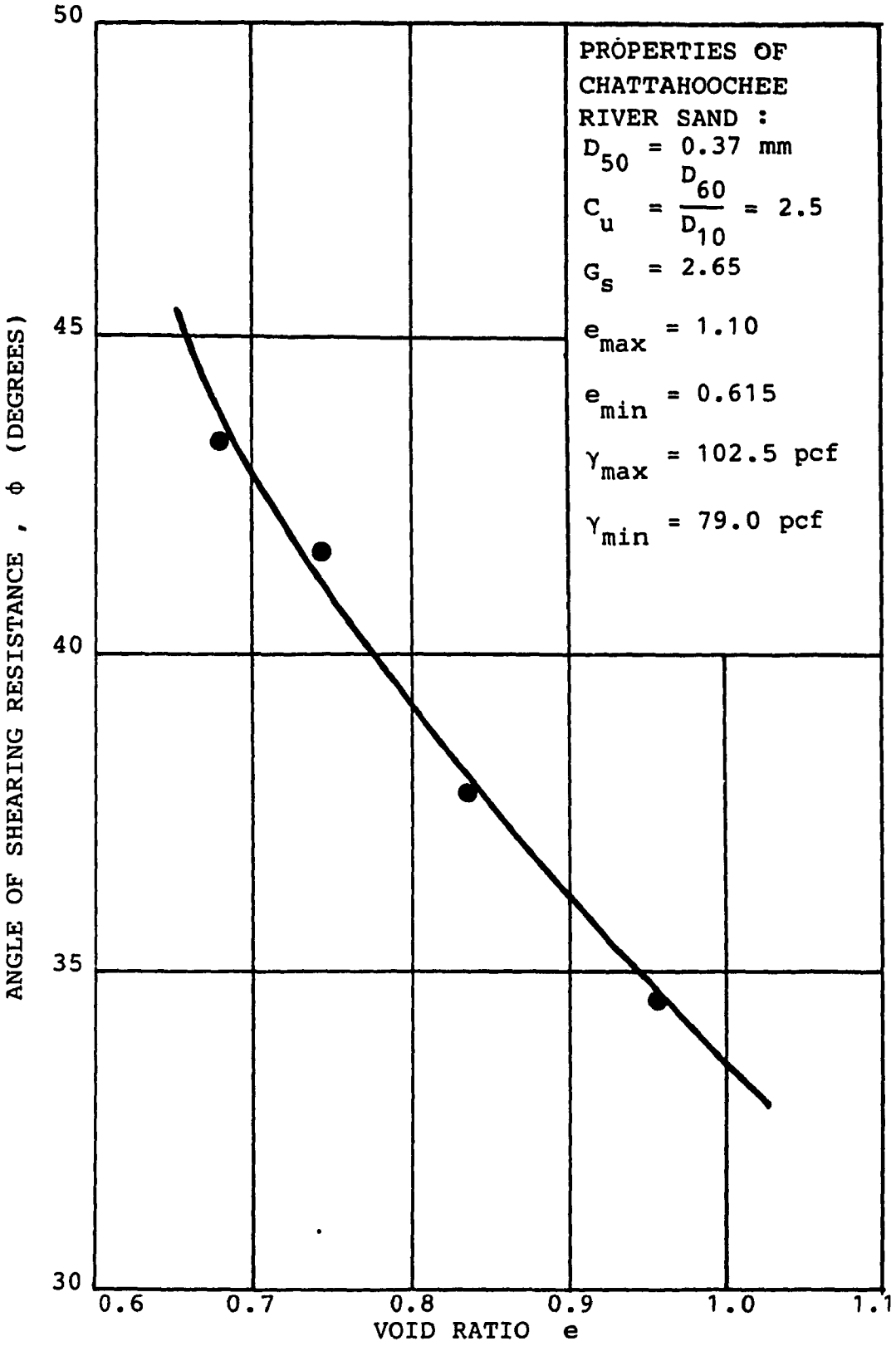

Fig. A 3.2 Angle of Shearing Resistance Versus Void Ratio for Chattahoochee River Sand (Data from Vesic, 1967)

Table A3.1: Results of Triaxial Tests on Chattahoochee Sand.

Vesic's Triaxial Test Data (Vesic, 1967; Table 3)				Results of Analysis in Present Study		
Test No.	Void Ratio, e	Cell Pressure, σ_3 (psi)	Deviator Stress at Failue, $(\sigma_1 - \sigma_3)$ (psi)	$\phi = \sin^{-1}\left[\frac{\sigma_1-\sigma_3}{\sigma_1+\sigma_3}\right]$ (deg.)	Mean ϕ (deg.)	Mean Void Ratio, e
1	0.957	5	13.3	34.8		
2	0.952	10	27.4	35.3		
3	0.957	10	31.0	37.4		
4	0.961	20	49.1	33.4		
6	0.970	40	90.4	32.0		
8	0.957	80	182.0	32.2	34.5	0.957
34	0.945	10	24.5	33.4		
40	0.957	40	96.0	33.0		
46	0.960	7	18.3	34.5		
47	0.956	7	20.6	36.9		
48	0.955	5	14.5	36.3		
5	0.830	20	62.2	37.5		
7	0.838	40	117.3	36.5		
11	0.847	5	16.9	38.9		
12	0.838	10	32.6	38.3		
13	0.838	20	62.4	37.5		
14	0.838	40	108.6	35.2		
15	0.830	10	40.5	42.0	37.8	0.836
31	0.813	20	60.1	36.9		
32	0.833	40	118.3	36.6		
33	0.830	55	156.2	35.9		
35	0.827	10	34.0	39.0		
38	0.859	40	115.7	36.2		
49	0.838	7	22.8	38.3		
50	0.836	7	25.0	39.9		
51	0.838	5	15.9	37.9		
16	0.747	5	22.5	43.8		
17	0.751	10	43.1	43.1		
18	0.742	20	78.3	41.4		
19	0.737	40	142.0	39.8		
20	0.737	75	247.9	38.6	41.6	0.745
39	0.755	35	125.7	40.0		
52	0.747	7	28.3	42.0		
53	0.745	7	31.0	43.5		
54	0.742	7	20.5	42.2		
21	0.691	5	24.3	45.1		
22	0.676	10	48.2	45.0		
23	0.678	20	79.4	41.7		
24	0.681	35	140.9	41.9		
25	0.678	70	250.7	39.9		
26	0.680	40	146.1	40.3	43.3	0.681
36	0.685	10	48.7	45.1		
41	0.681	5	23.5	44.5		
42	0.678	10	47.0	44.5		
43	0.681	20	83.2	42.5		
44	0.680	7	32.6	44.4		
45	0.682	7	34.1	45.1		

Table A3.2: A Summary of Vesic's Original Load Test Results on 4 in. Diameter Model Pile.

Type of Sand	Relative Density D_R (%)	Pile Embedment Depth, D (in.)	Relative Depth D/B	Mean Unit Weight (pcf)	Skin Friction, Q_s (lbs.)	Point Resistance, Q_p (lbs.)
Loose	31.2	20.1	5.0	85.0	220	716
		40.4	10.1		498	844
		60.5	15.1		654	814
		80.4	20.1		1020	894
		101.9	25.5		1511	986
		120.1	30.0		1811	1003
Medium Dense	59.8	21.2	5.3	91.5	293	1495
		40.7	10.1		747	1949
		63.9	16.0		1317	2432
		79.7	19.9		1963	2453
		103.3	25.8		2324	1717
		124.3	31.3		2421	2028
Dense	83.1	21.3	5.3	97.6	474	3814
		39.8	10.0		1435	6022
		61.6	15.4		2895	7542
		79.6	19.9		4561	9867
		104.0	26.0		6965	11199
		120.1	30.0		7561	10838

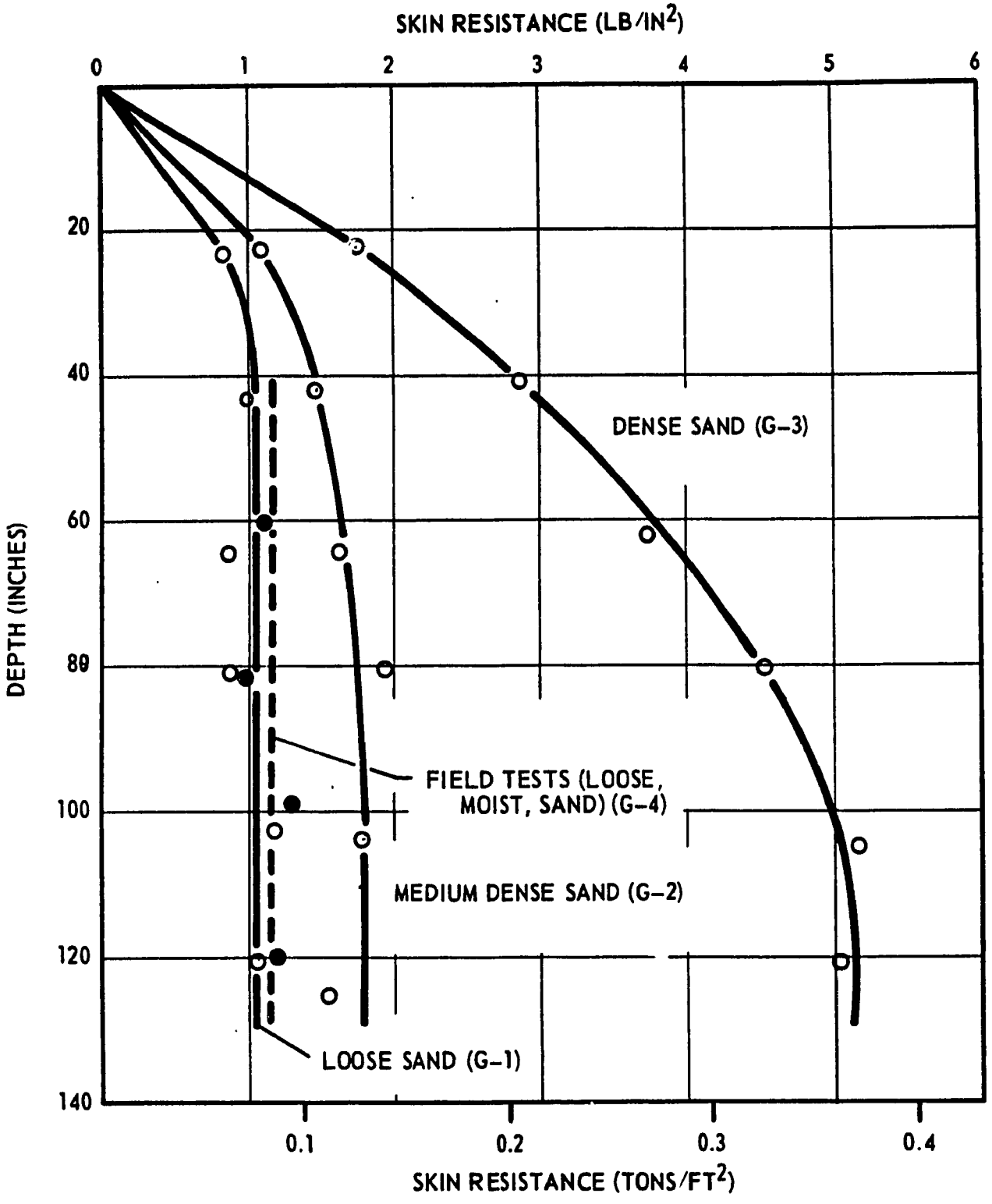

Fig. A 3.3 Vesic's Load Test Results on 4 in. Diameter Pile (Vesic, 1967)

APPENDIX 4

DETAILED DRAWINGS OF COMPONENTS AND ACCESSORIES OF MODEL PILES

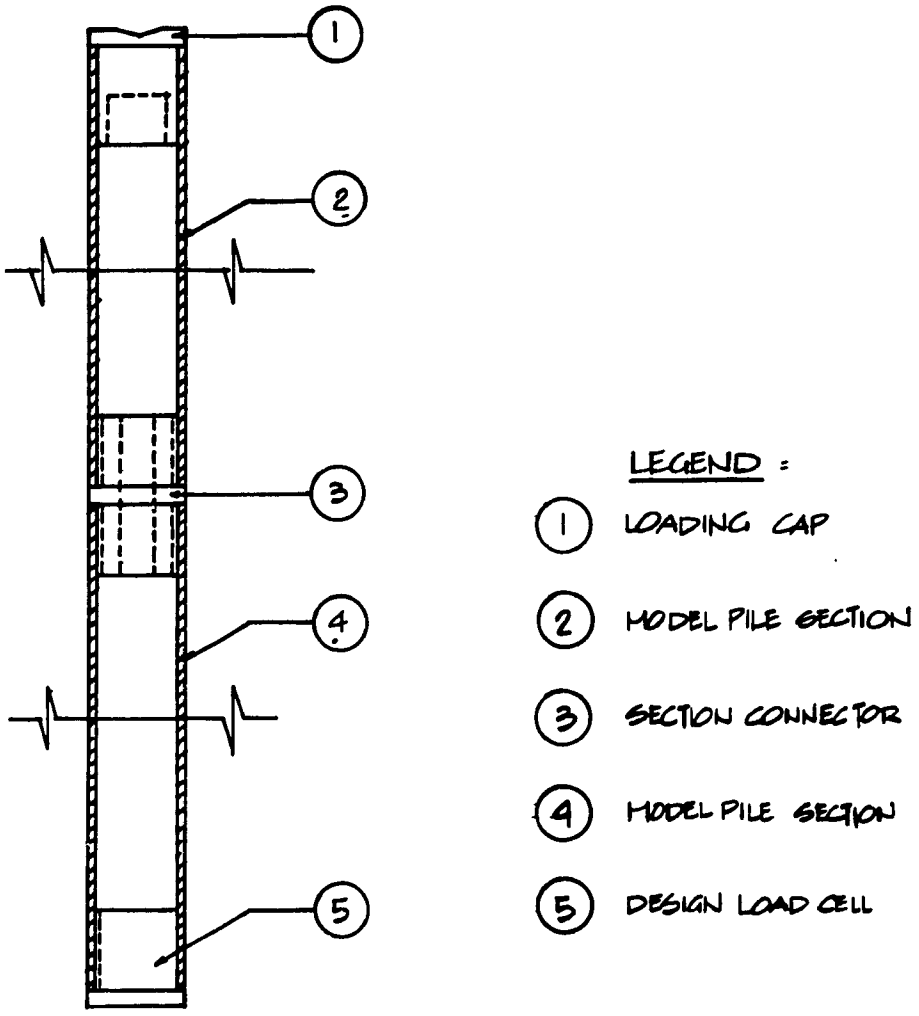

Fig. A 4.1 A Schematic Diagram of 1.5 in. Diameter pile

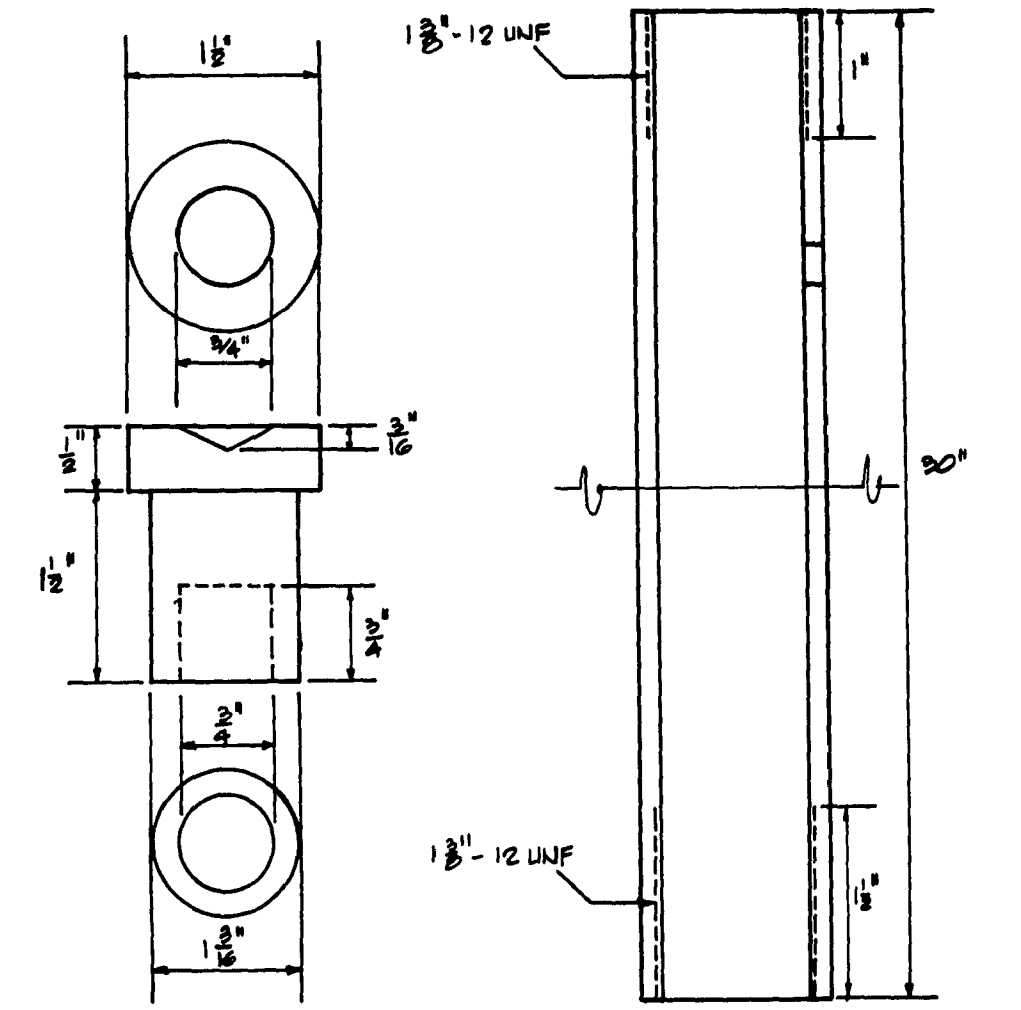

Fig. A 4.2 Components of 1.5 in. Diameter Pile (Part Nos. 1, 2)

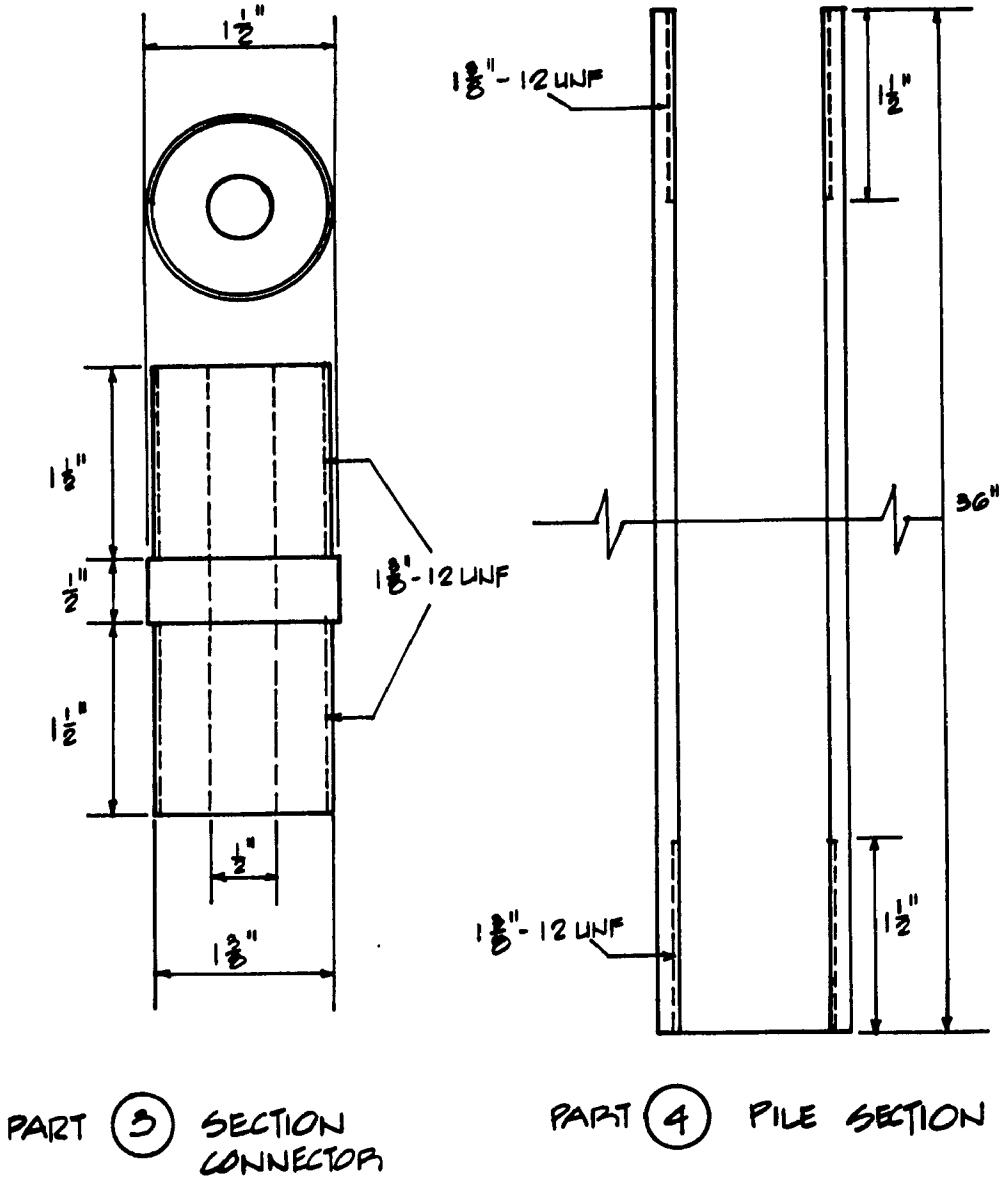

Fig. A 4.3 Components of 1.5 in. Diameter Pile (Part Nos. 3, 4)

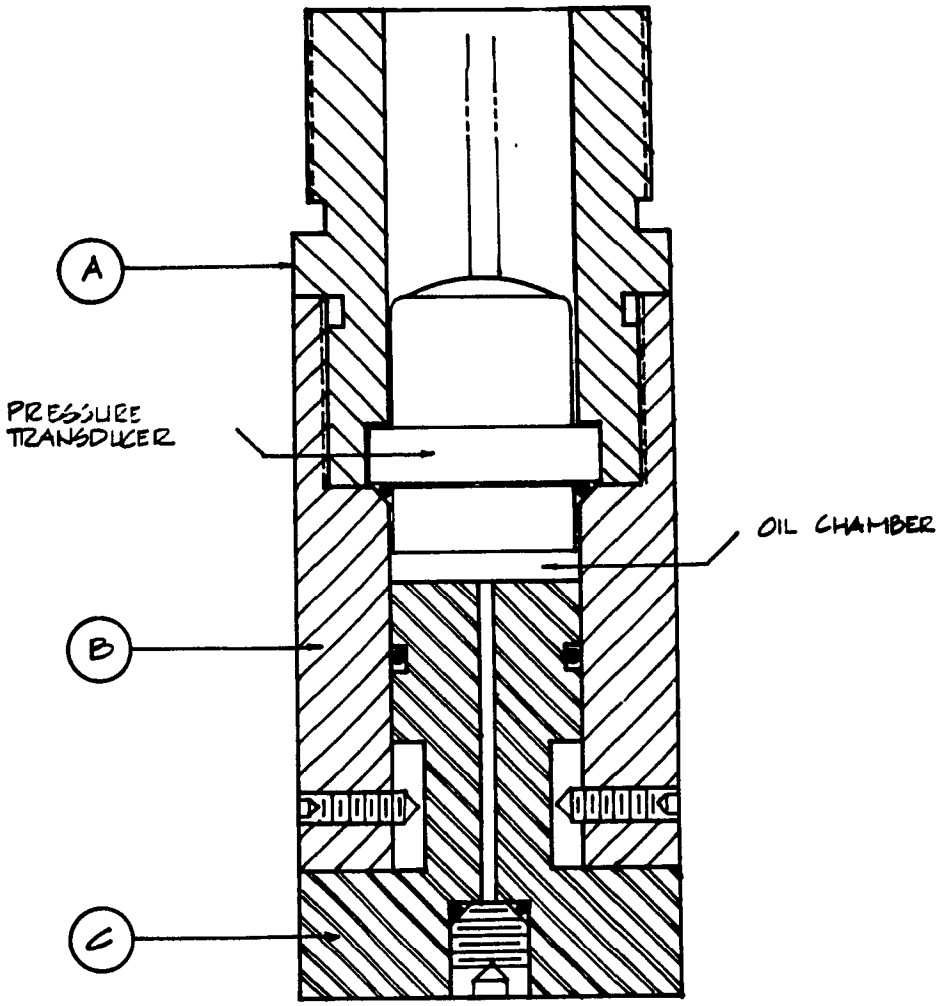

Fig. A 4.4 General Assembly of Load Cell at Pile Tip (Closed Position)

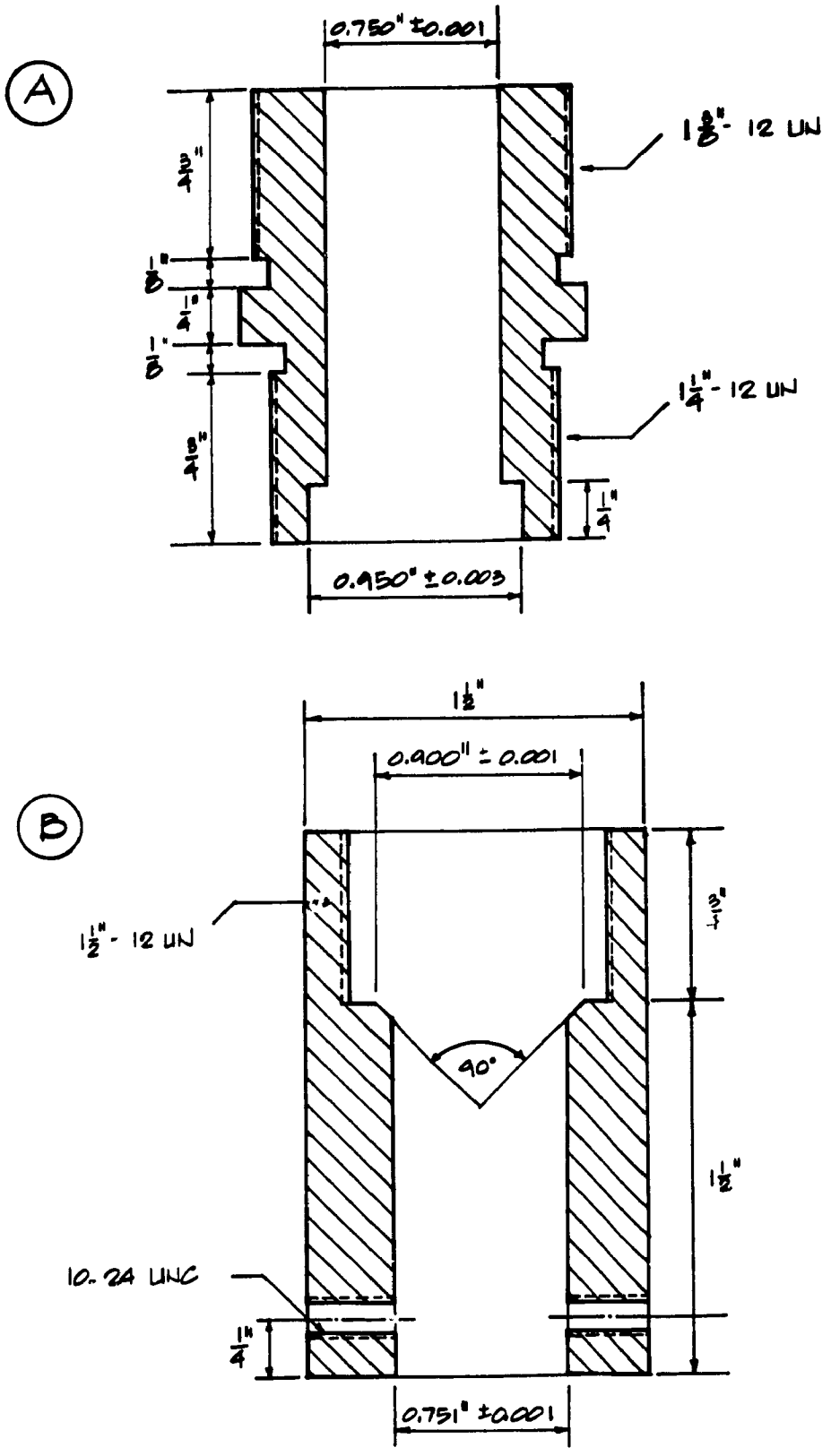

Fig. A 4.5 Details of Load Cell Components A and B (Fig. 3.13)

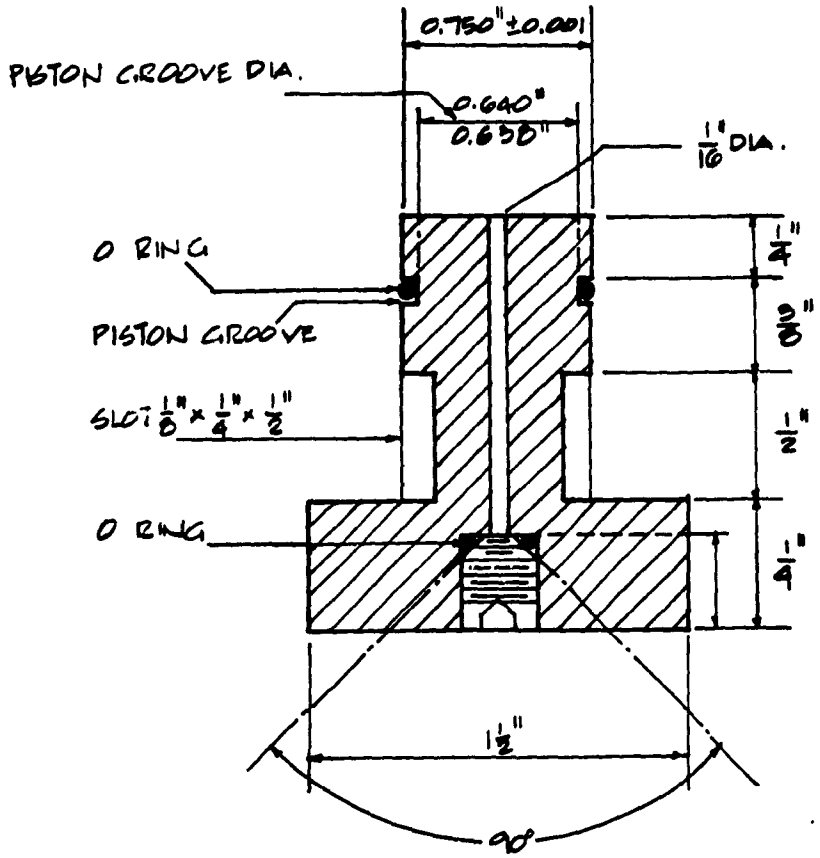

Fig. A 4.6 Details of Load Cell Component C (Fig. 3.13)

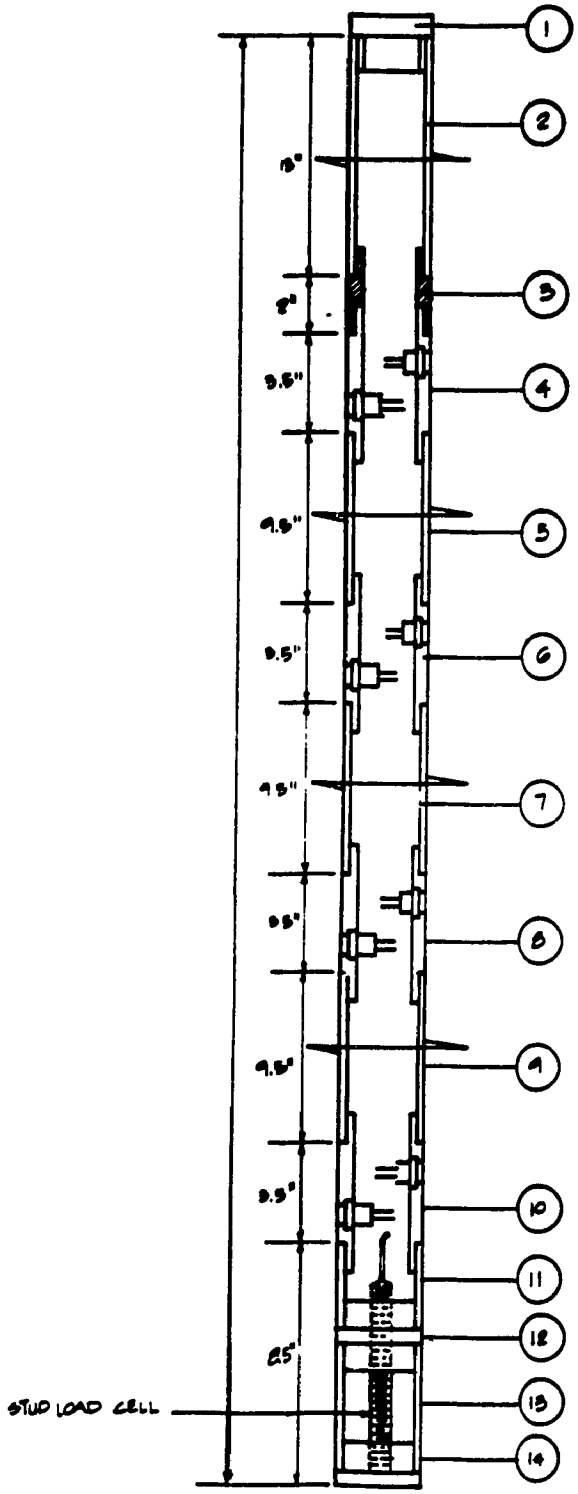

Fig. A 4.7 A Schematic Diagram of 3 in. Diameter pile

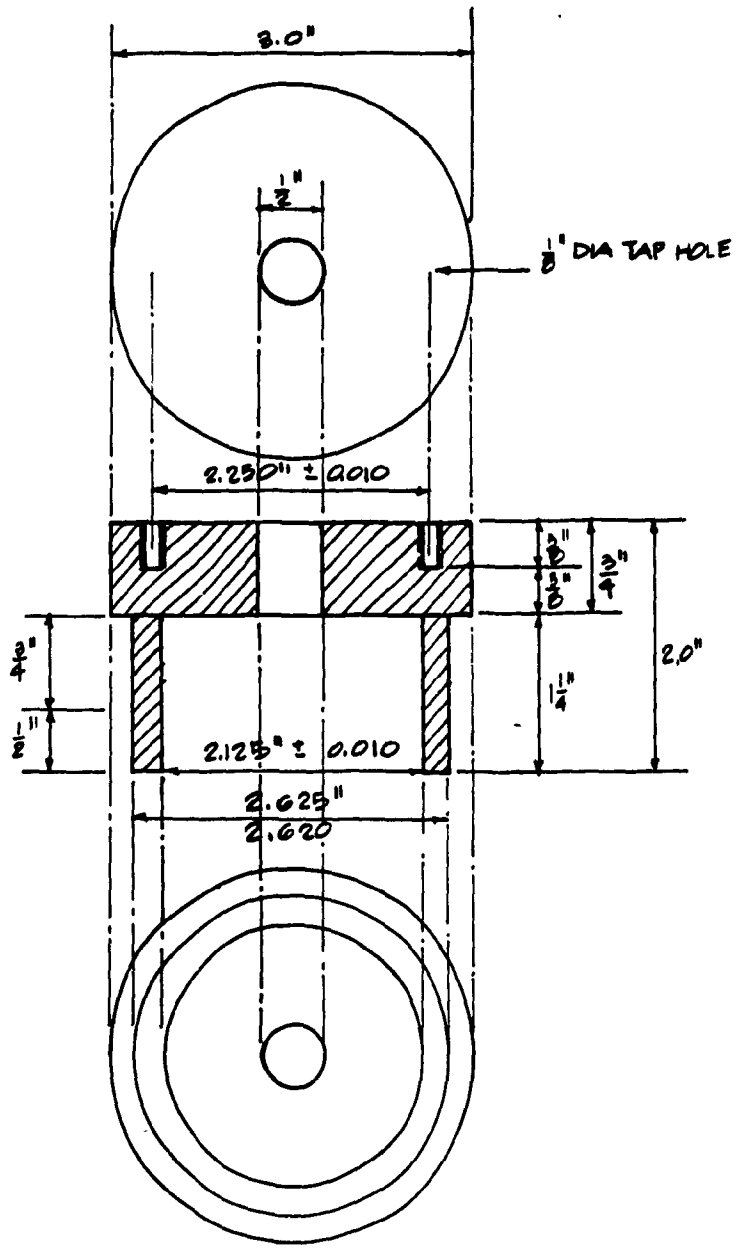

Fig. A 4.8 Pile Loading Cap (Part No. 1, Fig. A 4.7)

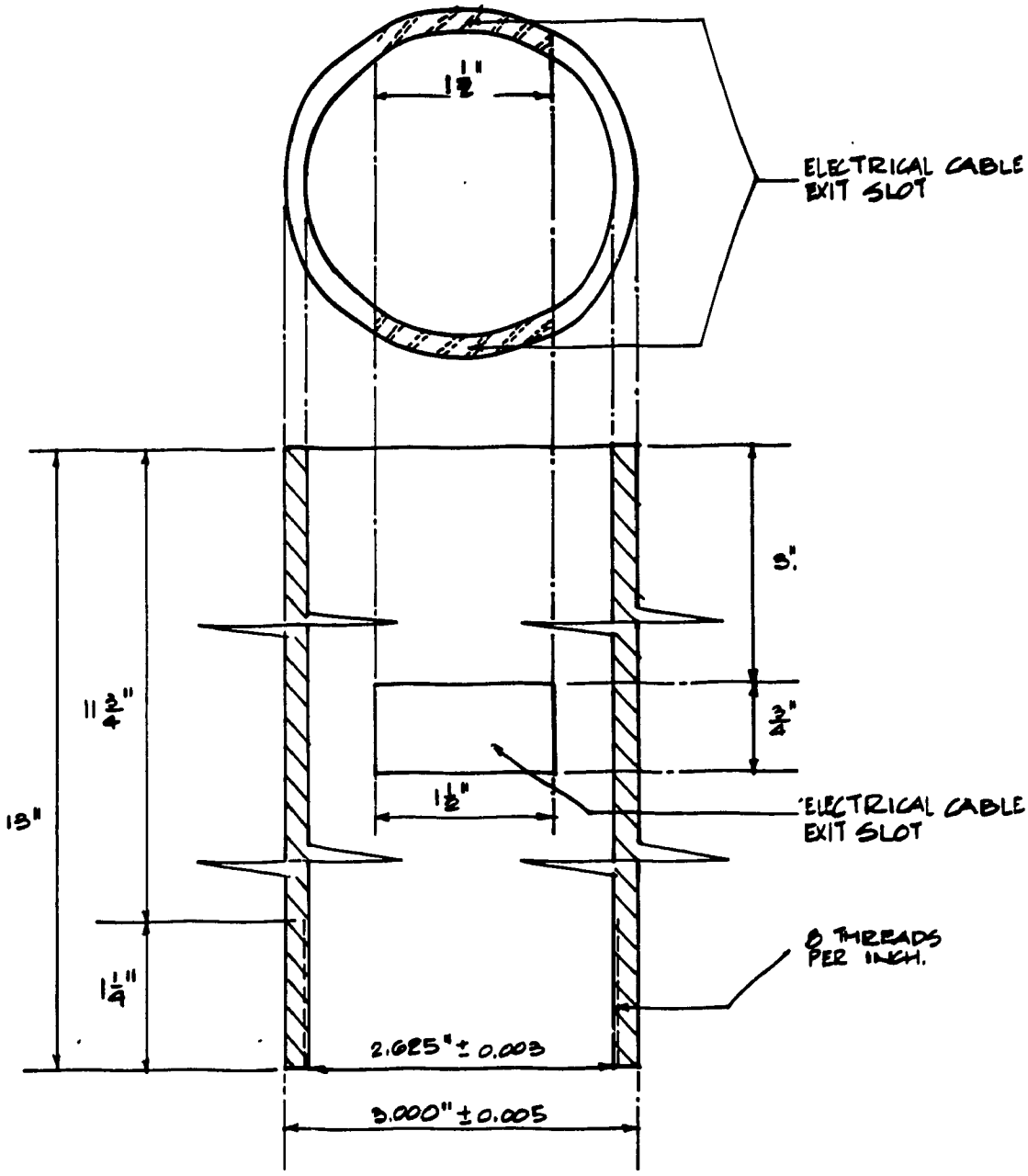

Fig. A 4.9 Steel Pipe Section (Part No. 2, Fig. A 4.7)

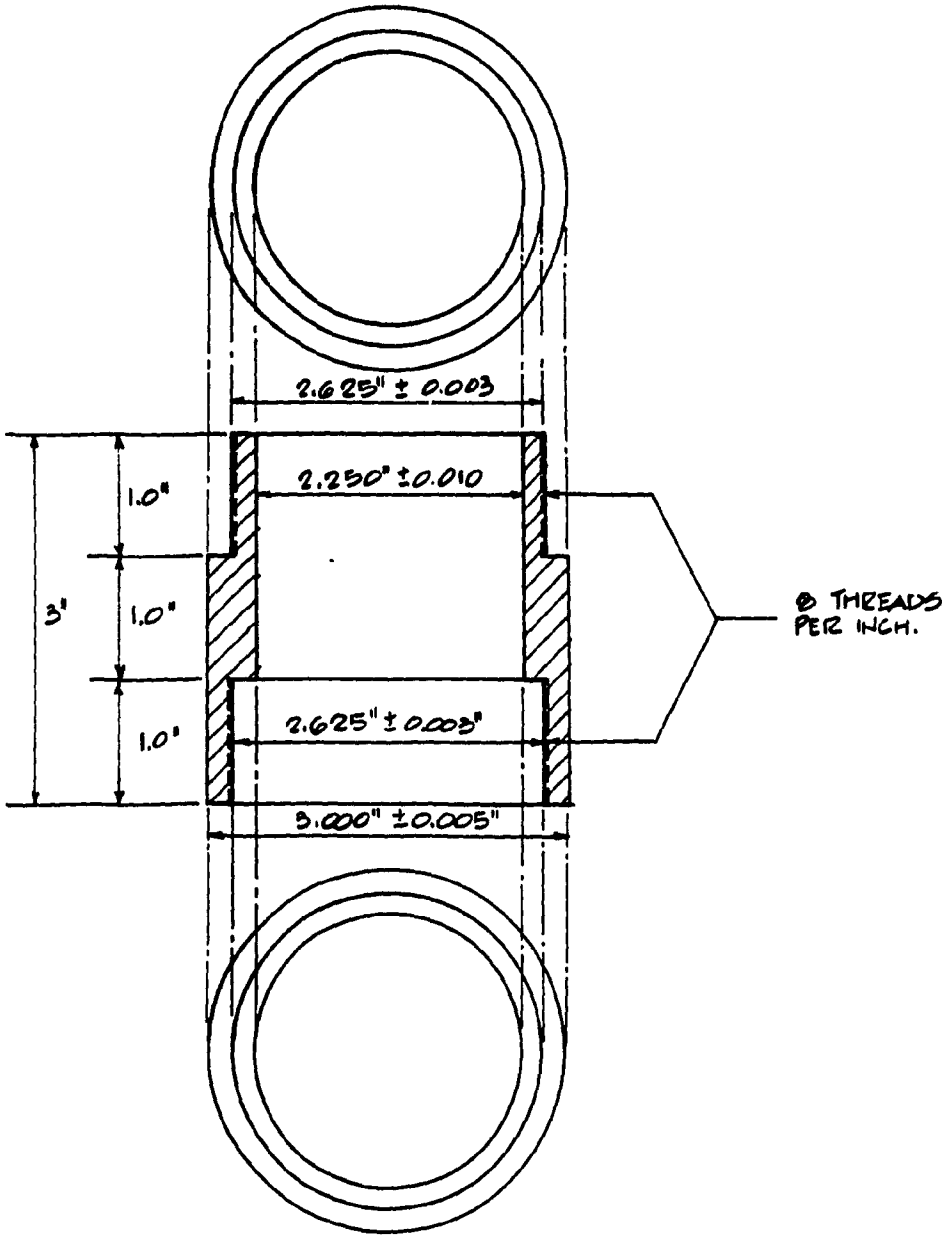

Fig. A 4.10 Steel Pipe Adaptor (Part No. 3, Fig. A 4.7)

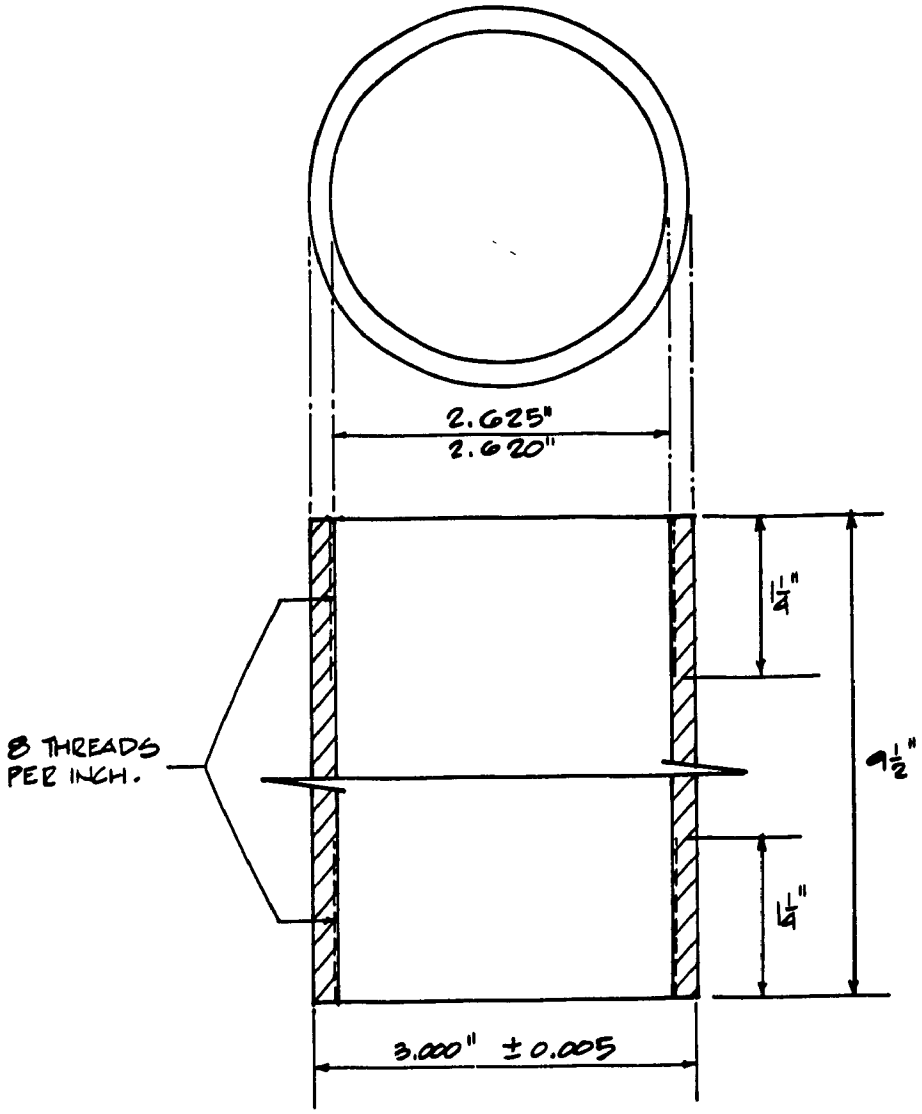

Fig. A 4.11 Steel Pipe Section (Parts No. 5, 6, 7, 9; Fig. A 4.7)

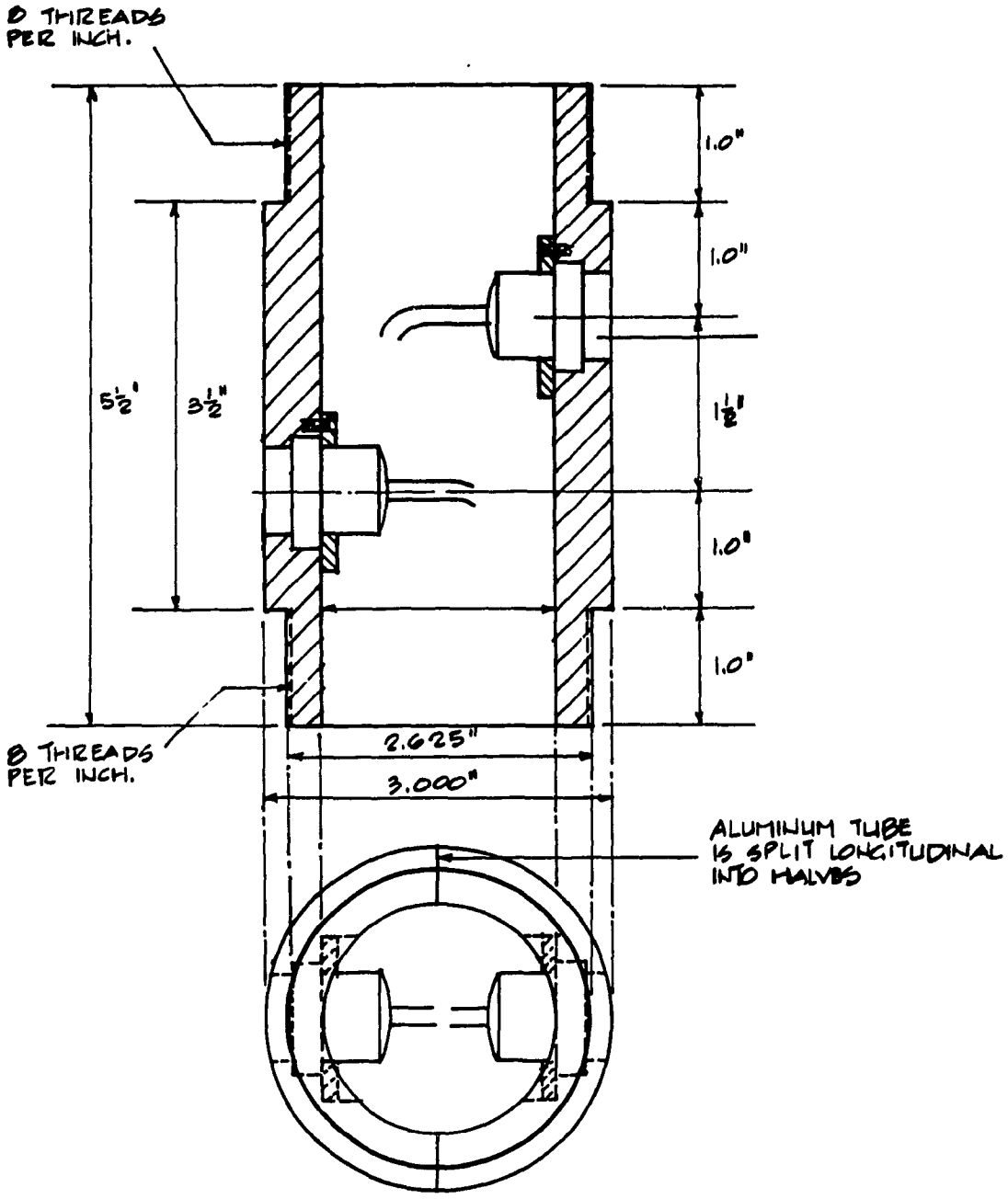

Fig. A 4.12 Aluminum Section (Parts No. 4, 6, 8, 10, Fig. A 4.7)

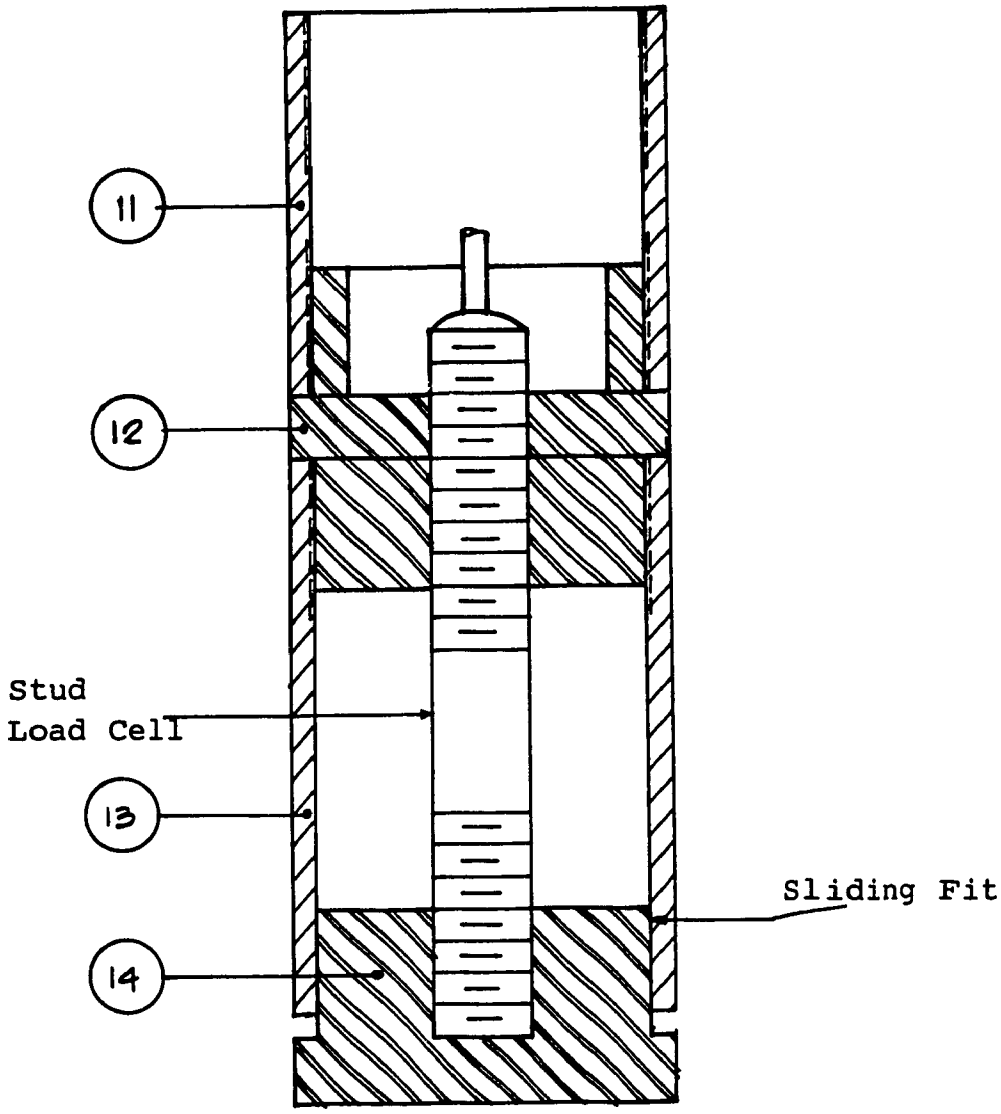

Fig. A 4.13 A Schematic Diagram of Stud Load Cell Installation

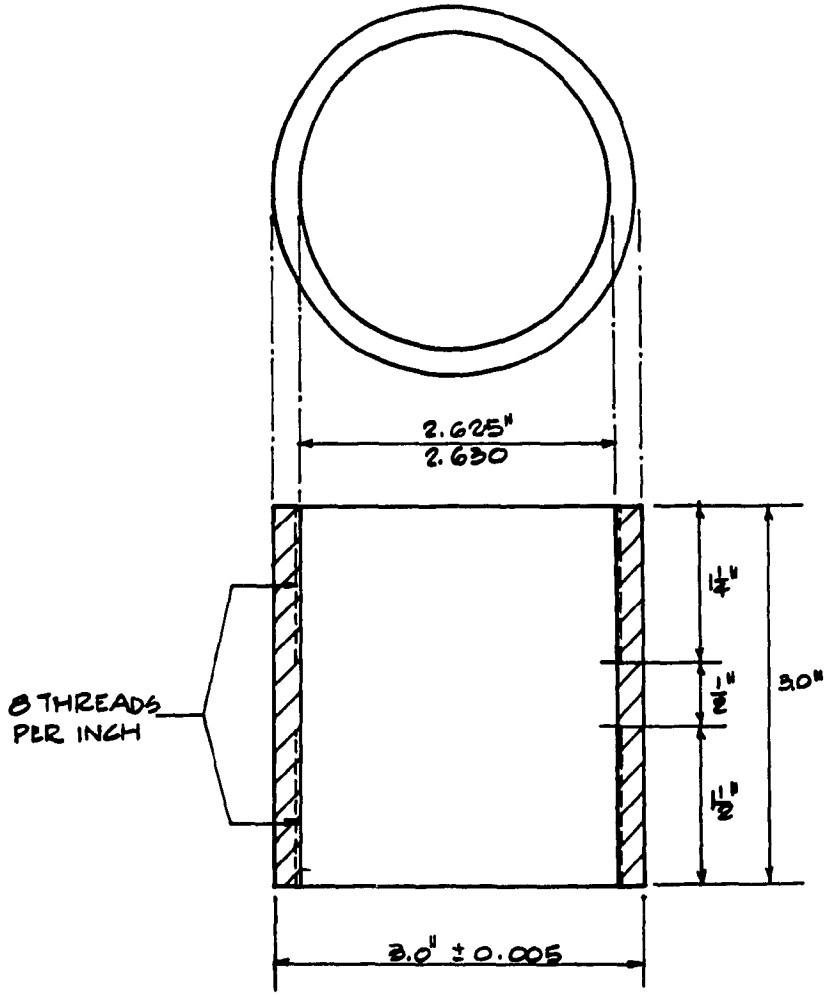

Fig. A 4.14 Steel Coupling (Part No. 11; Fig A 4.13)

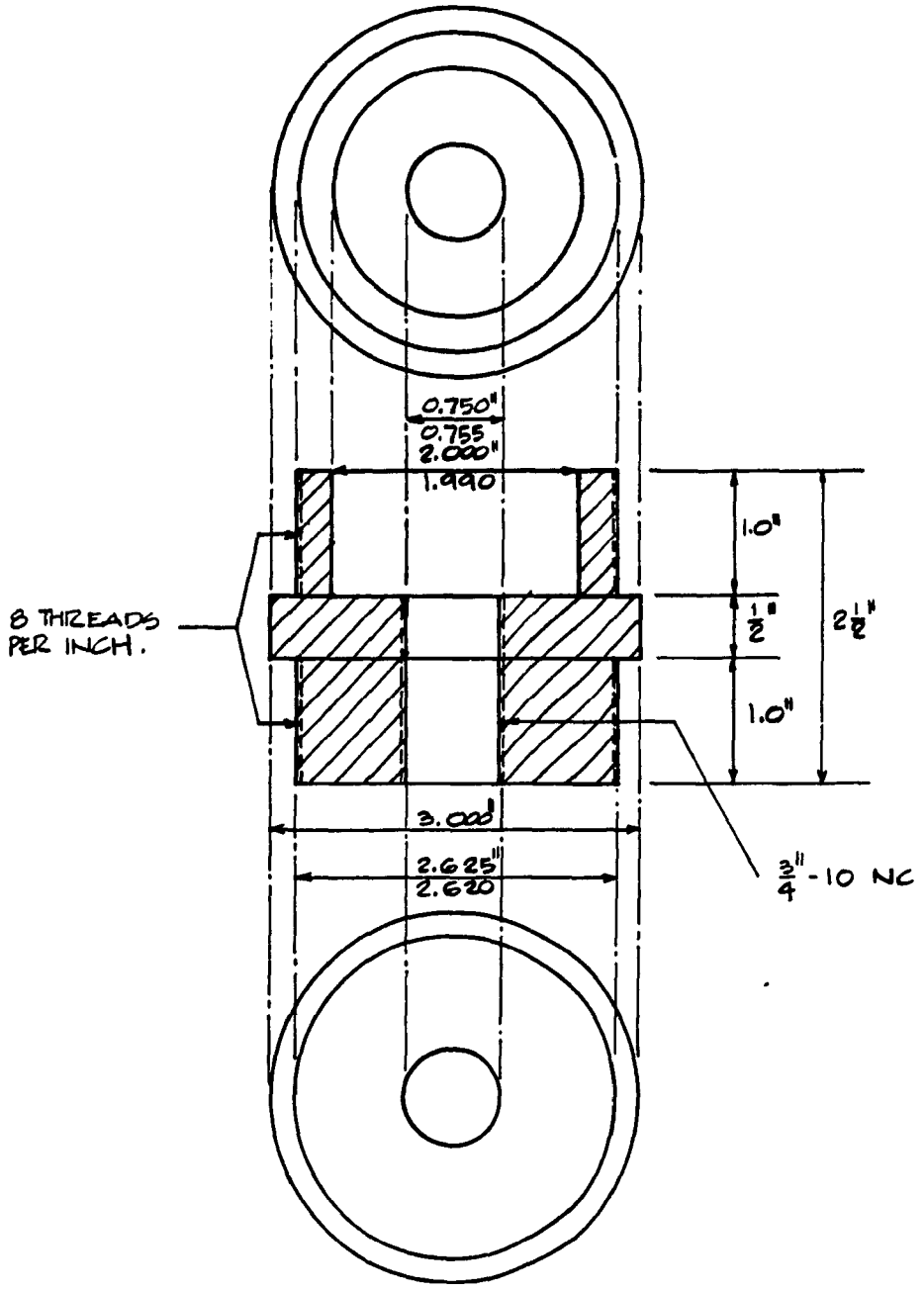

Fig. A 4.15 Steel Connector (Part No. 12; Fig A 4.13)

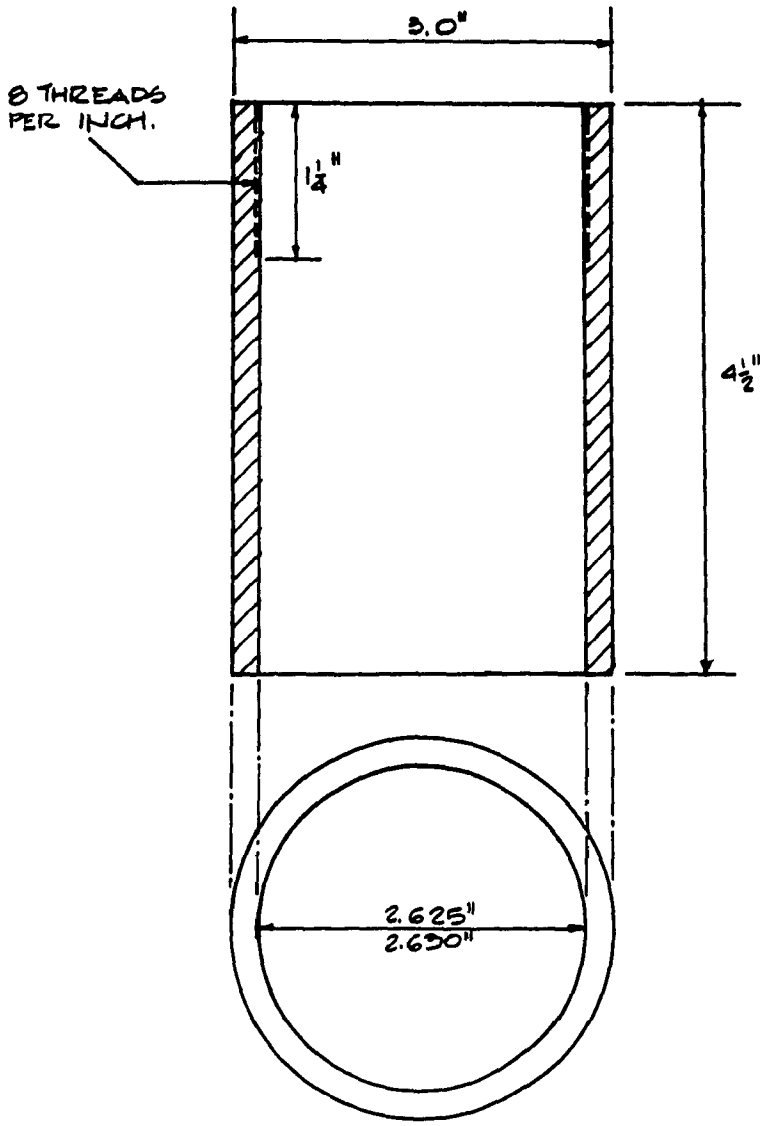

Fig. A 4.16 Steel Pipe Section (Part No. 14; Fig A 4.13)

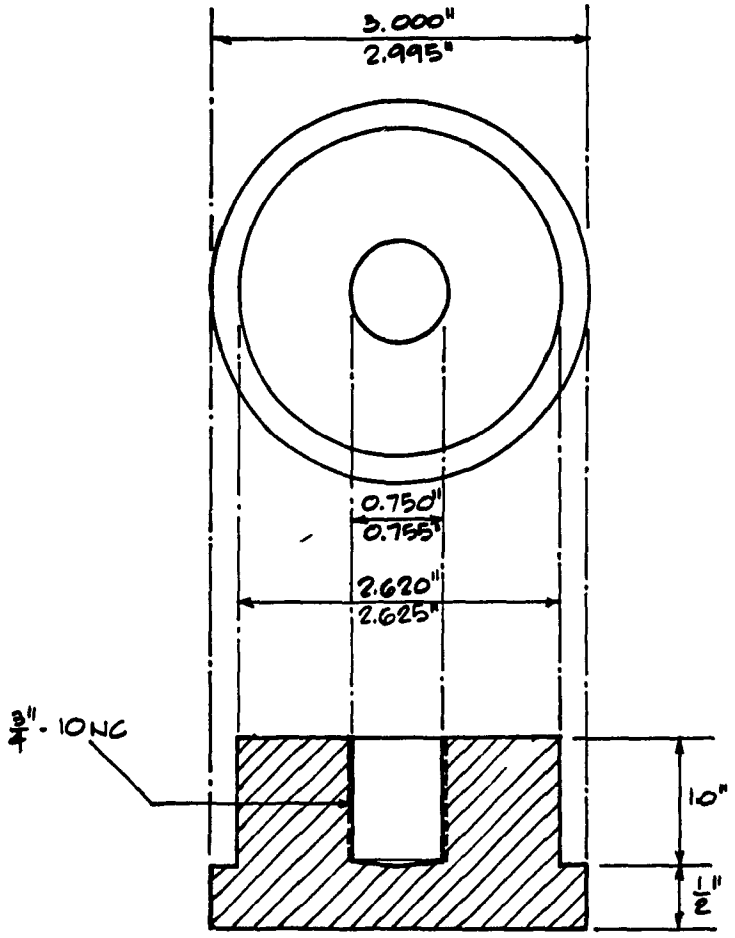

Fig. A 4.17 Pile Plug (Part No. 12; Fig A 4.13)

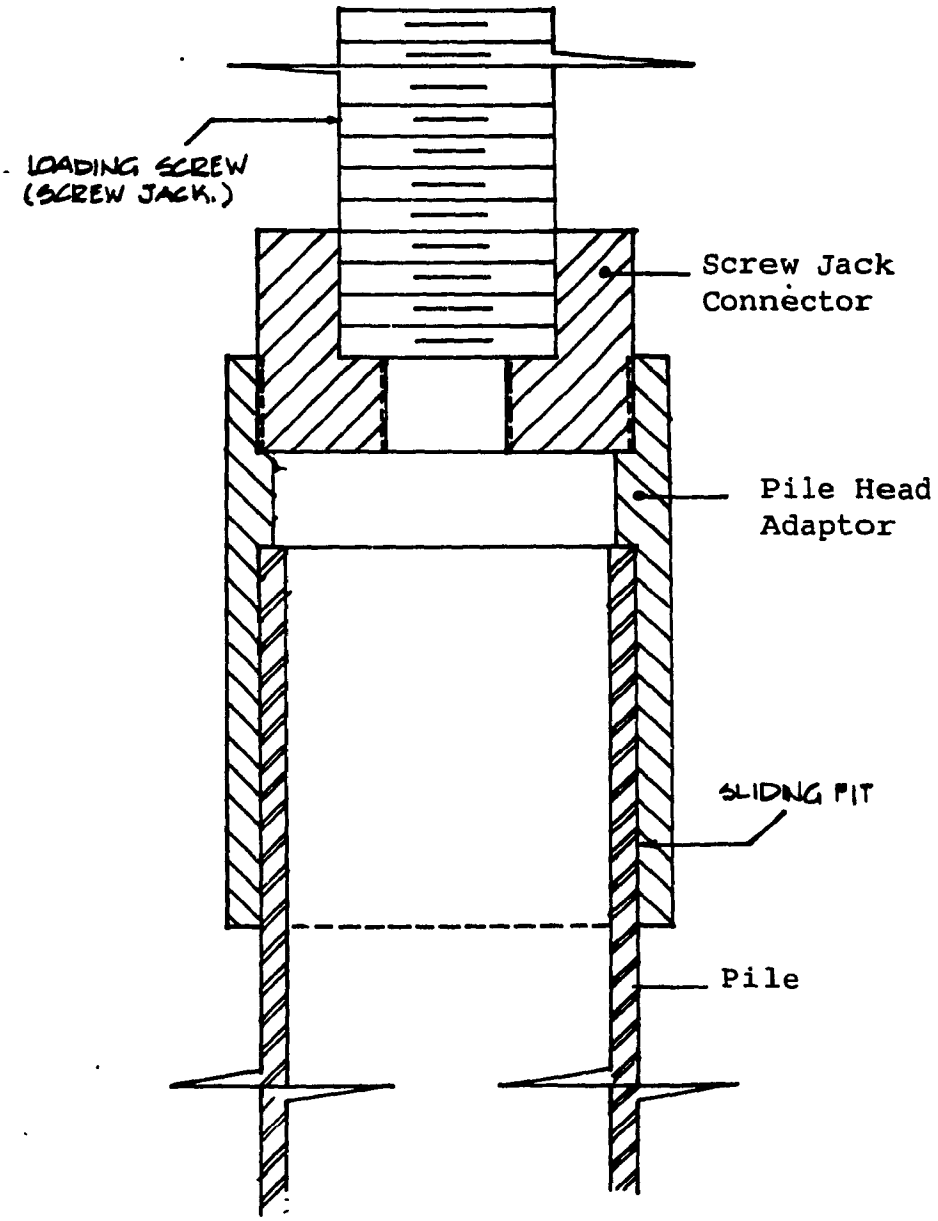

Fig. A 4.18 Arrangement for Pushing Pile Into Sand

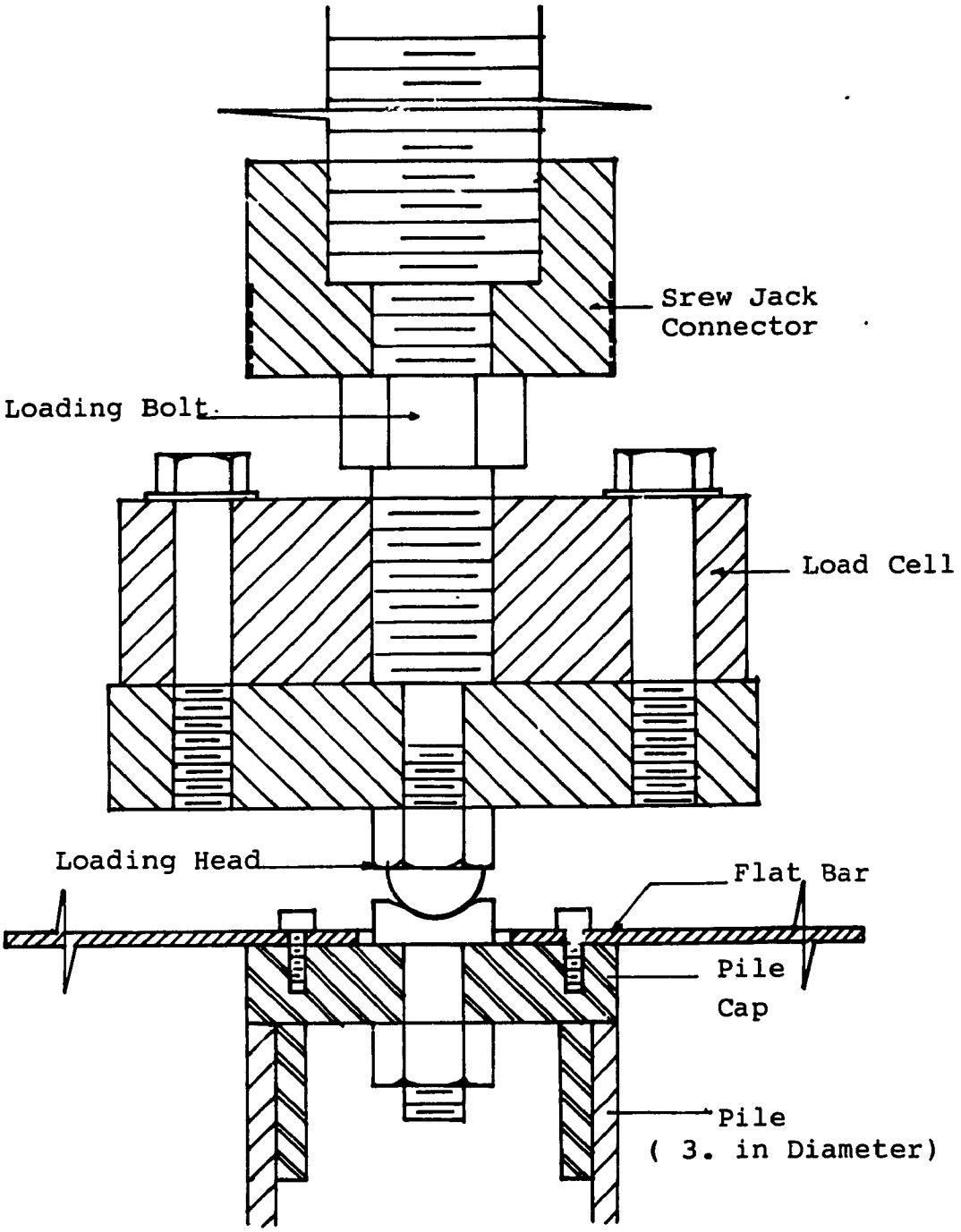

Fig. A 4.19 Load Test Arrangement for 3 in. Diameter Pile